8th International Conference on Magnetic Resonance Microscopy

The Heidelberg Conference

August 22 -26, 2005

Dokkyo University School of Medicine, Mibu, Japan

Groupement Ampère

division of spatially resolved magnetic resonance

Conference Program Abstracts

Table of Contents

WELCOME

Welcome to Mibu and Utsunomiya for the 8th International Conference on Magnetic Resonance Microscopy (ICMRM, 'Heidelberg Conference') .

The ICMRM is a meeting of the Division of Spatially Resolved Microscopy of the AMPERE Society. Starting from the first meeting in 1991 in Heiderberg, then followed by biennially. This is the first time to trip to Asia.

The Dokkyo University School of Medicine (DSUM) and its president, Dr. Akira Terano, have provided us with comfortable facilities, Seki-Minato Memorial Hall, including 400-seat lecture theater with a modern foyer for exhibitions by NMR venders and an adjacent arena for poster display.

The meeting starts with the Educational Program on Monday 22nd August. Six outstanding lectures will cover all the topics: introduction of NMR, flow and diffusion, hardware, solid MRI, biomedical MRI, and X-nuclei. After the program, the Welcome Reception will be held at Tobu Hotel Grande Utsunomiya. You can take a free bus transportation, and may have opportunities to ask questions to the lectures. (The organizer never ask you extra charge on your questions.)

The Scientific Program will open on Tuesday 23rd August with a Keynote Lecture by a Prof. Seiji Ogawa entitled 'Expectation to MR Microimaging'. The Scientific Program will include 9 invited talks, 34 contributed talks, and 8 talks by Young Investigator Awards finalists. Sessions are including hardware, engineering/flow, biomedicine, materials, gas, food/plant, and imaging methodology until at noon on Friday 26th August.

The finalists of the Young Investigator Awards were chosen by a special committee on the basis of their submitted abstracts (and also financial status of the Local organizer). The eight finalists have their conference fees waived. The winner will be announced during the banquet on Friday night, and will receive an award.

Two poster sessions are scheduled in evenings on Tuesday 23rd and Thursday 25th August. We have 68 Poster presentations and 9 Late Poster presentations. During the poster sessions, light meals will be served.

As your Local Organizer of this year, I hope you will enjoy scientific meeting. In addition, we have some social events on program. On Wednesday afternoon, two optional courses of Excursion will be planned. One is keen on science may choose the Tour to the NMR Imaging Laboratory in Tsukuba University. One is interested in the culture may visit the Mashiko Pottery, there you can make your own cup by your hands. On Friday afternoon, we will visit Nikko Shrine and its horest. After the tour we will enjoy a Dinner in the Old main dinning of Nikko Kanaya Hotel, one of the oldest resort hotel in Japan. I do hope you enjoy not only good food and drink but also a mixture of cultures in of Asia and Europe.

Division of Spatially Resolved Magnetic Resonance of AMPERE Society

The Division was founded in 1995 during the 3rd meeting on ' Magnetic Resonance Microcopy'. The purpose of the Division is to advance the subject of 'Spatially Resolved Magnetic Resonance' by means of

International Conference organized biennially in the world,
Symposia, Summer Schools and Workshops.

The main organs of the Division are:

The *Executive Committee*
The *Division Committee*
The *General Meeting*

The *General Meeting* has the final authority of the Division and takes place at the International Conferences of the Division. All participants of the conference are automatically members of the *General Meeting*. This year, the *General Meeting* will be taken from 14:00 on Thursday. Do not miss it.
The *Division Committee* is responsible for carrying out the business of the Division, including the scientific organization of the conference. The *Executive Committee* is responsible for the management, administration and finances of the Division.

The current member of the Executive Committee (Division Office) are listed below:

Chair	E. Fukushima (US)
Vice Chair	K. Kose (J)
Treasurer	R. Kimmich (G)
Secretary General	A. Haase (G)
Vice Secretary General	R. Botto (US)
Past –Chair	P. C. Lauterbur (US)
Former Conference Chair	D. C. Ailion (US)
Conference Chair	Y. Seo (J)
	K. Kose (J)
Advisors	B. Blümich (G)
	L. Berliner (US)
Honorary Member	E. R. Andrew (US)

(2001- 2005)

The Division Committee has the following members:

A. Bifone (IT)	D. Doty (US)	G. Guillot (FR)
I. Koptyug (RU)	J. Stepisnik (SL)	M. Vilfan (SL)
J. Walton (US)	A. Webb (G/US)	R. Wind (US)

(2001 - 2005)

S. Beyea (CA)	P. Callaghan (NZ)	M. Conradi (US)
F. Grinberg (G)	T. Haishi (J)	S.-I Han (US)
R. Jacobs (US)	W. Köckenberger (UK)	D. Kuethe (US)
P. McDonald (UK)	K. Minard (US)	G. Navon (IS)
K. Ogawa (J)	P. Prado (US)	B. Saam (US)
J. Seymour (US)	Y.-Q. Song (US)	S. Stapf (G)
H. Van As (NE)	Y. Xia (US)	

(2003 - 2007)

All members of the Division Office and Division Committee contributed the preparing the Scientific and Educational Program. The final program was completed with the valuable

assistance of the Local Organizing Committee and advisors:

Y. Arata	H. Kamei	N. Ishida	K. Ogawa
Y. Kanazawa	K. Saito	M. Hattori	T. Haishi
S. Matsui	F. Mitsumori	M. Murakami	T. Watanabe

Transportation

Tobe Hotel Grande Utsunomiya and Hotel Maruji are located the center of the Utsunomiya City. Free bus transportation will be available between the hotels and the meeting place in the Dokkyo University School of Medicine (DUSM). This bus service is only available in the morning and after the session as follows:

August 22 (Mon)	8:00 Departure from the hotels to the DUSM
	18:10 Departure from the DUSM to the hotels
August 23 (Tue)	8:00 Departure from the hotels to the DUSM
	21:10 Departure from the DUSM to the hotels
August 24 (Wed)	8:00 Departure from the hotels to the DUSM
	12:00 Departure from Tobu Hotel Grande
	13:30 Departure from DUSM to Tsukuba Univ.
	14:00 Departure from DUSM to Mashiko Pottery
	18:30 Arrival at the hotels
August 25 (Thr)	8:00 Departure from the hotels to the DUSM
	21:10 Departure from the DUSM to the hotels
August 26 (Fri)	8:00 Departure from the hotels to the DUSM
	12:00 Departure from Tobu Hotel Grande
	12:45 Departure from DUSM to Nikko
	22:00 Arrival at the hotels

You also can take the Tobu train (16 min) and 10 min walks to and from DUSM anytime as you like. Details will be presented in the travel information in the Registration desk.

Registration Desk

The desk in the Foyer of the Hall will be manned beginning Monday morning at 8:20 and through the conference. Office hour is listed in the below. Here you will receive the conference materials and a tote bag and hopefully be able to get useful information and help for any problems.

August 22 (Mon)	8:20 to 18:00
August 23 (Tue)	8:20 to 21:00
August 24 (Wed)	8:30 to 14:00
August 25 (Thr)	8:30 to 21:00
August 26 (Fri)	8:30 to 13:00

Oral Presentations

For oral presentations, you can use either a PC projector or an overhead projector. You can use your own PC or PC we will prepare. The PC we will prepare is running under Windows XP/Pro (English version) and you can use Office Professional 2003 Word/ Excel/ PowerPoint/ Outlook. The interface to the PC (Dell Latitude V740) is USB2.0 and CD. But DVD cannot be used.

When you use your own PC, please set up your PC during the coffee break. Then, check it works properly. The PC projector is capable to project the SXGA, but recommend to use by the XGA (1024 x 768) mode.

Preview Room

In order to confirm your presentation material or connection to the PC projector before your talk, we will prepare two identical PCs: one in the lecture hall and the other in the preview room at the 2nd floor. Two video projectors are also available to test your own PCs.

Poster Presentations

The poster boards are lined in the running road in the 2nd floor of the Arena. The number assigned to your Poster is given in the Abstract Book. The maximum mounting space available for each Poster is 120 cm wide, 180 cm high. Push-pins will be provided for mounting. Poster boards are ready at 11:30 on Monday. Posters should be mounted before the poster session on Tuesday evening. Posters should be viewable throughout the entire conference, but must be removed before the noon on Friday.

Welcome Reception (Monday 22nd August)

After the Educational Program on Monday 22nd August, two buses will depart from the DUSM at 18:10 to the Tobu Hotel Grande Utsunomiya. The Welcome Reception will be scheduled in the ShouHaku (松柏) Room in the Tobu Hotel Grande Utsunomiya (4th floor). The reception will start at 19:00 and will last until 21:00 (or whenever the meals runs out).

Lunches

Lunches will be served in the student Mensa just nearby the Seki-Minato memorial Hall from 13:00 to 14:00. In a set of conference materials, you can find a set of *Lunch-Coupon*. You can select either 'A-day Special' dish or 'Vegetarian' dish.

On Wednesday, the trip to Tsukuba University will start at 13:30. Lunch box will be provided. You need not to rush to the Mensa. Those who are going to the Pottery in Mashiko, start at 14:00, may have time to take lunch in the Mensa.

On Friday, Lunch box will be provided for participants in the Nikko Excursion.

Coffee Break and Refreshments in the Poster session

Coffee, tea and soft drink are available during the short break between the session. However, we recommend to the speakers in the next session to set your PCs at the first. Then, enjoy coffee break.

During the two Poster Sessions, light meals and drinks (including Beer) will be served in the Foyer. I remind you that taking food is prohibited in the Poster area in the Arena.

Nikko Excursion and Conference Dinner (Friday 26th August)

There are 3 buses to Nikko Excursion. Those who would like to visit Furukawa Electric Co Ltd., take the first bus. This company is the home of the superconducting wire that is in your super conducting magnet. After one hour trip in the factory, you are to visit Nikko Shrine. The rest of the two buses directly go to Nikko Shrine. In Nikko, there all of you will be divided into groups (20-23 persons), each of which will be led by a volunteer guide who can speak English.

The Conference dinner will start at 18:00 in the Old main dinning of the Nikko Kanaya Hotel. The dinner is French cuisine with fish and beef. For your convenience, we offer you two choices: one with fish and fish, and a vegetarian dish. You can find the menu listed in the registration desk, and should mark one of them at the Registration desk by the evening of Tuesday. After the dinner and cerebration on the YIA finalists, buses will depart at 21:00 to the hotels in Utsunomiya.

Optional Excursions (Wednesday 24th August)

1. Mashiko Pottery

12:00	Departure from the Tobu Hotel Grande to DUSM
14:00	Departure from DUSM
15:00	Mashiko Pottery
	Mashikoyaki experience: make your cup by your hand.
	Walking and Shopping in the Mashiko Pottery
17:30	Departure from Mashiko to the hotels

Make a reservation at the registration desk (42 persons limited) by the lunch time on Tuesday. The fee is 3,000yen per person. (Additional delivery fee is required to receive the product, and may ask you to fill a shipping form. It will take few weeks to be finished, you may get your cup by this Christamas.)

2. Tukuba University and Mount Tsukuba

13:30	Departure from DUSM (Lunch box provided)
15:00	NMR Imaging Laboratory Tour
	Mount Tukuba Tour
17:30	Departure from Tsukuba to the hotels

The group of Prof. Kose has a number of MRI systems of which magnetic field strength is from about 0.1 T to 9.4 T. However, all of the MRI consoles have an identical architecture. Graduate students will show and explain how the MRI systems are used. This is a free tour, but it is necessary to make a reservation at the registration desk (42 persons limited) by the lunch time on Tuesday.

Sponsor ship:

We are grateful to the following corporate sponsors for the this conference.

Bruker Biospin
Dokkyo University School of Medicine
Japan Superconductor Technology
JEOL
Kyouei Shoji
LA Systems
Magritek
MR Technology
Tochigi Prefecture
VARIAN

We also thank to the following technical supporters fro this conference.

Center of Medical Informatics (DUSM)
International Researchand Educational Centre (DSUM)

Maps

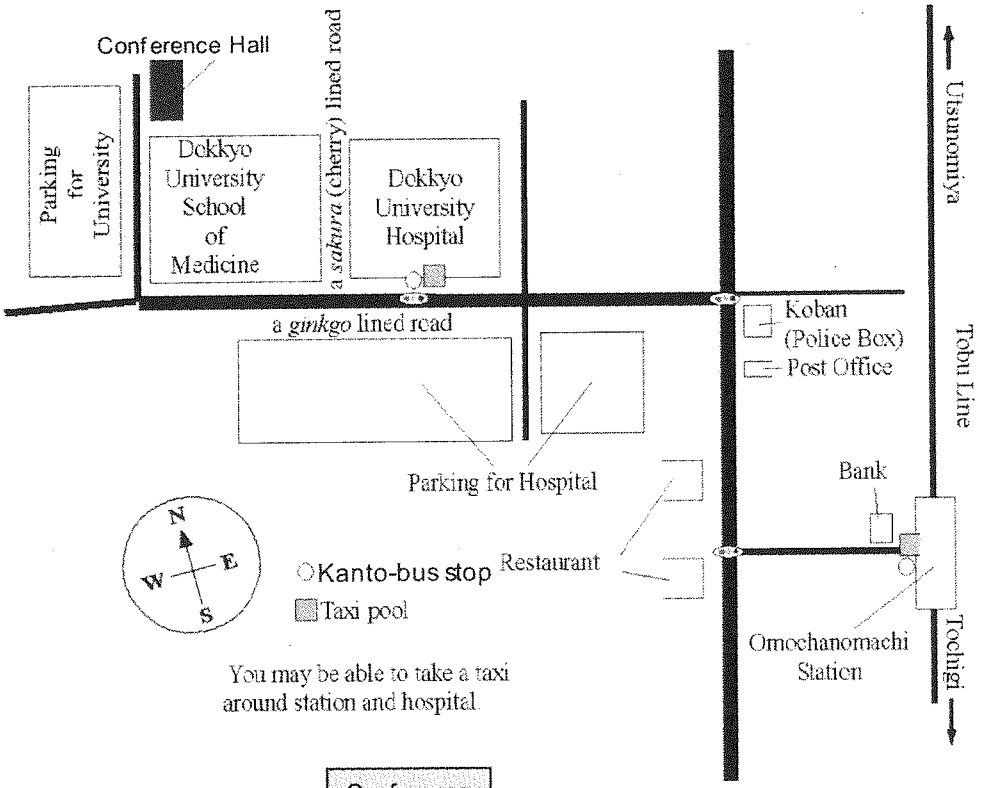
Conference Hall
Parking for University
Dokkyo University School of Medicine
a *sakura* (cherry) lined road
Dokkyo University Hospital
Utsunomiya
Tobu Line
Koban (Police Box)
Post Office
a *ginkgo* lined road
Parking for Hospital
Bank
N
W
E
S
Kanto-bus stop
Restaurant
Taxi pool
Omochanomachi Station
Tochigi
You may be able to take a taxi around station and hospital.

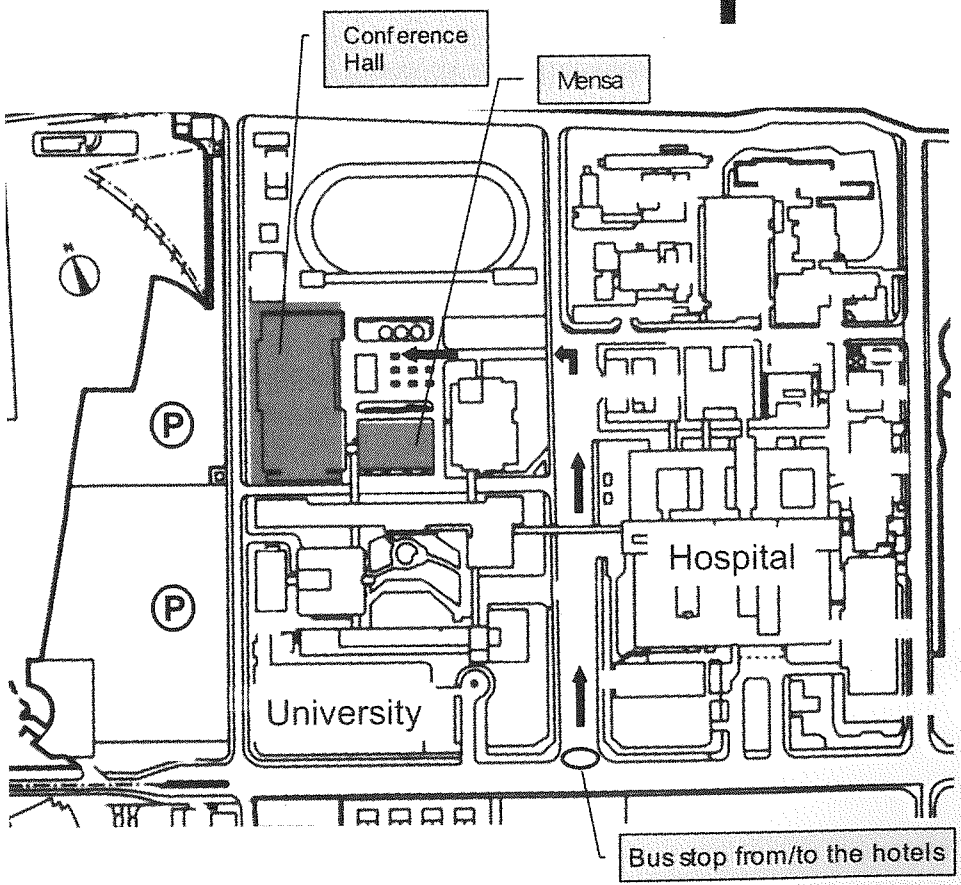
Conference Hall
Mensa
P
P
Hospital
University
Bus stop from/to the hotels

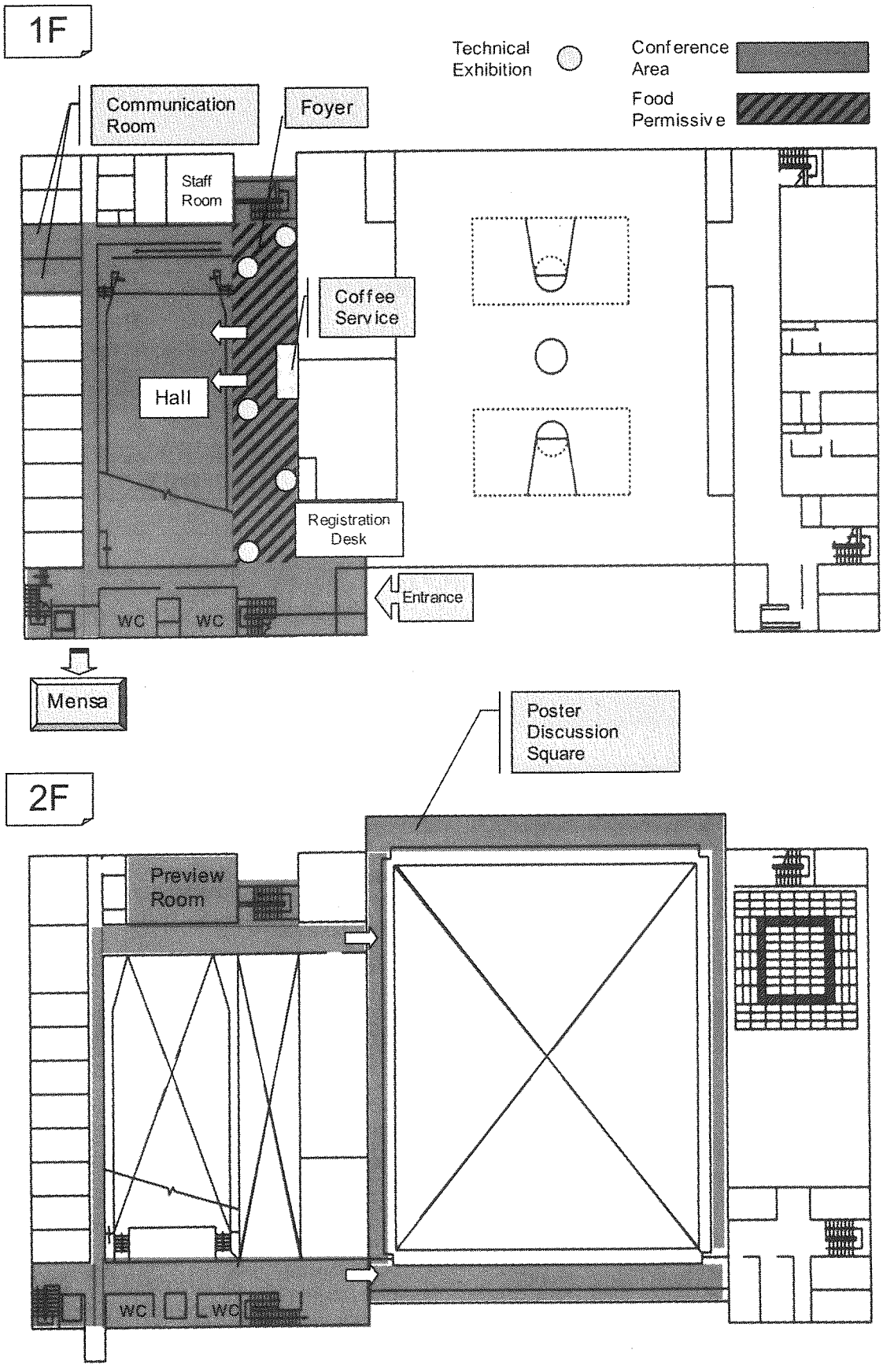
1F
Technical Exhibition
Conference Area
Food Permissive
Communication Room
Foyer
Staff Room
Coffee Service
Hall
Registration Desk
Entrance
WC
WC
Mensa
Poster Discussion Square
2F
Preview Room
WC
WC

Corporate Sponsorship of the 8th ICMRM

We gratefully acknowledges the financial support of our sponsors:

Bruker Biospin

Dokkyo University School of Medicine

Japan Superconductor Technology

JEOL

Kyouei Shoji

LA Systems

Magritek

MRTechnology

Tochigi Prefecture

VARIAN

8th ICMRM Educasional session program

Monday	Aug.22,2005		
9:15-9:30	Greetings and Announcements		
Educational Lecturer(1) Chair :			
Time	**Lecturer**	**Title**	
9:30-10:30	Eiichi Fukushima	Introduction to NMR : Nuts and bolts approach	E1
10:30-11:30	Paul Callaghan	MRI,flow,and diffusion	E2
11:30-12:00	Coffee Break		
12:00-13:00	Bernhard Blümich	Hardware : NMR in inhomogeneous fields	E3
13:00-14:10	Lunch Break		
Educational Lecturer(2) Chair : Yang Xia			
Time	**Lecturer**	**Title**	
14:10-15:10	Bruce Balcom	MRI of Solid-like Materials	E4
15:10-15:40	Coffee Break		
15:40-16:40	Axel Haase	Biomedical MR microscopy	E5
16:40-17:40	Gil Navon	X-Nuclei in Biological MR Microscopy	E6
19:00-	Welcome Reception		

Scientific Program

Tuesday	Aug.23,2005			
9:30-9:45	Greetings and Announcements			
Opening Lecture Chair : Katsumi Kose				
Time	**Author(s)**	**Affiliation**	**Title**	**Page**
9:45-10:45	**Seiji Ogawa**	Ogawa Laboratories for Brain Function Research, Hamano Life Science Research Foundation, Japan	Expectation to MR Microimaging	
10:45-11:00	Coffee Break			
New Frontiers in MRI / MRM Chair : Siegfried Stapf				
Time	**Author(s)**	**Affiliation**	**Title**	**Page**
11:00-11:20	**Mladen Barbic**	California State University,USA	Ferromagnetic Nanostructures for Atomic Resolution Magnetic Resonance Microscopy	O1
11:20-11:40	**Vasiliki Demas**, John Franck, Rachel Martin, Alejandro Bussandri, Pablo Prado, Jeffrey Reimer, and Alexander Pines	University of California,USA	Methodology and Hardware Development on Ex-Situ NMR/MRI: Let the Spins do the Work!	O2

11:40-12:00	**Federico Casanova**, Juan Perlo, and Bernhard Blümich	ITMC - RWTH-Aachen,Germany	High-resolution sample profiling by single-sided NMR	O3
12:00-12:20	C. C. Poirier, Yang Zhi, **B. Newling**	University of New Brunswick,Canada	Mapping Fast, Turbulent Gas Flow	O4
12:20-12:40	J. M. Tyszka, E. L. Bearer, and **R.E. Jacobs**	California Institute of Technology,USA	Correlating histology with the diffusion tensor: Specific findings in the dysmyelinating shiverer mouse	O5
12:40-13:00	**Yutaka Sasaki**, Takayoshi Tanaka, and Takao Mizusaki	Kyoto University,Japan	Development of Ultra Low Temperature Magnetic Resonance Microscope	O6
13:00-14:20	Lunch Break			

Tuesday	**Aug.23**			
Hardware Chair : Tomoyuki Haishi				
Time	**Author(s)**	**Affiliation**	**Title**	**Page**
14:20-14:40	**P. Blümler**, H. Raich, C. Bauer, G. Jeschke	Max Planck Institute,Germany	NMR-MANDHALAS:Mobile NMR, MRI and EPR	O7
14:40-15:00	**Pablo Prado**, Serge Bobroff, Alejandro Bussandri, and Jess Lawton	GE Security,USA	Magnet, Coil, and Gradient Set for Single-Sided MR	O8
15:00-15:20	**Andrew E. Marble**, Igor V. Mastikhin, Bruce G. Colpitts, and Bruce J. Balcom	University of New Brunswick,Canada	An analytical target field approach for B_0 control in unilateral NMR	O9
15:20-15:40	**V.C. Behr**, I. Kaufmann, A. Haase, P. Jakob	University of Würzburg,Germany	A novel modular probe base for multi-channel multi-nuclei MRI and MRS experiments	O10
15:40-16:00	Coffee Break			
Engineering/Flow Chair : Steve Altobelli				
Time	**Author(s)**	**Affiliation**	**Title**	**Page**
16:00-16:30	**Kuniyasu Ogawa**, Yoshiro KAWASOE	Keio University,Japan	MRI-monitoring for hydrate formation process:Time-evolution maps of gas-storage ratio in gas-hydrate mash	L1
16:30-17:00	Eric Sigmund, Xiaoping Tang, and **Yi-Qiao Song**	Schlumberger-Doll Research, USA	Simultaneous measurement of diffusion along multiple directions and imaging application- An ultrafast technique for diffusion and diffusion anisotropy	L2
17:00-17:20	**I.V. Mastikhin**, B.Newling	University of New Brunswick,Canada	MRI measurements of cavitating fluid	O11
17:20-17:40	Eiichi Fukushima & Arvind Caprihan	New Mexico Resonance,USA	NMR of Granular Materials	O12

17:40-18:00	Artem G. Goloshevsky; **Jeffrey H. Walton**; Young Jin Choi; Jeffrey S. de Ropp; Scott D. Collins; Michael J. McCarthy	UC Davis,USA	Viscosity Measurements via a Low Field MRI Viscometer	O13
18:00-18:20	**Steve Altobelli**, Lisa Mondy, Rekha R. Rao	New Mexico Resonance,USA	NMR Profilometry and Normal Stress Differences in Concentrated Suspensions	O14
8:20-	**Poster Session**			

Wednesday	**Aug.24,2005**			
Biomedicine	**Chair : Yoko Kanazawa**			
Time	**Author(s)**	**Affiliation**	**Title**	**Page**
9:00-9:30	**Yang Xia**	Oakland University, USA	Microscopic Imaging of Articular Cartilage:Loading-induced Adaptation of Molecular Matrices	L3
9:30-9:50	**Masayuki Yamaguchi**, Fumiyuki Mitsumori, Hidehiro Watanabe, Nobuhiro Takaya, and Manabu Minami	National Institute for Environmental Studies University of Tsukuba,Japan	Visualization of seminiferous tubules of rat testes by high resolution MR imaging	O15
9:50-10:20	**Ichio Aoki**	Meiji University of Oriental Medicine, Japan	Manganese-enhanced MRI	L4
10:20-10:40	**E.L. Bearer**, X. Zhang, J.M. Tyszka and R. E. Jacobs	Brown Medical School,USA	Using transport to map the brain: Stereotaxic Mn^{2+} injection and tract tracing by μMRI in animal models	O16
10:40-11:00	**Armin Purea**, Robert Hock, Peter M Jakob, Andrew G Webb	University of Würzburg,Germany	NMR microscopy and relaxation time quantification of *Xenopus laevis* embryos using antibody-labeled iron oxide particles	O17
11:00-11:20	Coffee Break			
Material(1)	**Chair : Farida Grinberg**			
Time	**Author(s)**	**Affiliation**	**Title**	**Page**
11:20-11:50	**Igor V. Koptyug**	International Tomography Center,Russia	Multinuclear imaging of liquids, gases and solids: applications in catalysis and beyond	L5
11:50-12:10	Quan Chen and **Bruce J. Balcom**	University of New Brunswick,Canada	A Single-Shot Method for Capillary Pressure Measurement of Porous Media Using Centrifuge and SPRITE MRI	O18
12:10-12:40	**Rainer Kimmich**,Bogdan Buhai	Universität Ulm,Germany	NMR mapping of electroosmotic flow in pore networks	L6

12:40-13:10	**Joseph D.Seymour**	Montana State University,USA	Magnetic Resonance Microscopy of Scale Dependent Transport Phenomena:Bioactivity in Porous Media	L7
13:10-	Excursion (Tsukuba or Mashiko)			

Thursday	Aug.25,2005			
Young Investigator Awards(1) Chair : Steven D. Beyea				
Time	**Author(s)**	**Affiliation**	**Title**	**Page**
9:00-9:25	**Mi Jung Kim** and A. K. Khitrin	Kent State University,USA	MRI of objects with dipolar-broadened spectra using soft excitation pulses	Y1
9:25-9:50	**Alexandre A. Khrapitchev**, Ben Newling and Bruce J. Balcom	University of New Brunswick,Canada	Contrast preparation for SPRITEly methods	Y2
9:50-10:15	**C.H. Arns**, A.P. Sheppard, R.M. Sok, and M.A. Knackstedt	Australian National University,Australia	NMR as a probe of pore geometry, permeability, and fluid saturation: a computational analysis using micro-CT images	Y3
10:15-10:40	**Antoine Lutti** and Paul T. Callaghan	MacDiarmid Institute ,New Zealand	Study of a lamellar system by diffusion measurement	Y4
10:40-11:00	Coffee Break			
Young Investigator Awards(2) Chair : Pablo Prado				
Time	**Author(s)**	**Affiliation**	**Title**	
11:00-11:25	**Andrea Amar**, Siegfried Stapf, Bernhard Blümich	RWTH Aachen,Germany	Velocity distributions in single levitated drops by NMR	Y5
11:25-11:50	**Juan Perlo**, Vasiliky Demas, Federico Casanova, Carlos A. Meriles,Jeffrey Reimer, Alexander Pines, Bernhard Blümich	RWTH-Aachen,Germany	High-Resolution NMR spectroscopy with a Portable Single-Sided Sensor	Y6
11:50-12:15	**Susie Y. Huang,** Sandip Datta, Massoud Akhtari, Gary W. Mathern, Harry V. Vinters,Dennis J. Chute, Yung-Ya Lin	University of California,USA	Avalanching Amplification of MR Imaging Contrast by Feedback Fields for Lesion Characterization and Detection	Y7
12:15-12:40	**Shin Utsuzawa**	MRT / Tsukuba Univ.Japan	Non-destructive observation of pine wilt disease using an open-type NMRI system	Y8
12:40-14:00	Lunch Break			

Thursday	Aug.25			
14:00-14:30	General Division Meeting			
Gas NMR/MRI Chair : Koji Saito				
Time	**Author(s)**	**Affiliation**	**Title**	**Page**
14:30-14:50	**Koji Saito** , Moriaki Hatakeyama , Satoshi Mitani and Isao Mochida	Nippon Steel Corporation,Japan	Hp-Xe NMR Study on Activated Carbon Electrode in EDLC	O19
14:50-15:10	**Ross Mair**; Tina Pavlin, Ruopeng Wang; Matthew Rosen; Donald Candela; Ronald Walsworth	Harvard-Smithsonian Center for Astrophysics,USA	Measurement of Inter-Phase Exchange Rates and Bubble Velocity in Gas-Fluidization with Laser-polarized ^{129}Xe	O20
15:10-15:30	**Hirohiko Imai**, Michiko Narazaki, Hiroyuki Inoshita, Atsuomi Kimura, and Hideaki Fujiwara	Osaka University,Japan	Handy Production of Hyperpolarized ^{3}He and MRI of Mouse Lung	O21
15:30-15:50	**Natalie Adolphi** and Dean Kuethe	New Mexico Resonance,USA	Imaging V/Q in Lungs by Mapping the ^{19}F T_1 of Inert Fluorinated Gases	O22
15:50-16:10	**Dean O. Kuethe** and Markus D. Scholz	New Mexico Resonance,USA	Detecting cracks by imaging inert fluorinated gases	O23
16:10-16:30	Coffee Break			
Methods Chair : Igor V. Koptyug				
Time	**Author(s)**	**Affiliation**	**Title**	**Page**
16:30-17:00	**M.L.Johns**, L.F.Gladden, A.J.Sederman, D.I. Wilson and J.P.Hindmarsh	University of Cambridge, UK	Magnetic Resonance Studies of Drop Freezing Processes	L8
17:00-17:20	**Gregory Stoch**, Bruce Balcom	University of New Brunswick, Institute of Nuclear Physics PAN,Poland	Elementary Premises for Pure Phase Encoding -The Role of Time.	O24
17:20-17:40	**Nikolas Salisbury Andersen** & Walter Köckenberger	University of Nottingham,UK	Fast Gradient-Assisted Correlation Peak Imaging	O25
17:40-18:00	**Yung-Ya Lin**, Susie Y. Huang, Sandip Datta	University of California,USA	Hurricanes in a Tube: Visualizing and Applying Spin Turbulence in MR Microscopy	O26
18:00-18:30	**Shin-ichiro Meguro**	Furukawa Electric Co. Ltd.	Key Technologies for Superconductivity	SE1
18:30-	**Poster Session**			

Friday	Aug.26,2005			
Food/Plant Chair : Walter Köckenberger				
Time	**Author(s)**	**Affiliation**	**Title**	**Page**
9:00-9:20	**Nobuaki Ishida**	Food Research Institute, Japan	MRI of Foods	L9
9:20-9:40	Heather Hickey, Bryce MacMillan, **Ben Newling**, Manoharan Ramesh, Paul Van Eijck, Bruce Balcom	University of New Brunswick,Canada	Magnetic Resonance Measurements of Starch Food Samples to Determine Spatially Resolved Oil and Water Content	O27
9:40-10:00	Kentaro Irie, Akemi K. Horigane, Shigehiro Naito, Akio Fujita, Hirofumi Motoi, and **Mitsuru Yoshida**	Initio Foods Inc,Japan National Food Research Institute,Japan	Observation of Moisture Distribution in Various Types of Cooked Spaghetti	O28
10:00-10:20	**Akemi K. Horigane**, Hitoshi Takahashi, Sachio Maruyama, Kenichi Otsubo and Mitsuru Yoshida	National Food Research Institute,Japan	A Study of Moisture Distribution in Rice Grains during Soaking Using Gradient Echo Method	O29
10:20-10:40	**Carel Windt**,Frank Vergeldt and Henk Van As	Wageningen University,Netherlands	MR flow imaging in plants:Using new techniques to solve old questions	O30
10:40-11:00	Maks Merela, Primoz Oven and **Igor Sersa**	Jozef Stefan Institute,Slovenia	MR Study of Morphology and Water Content in Living Tree Tissues	O31
11:00-11:20	Coffee Break			
Material(2) Chair : Kikuko Hayamizu				
Time	**Author(s)**	**Affiliation**	**Title**	**Page**
11:20-11:40	**E. Karakosta** and P. J. McDonald	University of Surrey,UK	Magnetic Resonance Imaging of Soluble Drug Release from non-Swelling Polymer Matrices	O32
11:40-12:00	**Shohji TSUSHIMA**, Kazuhiro TERANISHI, Shuichiro HIRAI	Tokyo Institute of Technology,Japan	Determination of Water Transfer Coefficient into a Polymer Electrolyte Membrane in a Fuel Cell by Time-lapse Magnetic Resonance Imaging	O33
12:00-12:20	Daniel T. Howe, **Joseph D. Seymour**, Sarah L. Codd, Scott C. Busse, Eric S. Peterson, E. Hubble Werre and Benjamin F. Taylor	Montana State University,USA	MRM Measurement of Material Heterogeneity in Polymer Electrolyte Membranes	O34
12:20-	Conference Tour - Banquet			

Poster

Category : Hardware			
No.	**Author(s)**	**Affiliation**	**Title**
P1	**Eiichi Fukushima**	New Mexico Resonance,USA	A concentric barrel-type magnet assembly for unilateral NMR
P2	Andrew E. Marble, **Igor V. Mastikhin**,Bruce G. Colpitts, and Bruce J. Balcom	University of New Brunswick,Canada	A Fourier-series based technique for simulating permanent magnets with applications in unilateral MR
P3	Nathan Kelso, Kristie Koski, Michael Moessle, Whittier Myers, John Clarke, **Jeffrey Reimer**	University of California,USA	SQUID-Detected Magnetic Resonance Elastography in Microtesla Magnetic Fields
P4	**Andrew F. McDowell**, Eiichi Fukushima	New Mexico Resonance,USA	Low-field micro-coil probe development for portable NMR
P5	**Mikio Suga**, Kotaro Minato	Chiba University,Japan	Development of Local Shear Modulus Measurement System by MR Microscope
P6	Leo L. Tsai; Matthew S. Rosen; **Ross W. Mair**;Ronald L. Walsworth	Harvard-Smithsonian Center for Astrophysics,USA	Construction and Initial Testing of an Optimized, Open-Access, Human-Scale, Very-Low-Field MRI Magnet for Orientational Lung Study
P7	**Gregory Stoch**, Bruce Balcom	University of New Brunswick, Institute of Nuclear Physics PAN,Poland	Ultra Fast Acquisition Open Subsystem for EPRI Measurement
P8	**Tomoyuki HAISHI**, Masaaki Aoki, Eiji Sugiyama	MRTechnology, Inc.,Japan	Development of a 2.0 Tesla permanent magnetic circuit for NMR/MRI
P9	**Shin Utsuzawa**, Ron Kemmer, Yoshito Nakashima	MRT / Tsukuba Univ.,Japan	Unilateral NMR system by using a novel barrel shaped magnet
P10	**Shin Utsuzawa**, Kenji Fukuda, Daisuke Sakaue	MRT / Tsukuba Univ.,Japan	Portable NMRI system for plant study by using a compact permanent magnet
P11	**Sadanori Tomiha**, Takeshi Furuya, Nachiko Iita, Fumi Okada, Katsumi Kose,Tomoyuki Haishi	Tsukuba Univ.,Japan	Development of compact MRI systems for bone density measurements
P12	**Shinya Handa**, Sadanori Tomiha, Katsumi Kose, Tomoyuki Haishi	Tsukuba Univ.,Japan	Optimized system design and construction of a compact whole hand scanner
P13	**Ryo Tanaka**, Norio Ohtake, Mineyuki Hattori, Koji Saito	Toyoko Kagaku Co. Ltd,Japan	Development of Automatic Generator for Hyperpolarized ^{129}Xe Gas for NMR/MRI Applications
Category : Methods			
No.	**Author(s)**	**Affiliation**	**Title**
P14	**Nicole Seiberlich**, Daniel Haddad, Mark Griswold, Andrew Webb, Peter M. Jakob	University of Würzburg,Germany	Sensitivity Advantages of Chemical Shift Imaging in Magnetic Resonance Microscopy

P15	Yuesheng Cheng, **Bruce Balcom**	University of New Brunswick,Canada	CO Oxidation over CuO Catalyst Studied by ^{13}C MRI
P16	C. Coarna, T. J. Marshall, **B. Newling**	University of New Brunswick,Canada	Shaped Pulses in Inhomogeneous Magnetic Fields
P17	**G.Fagiolo**, D. Rourke, W. Köckenberger	University of Nottingham,UK	Selective excitation pulse design for imaging short-T_2 materials
P18	**Gregory Stoch**, Bruce Balcom	University of New Brunswick, Institute of Nuclear Physics PAN,Poland	Does a k-space span limitation effect MRI resolution?
P19	**Nachiko Iita**, Katsumi Kose	Tsukuba Univ.,Japan	Development of a projection reconstruction method for a desktop MR microscope using a permanent magnet
P20	**Fumi Okada**, Shinya Handa, Katsumi Kose	Tsukuba Univ.,Japan	Development of a 3D image distortion correction method

Category : Diffusion/Flow

No.	Author(s)	Affiliation	Title
P21	Jason P. Hindmarsh, Jiahong Su, John Flanagan and Harjinder Singh	Massey University,New Zealand	PFG-NMR Analysis of W/O/W Emulsions with Inter-Compartment Exchange
P22	**Kikuko Hayamizu** and Mineyuki Hattori	National Institute of Advanced Industrial Science and Technology,Japan	Behaviors of ions in liquid electrolytes under the steady direct current measured by multi-nuclear DC-PGSE NMR
P23	Ziheng Zhang,Alexei V.Ouriadov,Chris Willson,Bruce J Balcom	University of New Brunswick,Canada	Membrane Gas Diffusion Measurements with MRI
P24	**M.E. Komlosh**, R. Z. Freidlin, F. Horkay, Y. Assaf, P. J. Basser	NICHD,USA	Detecting microscopic anisotropy in gray matter and in a tissue phantom using d-PGSE
P25	Andrew J. Sederman, Michael D. Mantle, Christopher P. Dunckley, Zhenyu Huang and Lynn F. Gladden	University of Cambridge,UK	*In situ* MRI Measurement of Conversion and Selectivity within a Three-Phase Trickle-Bed Reactor
P26	**Justin P. Gage**, Joseph D. Seymour, Robert S. Maier, Sarah L. Codd and H. Ted Davis	Montana State University,USA	MR Measurement of the Impact of Column Walls on the Dispersion Time Dependence of Flow in a Cylindrical Bead Pack
P27	C. C. Poirier, B. Colpitts, **B. Newling**	University of New Brunswick,Canada	A Fast-Switching, Large-Volume Gradient Set for Imaging Fast Flows
P28	**G. Maddinelli**, S. Carminati and A. Guarneri	EniTecnologie S.p.A,Italy	NMR Imaging study of flow behaviour of fluids viscosified by polymers
P29	**Sarah L. Codd**, Erica J. Gjersing, Joseph D. Seymour, Philip S. Stewart and Kathryn O. Hoyt	Montana State University,USA	Magnetic resonance microscopy analysis of advective transport in a biofilm reactor
P30	**Jennifer R. Brown**, Sarah L. Codd, Giles R. Cokelet and Joseph D. Seymour	Montana State University,USA	NMR Determined Velocity and Hematocrit Profiles in a Couette Viscometer
P31	Silke Harms, **Siegfried Stapf**, Bernhard Blümich	RWTH Aachen University,Germany	Dynamics in gas-fluidized granular systems by NMR velocity imaging

P32	**Ursa Mikac**, Jasna Urbanija and Igor Sersa	Jozef Stefan Institute,Slovenia	Convection Flow Imaging by Dynamical MR Microscopy
Category : Gas NMR/MRI			
No.	**Author(s)**	**Affiliation**	**Title**
P33	**I.V. Mastikhin**, B.Newling	University of New Brunswick,Canada	MRI detection of acoustic streaming in gases
P34	**Dean O. Kuethe**and Andrew F. McDowell	New Mexico Resonance,USA	Measuring nanopore sizes with the T_1 of CF_4
P35	**Dean O. Kuethe** and Natalie L. Adolphi	New Mexico Resonance,USA	Imaging SF_6 and C_2F_6 gases in lab rat lungs: To avoid cooking larger animals, use C_2F_6
P36	**Michiko Narazaki**, Hirohiko Imai, Tetsuya Wakayama, Atsuomi Kimura, and Hideaki Fujiwara	Osaka University,Japan	Estimation of the True Relaxation Time T_1 of Hyperpolarized ^{129}Xe Gas in Mouse Lung: Calculation on a Ventilation Model with the Aid of Normal Gas at Thermal Equilibrium
P37	Takako Yamamoto, **Kiyoshi Ishikawa**, and Yoshihiro Takagi	University of Hyogo,Japan	Spin relaxation of polarized Xe atoms at the liquid-solid interface
P38	**Tatsuya Asanuma**, Takashi Hiraga, and Mineyuki Hattori	AIST,Japan	Long-distant delivery of hyperpolarized ^{129}Xe using a capillary tube
P39	**P. P. Zänker**, P. Blümler, H. D. Lemke, H. W. Spiess	Max Planck Institute for Polymer Research,Germany	Direct Molecular Solution of Hyperpolarized Gases through Hollow Fiber Membranes
P40	**Kerstin Münnemann**, Bernard Blümich, Wolfgang Häsing, Stephan Appelt	RWTH Aachen,Germany	On line monitoring of polymerisations by hyperpolarized ^{129}Xe NMR
Category : Materials			
No.	**Author(s)**	**Affiliation**	**Title**
P41	F. Marica, Q. Chen, A. Hamilton, C. Hall, T. Al, and **B.J. Balcom**	University of New Brunswick,Canada	Spatially Resolved Measurement of Core Porosity
P42	**Makoto Yamaguchi**, Kazunori Suzuki, Stephen Altobelli, and Dean Kuethe	Institute of Research and Innovation,Japan	Magnetic Resonance Imaging of Water Distribution in Thermally and Mechanically Fractured Granite
P43	**Kaz Nagashima**	Tokyo Magnetic Resonance Inc,Japan	Influences of Magnetic Impurities on Proton Spin Relaxation of Water in Clay
P44	**Steve Altobelli**, Lisa Mondy, Rekha R. Rao, Ed Russick	New Mexico Resonance,USA	^{1}H and ^{19}F MRI of Physically Blown Foam
P45	Joshua M. Bray , Steven D. Beyea , Mark Filiaggi & Carlo Petrone	Institute for Biodiagnostics (Atlantic), Dalhousie University,Canada	NMR Microscopy of Calcium Polyphosphate Drug-Delivery Bioceramics
P46	**Joshua J. Young**, Bruce J. Balcom, Theodore W. Bremner, M.D.A. Thomas	University of New Brunswick,Canada	Lithium Imaging in Concrete Materials
P47	Xiaohong Ren, Dahai Tang, **Siegfried Stapf**, Andreas Jess, Bernhard Blümich	RWTH Aachen University, Germany	Parameter imaging for analysing the spatial distribution of coke residues in porous catalyst pellets

P48	Xiaohong Ren, **Siegfried Stapf**, Bernhard Blümich,Jie Zhou, Geng Li, Yongrong Yang	RWTH Aachen University, Germany	NMR studies on rubber reinforcement properties of pyrolysis carbon black
P49	**Farida Grinberg**	University of Leipzig,Germany	Structure and Molecular Dynamics of Constrained Soft Materials as Studied by NMR and MRI Techniques[1]

Category : Food/Plant			
No.	**Author(s)**	**Affiliation**	**Title**
P50	**Bruce J. Balcom**, Kumud Deka, Bryce MacMillan, Alejandro G. Marangoni,Gregory R. Ziegler and Ben Newling	University of New Brunswick,Canada	Spatial Mapping of Solid and Liquid Lipid in Confectionery Products using a 1D Pure Phase Encode MRI Technique
P51	**Akemi K. Horigane**, Kentaro Irie, Shigehiro Naito, Tatsurou Maeda, Hirofumi Motoil and Mitsuru Yoshida	National Food Research Institute,Japan	Estimation of Ungelatinized Region in Cooked Spaghetti from Moisture Distribution and Mechanical Property
P52	Shinichiro Kuroki, Jeffrey H. Walton, Yoshinori Kawagoe, Yoshio Makino, Seiichi Oshita	Hiroshima University Collaborative Research Center,Japan	The relationship between NMR parameters and respiratory metabolism inside cucumber fruit after harvest
P53	**Suravoot YOOYONGWECH**, Akemi K. HORIGANE, Mitsuru YOSHIDA, Masami YAMAGUCHI, Sumiko SUGAYA and Hiroshi GEMMA	University of Tsukuba,Japan	Water Behavior and Water Channel Gene Expression in Vegetative and Flower Dormant Buds of Peaches Having Different Chilling-requirement during Winter Period
P54	A. Pohlmeier, J. Lindenmair, A. M. Oros-Peusquens and **P. Blümler**	Institute Phytosphere ICGIII,Germany	Visualisation of the water distribution in plant roots and model soils for the study of root/soil interactions

Category : Biomedicine			
No.	**Author(s)**	**Affiliation**	**Title**
P55	**Fuminori Sugihara**, Sewon Ki, Koji Kasahara,Kaoru Serizawa, Akiko Kobayashi,Kiyoshi Watanabe, Masahiro Shirakawa, Tetsuro Kokubo	Yokohama City Univ,Japan	Development of a novel reporter system using NMR and MRI to measure gene expression in living cells
P56	**A Haapanen**, U AboRamadan, C von Schantz, J Fuhrmann, TJ Jentsch, T Braulke, P Saftig, A Jalanko, T Autti and J Tyynelä	University of Helsinki,Finland	Magnet resonance imaging of NCL- and NCL related mouse models

P57	Laurel Sillerud, **Natalie Adolphi**, Rita Serda, Marco Bisoffi and Dean Kuethe	New Mexico Resonance, USA	Development of Targeted Contrast Agents for MRI of Prostate Cancer
P58	J. Munasinghe, M.Acosta, M. Banerjee, A. Silva, A. Koretsky, M Rogawski, A. Yamaguchi, W. Theodore	National Institute for Neurological Disorders and Stroke,USA	Diffusion and T_2 changes after seizures induced by glutamatergic drugs lasting 60 minutes
P59	**Roger Meder**, Sally K. de Visser and James M. Pope	Queensland University of Technology,Australia	Articular Cartilage Microstructure Analysis Using Diffusion Tensor Imaging
P60	**Kazuya Ikoma**, Yoshiteru Seo, Yasuo Mikami,Yoshiaki Kusaka, Toshikazu Kubo	Kyoto Prefectural University of Medicine,Japan	Effects of stress-shielding on the dynamic viscoelasticity and ordering of the collagen fibers in the Achilles tendon
P61	**Dean O. Kuethe** and Natalie L. Adolphi	New Mexico Resonance,USA	Lung tissue: for good resolution, keep acquisition time even shorter than $2T_2^*$
P62	**R.A. Waggoner**, M. Costagli, K. Ueno, K. Tanaka, and K. Cheng	RIKEN - Brain Science Institute,Japan	Physiological Noise in SENSE-EPI
P63	**Yusuke Inoue**, Tomoyuki Haishi, Yukihiro Nomura, Kohki Yoshikawa, Takahiro Seki, Kyoko Kohara, Chieko Kai, Toshiyuki Okubo, Kuni Ohtomo	University of Tokyo,Japan	Imaging of living mice using a 1-T compact MR imaging system
P64	Dusan Sustercic,**Igor Sersa**	Jozef Stefan Institute,Slovenia	3D High-Resolution MR Imaging of a Human Tooth Pulp Chamber
P65	Daniel Haddad, Torsten Rohlfing, Frank Schaupp, Randolf Menzel, Axel Haase	Universität Würzburg,Germany	Quantifying Inter-Subject Differences Between Two In-Situ Bee Brains Using Magnetic Resonance Microscopy and Nonrigid Registration
P66	**Yosuke Otake**, Shinya Handa, Shogo Hara, Katsumi Kose	Tsukuba Univ.,Japan	High resolution 3D MR microscopy of chemically-fixed human embryos for 3D anatomical database
P67	**Yoshimasa Matsuda**, Shinya Ono, Shinya Handa, Yousuke Otake, Katsumi Kose, Tomoyuki Haishi, Shigehito Yamada, Chikako Uwabe, Kohei Shiota	Tsukuba Univ.,Japan	3D MR microscopy of a large number of chemically-fixed human embryos using a super-parallel MR microscope

Category : Theory

No.	Author(s)	Affiliation	Title
P68	Mohammad Saeed Bahramy, Marcel H.F.Sluiter, and Yoshiyuki	Tohoku Univ.,Japan	Ab initio study of hyperfine parameters using the all-electron mixed-basis method

Category : Late Poster Application			
No.	**Author(s)**	**Affiliation**	**Title**
LA-1	**Yoko Kanazawa**, Yoshiyuki Hirano, Sachiko Koike, Eiji Yoshitome, Koichi Ando, Masafumi Fujita, Minoru Onozuka, Hiroo Ikehira	National Institute of Radiological Sciences, Japan	*In vivo* observation of 5FU dynamics by chemical shift imaging- Comparison of fast imaging sequences -
LA-2	E. Gunde, **S.D. Beyea**, K. Good, R. Leslie, H. Milliken and N. Carrey	Departments of Physics,NRC,Canada	Accurate Determination of the Human Olfactory Bulb and Tract using High Resolution MR Imaging at 4 Tesla
LA-3	**Nikolas Salisbury Andersen** & Walter Köckenberger	University of Nottingham,UK	Excitation Methods for Single-Scan 2D NMR
LA-4	**Meghan E. Halse**, Craig D. Eccles, Andrew Coy and Paul T. Callaghan	magritek Limited, New Zealand	2D NMR Imaging in the Earth's Magnetic Field using Bar Magnets
LA-5	**Meghan E. Halse**, Andrew Coy, Craig D. Eccles and Paul T. Callaghan	magritek Limited, New Zealand	Tracking Diurnal Variations in the Earth's Magnetic Field using ^{1}H EFNMR
LA-6	**Kai Kremer**, Bernhard Blumich, Federico Casanova, Juan Perlo	RWTH Aachen University, Germany	Nondestructive testing of PE pipes for gas and water transport
LA-7	**H. Wakamatsu**, M. Yokoi, Y. Imaizumi, F. Sugihara, Y. Seo	Dokkyo University of Medicine,Japan	Mouse MRI Probe for *Micro2.5*
LA-8	**Hideto Kuribayashi**, David R Checkley, Yi-Xiang Wang, Daniel P Bradley and John C Waterton	AstraZeneca Global Sciences & Information,UK	3D Isotropic High Spatial Resolution Gd-DTPA-Enhanced MRI of the Rat Choroid Plexus
LA-9	**Daniel Marek**, Oskar Schett, Dieter Gross, Marco Sacher, Thomas Oerther	Bruker BioSpin AG, Switzerland	Micro-Imaging Cryogenic Probes

Introduction to NMR: Nuts and Bolts Approach

Eiichi Fukushima
New Mexico Resonance, Albuquerque, USA

Nuclear magnetic resonance (NMR) is a venerable field that keeps growing, seemingly without slowing down. While its subfield MRI has recently become a household word, the science of NMR recently celebrated its 50th anniversary. The original Nobel Prize for NMR were given to Bloch and Purcell but subsequent prizes were given to Ernst and Wuethrich. At last, Lauterbur and Mansfield received the prize for MRI (magnetic resonance imaging) in 2003.

At the very basic level, NMR itself is a subfield of magnetic resonance which includes nuclear quadrupole resonance (NQR) and electron spin resonance (ESR or EPR). In the simplest conceptual terms, NMR works because 1) specific nuclear spins precess in a magnetic field at a unique rate proportional to the strength of the magnetic field and gyromagnetic ratio, a property of the spin, and 2) such precessing spins, under suitable conditions, can be detected by electrical currents induced in a coil that experiences the changing magnetic field from the precessing spins. The amplitude of the induced signal is related to the number of spins detected while the phase (and, therefore, the frequency) tells us about the strength of the magnetic field which, in turn, depend on all the other parameters we wish to investigate such as chemical environment of the spin, velocity of the spin, if moving, and so on.

The quality that distinguishes NMR from other techniques is its versatility. On the broad level, it can yield physical, chemical, and spatial information or combinations of any two or three of these kinds of data. An example of physical information accessible by NMR might be phase transitions, diffusion, superconductivity, or quantum computing. As for chemical information, the most common use for NMR over the past 50 years has been in analytical chemistry and molecular structure studies. Recently, spin density imaging (or something related to it), the most straightforward imaging, has brought clinical MRI into common vocabulary. However, it is possible to spatially resolve all manners of NMR-sensitive parameters such as velocity, velocity correlation, diffusion, spin-lattice relaxation time T_1, spin-spin relaxation time T_2, as well as chemical information. Thus, other 'competing' technologies may have a particular capability that is superior to NMR but no other method has the versatility of NMR. In addition, NMR does not use ionizing radiation which is a boon for in-vivo studies.

The subject of this conference, now in its 8th meeting, deals with spatially resolved magnetic resonance that is outside of the medical arena. There will be presentations ranging from basic spin physics to important applications in industry and subjects that include fuel cells, biofilms, rice, pine trees, foams, hydrogen storage, lungs, granite, catalysts, and drugs. Methods covered include atomic force microscopy, SQUIDs, ex-situ NMR, fast imaging methods, magnet and coil design, novel pulse sequences, isotope production, etc. Magnetic resonance, particularly NMR, is an incredibly broad subject and I hope to impart information that is useful in understanding its breadth and depth in this lecture.

An introduction to magnetic resonance imaging, diffusion and flow

Paul T. Callaghan

MacDiarmid Institute for Advanced Materials and Nanotechnology,
School of Chemical and Physical Sciences
Victoria University of Wellington, New Zealand

The idea that magnetic resonance could be used to obtain a 'picture' of the distribution of molecules inside materials or biological organisms is remarkable both for its practical relevance and for the time it took for the pioneers of NMR to become aware of this possibility.

This lecture will give a simple introduction to magnetic resonance imaging (MRI). The idea of "reciprocal space" will be introduced and used to explain the various different imaging strategies. The talk will range over all the different sorts of "contrasts" which are possible, so that we can image not only where the molecules are, but which molecules, how fast they flow, how fast they diffuse, how fast they tumble, which way they point. When we want to get the finest spatial resolution, we enter the realm of NMR microscopy. Some limits to resolution, time and space will be explored.

Given that 2005 is the 100th anniversary of the *annus mirabilis* of Einstein's remarkable paper on Brownian motion, special attention will be paid to the role of NMR in elucidating diffusion, and flow.

Pulsed Gradient Nuclear Magnetic Resonance provides direct insight regarding the translational motion of spin-bearing molecules. These methods gain a second dimension when the simple gradient pulse pair is enhanced by a second pair. Where the motion encoding of the two pairs is opposite, flow effects are removed from the echo attenuation, making it possible to measure diffusion in the presence of shear flow, or to measure the stochastic part of dispersive flow, and in particular the velocity auto-correlation function. Where the gradient pulse pairs are stepped in independent dimensions, two-dimensional experiments become possible.

This lecture is aimed at a graduate student audience. Suitable references for MRI, NMR Microscopy, or Spatially Resolved NMR are listed below.

1. P. T. Callaghan, *Principles of Nuclear Magnetic Resonance Microscopy* , Clarendon Press, Oxford, 1991.

2. *Spatially Resolved Magnetic Resonance*, eds. P. Bluemler, B. Bluemich, R.E. Botto and E. Fukushima, Wiley-VCH, Weinheim, 1998

3. B. Blümich, *NMR Imaging of Materials* , Oxford University Press, Oxford, 2000.

Hardware: NMR in inhomogeneous fields

Bernhard Blümich

Institute of Technical and Macromolecular Chemistry, RWTH Aachen, D-52056 Aachen, Germany

NMR in inhomogeneous fields is of interest in desk-top and mobile or portable NMR, where, contrary to mainstream NMR, the instrument is carried to the object of interest. Such instrumentation uses simple magnets, which at present are not shimmed to the high homogeneity of high field instruments. While the spectrometer hardware required to conduct NMR in inhomogeneous fields does not differ conceptually from conventional NMR spectrometers, small instruments are preferred for mobile applications [1]. The most distinctive feature of mobile NMR is the magnet, which is designed to either enclose the object so as to expose the object to an approximately homogeneous $\boldsymbol{B}_0$ field, or it is designed to be positioned on the object from one side, generating a more inhomogeneous field. Similar considerations apply to the radio frequency coil, which produces either a homogeneous $\boldsymbol{B}_1$ field when enclosing the object or an inhomogeneous field when a surface coil is used. When discriminating homogeneous and inhomogeneous $\boldsymbol{B}_0$ and $\boldsymbol{B}_1$ fields, four cases result. Each of them is characterized by different sample requirements, representative applications, and NMR methods (Tab. 1).

Tab. 1: Classification of NMR according to field homogeneity

	homogeneous $\boldsymbol{B}_0$ fields	inhomogeneous $\boldsymbol{B}_0$ fields
small samples	$\boldsymbol{B}_0$ constant $\boldsymbol{B}_1$ constant spectroscopy relaxometry research & development	$\boldsymbol{B}_0$ distribution $\boldsymbol{B}_1$ constant relaxometry diffusometry imaging medicine, engineering
large samples	$\boldsymbol{B}_0$ constant $\boldsymbol{B}_1$ distribution surface-coil NMR: spectroscopy relaxometry engineering	$\boldsymbol{B}_0$ distribution $\boldsymbol{B}_1$ distribution unilateral NMR: relaxometry diffusometry imaging engineering

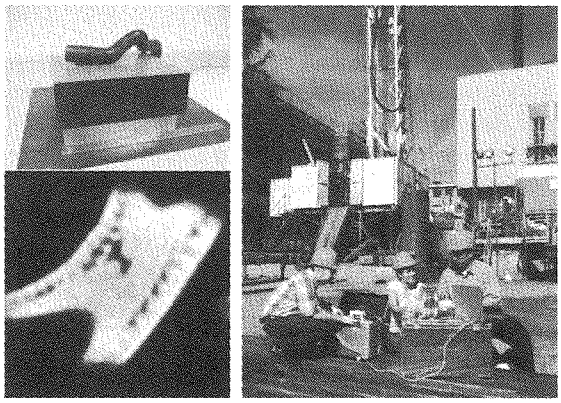

Fig. 1: Left: Unilateral NMR Tomograph and 3 × 3 cm^2 image of a defect in a textile reinforced rubber hose. Right: portable Halbach scanner for measuring porosity in drill cores

The case of inhomogeneous $\boldsymbol{B}_0$ and inhomogeneous $\boldsymbol{B}_1$ is given particular attention, as large samples can be investigated nondestructively. This concerns the different devices for unilateral NMR, including well logging tools, the NMR-MOUSE, unilateral tomographs, and *ex situ* spectroscopy. Different concepts and magnet designs are discussed with reference to the literature. Two primary design goals are followed: 1) to achieve a large homogeneous regions *ex situ* of the sensor in a sweet spot, 2) to accept strong field gradients. Homogeneous field regions are preferred to suppress diffusive signal attenuation in fluid-containing objects, to achieve large sensitive volumes for good sensitivity [2], and to measure chemical shift resolved spectra [3]. Large field gradients are preferred when measuring high-resolution depth profiles [4] or stray-field images [5].

The case of inhomogeneous $\boldsymbol{B}_0$ and homogeneous $\boldsymbol{B}_1$ concerns NMR with space encoding, in particular, NMR imaging but also NMR of transport phenomena. Also here portable magnets weighting less than 10 kg have become available, where the Halbach design is particularly attractive [6]. Earth field NMR (homogeneous $\boldsymbol{B}_0$ and homogeneous $\boldsymbol{B}_1$) becomes increasingly more important, in particular in combination with hyper-polarization techniques. The equipment for this type of NMR is readily mobile, as the magnet does not need to be carried along, and the development of small and mobile hyper-polarizers is a field of active research [7].

[1] B. Blümich, Essential NMR for Scientists and Engineers, Springer, Berlin, 2005.
[2] Pulyer Y M, IEEE Transactions on Magnetics 38, 1553 – 1563 (2002)
[3] Perlo J et al, Science 308, 1279 (2005)
[4] Perlo J, Casanova F, Blümich B, J. Magn. Reson. 176, 64 – 70 (2005)
[5] McDonald P J, Prog. Nucl. Magn. Reson. Spect. 30, 69 (1997)
[6] Raich H, Blümler P, Conc. Magn. Reson. 23B, 16-25 (2004)
[7] Appelt et al, Phys. Rev. Lett. 94, 197602-1 – 4 (2005)

Magnetic Resonance Imaging of Solid Like Materials

Bruce J. Balcom
MRI Centre, Department of Physics, University of New Brunswick, Fredericton, Canada

Magnetic Resonance Imaging of materials, while conceptually similar in almost all respects to clinical MRI, nevertheless faces several additional difficulties. (1) In clinical MRI, an image with relaxation time contrast is almost always advantageous, the quantitative separation of density and relaxation time effects is of secondary importance. For materials MRI however, quantification of the image intensity (through relaxation time or other contrasts, including simple density) is far more important especially if we wish to consider MRI an analytical technique. (2) The non-invasive nature of MRI, while necessary for clinical and animal studies, is not essential for microscopy of materials. A large number of high resolution microscopy techniques already exist for examination of materials. The non-invasive nature of MRI, in a materials context, is most useful in that it permits examination of samples as they change. This suggests that sensitivity and rapid data acquisition is highly desirable for materials imaging with MRI. (3) Finally and perhaps most importantly, a large number of different relaxation mechanisms conspire to produce transverse MR relaxation times in solid like materials, and materials more generally, which are sub-millisecond. Clinical MRI methods are thus not amenable to the study of solid like materials, and alternate methods are required.

This lecture will outline the critical problem in materials MRI, item 3 above, and the various solutions which have been proposed in the literature. These include projection reconstruction, strayfield imaging, multiple pulse line narrowing, continuous wave imaging and pure phase encoding. The various solutions will be examined in terms of items 1 and 2 above. The pure phase encoding approach to MRI of solid like materials will be developed in the greatest detail.

Biomedical MR microscopy

Axel Haase
University of Würzburg

X-Nuclei in Biological MR Microscopy

Gil Navon
School of Chemistry, Tel Aviv University, Tel Aviv 69978, Israel

The two X-nuclei that will be dealt with in my talk are the two naturally occurring nuclei ^{2}H and ^{23}Na. The natural abundance of ^{23}Na is 100% and its sensitivity is relatively high (9.25% of that of protons). However its concentrations of about 140 mM in body fluids and 5-10 mM intracellularly makes it unlikely candidate for microscopic MRI. Cartilage is exceptional in that respect as its high content of the negatively charged proteoglycans attract sodium ions reaching concentrations of about 300 mM. The relative sensitivity and the natural abundance of ^{2}H are very low (0.965 % and 0.0156 % respectively) however its concentration in water is 1.72 M and in D_2O 110 M. Therefore one can perform ^{2}H microscopic MRI quite readily.

All connective tissues contain collagen fibers that exert motion anisotropy to water molecules interacting with them. This anisotropy results in the presence of residual dipolar and quadrupolar interactions, allowing the use of double quantum filtered (DQF) NMR techniques to specifically imaging of those water molecules [1]. Examples will be given for ^{2}H DQF spectroscopic MRI of (a) blood vessel walls, where the DQF technique allows to distinguish between the different layers and to obtain a strain map of the vessels [2]; (b) cartilage, where information about the effects of pressure, separation from the bone and decalcification on the collagen fibers orientation and density are obtained [3-5], and (c) sciatic nerves, where signals from the different compartments could be clearly resolved [6-7]. Here, while investigating the effect of Wallerian degeneration following nerve injury, an astonishing result was found: an injury inflicted on a sciatic nerve in one leg affects the spectrum of the sciatic nerve in the other leg [8].

One of the first stages of osteoarthritis is the reduction in the proteoglycan contents of articular cartilage. Consequently, the sodium content is reduced as well [9-10]. However, quantitation of the sodium content is quite difficult. We have found that the residual quadrupole interaction of ^{23}Na is doubled upon the proteoglycans depletion. Ways of measuring this parameter in cartilage [11-12] will be described.

References

1. G. Navon, H. Shinar, U. Eliav and Y. Seo, Multiquantum Filters and Order in Tissues (Minireview), NMR Biomed 14, 112-132 (2001).
2. Y. Sharf, Y. Seo, U. Eliav, S. Akselrod, and G. Navon, Mapping Strain Exerted on Blood Vessel Walls Using Deuterium Double-Quantum-Filtered MRI. Proc. Natl. Acad. Sci. USA, 95, 4108-4112 (1998).
3. H. Shinar, Y. Seo, K. Ikoma, Y. Kusaka, U. Eliav, and G. Navon, Mapping the Fiber Orientation in Articular Cartilage at Rest and Under Pressure Studied by ^{2}H Double Quantum Filtered MRI. Magn. Reson. Med. 48, 322-330 (2002).
4. K. Keinan-Adamsky H. Shinar and G. Navon, The Effect of Detachment of the Articular Cartilage from its Calcified Zone on the Cartilage Microstructure, Assessed by ^{2}H- Spectroscopic Double Quantum Filtered MRI. J. Ortho. Res. 23, 109-117 (2005).
5. K. Keinan-Adamsky, H. Shinar, and G. Navon, The Effect of Decalcification on the Microstructure of Articular cartilage and Its Underlying Bone Assessed by ^{2}H- Spectroscopic MRI. MAGMA, In Press.
6. H. Shinar, Y. Seo, and G. Navon, Discrimination between the Different Compartments in Sciatic Nerve by ^{2}H Double Quantum-Filtered NMR. J. Magn. Reson., 129, 98-104 (1997).
7. Y. Seo, H. Shinar and G. Navon, Anisotropic and Restricted Diffusion of Water in Sciatic Nerve – a ^{2}H Double Quantum-Filtered NMR Study. Magn. Reson. Med. 42, 461-466 (1999).
8. H. Shinar, Y. Seo, Y. Morita, K. Ikoma, G. Navon, The Bilateral Effect of Unilateral Nerve Injury - ^{2}H DQF NMR Study of Rat Sciatic Nerves, Int'l. Soc. Magn. Reson. Med. 13th Mtg. 804, (2005).
9. L. M. Lesperance, L. M. Gray, D. Burstein, Determination of Fixed Charge Density in Cartilage Using Nuclear Magnetic Resonance, J. Orthop. Res. **10**, 1 (1992).
10. E. M. Shapiro, A. Borthakur, A. Gougoutas, R. Reddy, ^{23}Na MRI Accurately Measures Fixed Charge Density in Articular Cartilage. Magn. Reson. Med. **47**, 284 (2002).
11. O. Danziger, H. Shinar, U. Eliav, G. Navon, Differentiation Between the Action of Different Enzymes on the Structure of Articular Cartilage Using Multiple Quantum Filtered ^{23}Na NMR. Int'l. Soc. Magn. Reson. Med. 7th Mtg. 1522 (1999).
12. U. Eliav K. Keinan-Adamsky and G. Navon, A New Method for Suppressing the Central Transition in I=3/2 NMR Spectra with a Demonstration for ^{23}Na in Bovine Articular Cartilage. J. Magn. Reson., 165 276-281 (2003).

MRI-monitoring for hydrate formation process: Time-evolution maps of gas-storage ratio in gas-hydrate mash

Kuniyasu OGAWA and Yoshiro KAWASOE
Dept. of Mech. Eng., Keio University, 3-14-1 Hiyoshi, Kohoku-ku, Yokohama, 223-8522 Japan
E-mail: ogawa@mech.keio.ac.jp

1. Introduction

Methane hydrate is formed from a guest gas and water at a temperature of about 3 ºC and a pressure of about 3 MPa. Utilization of gas hydrates as a gas-storage medium could provide highly economical transport and safe storage of natural gas because gas hydrates can be formed under moderate thermodynamic conditions [1], [2]. Based on this concept, industrial techniques for high-rate formation of gas hydrates with a high gas-storage ratio must be developed. In order to improve the formation process of gas-hydrate mash with a high-storage ratio, a new method for monitoring the gas-storage ratio map in gas-hydrate mash by magnetic resonance imaging (MRI) was developed. In this study, the gas-hydrate mash was formed from HFC-32 and water in a nonmagnetic high-pressure vessel with fine-bubble injection and mixing paddles, and MR images of the gas-hydrate mash were obtained using a portable MR microscope [3].

2. MRI monitoring system and high-pressure vessel

Some researchers have measured gas-hydrate formation in a high-pressure vessel using MRI systems with super-conductive magnets [4]. In these experiments, optical measurement could not be applied simultaneously. The optical measurement, which has a high time-resolution but is unable to sense the gas-storage ratio in a gas-hydrate mash, can observe the motion of gas particles and flow patterns in the vessel. In this study, a nonmagnetic high-pressure vessel made from cylindrical Pyrex glass with a 70.4 mm inside diameter and 10 mm thickness was constructed as illustrated in Fig. 1 (a). This vessel can be applied in both MRI measurements and in optical measurements using a CCD camera.

The compact MRI system consists of a permanent magnet of 0.3T with a 170mm air-gap (NEOMAX MATERIALS Co., Ltd.) and an MRI console (MRTechnology, Inc.) and is shown in Fig. 1(b). A solenoid coil was wound around the glass vessel as an RF detection coil. The temperature and pressure in the vessel were controlled by circulating Flourinert of 0.3 to 0.5 ºC and injecting HFC-32 gas from the bottom of the vessel. Gas hydrate was mixed by the stirrer at the center of the vessel.

MR images of the gas-hydrate formation from HFC-32 as a guest gas and water in the vessel were obtained using the compact MR microscope system. At a same time, the fluid motion of the hydrate mash mixed by the paddle was observed in the vessel through a transparent glass cylinder using an optical camera.

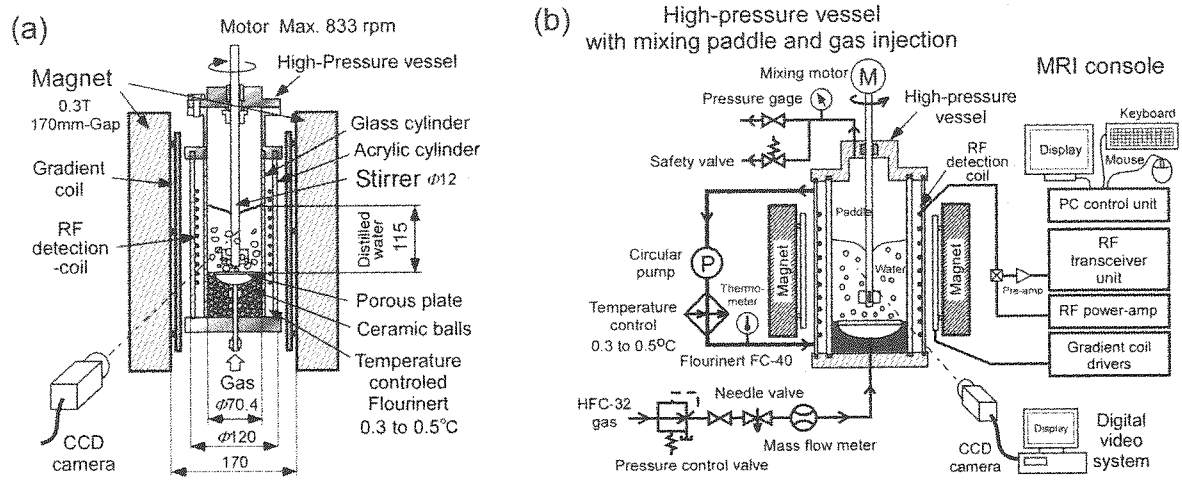

Fig. 1 (a) The nonmagnetic high-pressure vessel for the observation of hydrate formation using MRI, (b) The compact MRI system and the vessel with temperature-pressure control system

3. Results and Discussions

3.1 Relationship between NMR signal intensity and gas-storage ratio in a gas-hydrate mash

The spin-lattice relaxation time, T_1, and the spin-spin relaxation time, T_2, of a uniformly mixed hydrate mash were obtained quantitatively as a function of the gas-storage ratio, which is defined as the ratio of the net gas volume included in a gas-hydrate mash to the water volume in the vessel. MRI acquisition parameters were set to TR=20s and to TE=16ms for T_1 measurement and TE=(16+160*i, i=0, 1,2,..)ms for T_2 measurements using CPMG and Hahn methods. It was experimentally demonstrated that relaxation times T_1 and T_2 did not change from the relaxation times of distilled water before gas-hydrate formation.

Based on these results, a linear relationship was established between the NMR signal intensity from gas-hydrate mash and the gas-storage ratio in it (Fig. 2). The derived equation agrees with the experimental result measured for the gas-hydrate mash mixed uniformly by the paddle.

3.2 Map of gas-storage ratio in a gas-hydrate mash

The maps of the gas-storage ratio in a hydrate mash can be quantitatively calculated from MR images. This method was applied to the non-uniform measurement of the gas-storage ratio formed in the gas-hydrate mash under non-uniform mixing conditions. Three images of the gas-hydrate mash formed at the averaged gas-storage ratio of 53.0 (defined as $V_{net\text{-}gas}/V_{H2O}$) and at a temperature of 0.2 °C are shown in Fig. 3 as examples. The three images are (a) the optical image observed by CCD camera, (b) the obtained map of the gas-storage ratio in the gas-hydrate mash, and (c) the schematic of flow pattern induced by the mixing paddle. This figure reveals that the stagnant area in the upper portion of the mash has a higher gas-storage region. The formation mechanism of the gas-hydrate mash with a non-uniform ratio was discussed from the obtained maps of gas-storage ratio and the observation of fluid motion using optical methods.

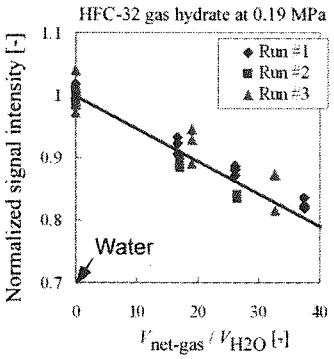

Fig. 2 Relationship between $V_{net\text{-}gas}/V_{H2O}$ as a hydrate density and the normalized signal intensity of MR images

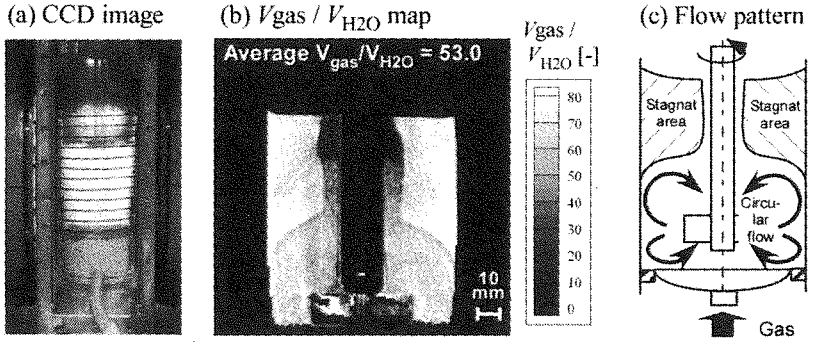

Fig. 3 (a) CCD camera image, (b) The obtained map of gas-storage ratio in the gas-hydrate mash at the case of averaged $V_{net\text{-}gas}/V_{H2O}$=53.0 and 0.2 °C, and (c) Schematic of flow pattern induced by the mixing paddle

Acknowledgements

The authors thank Dr. Tomoyuki HAISHI and Dr. Shin UTSUZAWA, MRTechnology Inc., and Dr. Andrew McDowell, NewMexico Resonance Inc., for technical instructions of the MRI system and the software development of multi-slice measurement.

References

[1] Gudmundsson, J. S. et al., Frozen hydrate for transport of natural gas, *Proc. 2nd Int. Conf. on Natural Gas Hydrate*, 415-423 (1996)

[2] Rogers, R. et al., Hydrate for storage of natural gas, *Proc. 2nd Int. Conf. on Natural Gas Hydrate*, 423-429 (1996)

[3] Haishi, T. et. al., Development of 1.0 T MR microscope using a Nd-Fe-B permanent magnet, *Mag. Res. Imag.*, 19, 875-880 (2001)

[4] Moudrakovski, I.L et al., Application of Magnetic Resonance Microimaging (MRM) to Monitor the Formation of Gas Hydrate, *Proc. 4th Int. Conf. on Natural Gas Hydrate*, 444-448 (2002)

Simultaneous measurement of diffusion along multiple directions and imaging application
- An ultrafast technique for diffusion and diffusion anisotropy

Eric Sigmund[1], Xiaoping Tang[2], and Yi-Qiao Song[1] (ysong@slb.com)
[1]Schlumberger-Doll Research, Ridgefield, CT 06877; [2]Univ of Nevada, Reno, NV 89557

Diffusion is usually determined by using PFG along the applied gradient direction and repeating the measurements for other gradient orientations in order to obtain diffusion anisotropy. A new method can produce multi-echoes separated in the time domain by using several rf pulses. Each echo corresponds to a specific coherence pathway and exhibits a unique diffusion weighting. Thus one scan of such sequence is sufficient to obtain diffusion constant. We have expanded this method to include additional gradient pulses to redirect the gradient direction during the sequence. As a result, each echo measures diffusion along a different direction. We demonstrate this technique to obtain anisotropic diffusion tensor.

JMS 126 (2004) 16 336
JCP 122 (2005) 104104
JMR 174 (2005) 314-324

Microscopic Imaging of Articular Cartilage:
Loading-induced Adaptation of Molecular Matrices

Yang Xia
Department of Physics and Center for Biomedical Research,
Oakland University, Rochester, MI 48309, USA
Phone: (248) 370-3420; Fax: (248) 370-3408; Email: xia@oakland.edu

Introduction
Covering the load-bearing ends of bones in joints, articular cartilage is a thin layer of highly specialized tissue consisting of at least three sub-tissue structural zones, each defined by its collagen fibril orientation [1]. The close interactions between the water protons and the collagen fibrils impose a depth-dependent anisotropy to T_2 relaxation in cartilage, which becomes the origin of the laminar appearance in clinical MRI of cartilage (also known as the magic angle effect in MRI of cartilage) [2]. Because T_2 anisotropy is sensitive to organizational changes in cartilage matrices, external loading will inevitably have profound effects on the characteristics of T_2 anisotropy in cartilage.

Methods
Canine cartilage from healthy humeral heads was imaged using a Bruker AMX 300 NMR micro-imager. Each cartilage specimen contained the full thickness of tissue that was still attached to the underlying bone. These specimens were T_2 imaged while being compressed at the strain levels of 0% to 27% and with a minimum of two orientations (0°and 55°) with respect to B_0. The echo time of the contrast segment had four increments (0, 16, 30, 60 ms), the echo time of the imaging segment was 8.7 ms, and the repetition time of the imaging experiment was 2 s. The in-plane resolutions across the tissue depth were 19.8 μm and the slice thickness was 1 mm. Histology work were performed on selected cartilage specimens using polarized light microscopy (PLM) [3].

Results
At the magic angle and under compression, instead of having the usual homogenous appearance, articular cartilage shows alternating hypo- and hyper-intense layers [4-5]. At 20% strain, we have found that (1) The % thickness of the superficial zone (SZ) was nearly *doubled*; (2) The % thickness of the transitional zone (TZ) changed little; and (3) The % thickness of the radial zone (RZ) decreased significantly. Additional experiments at 10% strain show that the deformation of SZ was the same while the deformations of TZ and RZ were reduced. We also observe a reduction in averaged T_2 in cartilage ("bulk" T_2) at both 0° and 55°. The higher sensitivity of 'bulk' T_2, which is measurable in clinical MRI, to compression at the magic angle offers a potent way to study changes in the structure of macromolecules in cartilage clinically. Based on the μMRI and PLM results, the response of the collagen fibrils in articular cartilage under compression has been proposed in a model.

Discussion and Conclusion
The fact that the tissue can become laminated under compression even *at the magic angle* clearly indicates the structural modifications of macromolecular organization associated with compression. Even neither μMRI nor PLM has the resolution to identify individual collagen fibrils, the use of T_2 anisotropy maps enables the identification of subtle adaptations of molecular matrices in cartilage due to external loading *non-destructively*. This result demonstrates that static compression in MRI can become a tool to induce a novel image contrast, providing new scientific and clinical knowledge that could not be obtained elsewhere.

Acknowledgement
The author is grateful to the lab of Drs G Lust and N Burton-Wurster (Baker Institute, Cornell University, Ithaca, New York) for providing the canine joints, and to Dr H Alhadlaq (King Saud University, Riyadh, Saudi Arabia) for his thesis work in cartilage imaging. The funding for this work was provided by Research Excellence Fund in Biotechnology from Oakland University, an instrument endorsement from R.B. and J.N. Bennett, and an R01 grant (AR 45172) from National Institutes of Health.

References
[1] Maroudas A, Bayliss MT, Venn M, *Ann Rheum Dis*, **39**, 514-534 (1980).
[2] Xia Y, *Investigative Radiology*, **35**(10), 602-621 (2000).
[3] Xia Y, Moody J B, Burton-Wurster N, Lust G, *Osteoarthritis Cartilage*, **9**(5), 393-406 (2001).
[4] H Alhadlaq and Xia Y, *Osteoarthritis Cartilage*, **12**(11), 887-894 (2004).
[5] H Alhadlaq and Xia Y, *J Magn Reson Imaging*, in press (2005).

Manganese-enhanced MRI

Ichio Aoki, Ph.D.[1, 2]

[1]Meiji University of Oriental Medicine, Kyoto, Japan

[2]Laboratory of Functional and Molecular Imaging (LFMI), National Institute of Neurological Disorders and Stroke (NINDS), NIH, Bethesda, USA

Divalent manganese (Mn^{2+}) is known as a useful MRI contrast agent (1-2), which has recently been used for the tracing of specific neuronal pathways (3-4), for the enhancement of neuro-architectural structures in the brain, such as the cortical layers and the hippocampus (5-6), and for functional MRI (7). These applications using manganese as a contrast agent are generally named Manganese-enhanced MRI (MEMRI).

1. *Activity-Induced Manganese-enhanced (AIM) MRI:* The manganese-based functional MRI technique, referred to as Activity-Induced Manganese-enhanced (AIM) MRI, was introduced by Lin and Koretsky as it is independent of the surrogate hemodynamic changes arising in functional MRI (7). This AIM methodology is based on following three hypotheses: 1) Mn^{2+} can reach the brain parenchyma through the blood-vessels via an open or disrupted BBB; 2) Mn^{2+} can enter excitable cells through voltage-gated Ca^{2+} channels during neuronal action potentials; 3) Mn^{2+} accumulates and remains inside or around these cells. Although AIM MRI suffers from technical and biological difficulties such as BBB disruption and baseline signal enhancement (8), this is so far the only method in functional MRI, which is hemodynamic-independent and can provide the high signal to noise ratio of 80-100%. AIM-MRI will be applied in functional micro-imaging of the rodent brain, in order to visualize the "column structure" as a functional module.

2. *MEMRI for "Micro-imaging" of Neuroarchitecture:* Micro-imaging of the rodent neuroarchitecture is performed following systemic administration of $MnCl_2$ (5, 6). Manganese enters into the ventricles from the choroid plexus (CP) after systemic intravenous (IV) administration in mature rats with intact BBB, and spreads out into the entire brain within 24 hours (6). Manganese can provide tissue specific signal enhancement after 1 to 14 days, especially in the pituitary, olfactory bulb, cortex, hippocampus, hypothalamus, and cerebellum. In addition, layer structures are revealed in the olfactory bulb, cortex, and cerebellum. MEMRI can not only be used for anatomical micro-imaging, but also for functional and extra physiological imaging. I would like to introduce some applications of neuroarchitectural MEMRI into research addressing disorders in the hippocampal CA1, spinal cord injury, focal ischemia, and activity detection in the hippocampus after electrical stimulation.

3. *In-vivo tract tracing using MEMRI*: Recently, MEMRI has also been used for determination of specific sensory pathways (3) and for the analysis of specific physiological brain processes (4).

In conclusion, MEMRI can contribute to in-vivo micro-imaging in anatomical as well as functional applications. In the future, the application of this method is expected to be extended and improved for further

studies of the brain functions, studies of regeneration and transplantation, for phenotype examination, and research in cellular tracking.

References

1. Mendonca DM, Gaggelli E, Lauterbur PC. *Semin Nucl Med*. **13**: 364-376 (1983).
2. Geraldes CF, Sherry AD, Brown Rd, et al. *Magn Reson Med*. **3**: 242-250 (1986).
3. Pautler RG, Silva AC, Koretsky AP. *Magn Reson Med*. **40**: 740-748 (1998).
4. Van der Linden A, Verhoye M, Van Meir V, et al. *Neuroscience*. **112**: 467-474 (2002).
5. Watanabe T, Natt O, Boretius S, et al. *Magn Reson Med*. **48**: 852-859 (2002).
6. Aoki I, Wu YJ, Silva AC, et al. *Neuroimage*. **22**: 1046-1059 (2004).
7. Lin YJ, Koretsky AP. *Magn Reson Med*. **38**: 378-388 (1997).
8. Aoki I, Naruse S, Tanaka C. *NMR Biomed.* 17(8): 569-80 (2004).

Multinuclear imaging of liquids, gases and solids: applications in catalysis and beyond

Igor V. Koptyug
International Tomography Center, SB RAS, Novoisbirsk, Russia

Introduction

The field of non-medical applications of MRI/MRM technique, including applications in chemical and process engineering and in catalysis, is growing rapidly. The most developed area is the investigation of mass transport in various geometries. Nevertheless, there are further possibilities to expand the MRM transport studies to a broader range of systems and processes. In particular, studying mass transport under reactive conditions is of significant interest since mass transport characteristics can change significantly due to the non-linear coupling of mass transport, heat transport and chemical transformation.

The majority of the MRM studies performed to date utilize ^{1}H NMR signal detection of a liquid or liquid-like phase. While definite progress in multinuclear MRI of rigid solids has been achieved, at present such applications are by no means routine. One of the purposes of this work is to demonstrate that novel and useful tools can be added to the MRM toolkit based on the development of routine strategies for imaging of rigid solid materials and multinuclear MRM. The potential catalytic applications range from supported catalysts preparation to the studies of a functioning catalytic reactor, but are clearly not limited to catalysis only.

Experimental

All imaging experiments were performed on a Bruker Avance DRX 300 MHz wide bore spectrometer. For ^{1}H MRM experiments, a 25 mm birdcage rf insert was used. For other nuclei, a standard broadband rf probe with a 6 mm i.d. saddle-shape rf coil was used with the external aluminum shield of the probe removed. All imaging experiments used the two-pulse spin-echo sequence α - τ - 2α - τ - echo. Images of the liquid phase in the individual catalyst pellets and beds were obtained with 230×140 μm^2 or 230×310 μm^2 resolution. Spatially resolved spectroscopic studies were done with 1.3×0.66 mm^2 spatial resolution and 2 mm thick slice. All solids imaging experiments were performed with $\tau \approx 300$ μs, the nominal flip angle $\alpha = 90^0/(I+1/2)$, and 30 (α) and 60 μs (2α) long rf pulses, The gradient pulses (< 80 G/cm) were 200 μs long, providing (288 $\mu m)^2$ in-plane spatial resolution.

Results and Discussion

Elucidation of the interrelation of structure and mass transport is important in catalytic research. Examples from our practice include MRM of the flow patterns and mixing in crossing channels studied by flow mapping and 2D and 3D POXSY techniques. Drying of various porous materials is important in many technological processes and also often serves as a model mass transfer process. We have used MRM to study drying of wet honeycomb monoliths and fabric materials. Gas flow imaging and PFG NMR can be useful for the studies of gas transport in various channels and in porous media [1,2]. In particular, gas flow imaging can be helpful to verify gas flow uniformity in the drying experiments. Furthermore, combination of liquid and gas flow studies can be used to reveal the differences in the transport of gases and liquids. In particular, we have studied fluid transport in the sub-millimeter channels of string-reactors. In such a case, large diffusivity of gases narrows the residence time distribution substantially. Gravity driven flow and filtration of granular solids in pipes and in packed beds has been studied using solid particles partially saturated with a suitable liquid.

If mass transport is accompanied by a chemical transformation, especially in multiphase systems, transport and chemical conversion are coupled and therefore cannot be studied separately. Therefore, the studies of mass transport under non-reactive conditions will be of limited use. Our MRM studies of the catalytic hydrogenation of α-methylstyrene, octene and heptene on Pt/Al_2O_3 or Pd/Al_2O_3 have revealed a number of interesting dynamic processes [3], such as oscillations of liquid phase content, ignition of individual catalyst pellets in the granular catalyst bed, and capillary transport of reactant to a dry catalyst particle from its liquid filled neighbors. Spatially resolved NMR spectroscopy of an operating reactor is a new field of MRM applications, but the results obtained demonstrate its significant potential in the evaluation of reactor performance.

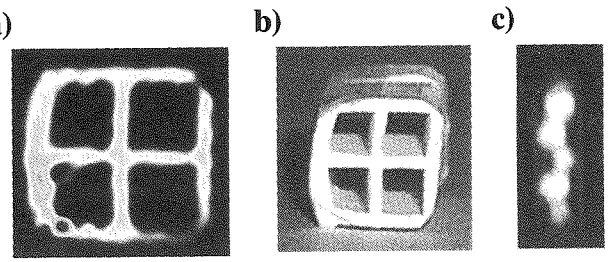

Figure 1. Two-dimensional NMR image (a) and a digital photo (b) of a fragment of alumina monolith. The image was detected using the ^{27}Al NMR signal within 15 min of acquisition time. (c) One of the planes of a complete 3D image of a glass tube containing glass beads detected using the ^{23}Na NMR signal of glass.

Contrary to a widely accepted opinion, imaging of rigid solids does not necessarily require the utilization of solids NMR hardware and techniques. For our initial studies [4] we have chosen ^{27}Al NMR signal of alumina (γ-Al_2O_3) since the latter is widely used for preparation of supported catalysts. Successful detection of an echo signal with reasonably high S/N and echo time (>600 μs) has allowed us to perform ^{27}Al MRI of a number of alumina samples (pellets, beads, powder, honeycomb monoliths) with sub-millimeter spatial resolution and reasonable imaging time (Fig. 1a). It should be stressed that all experiments were performed on a conventional liquid phase instrument using a 2-pulse echo sequence.

The possibility to detect half-integer nuclei other than ^{27}Al can significantly broaden the scope of possible applications. Further experiments have shown that an order of magnitude larger broadening of ^{51}V NMR spectrum of V_2O_5 compared to ^{27}Al NMR of Al_2O_3 is not a major obstacle for performing ^{51}V MRI of V_2O_5 powder [4]. Other examples of solid materials and nuclei successfully imaged using the same instrument include glass (^{27}Al, ^{11}B, ^{23}Na, ^{29}Si), silica gel (^{29}Si), bones (^{31}P), and NaCl (^{23}Na), LiBr (^{7}Li) and phosphate (^{31}P) dispersed in alumina. Extension to 3D imaging is demonstrated with 3D MRI of alumina (^{27}Al) and glass (^{23}Na) beads (Fig. 1c).

The results obtained demonstrate that imaging of rigid solids can in many cases be performed on commercially available instruments, without recourse to solids NMR hardware and techniques. This hopefully will lead to a substantial progress with the imaging of rigid solids. In catalytic research, the ability to image ceramics and glass provides the possibility to evaluate structure of reactors (e.g., of a packed bed reactor) directly. Imaging of materials comprising a solid finely dispersed in a porous solid matrix will be useful, for instance, for mapping NaCl distribution in building materials, LiCl and other salts in selective water sorbents, etc. An entirely new dimension in MRM of solids can be developed based of the use of contrast mechanisms other than simple spin density. In particular, spatially resolved thermometry and transport of solid materials appear to be within the reach.

Another direction pursued in our studies is the combination of multinuclear MRM of liquids (solutes) and solids. This approach appears to be promising for the in situ studies of the preparation of supported catalysts and composite water sorbents. During the impregnation stage, transport of the solute (catalyst precursor, salt) can be visualized as it permeates the porous support immersed in the impregnation solution. Imaging of the solid phase is helpful to evaluate the final distribution of a catalyst or salt after the pellet is dried. Comparison of the imaging results of the liquid and solid phases allows one to study interaction of the active component with the porous support and to assess its redistribution within the support during the drying stage.

Conclusions

The results of MRM studies in the field of heterogeneous catalysis are presented. It is demonstrated that further substantial progress in this and related fields can be achieved through the development and combination of multinuclear and multiphase imaging strategies using commercially available instruments usually employed for liquid phase imaging.

Acknowledgments. This work was supported by the grants from RFBR-NWO (03-03-89014-NWO, 047.015.006), RFBR (05-03-32472), CRDF (RU-C1-2581-NO-04), and SB RAS (integration grants 41, 166). The author thanks Russian Science Support Foundation for financial support.

References.

1. Koptyug, I.V., Matveev, A.V., Altobelli, S.A., *Appl. Magn. Reson.* **22**, 187-200 (2002).
2. Koptyug, I.V., Lysova, A.A., Matveev, A.V., et al., *Topics Catal.* **32**, 83-91 (2005).
3. Koptyug, I.V., Lysova, A.A., Kulikov, A.V., et al., *Appl. Catal. A* **267**, 143-148 (2004).
4. Koptyug, I.V., Sagdeev, D.R., Gerkema, E., et al., *J. Magn. Reson.*, (2005, in press).

NMR mapping of electroosmotic flow in pore networks

Rainer Kimmich, Bogdan Buhai

Universität Ulm, Sektion Kernresonanzspektroskopie, 89069 Ulm, Germany
rainer.kimmich@uni-ulm.de

Electroosmotic flow arises when an electric field is applied to an electrolyte solution in a channel with polar walls [1]. Surface charges in the walls are compensated by solute counterions forming the thin and immobile "compact layer". As a consequence, coions are enriched in the "diffuse layer". These coions form a net charge density in the diffusive layer and are mobile. They are consequently driven along the electric field towards the counter-electrode. That is, viscous friction between the coions and the solvent causes shear flow of the solution in the diffusive layer whereas the electrically neutral solution in the middle of the channel is characterized by a flat flow velocity profile.

This is the standard scenario one has in mind when speaking of electroosmotic flow. However, when the electrolyte solution is filled into a random porous medium or into a more or less complex channel system, and if the pore space is closed, totally different flow patterns arise. Using NMR velocity mapping and finite element computational fluid dynamics methods we have examined the velocity fields in electrolytic cells with increasing complexity starting from single straight, rectangular channels. For the same sort of systems we have directly examined current density maps again using a finite element simulation technique and NMR mapping experiments [2].

Random site percolation clusters are considered as a paradigm for particularly complex systems [3]. Corresponding model objects were designed on a computer and milled into ceramic matrices.

Electroosmotic flow patterns are strongly modified by hydrodynamic pressure gradients built up in the pore system. Especially flow in pore spaces sealed at the electrodes are characterized by a tendency to form closed loops and vortices. That is, electroosmotic flow following the electric field lines is accompanied by flow in opposite directions.

Velocity histograms and the mean velocity as a function of the porosity have been evaluated. At the percolation threshold, a sharp crossover from static to flowing liquid occurs not unlike the Rayleigh/Bénard percolation transition reported previously [4]. The general transport properties and characteristics will be discussed in detail on the basis of histograms.

[1] Li, D. *Electrokinetics in Microfluidics,* (Elsevier, London, 2004).

[2] Weber, M., Kimmich, R., *Phys. Rev. E* 66, 026306 (2002).

[3] Kimmich, R., *Chem. Phys.* 284, 253 – 284 (2002).

[4] Weber, M., Kimmich, R., *Phys. Rev. E* 66, 056301 (2002).

Magnetic Resonance Microscopy of Scale Dependent Transport Phenomena: Bioactivity in Porous Media

Joseph D. Seymour
Department of Chemical and Biological Engineering and Center for Biofilm Engineering
Montana State University
Bozeman, Montana, USA

MRM's ability to obtain data on the pore scale via imaging and the sample scale by bulk measurement allows for connection between microscale dynamics and macroscale transport phenomena to be made directly. This has led to MRM techniques becoming a preeminent method for characterization of dynamics in porous media. A significant question in modeling transport in porous media is definition of the porous media structure as homogeneous (ordered) or heterogeneous (disordered)[1]. One means of defining the 'complexity' of a porous media is based on the dynamics of the system[2]. The dynamics for flow in a model bead pack of 241 μm beads measured by MRM is shown in Figure 1 with the q-space data in a) and the Fourier transformed q-space data, or propagators in b). The flow induced diffraction effect is due to the spins undergoing displacements of a single pore diameter for displacement observation times greater than the velocity sampling time for a pore diameter a, $\Delta > a/\langle v_z \rangle$, analogous to the diffusive diffraction effect[3, 4], and indicates the homogeneous nature of the monodisperse bead pack pore space. In porous media transient pre-asymptotic dynamics impact transport processes. The ability of magnetic resonance microscopy (MRM) to measure the time dependent statistics of the dynamics [5, 6] provides quantification of the pre-asymptotic dynamics. The transition from preasymptotic to Gaussian transport consistent with models of homogeneous porous media is clearly visualized.

Biological activity in porous media, such as microbial growth, typically manifests itself as biofilms or colonies of microbes that adhere to surfaces and are surrounded by a hydrogel of extracellular polymeric substance (EPS). The impact of biofilm growth on porous media is of importance in environmental remediation, filtration processes and porous bioreactors. The growth of biofilm in the porous media generates variations in permeability which is useful in biobarrier applications but often detrimental in biofouling during oil recovery, microbial filtration processes and in bioreactor applications.

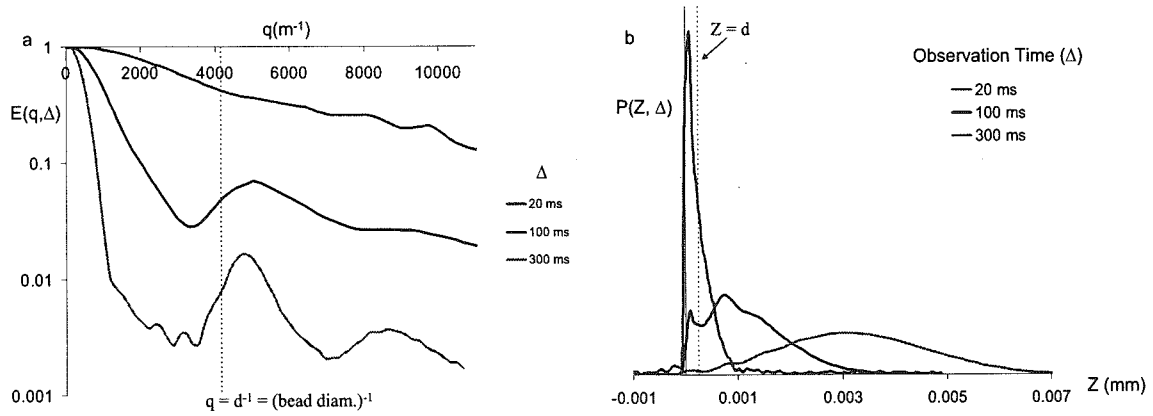

Fig. 1 a. Echo attenuation function and Fourier transformed b. averaged propagators for varying displacement observation times, Δ, of the flow of water in a model bead pack. The transition from pre-asymptotic to asymptotic transport is visualized.

The biofilm growth introduces complexity into the system structure in generation of physical pore blocking, trapping within the EPS gel, elastic interfaces due to the EPS and generation of channels in which faster flow occur. The hierarchy of length and time scales and multiple physical processes which are introduced by the biofilm growth impacts the porous media transport as reflected in the change in dynamics [7, 8].

Figure 2 shows the average propagator as a function of biofilm growth time[9]. Homogeneous transport characterized by the Gaussian shape of the propagator is observed for the clean porous media column as well as day 1 of biofilm growth. As the biofilm grows within the column, the propagator shifts from Gaussian (day 1) to highly non-Gaussian behavior (days 3, 5, 7) indicating a shift to anomalous transport behavior [10]. The transition can be modeled using statistical mechanical approaches based on continuous time random walk (CTRW) processes that generate fractional differential equations[11]. The transition from normal transport characterized by Gaussian statistics with a variance or mean squared displacement which varies linearly in time to anomalous transport with non-Gaussian statistics which generate either a variance scaling greater than linear in time, superdiffusive, or less than linear in time, subdiffusive[11], is indicative of an increase in complexity[2] of the system. The bioactivity alters the structure of the porous media from homogeneous to heterogeneous resulting in the transition from a Gaussian diffusive to a non Gaussian subdiffusive dispersion process.

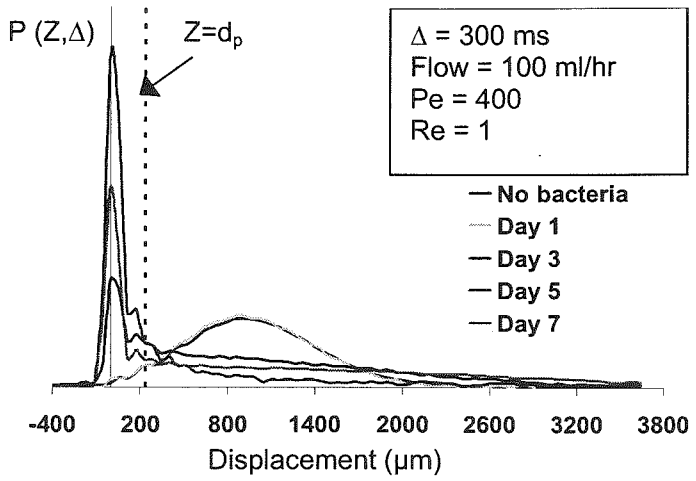

Fig. 2 Averaged propagators as a function of biofilm growth exhibiting the transition from normal transport with Gaussian statistics for the clean bead pack to anomalous transport with non-Gaussian statistics .

References

1. M. Quintard and S. Whitaker, Transport in ordered and disordered porous media: Volume averaged equations, closure problems and comparison with experiment. *Chemical Engineering Science*, **48**(14): 2537-2564 (1993).
2. N. Goldenfeld and L.P. Kadanoff, Simple lessons from complexity. *Science*, **284**: 87-89 (1999).
3. J.D. Seymour and P.T. Callaghan, "Flow-Diffraction" structural characterization and measurement of hydrodynamic dispersion in porous media by PGSE NMR. *Journal of Magnetic Resonance Series A*, **122**: 90-93 (1996).
4. J.D. Seymour and P.T. Callaghan, Generalized approach to NMR analysis of flow and dispersion in porous medium. *AIChE Journal*, **43**: 2096-2111 (1997).
5. S.L. Codd, B. Manz, J.D. Seymour, and P.T. Callaghan, Taylor dispersion and molecular displacements in poiseuille flow. *Physical Review E*, **60**(4): R3491-R3494 (1999).
6. P.T. Callaghan, *Principles of Nuclear Magnetic Resonance Microscopy*. New York: Oxford University Press (1991).
7. G.K. Batchelor, *Developments in microhydrodynamics*, in *Theoretical and Applied Mechanics*, W.T. Koiter, Editor. North-Holland: Amsterdam. p. 33-55 (1976).
8. R.F. Probstein, *Physicochemical Hydrodynamics*. Butterworth -Heinemann Series in Chemical Engineering, ed. H. Brenner. Stoneham, MA: Butterworth -Heinemann (1989).
9. J.D. Seymour, J.P. Gage, S.L. Codd, and R. Gerlach, Anomalous fluid transport in porous media induced by biofilm growth. *Physical Review Letters*, **93**: 198103 (2004).
10. B. Berkowitz and H. Scher, Anomalous transport in random fracture networks. *Physical Review Letters*, **79**(20): 4038-4041 (1997).
11. R. Metzler and A. Compte, Generalized diffusion-advection schemes and dispersive sedimentation: A fractional approach. *Journal of Physical Chemistry B*, **104**(16): 3858-3865 (2000).

Magnetic Resonance Studies of Drop Freezing Processes

M.L. Johns, L.F. Gladden, A.J. Sederman D. I. Wilson and J.P. Hindmarsh
Department of Chemical Engineering, University of Cambridge

Drop freezing is a fundamental process during spray freezing operations, where liquids are sprayed into a flowing cold air environment and frozen; they are usually subsequently dried. The resultant particulates display a more homogeneous microstructure, improved drying characteristics and, in the case of food, improved flavour retention, when compared with conventional freeze-drying methods. A range of magnetic resonance (MR) techniques have been applied to the characterization of this drop freezing process (1- 10 μl). These have been used to investigate both the kinetics of the freezing process, as well as the final microstructure formed. The quantitative MR data thus produced has enabled stringent model validation.

With respect to the kinetic of drop freezing, RARE imaging sequences have been used to follow the freezing of a range of drop compositions (e.g. sucrose and fat solutions, coffee solutions and various fats) [e.g. 1]. Nucleation points were identified and conditions promoting anomalous freezing and macroscopic phase separation were identified (an example is shown in figure 1). For fully quantitative data, rapid spectroscopy, corrected for relaxation effects, was used to produce drop component specific changes as freezing progressed, both as a consequence of supercooling as well as subsequent heat-transfer. These were used to verify models of the freezing process [2] as well as identify phase changes in the freezing mixtures. Essential to these models was a quantification of internal motion in the drop, prior to and during the freezing process. Rapid MR dispersion and velocity measurements were successfully used to provide such data [3].

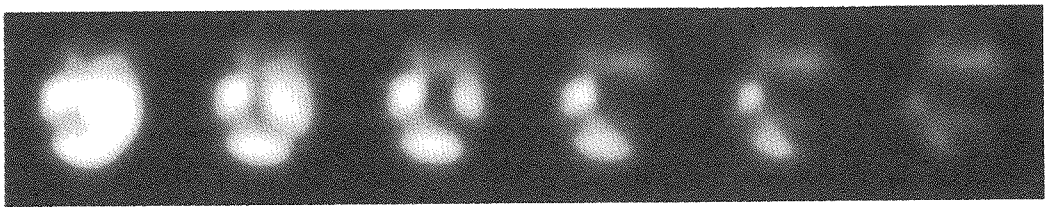

Figure 1: Freezing of a phase separated drop

Frozen drop microstructure was probed in a variety of ways. Chemical shift imaging was used to analysis the composition of a distinct skin formed on the drop. In the case of emulsions, diffusion measurements were used to produce droplets size distributions in the drops. These were studied as a function of freeze-thaw cycles [4]. Further micro-structural analysis was provided via a diffusion analysis as a function of Δ. This enabled S/V ratios of the unfrozen concentrated residual to be measured and compared with SEM micrographs. Diffusion simulation on these micrographs produced an excellent agreement with the MR results.

A brief overview of current and future work in this area will also be presented. The integration of the model, verified on the basis of MR data, into a CFD simulation of a pilot-plant will be briefly outlined. Some on-going MR studies on measuring freezing profiles in falling droplet streams will also be presented as will the measurement of freezing of drops composed of biological suspensions.

References

[1] Hindmarsh, J.P., Buckley, C., Russell, A.B., Chen, X.D., Wilson, D.I. and Johns, M.L., (2004) Imaging Droplet Freezing using NMR, *Chem Engng Sci.,* **59**(10), 2113-2122

[2] Hindmarsh, J.P., Russell, A.B., Chen, X.D., Wilson, D.I. and Johns, M.L., NMR verification of single droplet freezing models, *in press A.I.Ch.E. J.*

[3] Hindmarsh, J.P., Sederman, A.J., Gladden, L.F., Wilson, D.I. and Johns, M.L, (2005) Rapid measurement of dispersion and velocity in freezing droplets using magnetic resonance methods, *Experiments in Fluids*, **38**(6), 750-758.

[4] Hindmarsh, J.P., Hollingsworth, K.G., Wilson, D.I. and Johns, M.L., (2004) An NMR study of the Freezing of Emulsion-containing Drops, *J. Colloid Interface Sci.,* **275**(1), 165 –171.

MRI of Foods

Nobuaki Ishida
National Food Research Institute, Tsukuba Science City, Ibaraki 305-8642, Japan

Introduction

MRI measures the physical conditions of the nuclear spins of an objective atom in a defined small picture element (PIXEL) and aligns the signals along the order of the picture elements to create an image on a computer. It provides anatomical images of materials nondestructively. But the most important point is that MRI is mapping water distribution and the amount and quality (mobility) of water is very important factor for food quality, which cannot be obtained by other methods [1]. In this paper, I introduce some application of MRI to food science.

Water is the medium which carry substrates and O_2 gas for biological reaction and transport product materials and also extrude heat produced biological reaction. Mobility of water is closely related to biological activity. MRI parameters, T1, T2, diffusion coefficient, are good indicator of the change of biological activity of each tissue along with growing. In Fig.1 changes of NMR image, soluble compounds, T1 value of growing cherry fruits are shown [2]. There is different tendency in changes of water status between seed and pericarp of the fruits. Large amount of free water was observed in the seed until the third stage when the fruit size reached approximately 80% of that of the ripened stage. After that, water in the seeds decreased with seed maturation associated with accumulation of stored materials. On the other hand, there were small amount of water in the pericarp of the young fruits. The amount of water in the pericarp increased after the mature stage, while water content decreased in the seed. Localized spectral images in which x-axis indicates chemical shifts and y-axis the corresponding y-axis position on the left image show the distribution of chemical substances. Sugars (indicated by "s") were detected in pericarp at mature stage and oils (indicated by "o") in seed at ripened stage. The T1 images show that water in the seeds increased in mobility until the third stage when seeds contained large amount of water and declined afterward along with decrease of water content. The changes of three different kinds of images show the physiological and textural changes of sweet cherry fruits during growing.

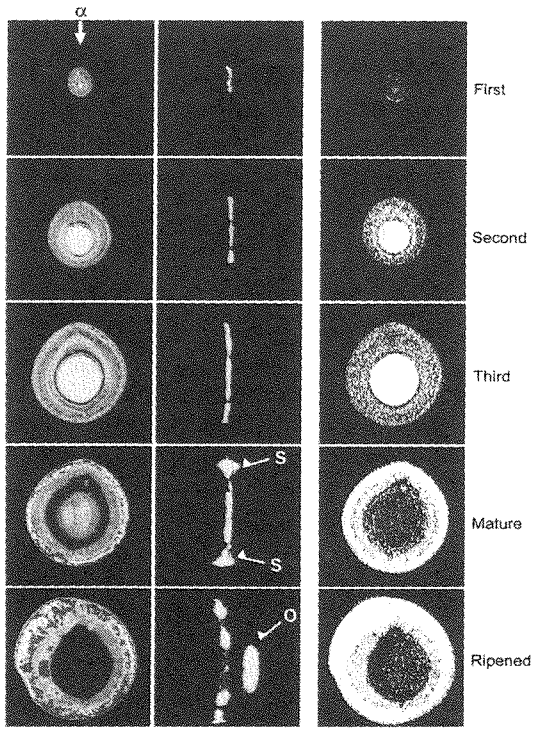

Fig.1 NMR images (left), localized spectral images (center), and T1 images (right).

Another prominent feature of MRI is to create three dimensional structures of materials non-destructively. The architecture of the networks of baked breads is a major element in determining the quality of breads. Fig. 2 shows the three dimensional structure of baked bread recreated using MRI data [3]. Because baked bread is porous structure and

has not much water in it, it is difficult to obtain clear images by conventional spin-echo method. Therefore, the bread was soaked in acetone and was imaged as shadow in the solvent image by detecting solvent signals (Fe-acetone method).

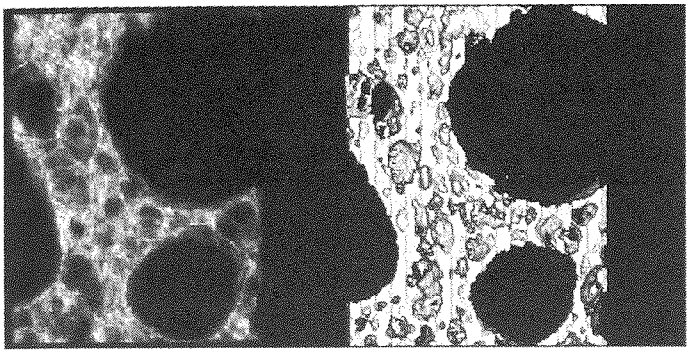

MIP Surface rendering

Fig.2 3D images of baked bread

MIP image (Fig.2 left) shows 3D structure of gluten network of bread, and cell and wall structure of air cell can be visualized by surface rendering image. French type of bread composed of big and small air cells with thick cell wall. Two dimensional slice images shows clear structure of air cells. Size and distribution of air cell is good indicator of the quality of bread. Image analysis of sliced bread using photo image were used for the evaluation of bread quality, but there are always existed the difficulty to extract the sliced edge (outline) of the cell from photo image. In MR image there is no problem for extraction of the shape of cell because clear image which is suit for image analysis can be easily obtained as a thin slice of 3D data set. MRI is a good means for characterizing baked bread.

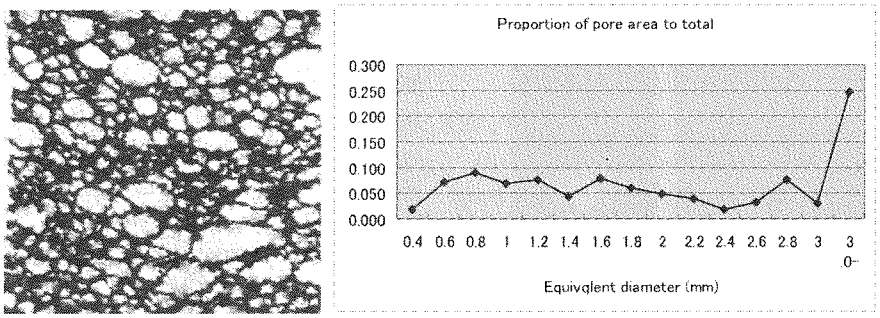

Fig.3 2D slice image (left) and image analysis of MR image (right) of baked bread.

References

1. Ishida,N., Koizumi,M., Kano,H., The NMR Microscope: a Unique and Promising Tool for Plant Science, *Ann. Bot.*, 86, 259-278 (2000).
2. Ishida,N., Ogawa,H., Koizumi,M., Kano,H., Ontogenetic changes of the water status and accumulated soluble compounds in growing cherry fruits studied by NMR imaging, *Magn. Reson. Chem.*, 35, S22-S28 (1997).
3. Ishida,N., Takano,H., Naito,S., Isobe,S., Uemura,K., Haishi,T., Kose,K., Koizumi,M., Kano,H., Architecture of baked breads depicted by a magnetic resonance imaging, *Magn. Reson. Imag.*, 19, 867-874 (2001).

MRI of objects with dipolar-broadened spectra using soft excitation pulses

Mi Jung Kim and A. K. Khitrin

Department of Chemistry, Kent State University, Kent, OH 44242-0001, USA

Recently, we have demonstrated that long-lived coherent response signals produced by long and weak excitation pulses can be used in NMR imaging, and presented 1D profiles of model samples as a "proof of principle" [1]. In this work, we show that intensity of the coherent response signals is, in some cases, sufficient to produce high-resolution 3D images of objects with dipolar-broadened conventional NMR spectra. The model samples are liquid-crystalline phantoms and a pencil eraser. In NMR imaging, the achievable spatial resolution Δx in x-direction can be estimated as $\Delta x = 2\pi\Delta f/(\gamma G_x)$, [2] where Δf is the NMR linewidth, G_x is the magnetic field gradient in the x-direction, and γ is the gyromagnetic ratio of the nucleus. Therefore, high spatial resolution can be achieved by either narrow NMR signals or strong magnetic field gradients. Today, most of MRI applications use narrow NMR signals of liquids, with spatial resolution reaching one micron for small objects (NMR microscopy [3]). In solids, NMR lines are 3-5 orders of magnitude broader than in liquids and one would expect proportionally degraded spatial resolution. With the existing NMR imaging techniques, spatial resolution remains considerably less for solids or "soft solids" where the dipolar interactions between nuclear spins are not averaged out by molecular motions. In addition, a necessity of using strong RF and/or gradient pulses creates serious technical challenges for imaging large objects.

Our experiments were carried out with a Varian Univty/Inova 500MHz NMR spectrometer equipped with a 5-mm Varian probe with three orthogonal gradients of maximum strength 60 G/cm in z-direction and 28 G/cm in x- and y-directions. We have chosen three models for the present demonstration. Two of them are liquid-crystalline phantoms and the third one is a pencil eraser of RoseArt X500™ mechanical pencil. Liquid crystal 5CB was purchased from Aldrich and used without further purification. The first 5CB phantom for 3D images is a 5mm flat-bottom NMR tube filled with liquid crystal and there is an axially symmetric Teflon insert inside of the tube. The second 5CB phantom is two concentric glass tubes filled with 5CB. The eraser is a cylinder of 5mm height and 4mm diameter placed in a standard 5 mm NMR tube. The gradient-echo 3D multi-slice acquisition protocol of Varian's VNMRJ software was used for all the phantoms in this work.

Small integral intensity of the signals excited with soft pulses is the major limitation for using them in MRI. Acquisition of each of the three 3D images was a weekend-long experiment. However, images of the same quality could be acquired an order of magnitude faster by using a dedicated imaging probe and much shorter repetition times. Similar to the FLASH technique [4], which uses pulses with small flip angles, each soft pulse produces only a small change of the total z-component of magnetization and, therefore, acquisitions can follow much faster than T_1. In our experiments, use of long repetition times was dictated by safety requirements of the available probe.

With weak excitation pulses, RF power is extremely small and the strength of gradients needed to achieve a desired spatial resolution is significantly decreased. This makes this technique suitable for imaging large objects. Excitation at the generator frequency, rather than the Larmor frequency, eliminates the distortions caused by a static field inhomogeneity, and there are no distortions from interaction between RF-pulses and gradient pulses. The major limitation of the technique comes from small integral intensity of the coherent response signals. We expect that ^{1}H MRI with soft excitation pulses will be efficient for objects where NMR line is narrowed by molecular motions to a residual width of several kHz. In such systems, S/N of the coherent response signal is often comparable to S/N of the conventional NMR spectrum. It is possible that there exist more efficient methods of exciting long-lived signals in systems with dipolar-broadened spectra. However, insufficient theoretical understanding of these signals makes it difficult today to identify promising schemes.

References

[1] Antochshuk V, Kim MJ, Khitrin AK, *J Magn Reson* **167**,133-137(2004)
[2] Callaghan PT, Principles of nuclear magnetic resonance microscopy. Clarendon Press, Oxford (1991)
[3] Lee SC, Kim K, Kim J, et al. *J Magn Reson* **150**, 207-213 (2001)
[4] Haase A, Frahm J, Matthaei D, Hänicke W, Merboldt K-D, *J Magn Reson* **67**,258-266(1986)

Contrast preparation for SPRITEly methods.

Alexandre A. Khrapitchev, Ben Newling and Bruce J. Balcom

Department of Physics, University of New Brunswick, Fredericton, NB, E3B 5A3, Canada.

A principal goal of MRI techniques in material science, we argue, is to eliminate any influence of the signal time evolution upon final image contrast. SPRITE is a leading candidate to deliver truly density-weighted MRI. Once this goal has been achieved any imaginable well-controlled, quantitative image contrast can immediately follow.

Nuclear Magnetic Resonance (NMR) plays an important role in a variety of scientific disciplines [1, 2]. MRI provides a truly non-invasive tool to investigate a wide range of material properties and behaviours. The principal limit for conventional MRI methods is the transverse lifetimes T_2^* and T_2 of the MRI signal, which are sufficiently short in solids, semi-solids, liquid crystals and many gases to make traditional MRI impossible. Single-Point Imaging (SPI) is quite distinct from conventional MRI methods and is able to cope with these limitations. The possibility of using a relatively short encoding time makes, SPI well-suited to the imaging of materials with extremely short signal lifetimes (T_2^* and $T_2 < 1$ ms).

The most generally applicable SPI MRI method is the SPRITE (Single Point Ramped Imaging with T_1 Enhancement) family of techniques, developed by Balcom *et al.* [3, 4]. One of the principal adaptations of SPRITE employs continuously ramped gradients started at the centre of *k*-space (Centric Scan SPRITE), which allows a significantly reduced repetition time and, therefore, total acquisition time. Perhaps the greatest appeal of MRI as an imaging modality lies in the flexibility of contrasts which may be imposed upon the image. A careful selection of imaging method can result in quantitative maps of temperature, pH, speed, diffusion, chemical activity and many other important properties of materials. Serious care must be taken in order to avoid superposition of additional weighting due to temporal signal evolution upon the desired contrast. Minimised relaxation time contrast, when desired, makes SPRITE an intuitively appealing MRI technique.

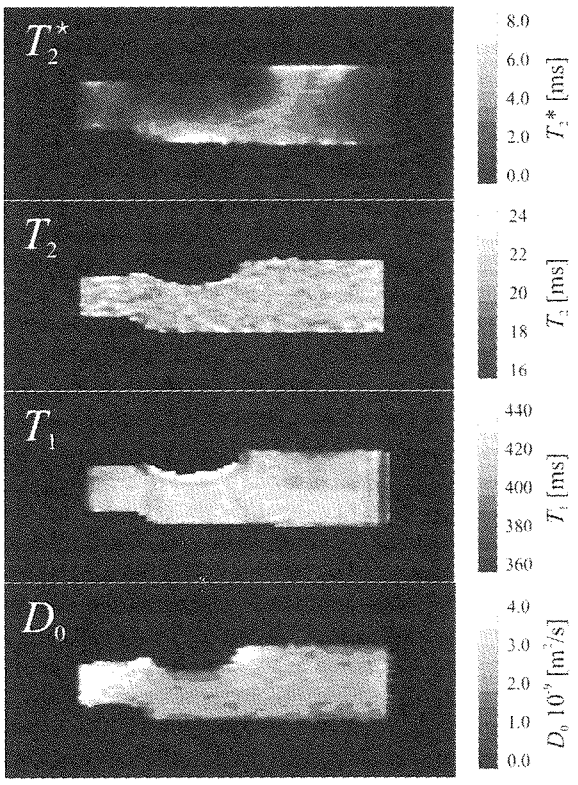

Figure 1. T_2^*, T_2, T_1 and D_0 contrast images of a phantom.

Obvious candidates for contrast imaging are the signal lifetimes T_2^*, T_2, T_1 and also the self-diffusion coefficient D_0. Examples of such contrast images are presented in Figure 1. A typical disturbance pattern can be observed on the right edge of the T_2^* image and also due to an air bubble at the top left. At the same locations some disturbance is present in the T_1 image, but the T_2 image remains fairly homogeneous. Even the D_0 image is relatively flat and has an appropriate value of the self-diffusion coefficient of water. There is a small artefact at the left top edge due to the eddy currents generated in the copper shield of the *rf*-probe.

The short encoding time inherent to SPI methods helps in developing truly quantitative images, since signal amplitude is no longer a complex function of the signal lifetimes. SPRITE methods may also be tailored to generate a variety of image contrasts, which can reflect physical properties of interest. This broadens the range of material structure and behaviour which may be studied by SPRITE in comparison with conventional MRI methods. This paper will explore the generalised idea of SPI MRI. As a powerful example of this approach the SPRITE family will be introduced. The idea of contrast preparation imaging will be presented and accompanied by recent results. Strategies for selection of the most advantageous solution in given measurement situations will be reviewed.

[1] Callaghan P.T., "Principles of NMR Microscopy", *Oxford: Clarendon Press*, (1991).
[2] B. Blümich, "NMR Imaging for Materials", *Oxford Science Publications*, (2000).
[3] Halse M. *et al.*, *J. Magn. Reson*, **165**, 219–229 (2003).
[4] Halse M. *et al.*, *J. Magn. Reson*, **169**, 102–117 (2004).

NMR as a probe of pore geometry, permeability, and fluid saturation: a computational analysis using micro-CT images

C.H. Arns, A.P. Sheppard, R.M. Sok, and M.A. Knackstedt
Department of Applied Mathematics, Research School of Physical Sciences and Engineering, Australian National University, Canberra, Australia

Introduction and Purpose

NMR is often used as a probe of pore geometry [1,2]. Typically one assumes the fast diffusion limit, a distribution of pores in the weak coupling limit, constant bulk and surface relaxivities, and no susceptibility artefacts. Under those conditions, the magnetisation decay can be represented by a sum of exponentials, where each relaxation time refers to a single pore and is related to the ratio between pore volume and pore surface area. A suitable average over these ratios provides a length scale of the pore structure used in permeability predictions [3,4]. It is difficult to test the underlying assumptions for complex materials, and to date studies have been mainly concentrated on simulations of simplified microstructures [5,6]. This work uses micro-CT images of sandstones, carbonates, and bead packs to characterise the sensitivity of length scale predictions under controlled conditions to heterogeneities in surface relaxivities, diffusion coupling, and partial saturation effects. A detailed analysis of pore-pore coupling using pore-partitioning and the concept of topological distance provides insight into the assumption of weak coupling. Additionally, we analyse for a limited number of samples the applicability of fluid typing [7] under conditions of varying relaxivities and susceptibilities, using simulations of 2D-correlation spectroscopy experiments (T1, T2, diffusion).

Methods

Micro-CT images of a set of 20 sandstones and a few carbonates are acquired on the micro Xray-CT facility at ANU [8]. The images are segmented into two or three phases [9]. Drainage simulations are carried out to obtain realistic fluid distributions [10]. Permeabilities to fluid flow are calculated on all samples using a lattice-Boltzmann technique [11]. The pore space is partitioned into simple elements (pores) by making use of the medial axis and a set of distance measures [9,12]. The NMR responses are simulated on the images using a random walk method [13-16]. Each phase and interface has a relaxivity for T1 and T2 assigned to it. Additionally, each phase is assigned a susceptibility and the internal field distribution is calculated using a dipole approximation [17]. The random walk tracks the phase evolution of the spins as well as the number of pores crossed and their topological distance. Relaxation time distributions or T1-T2 maps are derived by an inverse Laplace transform [18].

Results, Discussion, and Conclusions

Two common permeability correlations to NMR responses are tested. The range of prefactors found, indicate an order of magnitude variation of permeability due to *structural heterogeneity* on image data from 20 sandstones and 2 carbonates. *Heterogeneities in surface relaxivity* have an effect of about a factor of two in the permeability prediction. Partial saturation effects and surface relaxivity heterogeneity affect the log mean relaxation time in opposite ways. The pore-pore coupling analysis shows, that for the sandstones considered here, typically five pores are traversed in 2s with significant remaining signal, while for the carbonates about 30 pores are traversed in less than 1s.

References

[1] Brownstein, K.R. and Tarr, C., Phys. Rev. A 19, 2446-2453 (1979).
[2] Banavar, J.R., Schwartz, L.M., Phys. Rev. Lett. 58, 1411-1414 (1987).
[3] Sen, P.N., Straley, C., Kenyon, W.E., et al., Geophysics 55, 61-69 (1990).
[4] Kenyon, W.E., Nucl. Geophys. 6, 153-171 (1992).
[5] Dunn, K.-J., LaTorraca, G.A., Bergman, D.J., Geophysics 64, 470-478 (1999).
[6] McCall, K.R., Johnson, D.L., and Guyer, R.A., Phys. Rev. B 44, 7344-7355 (1991).
[7] Hürlimann, M.D., Venkataramanan, L., and Flaum, C., J. Chem. Phys. 117, 10223-10232 (2002).
[8] Sakellariou, A., Sawkins, T.J., Senden, T.J. et al., Physica A 339, 152-158 (2004).
[9] Sheppard, A.P., Sok, R.M., and Averdunk, H., Physica A 339, 145-151 (2004).
[10] Hilpert, M., and Miller, C.T., Advances in Water Resources 24, 243-255 (2001).
[11] Arns, C.H., Knackstedt, M.A., Pinczewski, W.V., et al., J. Petr. Sc. Eng. 45, 41-46 (2004).
[12] Arns, C.H., Sheppard, A.P., Sok, R.M., et al., SPWLA 46th Annual Logging Symposium, June 26-269, (2005).
[13] Mendelson, K.S., Phys. Rev. B 41, 562-567 (1990).
[14] Bergman, D.J., Dunn, K.-J., Schwartz, L.M., et al., Phys. Rev. E 51, 3393-3400 (1995).
[15] Valckenborg, R.M.E., Huinink, H.P., v.d.Sande, J.J., et al., Phys. Rev. E 65, 21306 (2002).
[16] Arns, C.H., Physica A 339, 159-165 (2004).
[17] Sen, P.N., and Axelrod, S., Appl. Phys. 89, 4548-4554 (1999).
[18] Venkataramanan, L., Song, Y.-Q., and Hürlimann, M.D., IEEE Trans. On Sign. Process. 50, 1017-1026 (2002).

Study of a lamellar system by diffusion measurement

Antoine Lutti and Paul T. Callaghan
MacDiarmid Institute for Advanced Materials and Nanotechnology
Wellington, New Zealand

Diffusive behavior of small molecules can be used to probe the shape and orientation of surrounding liquid crystals. Pulsed Gradient Spin Echo (PGSE) NMR has proved to be a well-adapted method to measure self-diffusion within complex structures.
The formalism developed by Stepisnik[1] helps us correlate the results of this spin echo experiment with its gradient modulation spectrum and the diffusion spectrum within the system under study.

$$E(t) = e^{-\frac{1}{2\pi}\gamma^2 \int_{-\infty}^{+\infty} D(\omega) \times \frac{|F(\omega)|^2}{\omega^2} d\omega}$$

$$\text{with } F(\omega) = \int_0^{+\infty} F(t)\, e^{-i\omega t} dt \text{ and } F(t) = \int_0^t g^*(t')\, dt'$$

where $D(\omega)$ is the Fourier transform of the velocity autocorrelation function.
In this work, we apply the Stepisnik model on a lamellar lyotropic system whose dynamics remain an open issue. A new type of NMR diffusion-sequence has been designed that enables one to probe the diffusion spectrum of the solvent molecules surrounding the lamellae while suppressing the effect of flow when shear is applied. The obtained diffusion spectrum reveals the size and time characteristics of the lamellae as well as the effect of shear on the latter.

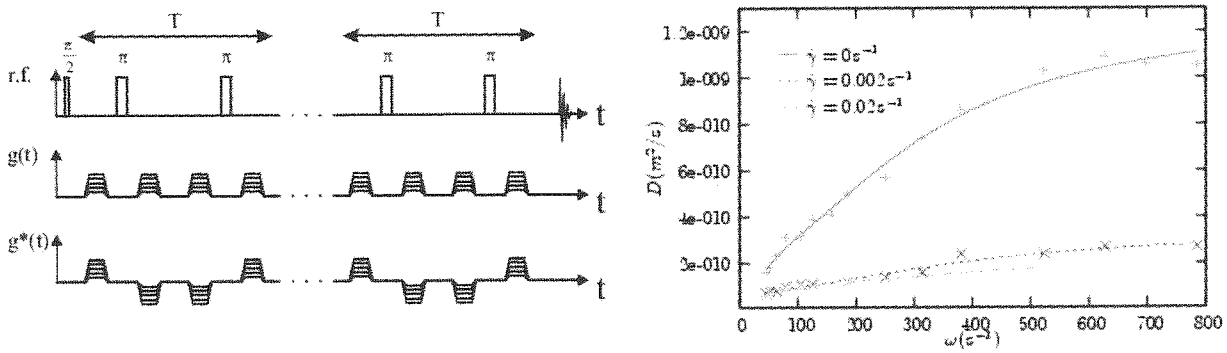

Figure 1. Left : The CPMG sequence and the effective gradient modulation in the time domain. The area of the diffusion spectrum scanned by the NMR sequence is changed by varying *T*. Right: resulting spectrum of the diffusion of the solvent molecules in the direction normal the lamellae.

The diffusion spectrum appears to obey a bimodal behavior with amplitudes of the order of the μm. The high frequency mode, which can be damped at very low shear rates, arises from a rapid diffusion of solvent molecules along the wavy bilayers and gives indications of the wavelength of these static bilayer undulations. The low frequency mode of the diffusion spectrum is the result of bilayer fluctuations and cannot be removed by shear below $0.1s^{-1}$.

References:

[1] J.Stepisnik, P.T.Callaghan, Advances in magnetic and optical resonance, **19**, 325 (1996).

"Velocity distributions in single levitated drops by NMR"

Andrea Amar, Siegfried Stapf, Bernhard Blümich

Lehrstuhl für Makromolekulare Chemie, ITMC, RWTH Aachen, Worringerweg 1, D-52056 Aachen, Germany.

The potential of pulsed field gradient (PFG) NMR for the investigation of flow processes has been demonstrated by application to fluid motion subject to vastly different geometries such as flow through packed beds [1], natural rocks [2] and vertical film flow [3]. One particular case, which also addresses problems of technical and engineering relevance such as encountered in evaporators and condensers, is represented by the investigation of the fluid dynamics inside a liquid drop (disperse phase) [4]. PFG NMR is an exceptionally suitable technique for non-invasively monitoring the drop's internal fluid dynamics and its change with time.

In this study [5], experiments on the oscillation and internal vortex patterns of 'levitated' drops were done. It is a well-known fact that the efficiency of mass transfer between the two phases is determined by convective transport made possible through circulation occurring both inside and outside of the droplets. The internal dynamics of the drops can generally be divided into different regimes. While small droplets behave like rigid spheres, larger droplets feature pronounced internal dynamics. The rigidity of the interface and therefore the internal behaviour of the drops are mostly characterized by the drop size, composition and purity of the system. In the present work, the two limit cases were studied: silicone oil (rigid interface) and toluene (mobile interface) drops are generated with a special pipette (that guarantees the reproducibility of the experiment and also allows to control the drop size) at the bottom of a glass tube filled with D_2O. When the drop rises to the centre of the NMR resonator, it is 'stopped' by the counter flow of the continuous D_2O phase. Velocity patterns in this free scheme can be studied. 1D, 2D, 3D NMR images and flow measurements of 3-4 mm diameter silicone oil drops and 4-5 mm diameter toluene drops in 4.7 T and 11.7 T magnets were performed and the velocity distributions analysed. In all cases, where experiments were performed in a controlled way and under strict purity conditions, a stable pattern was revealed for times of hours and even days, these patterns being characterized by the inherent impurities of the system. The latter was particularly well observed by the occurrence of a rigid cap next to a vortex region inside toluene drops with an overall mobile interface. It could also be shown that given a sufficient concentration of organic impurities during the experiment, the size if the rigid cap will grow with respect to the mobile surface as expected from the theory. Silicone oil drops, on the other hand, revealed a similar internal circulation pattern but with a much reduced velocity range. Interesting results are obtained when the glass measurement cell is not perfectly symmetric or when its orientation is not perfectly vertical. In this situation, axially symmetric results are no longer observed.

---

[1] Khrapitchev, A. A., Stapf, S., Callaghan, P. T., *Phys. Rev. E* **66**, 051203/1-16 (2002)
[2] Stapf, S., Packer, K. J., Békri, S., Adler, P. M., *Phys. Fluids* **12**, 566-580 (2000)
[3] Heine, C., Kupferschläger, K., Stapf, S., Blümich, B., *J. Magn. Reson.* **154**, 311-316 (2002)
[4] Han, S., Stapf, S., Blumich, B., *Phys. Rev. Lett.* **87**, 144501/1-4 (2001)
[5] Amar, A., Groß-Hardt, E., Khrapitchev, A., Stapf, S., Pfennig, A., Blümich, B., *J. Magn. Reson.*, accepted.

Corresponding Author: A. Amar
E-mail: aamar@mc.rwth-aachen.de

High-Resolution NMR spectroscopy with a Portable Single-Sided Sensor

Juan Perlo[1], Vasiliky Demas[2,3,4], Federico Casanova[1], Carlos A. Meriles[5], Jeffrey Reimer[3,4], Alexander Pines[2,4], Bernhard Blümich[1]

[1]Institut für Technische und Makromolekulare Chemie, RWTH-Aachen, Germany
[2]Department of Chemistry, [3]Department of Chemical Engineering, University of California, Berkeley, USA
[4]Material Sciences Division, Lawrence Berkeley Laboratory, Berkeley, USA
[5]Department of Physics, City College of New York, City University of New York, NY, USA

Unlike absorption and fluorescence spectrometers, nuclear magnetic resonance (NMR) instruments are not easily miniaturized for field use. Portable NMR systems have been built, with open single-sided probes for arbitrarily sized samples (1). However, the unavoidable spatial inhomogeneity of the static magnetic field has precluded the use of these devices for high-resolution spectroscopy. These field variations are usually orders of magnitude larger than those created by the microscopic structure of the molecules to be detected, so no chemical shift information can be extracted from the spectra. Thus far, the systems have mainly yielded relaxation times as a crude estimate of material composition, but more detailed information would benefit a broad range of fields, from medical diagnosis to archaeological analysis.

Recently, a solution to this ex situ challenge has been proposed (2). The strategy compensates for the main field inhomogeneity by using parallel variations in the applied radio frequency (rf) field. For spins with the same chemical shift, different Larmor frequencies throughout the sample give rise to progressive dephasing during a free evolution period. At any stage, this loss of coherence can be reversed if a proper position-dependent phase correction is applied. However, when this is done, phase differences accumulated during the evolution and arising from the chemical shift differences must be maintained. Such a position-dependent phase correction can be accomplished by the use of z-rotation pulses (3). In the presence of matched rf and static field profiles, these pulses induce echoes with a phase sensitive only to chemical shift differences. Sampling of the echo maxima occurring after incremental periods of free evolution leads to high-resolution NMR spectra. Unlike other approaches (4–7), this method can be used at low magnetic field strengths and does not rely on any special properties of a given substrate, such as intramolecular interactions.

Here we describe a portable single-sided sensor that functions on the above principle. Two concentric, U-shaped NdFeB magnets inducing opposing magnetic fields were arranged. We reconstructed a well-resolved spectrum by sequentially incrementing the length of the initial (spatially dependent) pulse β (8). As a proof of principle, we acquired ^{19}F spectra of several fluorinated hydrocarbons. Optimization of the coil and magnet geometry provided a preliminary linewidth of 2500 Hz, which further narrowed to 65 Hz when the refocusing pulse sequence was applied. This resolution, corresponding to a chemical shift of 8 parts per million (ppm), required only 3 min of acquisition time. These results suggest that proton chemical shift resolution could be achieved in the near future (the ^{1}H chemical shift range is 12 ppm).

1. Blümich, B., NMR Imaging of Materials (Clarendon Press, Oxford, 2000).
2. Meriles, C.A., *et al.*, Science 293, 82 (2001).
3. Ernst, R. R., *et al.*, Principles of Nuclear Magnetic Resonance in One and Two Dimensions (Clarendon Press, Oxford, 1994).
4. Weitekamp, D. P., *et al.*, J. Am. Chem. Soc. 103, 3578 (1981).
5. Balbach, J.J., *et al.*., Chem. Phys. Lett. 277, 367 (1997).
6. Hall, L.D., *et al.*, J. Am. Chem. Soc. 109, 7579 (1987).
7. Richter, W., *et al.* , Science 267, 654 (1995).
8. Perlo, J., *et al.* , Science 308, 1279 (2005). Published online 7 April 2005; 10.1126/science.1108944.

Avalanching Amplification of MR Imaging Contrast by Feedback Fields for Lesion Characterization and Detection

Susie Y. Huang,[1] Sandip Datta,[1] Massoud Akhtari,[2] Gary W. Mathern,[3] Harry V. Vinters,[4] Dennis J. Chute,[4] Yung-Ya Lin[1]

[1]Department of Chemistry and Biochemistry; [2]Department of Neurology; [3]Division of Neurosurgery; [4]Department of Pathology and Laboratory Medicine, University of California, Los Angeles, California, USA

Introduction

Limitations in endogenous contrast can pose challenges to delineating the exact extent of lesions by MRI. We have developed nonlinear feedback interactions known to emerge in aqueous media at high fields into a flexible, general contrast enhancement mechanism sensitive to versatile endogenous MR contrast sources *(1)*. The sensitivity of the individual and joint feedback interactions to small spatial variations in MR parameters is applied to amplify MRI contrast in brain lesions involved in epilepsy and cancer.

Theory and Methods

Recent studies have revealed that two nonlinear feedback fields – the distant dipolar field (DDF) and radiation damping – combine to generate dynamical instability *(2)* leading to chaotic spin dynamics *(3)* in MR experiments at high fields. The DDF arises in solution from long-range dipolar couplings that survive spatial and temporal averaging *(4)*, while radiation damping acts back on the spins through the induced current in the receiver coil *(5)*.

A sample sequence for contrast enhancement by the individual or joint feedback fields is shown in Fig. 1. The initial pulse tips the magnetization to regions of varying stability under radiation damping, while sample inhomogeneity introduces a weak gradient to enhance the DDF. Spatial variations in resonance frequency may be accentuated by the highly selective radiation damping field alone or together with the DDF through positive feedback *(1,3)*. The instability of the DDF may also be exploited to generate exponentially growing contrast based on differences in spin density.

Brain tissue samples excised from intracranial surgeries at the UCLA Medical Center were imaged by gradient echo imaging following the sequence in Fig. 1. The tissue was preserved in saline at 5°C and imaged in a 14.1-T Bruker microimaging system (5-mm coil optimized for ^{1}H sensitivity, radiation damping time τ_r=5.35ms).

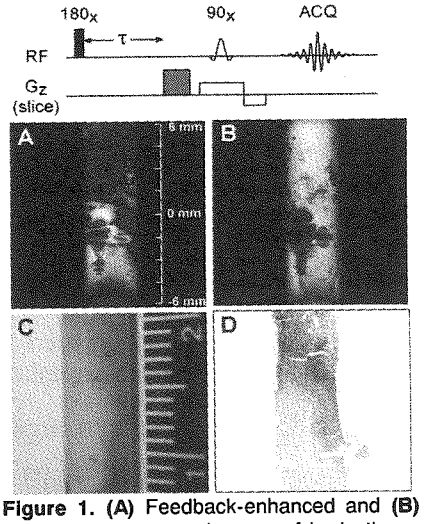

Figure 1. (A) Feedback-enhanced and **(B)** T_2-weighted contrast images of brain tissue excised from a patient with cortical dysplasia. Feedback-enhanced images show amplified contrast between dysplastic and normal gray and white matter, seen in **(C)** gross anatomy and **(D)** histology.

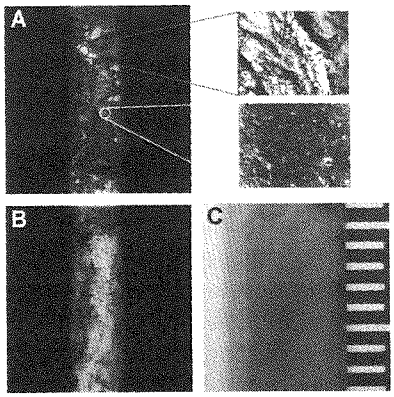

Figure 2. (A) Feedback-enhanced contrast image of brain tissue excised from a patient with GBM. Regions of enhanced signal intensity correspond to tumor cells surrounding the microvasculature (histology, red) compared to normal tissue (yellow). **(B)** Corresponding T_2-weighted image. **(C)** Gross anatomy for comparison.

Applications and Results

Under radiation damping alone, avalanching amplification of small variations in resonance frequency can complement and augment existing MR sequences for improved characterization of brain lesions associated with epilepsy (cortical dysplasia, Fig. 1) and cancer (glioblastoma multiforme, GBM, Fig. 2). The radiation damping feedback field is sensitive to differences in resonance frequency between the cells and fat in gray and white matter and differences in oxygenation level between tumor and normal tissue.

Discussion and Conclusion

We have demonstrated a method for amplifying small spatial variations in MR parameters through feedback fields. This technique may open new opportunities for enhancing contrast in clinical MR applications, such as more precise delineation of cortical dysplasia in patients with intractable epilepsy and the earlier detection and characterization of brain tumors.

References: 1. Huang, S. Y.; Datta, S.; Akhtari, M. et al. *Science* (submitted). 2. Jeener, J. *J. Chem. Phys.* **116**, 8439-8446 (2002). 3. Lin, Y.-Y.; Lisitza, N.; Ahn, S.; Warren, W. S. *Science* **290**, 118-121 (2000). 4. Warren, W. S.; Richter, W.; Andreotti, A. H.; Farmer, B. T., II *Science* **262**, 2005-2009 (1993). 5. Bloembergen, N.; Pound, R. V. *Phys. Rev.* **95**, 8-12 (1954).

Non-destructive observation of pine wilt disease using an open-type NMRI system

Shin Utsuzawa[1, 2]
[1]MRTechnology, Inc., Japan, [2]Institute of Applied Physics, University of Tsukuba, Japan

Introduction

Pine wilt disease induced by pinewood nematodes (*Bursaphelenchus xylophilus*) is the most serious tree epidemic in eastern Asia. Over the last 30 years, about 1 million m^3 of pine trees have been killed annually in Japan. To understand the symptom development, xylem cavitations have been observed by sectioning and staining of the stem. However, such destructive method makes it impossible to observe symptom development on the same individual, so that it is difficult to capture the rapid shift.

Recently, MRI has been used as a non-destructive way to study water status in plants [1, 2]. Though MR microscopes with super-conducting magnets have sufficiently high resolution (<100 μm) to observe small areas of cavitations, they cannot accommodate a whole pine seedling with spread branches. Moreover, because such magnets require large amount of space and costs, most botanists and plant pathologists are unable to use them over long period.

In this work, we used a compact MR microscope with an open-type permanent magnet to investigate the development of cavitations caused by pine wilt disease *in situ*.

Materials and methods

Experiments were performed on three 3-year-old Japanese black pine (*Pinus thunbergii Parl*) seedlings grown at the Experimental Station at Tanashi, University of Tokyo. These seedlings were planted in plastic pots prior to the experiment. Sample seedlings were inoculated with 10,000 nematodes (S-10) suspended in 0.01 ml of water to the current shoot through a notch made with a razor blade. A control seedling was injected with water but no nematodes in the same way. For MRI measurements, a solenoid RF coil was wound on the stem and installed in a shield box. These pine seedlings were placed in a compact MR microscope equipped with a four-column permanent magnet (1.0 T field strength, 6 cm air gap). Non-destructive observations were conducted throughout the experimental periods with keeping this setup. Illumination and water were supplied to the seedlings from open top and side of the magnet.

Results and discussion

On seedling No. 2, a dark spot representing cavitations caused by the pinewood nematode appeared in earlywood of the last year on day 7 (Fig. 1). The number and the area of the dark spots grew gradually until day 20; this period is regarded as an early stage. From day 20 to day 23, many new patches occurred simultaneously, expanded rapidly, and fused together; this period is regarded as an advanced stage. Cavitation developments in seedlings No. 1 and No. 3 followed a similar pattern as that in seedling No. 2. On the other hand, no changes were found on the control seedling. Our MR observations have indicated that the cavitations expanded explosively within only 2-4 days in the advanced stage. Such a rapid process would not be observable without continuous and non-destructive method.

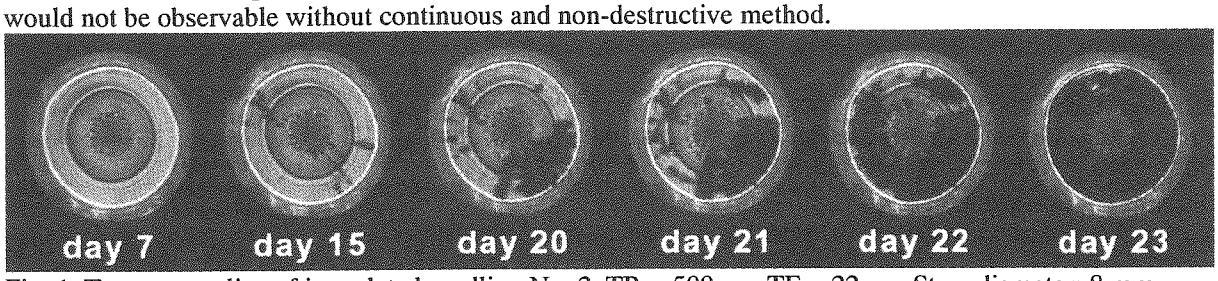

Fig. 1. Transverse-slice of inoculated seedling No. 2. TR = 500 ms, TE = 22 ms, Stem diameter: 8 mm.

Acknowledgements

The author thanks Professor Kenji Fukuda and Daisuke Sakaue for providing the pine seedlings and nematodes. The author also thanks Professor Katsumi Kose and Dr. Tomoyuki Haishi for their supports in constructing and using the apparatus.

Reference

[1] Kuchenbrod E, Kahler E, Thuermer F, Deichmann R, Zimmermann U, Haase A, Magn. Reson. Imag. 16 (1998) 331-338.

[2] Van der Weerd L, Claessens MMAE, Ruttink T, Vergeldt FJ, Schaafsma TJ, Van As H, J. Expt. Botany 52 (2001) 2333-2343.

Ferromagnetic Nanostructures for Atomic Resolution Magnetic Resonance Microscopy

Mladen Barbic
Department of Physics and Astronomy
California State University, Long Beach

The achievement of three-dimensional atomic resolution magnetic resonance microscopy remains one of the main challenges in biological and materials visualization. Two recent advances towards this goal will be presented. First, a nanomagnetic planar design will be described where a localized Angstrom-scale point in three-dimensional space is created above the nanostructure with a non-zero minimum of the magnetic field magnitude [1]. The design represents a magnetic resonance microscopy "lens" where potentially only a single nuclear spin located in the "focus" spot of structure is resonant. Introduction of this "lens" into a scanning probe microscopy type instrument might provide 3-D atomic resolution performance if appropriate quantum measurement methodology and spin sensitivity and can be engineered. Towards this end, a nanowire-based methodology for the fabrication of ultra-high sensitivity and resolution probes for atomic resolution magnetic resonance force microscopy will be introduced [2]. The fabrication technique combines electrochemical deposition of multi-functional metals into nanoporous polycarbonate membranes and chemically selective electroless deposition of optical plasmon nanoreflector onto the nanowire. The completed composite nanowire structure contains all the required elements for potentially single nuclear spin sensitivity and resolution force sensor with: (a) magnetic nanowire segment providing atomic resolution magnetic field imaging gradients as well as large force gradients for high sensitivity, (b) noble metal enhanced nanowire segment providing efficient scattering cross-section from a sub-wavelength plasmon source for optical readout of nanowire vibration, and (c) non-magnetic/non-plasmonic nanowire segment providing the cantilever structure for sensitive mechanical detection of magnetic resonance.

[1] M. Barbic and A. Scherer, *Nano Letters* **5**, 787 (2005).
[2] M. Barbic and A. Scherer, *Nano Letters* **5**, 187 (2005).

Methodology and Hardware Development on Ex-Situ NMR/MRI: Let the Spins do the Work!

Vasiliki Demas[a], John Franck[a],Rachel Martin[a], Louis Bussard[a],
Alejandro Bussandri[b], Pablo Prado[b] Jeffrey Reimer[a] and Alexander Pines[a]

[a] University of California-Berkeley, Departments of Chemistry and Chemical Engineering
Berkeley, CA 94720, [b]GE Security, San Diego, CA

July 1, 2005

Ex situ or single sided, portable NMR probes have several advantages over conventional NMR systems. They can be taken in the field for on-site studies, offer open access to arbitrary-sized or immovable samples, and are inexpensive and robust. For example, portable NMR systems are being used to determine relaxation times [1]. However, these devices have not been used for spectroscopy, due to the inherent inhomogeneities of the static magnetic field present in single sided systems.

We have previously shown that one can overcome the effects of field inhomogeneities, and unveil spectral information using ex-situ matching [2]. This methodology capitalizes on the use of spatially matched inhomogeneous radiofrequency coil for excitation and spin manipulation. The spatial matching between the static field and the set of the rf coil guarantees a correlation of the fields and the possibility of mutual canceling of their effects. The effects of an inhomogeneous static or rf field are similar and lead to dephasing in their respective frames of reference. Z-rotation composite or adiabatic pulses have been used to recover high-resolution spectra in the presence of inhomogeneous fields [2,3,4]. Ex-situ matching relies in precise hardware design and construction in order to achieve high-resolution spectra, which can be proven limiting. Another, complimentary way to create a crafted spatial field distribution is via the ex-situ shim pulses [5]. Static field gradients from imaging gradient coils impose a spatial dependence on the spin precession frequency. Frequency selective pulses applied in the presence of static field gradients, therefore affect spins in a spatially selective way. Suppose one such rf pulse provides a phase shift to the spins, in a spatially dependent manner. If the gradients change before a second selective pulse is applied, another phase is given that depends on space. One can optimize the way the gradients are modulated so that this space dependence cancels inherent static field inhomogeneities, resulting in either an effectively homogeneous field, or providing a linear spatial dependence for imaging in one or more dimensions. 3D imaging can be accomplished by simultaneously applying B_0 gradients in three directions. The B_1 field can be inhomogeneous (as in the case of ex-situ) or homogeneous (for in situ cases).

In the case of ex-situ shim pulses for spectroscopy, the combination of ex-situ matching and shim-pulses relaxes the hardware requirements on both techniques: matching doesnt have to be "perfect" and the strength of the shim pulse gradients doesnt have to be as high. The way that the ex-situ shim pulse scheme works as follows: first the static magnetic field is mapped via NMR: a $B_0 - B_1$ correlation NMR experiment- an rf coil geometry producing a field with a well known spatial dependence is used to label the position of the sample in space, and therefore the correlation experiment unambiguously gives the local B_0 field value). Second, a coil geometry that to a first degree, matches the static field in the ex-situ case is built (in the in-situ case the coil is designed according to the experiment requirements it could be inhomogeneous is a single sided coil is desired, or a homogeneous coil can be used). For a given set of gradient coils, rf geometry and static field profile, the shim pulses are optimized to either produce a homogeneous or linearly varying field.

The phase of spin ensembles in the presence of an effective field, B_{eff}, is

$$\phi(r,t) = \gamma \int_0^t \sqrt{|B_{eff}(r,t')|^2}dt' = \gamma \int_0^t \sqrt{B_1(r,t')^2 + (\frac{\Delta\omega(r,t')}{\gamma})^2}dt' \quad (1)$$

The static field is measured during field mapping. As an example, the static field is assumed to have a quadratic dependence in two dimensions (x and z).

$$Y(x,z) = Ax^2 + Bz^2 \tag{2}$$

A general form is given to the time modulated gradients (a sum of sinusoidal waves)

$$G_{shim}(t) = \Sigma_i a_i sin(\omega_i t + \phi_i) \tag{3}$$

The rf pulses as a first approach are adiabatic, where the amplitude and the frequency is modulated. A hyperbolic secant tangent pair for the amplitude and frequency modulated rf pulses is chosen for this example. The B_1 field can have a space dependence, but it is not necessary for the technique to work.

$$B_1(r,t) = B_1^{max}(r)sech(\beta t) \tag{4}$$

$$\omega_{RF}(t) - \omega_c = \mu\beta tanh(\beta t) \tag{5}$$

For shim pulses, one can set as the goal to create a phase that cancels that of the local inhomogeneity for a homogeneous overall effect. It is easy to project to imaging in the case the gradients are not pure, and the final goal is a phase that has a linear dependence in space. Calculate a_i, ω_i, ϕ_i so that the local dephasing is cancelled:

$$\phi(r,t) = \gamma \int_0^t \sqrt{B_1(r,t')^2 + (r * \vec{G}_{shim} + B_0(r) - \frac{\omega_{RF}(t')}{\gamma})^2} dt' - (Ax^2 + Bz^2)\gamma t \tag{6}$$

Our work involves methods for making the field of portable and/or single sided magnets more homogeneous or create effectively clean gradients for imaging both in in-situ and ex-situ setups. This technique, like its precursors, increases the useful sample volume of the homogeneous field or the field of linear gradient, while the hardware can be less expensive and easier to construct. A new hand portable system and application of our methodology is presented.

References

1. DP Weitekamp, JR Garbow, JB Murdoch, A Pines, J. Am. Chem. Soc. 103, 3578 (1981)
2. JJ Balbach et al., Chem. Phys. Lett. 277, 367 (1997).
3. B Blmich, NMR Imaging of Materials (Clarendon Press, Oxford, 2000).
4. CA Meriles, D Sakellariou, H Heise, A Moule, A Pines, Science 293, 82 (2001).
5. Henrike Heise, Dimitris Sakellariou, Carlos A. Meriles, Adam Moule, and Alexander Pines, J. Mag. Reson. 156, 146-151 (2002).
6. Carlos A. Meriles, Dimitris Sakellariou, and Alexander Pines, J. Magn. Reson. 164, 177-181 (2003).
7. US Patent 6,674,282 B2 (2004)
8.Dimitris Sakellariou, Carlos Meriles, Alexander Pines, Comptes Rendus Academie des Sciences Physique 5, 337-347 (2004).
9. V Demas, D Sakellariou, C Meriles, S Han, J Reimer, and A Pines, Proc. of the Natl. Acad. Sci. 101 (24), 8845-8847 (2004).
10. D Topgaard, RW Martin, D Sakellariou, CA Meriles, A Pines, Proc. Natl. Acad. Sci. 101(51), 17576-17581 (2004).
11. J Perlo, V Demas, F Casanova, C Meriles, J Reimer, A Pines, and B Blumich, Science, 308 1279 (2005).

High-resolution sample profiling by single-sided NMR

Federico Casanova, Juan Perlo, and Bernhard Blümich
ITMC - RWTH-Aachen Worringerweg 1, D52056 Aachen, Germany

Single-sided NMR sensors offer non-invasive access to arbitrarily sized objects. They combine open magnets and surface rf coils to generate a sensitive volume external to the sensor and inside the object under investigation [1-5]. The price paid to gain in access is the impossibility of generating homogeneous magnetic fields. Nevertheless, this natural gradient can be exploited to obtain depth resolution into the material. The procedure is fully equivalent to the one used by the STRAFI technique [6], where the strong stray field gradient of superconducting magnets is used to measure profiles with high spatial resolution. Although the strength of the static gradient generated by single-sided magnets is comparable to that in STRAFI experiments, the lateral gradients from small magnets results in rather poor depth resolution. Several attempts have been made to increase the gradient uniformity by tailoring the magnet geometry, but spatial resolution better than half a millimeter is hard to achieve [7-10]. The philosophy adopted in previous designs failed to request the magnet to generate a flat field profile in a large range of depths. This profile is convenient because it allows one to select planar slices at different depths into the object just by electronically switching the tuning frequency, but complicates the magnet and limits the resolution

In this work a new single-sided NMR sensor that provides microscopic resolution sample profiling is described. It uses a new magnet geometry that generates a magnetic field with a highly uniform gradient at a given depth from the magnet surface. Tuning the sensor to the resonance frequency defined at this plane selective excitation of a thin flat slice inside the object can be achieved. Repositioning the sample, 1D profiles with a resolution better than 5 μm can be achieved. For the first time a NMR sensor provides *in situ* microscopic profiling of samples unrestricted in size. Potential use of the profiling technique was demonstrated in a number of applications like the measurement of moisture profiles, the effects of cosmetics in human skin, solvent ingression in polymers, and the state assessment of paintings in the conservation of objects of Cultural Heritage.

1. Jackson JA, et al., J. Magn. Reson **41**, 411-421 (1980).
2. Kleinberg RL, et al., J. Magn. Reson. **97**, 466-485 (1992).
3. Eidmann G, et al., J. Magn. Reson. **A122**, 104-109 (1996).
4. Kleinberg RL, et al., pp. 4960-69 Wiley, New York (1996).
5. Matzkanin GA, in " Nondestructive Characterization of Materials", pp. 655, Springer, Berlin (1998).
6. McDonald PJ, Prog. Nucl. Magn. Reson. Spectrosc. **30**, 69-99 (1997).
7. Prado PJ, Magn. Reson. Imaging **19**, 505-508 (2001).
8. Casanova F, et al., J. Magn. Reson. **163**, 38-45 (2003).
9. Perlo J, et al., J. Magn. Reson. **166**, 228-235 (2004).
10. Prado PJ, Magn. Reson. Imaging, **21**, 397-400 (2003).

Mapping Fast, Turbulent Gas Flow

C. C. Poirier[2], Yang Zhi[1], B. Newling[1]
Departments of Physics[1] and Electrical & Computer Engineering[2], University of New Brunswick, PO Box 4400, Fredericton, NB E3B 5A3, Canada.

Introduction

Frequency-encoded imaging methods suffer in turbulent flows. Intravoxel phase dispersion causes localized signal cancellation and, where flow speeds are sufficiently high, the displacement of fluid parcels out of the sensitive volume of the probe during the acquisition interval may completely destroy an image. Purely phase-encoded techniques, such as single-point imaging (SPI) and single-point imaging with T_1 enhancement (SPRITE) [1] have the advantage of short, constant encoding times, which can permit mapping of fast flows (>10 m/s) even in a thermally polarized gas ($T_1 \sim T_2 \sim 1$ ms). We have demonstrated the applicability of motion-sensitised SPRITE to gas flow in a wind-tunnel type setting at Reynolds numbers in excess of 200 000, past a variety of obstructions [2].

Methods

Sulphur hexafluoride gas was pumped at up to 17 m/s around a closed network passing through the centre of a 2.4 T superconducting, horizontal-bore magnet. A centric SPRITE imaging technique (Fig. 1A) was adapted by the superposition of a bipolar gradient upon each of the gradient steps in the pointwise k-space trajectory (Fig. 1B). The size of the bipolar gradient step, g, was increased in each of a series of 8 measurements. Each image contained the same geometrical information, but was differently sensitised to motion. The phase evolution with g at each image pixel gave a measure of mean velocity (in the direction of applied gradient). The magnitude decay with g at each pixel gave a measure of local mechanical dispersion. These data were analysed in terms of a turbulent eddy diffusivity [3]. Data acquisition and analysis, in particular the assumptions inherent to that analysis, will be discussed.

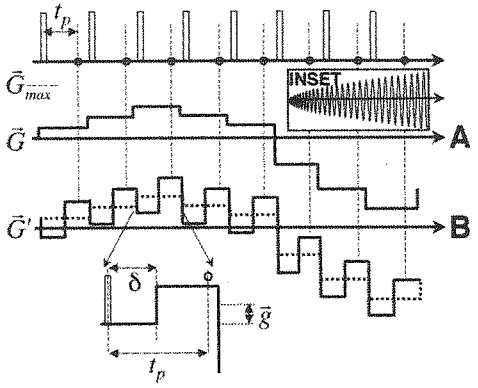

Fig. 1. Centric SPRITE pulse sequence (A) and the motion-sensitised adaptation (B).

Results

We will compare computational fluid dynamics (CFD) calculations (Fig. 2B & D) with the SPRITE maps of mean velocity (Fig. 2A) and turbulent eddy diffusivity (Fig 2C).

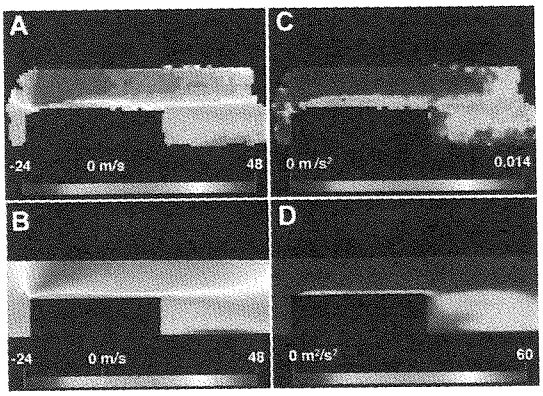

Fig. 2. (A) SPRITE maps of (A) mean velocity in z and (C) the principal component of eddy diffusivity in z compared with CFD maps of (B) mean velocity and (D) turbulence kinetic energy.

Conclusions

By virtue of a short encoding time, the new SPRITE method extends the range of fluid speeds and the range of fluids accessible to MRI. The method yields, of necessity, a time-averaged measurement and cannot aim to take a snapshot of the flow field like ultrafast imaging techniques [4,5], but has some peculiar advantages in gas flow, for which future prospects will be discussed.

References

[1] Halse M. *et al. J. Magn. Reson.* **165**, 219-229 (2003).
[2] Newling, B. *et al. Phys. Rev. Lett.* **93**, 154503 (2004).
[3] Kuethe D. O. *et al. Phys.Rev. E* **51**, 3252 (1995).
[4] Kose, K. *Phys.Rev. A* **44**, 2495 (1991).
[5] Sederman *et al. J. Magn. Reson.* **166**, 182 (2004).

Correlating histology with the diffusion tensor: Specific findings in the dysmyelinating shiverer mouse

J. M. Tyszka[1], E. L. Bearer[1,2], and R.E. Jacobs[1]
[1]California Institute of Technology, Pasadena CA 91125 USA
[2]Brown Medical School, Providence RI 02912 USA

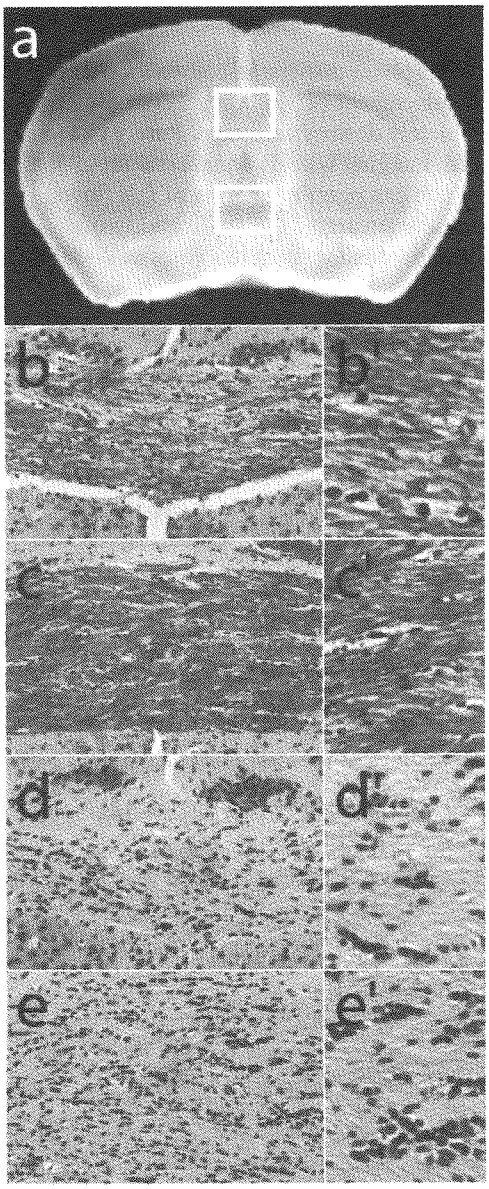

Diffusion tensor imaging (DTI) models anisotropy due to restricted diffusion within biological specimens as a second-rank tensor. When applied to the central nervous system, DTI is particularly sensitive to highly coherent structures such as white matter tracts. In this study, we compare high resolution, contrast enhanced diffusion tensor histology with conventional optical histological analysis of these same brains after embedding, sectioning and staining. Patterns in control mice (C3HeB.FeJ, n = 6) were compared to standard mouse brain atlases and to the histologic patterns in the same brains to determine the size of features detected by DTI. To determine the efficacy of DTI in detecting myelination defects and associated microhistological changes, the anisotropy patterns in these normal brains were compared to DTI obtained from mice carrying the shiverer mutation (C3Fe.SWV Mbp^{shi}/Mbp^{shi} n = 6) with CNS dysmyelination. Mice were anesthetized and the brains fixed by transcardiac perfusion with paraformaldehyde. The brains were retained within the skull and immersed in saline for one week followed by 5mM gadoteridol (Prohance®) for one week prior to MR microscopy. Diffusion weighted images and a single un-weighted reference were acquired in an optimized 6-point icosahedral encoding scheme using a conventional PGSE sequence (TR/TE = 150ms/11.6ms, 19.2mm x 15mm x 12mm FOV, 80μm isotropic voxel sizeδ = 3ms, Δ = 5ms, G_d = 750mT/m, nominal b-factor = 1450 s/mm^2) for a total imaging time of 6 hours. Following DTI, the brains were embedded in paraffin, sectioned and stained (Weil-Myelin and Nissl). Diffusion tensor images were accurately co-registered using non-linear warping allowing voxel-wise statistical parametric mapping of differences in tensor invariants between control and shiverer groups. Highly significant differences in the tensor trace and both the axial and radial diffusivity were observed within the major white matter tracts and in the thalamus, midbrain, brainstem and cerebellar white matter, consistent with dysmyelination effects in the shiverer mutant. In addition, DTI also revealed dysmyelination effects in the ventral midbrain and subthalamic nuclei. DTI of shiverer mice demonstrated only minor decreases in fractional anisotropy in the well-established tracks despite myelin defects. Close examination of major control brain fiber tracts in histological section revealed that the constituent nerve bundles are not aligned like parallel straws in a bundle, but rather form a complex braided structure (Figs b & c). Quantitative histologic analysis shows that dysmyelinated tracts in shiverer had 5-20 times more nuclei, were 1.5-3 fold wider, and appeared more loosely organized than in the control (Figs d &e). In the subthalamic region, tracts obvious in myelin stained wild-type histologic sections were far less pronounced in Shiverer, correlating with the mean diffusivity but not the anisotropy as measured by DTI, in that region.

Supported by NCRR-BIRN, NINDS (E.L.B) and NIGMS (E.L.B.)

Development of Ultra Low Temperature Magnetic Resonance Microscope

Yutaka Sasaki, Takayoshi Tanaka, and Takao Mizusaki

Research Center for Low Temperature and Materials Sciences, Kyoto University, Kyoto, Japan

and

Department of Physics, Graduate School of Science, Kyoto Univerisity, Kyoto, Japan

We have developed a Magnetic Resonance Microscope, which is specialized for imaging quantum condensate, such as nuclear ordered antiferromagnetic solid helium three. By the aid of the extremely strong NMR signal obtained from a sample, which is cooled down to well below 0.001 K, we could achieve good enough S/N to obtain 3D distribution of the magnetic domain structure of antiferromagnetic solid helium three with a few 10μm resolution. These achievement include (1)designing homemade compact MRI system, which is suitable in combining with dilution refrigerator and nuclear demagnetization refrigerator, both of which are necessarily to cool the sample down to such a ultra low temperature, (2)method of obtaining NMR spectrum from FID under constant magnetic field gradient, which is necessarily to avoid complicated non-linear NMR responses of the nuclear ordered antiferromagnet, (3)method of obtaining 3D image without using the pulsed field gradient, which disturbs ultra low temperature environment due to its vibration and possible eddy current heating onto the refrigerator. Combining those technology we could obtain 3D image of the magnetic domain distribution of the antiferromagnetic solid helium three, which has uniaxial spin symmetry called as U2D2 structure. A single crystal of this U2D2 helium three normally possess a spontaneous magnetic domain structure, whose domain size is comparable to the size of a crystal. The domain wall between each domains are a rather well defined flat wall , most popular direction of which is (1,1,0) in a bcc lattice structure. By sweeping up the external magnetic field through Bc=0.45T, this U2D2 helium three transforms into another phase of antiferromagnet called as CNAF phase, whose spin symmetry is cubic rather than uniaxial. This CNAF helium three has no apparent way to keep the original domain structure in U2D2 phase. However, when external magnetic field was swept back below Bc, we observed a remarkable recovery of the original domain distribution in the U2D2 phase. This "memory effect" is under investigation so far. We would conclude that our method could also be applied to study microscopic magnetism of magnetically ordered material, due to its method of avoiding nonlinear NMR response, which normally shows pretty much different behavior from the one from Bloch eqs.

Ref[1]. Sasaki, Y. *et al.*, J. Low Temp. Phys. 138(2005) 911-916.

NMR-MANDHALAS: Mobile NMR, MRI and EPR

P. Blümler[1,2], H. Raich[1], C. Bauer[1], G. Jeschke[1]

[1] *Max Planck Institute for Polymer Research, 55128 Mainz, Germany*
[2] *ICG-III: Phytosphere, Research Centre Jülich, 52425 Jülich, Germany*

Purpose: Magnets of the Halbach layout [1] are very interesting for the use in mobile magnetic resonance devices, because they can be designed to provide magnetic flux with high homogeneity over a wide area. In addition the flux is almost completely enclosed in the structure, so that only minimal stray fields are observed, and the field is transverse to the cylinder axis, which allows the use of solenoidal coils. However, the ideal Halbach magnet is difficult to manufacture due to variations in magnetic field strengths and directions of its various pieces.

Methods: Therefore, it was iterated using identical bar-magnets which are positioned and oriented based on analytical equations. The resulting field distributions suggested the acronym NMR-Mandhala (**M**agnet **A**rrangements for **N**ovel **D**iscrete **Ha**lbach **La**yout) [2] for such designs, which were simulated with two-dimensional finite-element methods. Performance factors were defined to relate field strength with homogeneity and mass.

Results: The homogeneity in the third dimension was optimized by stacking such rings with varying distance. With this principal design field strength in the order of 0.3 T and homogeneities of about 100 ppm were realized over a spherical volume with a radius of 15 mm. This magnet has a weight of about 8 kg.

Various alterations of the principal design are discussed with their advantages and disadvantages. The design of cylindrical gradient coils for generating transverse fields is presented together with first images and EPR measurements.

Conclusions: A magnet design is presented, with the following advantages:

- High homogeneity
- Close to optimum use of mounted magnetization (maximum field per weight)
- Very small stray field
- Transverse field direction (allows the use of solenoidal coils for NMR)
- Made from identical, simple magnets
- Robust
- Easy and cheap to produce (overcoming the individually shaped and polarized magnets of ideal Halbach magnets)

1 J. M. D. Coey, "Permanent magnet applications" J. Magnetism and Magn. Mat. 248 (2002) 441-456.

2 H. Raich and P. Blümler, "Design and Construction of a Dipolar Halbach Array with an Homogeneous Field from Identical Bar-Magnets — NMR-Mandhalas—" Concepts of Magnetic Resonance 23B(1) (2004) 16-25.

Magnet, Coil, and Gradient Set for Single-Sided MR

Pablo Prado, Serge Bobroff, Alejandro Bussandri, and Jess Lawton

GE Security, San Diego, USA

Introduction. Collecting MR signals from a sensitive volume entirely outside the probe facilitates non-invasive diagnosis. This is a powerful concept for industry and medicine. However a development challenge for single-sided MR, when compared to conventional in-magnet MR, is to deal with highly non-uniform static and RF fields [1-4]. The tradeoffs between sensitivity, resolution, and geometry of the sensed volume need close scrutiny. It is easily demonstrated that *one size fits all* is not a successful approach when designing open MR instruments.

Methods. Two configurations are discussed. An imaging modality, where spatial resolution is attained deep into the sampled volume and a high sensitivity modality. The units are built with NdFeB material due to its combination of high remanence and coercivity. Its energy product is as high as 52 MGOe. These units do not require cryogenic or water cooling for the magnets or gradients.

1. IMAGING. The probe head weighs about 6 kg and is operated up to 4 m from a portable console. Depth discrimination and phase encoding are attained over an extended depth of scan. The static magnetic field distribution presents flat regions of constant magnitude [4]. Depth selection by frequency stepping and imaging protocols are controlled by scripts driven from a GUI. Diffusion parameters, MR signal intensity and relaxation times are measured at selected depths into the sample. The sensor head houses the single-sided permanent magnet array, a flat RF coil, an automatic tune circuit, and the first receiver amplifier stage. A gradient set attached to the mobile sensing head further extends the imaging capabilities for in-plane spatial resolution using 2D phase encoding. A replacement set of dedicated gradient coils is under development. In the design of these planar elements, current patterns are modeled as linear combinations of harmonics in two dimensions on a surface. Coefficients of harmonics are optimized for linearity, while heat generation is used as the limiting parameter.

2. NEAR SURFACE MR. Compact configurations are used to attain small sensitive volume and relatively high sensitivity. The design is focused on high field strength and relatively high homogeneity at the cost of scanning over a small volume, close to the probe head. Two arrays have been built, a) a probe head weighing about 0.5 kg [5] and b) a highly tailored sensitive volume array weighing about 5 kg.

Results. The performance of the imaging system has been tested with a series of phantom samples, including stacks of thin polymers. Depth resolution better than 100 microns is achieved by slice selection using automated frequency shifting. This unit singles out sub-millimeter layers of materials up to 2 cm away from the probe head.

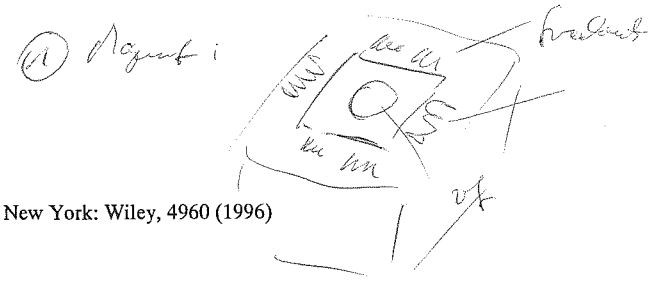

References

1. Hürlimann, M.D., et al, J Magn Reson 143, 20 (2000)

2. Blümich, B., et al, Magn. Reson. Imaging 16:479 (1998)

3. Kleinberg R.L., et al, Well Logging, in: Encyclopedia of NMR, New York: Wiley, 4960 (1996)

4. Prado, P.J., Magn. Reson. Imaging, 21, 397 (2003)

5. Prado, P.J., Magn. Reson. Imaging, 19, 506 (2001)

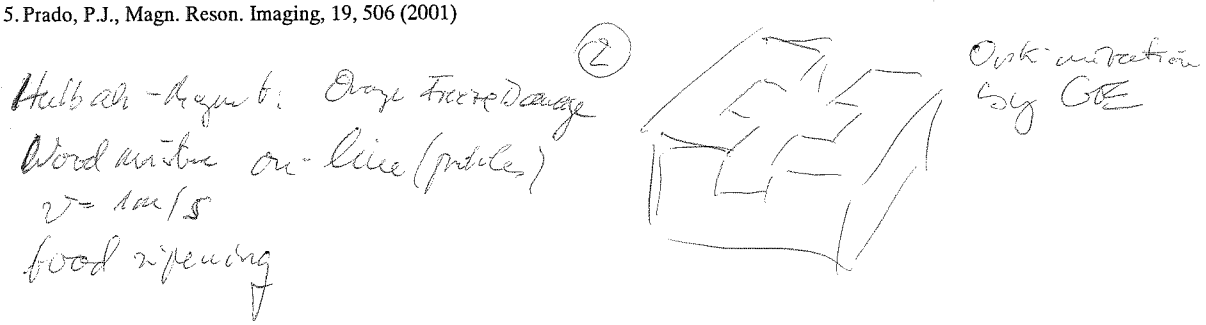

An analytical target field approach for B_0 control in unilateral NMR

Andrew E. Marble[1,2], Igor V. Mastikhin[1], Bruce G. Colpitts[2], and Bruce J. Balcom[1]

[1]MRI Centre, Department of Physics, and [2]Department of Electrical and Computer Engineering, University of New Brunswick, Fredericton, NB, Canada.

Introduction: Unilateral NMR (UMR) employs a planar array of permanent magnets (PMs) to produce a remote, MR compatible B_0 field[1]. While different PM topologies have been proposed, a common drawback is the lack of rational control of essential properties of B_0 such as the size and shape of the MR sensitive volume, and the homogeneity of the magnetic field. We have developed a systematic design strategy which allows a desired B_0 topology (strength, gradient, homogeneity) to be specified. From these parameters, a PM array fitted with high magnetic permeability pole caps shaped according to an analytical expression is synthesized to produce the required field. Here, we present an overview of the design strategy which has been validated through the construction of a new UMR array. Different designs, tailored to solve unique problems in material science MR are discussed, and sample applications are presented.

Methods: A magnetic field traversing the boundary between a high-permeability material and air can be approximated as being oriented perpendicular to the interface. When the magnetic field is defined through a scalar potential as $B = \nabla\phi$, the surface of the material then becomes an equipotential contour of ϕ[2]. Because B must be divergence free, ϕ must satisfy Laplace's equation. In two dimensions, a suitable solution is

$$\phi(z,y) = \sum_{n=1}^{N} e^{-a_n y}\left[b_n \cos(a_n z) + c_n \sin(a_n z)\right]. \qquad (1)$$

The associated B_0 field can be analytically determined as the gradient of Eq. (1). This field is described entirely by the coefficients a_n, b_n, and c_n, and can be shaped to approximate the desired B_0 topology through numerical or analytical optimization of these coefficients[3]. After a suitable B_0 field is achieved, ϕ can be calculated directly from the coefficients, and suitable contours of the scalar potential can be used to define the shapes of high permeability pole pieces. Permanent magnets beneath the pole pieces generate B_0. By extending the magnets and pole pieces in the third (x) dimension, a field matching the design parameters can be achieved over the center of the array.

Our technique was used to design a UMR array suitable for the detection of moisture within aerospace composite panels. These composites are made up of aluminum and graphite, conductive materials which can impede B_1 penetration and MR signal detection[4]. A large volume of homogeneous B_0 over the array was desired, along with a low resonant frequency to mitigate the effects of conductors on B_1.

Results: Figure 1 presents a photograph of a fabricated array (a), the measured field (b), and a test measurement of moisture within a composite panel (c).

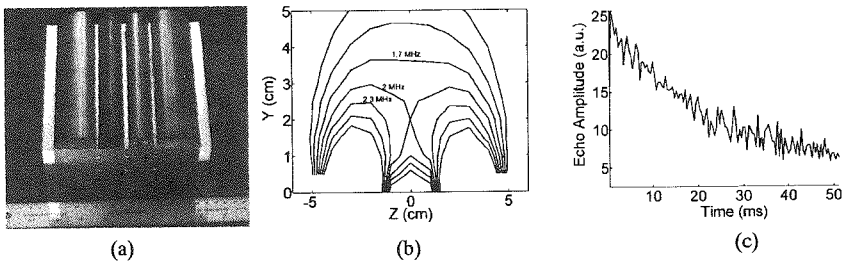

(a) (b) (c)

Figure 0: (a) the constructed PM array, designed according to our methodology. Four NdFeB permanent magnets are arranged under machined high-permeability pole pieces. The array is 15 cm by 15 cm; (b) the z-component of the measured magnetic field, expressed in ^{1}H resonant frequency. A saddle point is observed above the center of the array, indicating a relatively homogeneous field. Measurements indicate an average gradient of ~14 gauss/cm; (c) a CPMG detected signal from 2mL of doped water inside of a graphite-aluminum composite panel.

Discussion: The measured field profile of Fig 1(b) compares favourably with the design specifications. The MR sensitive volume was found to be over 1 cm wide and 1 cm in height. The average gradient within this volume was measured through a diffusive attenuation experiment, and found to be much lower than that of commercially available UMR arrays. This allowed a small quantity of water inside of a composite panel to be detected. This measurement would not be possible with a commercial UMR device because of decreased SNR from a smaller sensitive volume, and rapid signal decay due to diffusive attenuation.

Conclusions: This design strategy is general, and permits arrays to be tailor made for specific UMR applications. Construction of several arrays for relaxation measurement and 1D profiling applications is underway.

References: 1. Eidmann, Savelsburg, Blümler, et al., JMR A **122** 104-109 (1996). 2. Glover, Aptaker, Bowler, et al., JMR **139** 90-97 (1999). 3. Marble, Mastikhin, Balcom, et al., JMR, **174**, 78-87 (2005). 4. Marble, Mastikhin, Balcom, et al., JMR, **168**, 164-174.

A novel modular probe base for multi-channel multi-nuclei MRI and MRS experiments

V.C. Behr, I. Kaufmann, A. Haase, P. Jakob
Department of Physics, EP5 (Biophysics), University of Würzburg, Germany

Introduction:

Many spectrometers allow experiments on different nuclei. Up to now – especially in microscopic and spectroscopic studies - there had to be dedicated probe bases for each individual application that were adapted to a specific group or even a single resonator. Since it is often desirable to observe more than one nucleus during a study with different resonators it was necessary to come up with a novel hardware concept and design for probe bases that can handle a wide choice of probe heads to avoid the necessity to build an individual base for each resonator.
In this abstract the prototype of a modular probe base for a Bruker Avance 750 spectrometer with a field strength of 17.6 T and a gradient unit with 1 T/m and 40 mm inner diameter is presented.

Concept and Design:

The probe base consists of three major components. The basis is a socket (fig.1 *b*) providing lead-throughs for the conductors: the silver BNC connectors at the lower end of the socket are connected by 50 Ω cable to small golden plugs on the upper end (not visible in the figure). Furthermore the grey rods which are supported by springs within the socket give access to turning rods that move the shaft of variable capacitors in the tuning and matching networks for resonators. These networks are included in each of the modular channels (fig.1 *a*) at the upper end (white and golden parts at the right end of the modules in the figure). Placing them inside the probe base yields an improved decoupling of these networks from the resonator itself and gives additional room for resonator designs that require more space. The modules contain a coaxial semi rigid 50 Ω conductor from the lower end where it is soldered to socket outlets fitting onto the socket's plugs up to the network. These feeds contain at their upper part triaxial baluns to balance the voltages in the system and suppress unwanted coupling of the conductors within the probe base [1]; since their length depends on the frequency they are employed for, one channel module has to be dedicated to one specific nucleus and field strength. From the network silver wires (not visible in the figure) lead up to the probe head. Finally there is an outer shielding (fig.1 *d*) that covers the channel modules once the probe base is assembled. The probe base's basic material is all copper in order to achieve an optimal interconnection of all parts that are supposed to be on electrical ground level to avoid voltage differentials across the system. The probe base has a total length of about 60 cm.

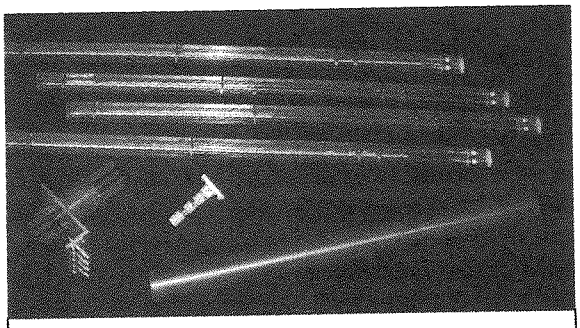

Figure 1: *parts of the new probe base*
a) 4 channel modules (top), b) probe base socket (bottom, left), c) birdcage resonator for this probe base (center) and d) outer channel shielding (bottom, right)

Results and Conclusions:

Channel modules for ^{1}H (2 times for quadrature use), ^{13}C, ^{19}F, ^{23}Na, ^{35}P and a generic module without balun are available, four of which can be arbitrarily combined to assemble a probe base. Furthermore a ^{2}D channel module with built-in solenoid coil and a deuterium cell is available to provide a deuterium-lock without the need to put deuterium into the sample.
Possible additional signal reflections due to the modular design were evaluated using an Agilent 8712ET vector network analyzer with a fault location option. Figure 2 shows the reflections along the signal pathway starting at the outer BNC connectors (marker 1) and through the base-module connector (marker 2). Inside the probe base no significant additional reflections could be detected.
First imaging experiments using a 5 mm birdcage resonator (fig. 1 *c*) were performed at 17.6 T on a phantom (figure 3) to confirm the function of the probe base.

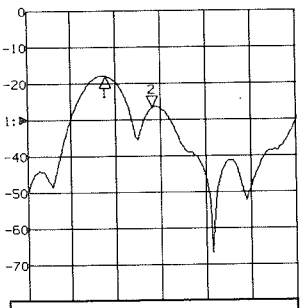

Figure 2: *fault location*
Values are given in [dB] of reflected power. Through the probe base from left to right: Marker 1: outer BNC connector Marker 2: module plug

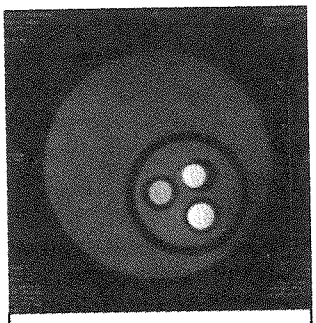

Figure 3: *FLASH image*
TR=100ms, TE=1.9ms, FoV=(12mm)², matrix=128², NEX=32

Acknowledgements:
We acknowledge the support during design and construction of the probe base of T. Grünebaum of our department's machine shop.

References:

[1] Chen C.N., Hoult D.I., "Biomedical Magnetic Resonance Technology", 138ff, Adam Hilger, Bristol and New York, 1989

MRI measurements of cavitating fluid

I.V. Mastikhin, B.Newling

MRI Centre, Physics Department, University of New Brunswick, Fredericton, NB Canada

Acoustic cavitation is the generation, oscillation and collapse of gaseous bubbles in fluids under the action of high-power ultrasound. The prevalent methods used in studies of cavitation are optical and acoustical.

In this work, we applied magnetic resonance imaging (MRI) methods to studies of the cavitating fluid. Spin-Echo PFG and motion-sensitized SPRITE sequences were employed. 31 kHz ultrasonic transducer was immersed into the cylindrical vessel aligned with the direction of the main magnetic field. The transient cavitation was studied. We obtained 1D and 2D velocity and dispersion maps of cavitating water. The measurements were performed for air-saturated water, degassed water, water with surfactants (SDS), and water with SDS and NaCl.

A pronounced streaming and dispersion were observed only in non-degassed water samples and only at ultrasound power above the cavitation threshold. Therefore, both streaming and increased dispersion can be attributed to the presence of cavitation bubbles. If the bubble dynamics are modified, the behaviour of surrounding fluid is changed on the macroscale.

A difference in streaming in water and water with SDS is significant. Much stronger streaming in water with the surfactant can be caused by, first, a larger number of stabilized bubbles and, second, a less disruptive cavitation. A modification of bubble dynamics by the surfactant can qualitatively explain the observed difference. A difference in dispersion in water and water with SDS was also substantial. The most interesting feature of the dispersion was its anisotropy in water with the surfactant: almost no dispersion increase across the vessel.

The authors thank the Natural Science and Engineering Council of Canada for financial support.

NMR of Granular Materials

Eiichi Fukushima & Arvind Caprihan, New Mexico Resonance, Albuquerque, USA

Introduction -- Granular materials are everywhere in nature and in the man-made arena. They behave as solids when stationary but can flow in a manner similar, in many ways, to liquids. Soil is normally considered solid enough for humans to build structures on but can flow as avalanches under certain conditions. Sand flows in an hourglass at a rate that is independent of the amount of sand in the reservoir, a behavior very different from water which flows faster if the reservoir is full. This behavior has similarities with traffic flows and there are efforts to model traffic flow as a granular flow. Thus, granular systems are complex and there is, as yet, no governing equation for their motion corresponding to Navier-Stokes equation for Newtonian liquids.

The engineering community has studied granular behavior extensively and systems for handling granular matter are highly developed. However, there are many additional problems that are significant barriers to efficient handling of granular materials. This fact can be attributed, in part, to the difficulty of making detailed observations because of the optical opacity of most granular matter. Computer simulations have contributed to the understanding of static and dynamic behavior of granular materials but the dearth of experimental information, especially in the bulk, has been a significant handicap. Nuclear magnetic resonance was first applied to granular flow some 12 years ago [1]. Experiments have now been done to study velocity profiles, end-wall effects, spatial segregation of unlike particles, and diffusion and fluctuation of velocity.

Method -- The first question that had to be asked was whether it was possible to study granular flow in the same way as liquid flow by NMR/MRI. These macroscopic particles move distances that are orders of magnitude larger than molecules do in their random Brownian trajectories that we are used to studying by NMR. Motions of molecules within the liquid are not problematic because translational motion of the molecules usually overwhelms motion due to molecular diffusion. Furthermore, for fast flows, the displacement of a spin due to rotation of the particle is small compared to that due to translation. Thus, measurements of molecular displacements, including the use of Stejskal-Tanner formalism for the spins, yield information about particle displacements and not molecular diffusion.

Granular flow NMR/MRI experiments usually use natural particles containing liquids such as mustard seeds and artificial materials such as pharmaceutical pills containing liquids or solids into which some liquid is absorbed. We study spherical particles flowing in a partially filled horizontal cylinder that is rotating about its axis. This is a convenient and robust flow geometry that is well suited to horizontal bore magnets. Our 8cm diameter cylinders are rotated in the 30cm bore of an Oxford 1.9T magnet by a motor that is placed ~2 meters away.

Results -- The flow occurs only near the free surface in a lens-shaped region. The velocity profile v(r) as a function of depth r in the flowing layer for a half filled cylinder obeys the relation

$$v(r)=-V_m(1-r/r_0)^2+\Omega r,\ r<r_0,$$

$$v(r)=\Omega r,\ r_0<r<R,$$

where Ω is the cylinder rotation rate, r is the radial coordinate from the free surface along its perpendicular bisector, r_0 is the depth of the flowing layer, and V_m is the magnitude of the velocity at the free surface.

We also measured the spatially resolved fluctuations of velocity by a variation of the standard Stejskal-Tanner sequence [2]. The modification is needed to isolate the signal attenuation due to the random process from attenuation due to a reversible cause, specifically, velocity distribution of particles not undergoing collisions in a voxel. These results give indications of valuable (and difficult to measure) parameters such as correlation times for collision and granular temperature, a measure of kinetic energy of collisions.

Discussion/Conclusions -- The fact that the velocity obeys such a simple relation implies that there is a single mechanism determining the velocity profile; we conjecture that the velocity profile arranges itself to minimize energy dissipation. As for the velocity fluctuations, NMR/MRI affords a rare technique to measure it, with or without spatial resolution.

NMR/MRI is an excellent tool to investigate granular flow in the bulk. No other technique can measure spatially resolved parameters in the bulk and NMR/MRI can measure so many parameters.

Much of this work was done by Masami Nakagawa, Braunen Smith, Jim Maneval, and Lori Sanfratello.

1. Nakagawa, M., et al., *Experiments in Fluids* **16**, 54-60 (1993).
2. Caprihan, A., et al., *J. Magn. Reson.* **144**, 96-107 (2000); Seymour, J. D., et al., *Phys. Rev. Lett.* **84**, 266-269 (2000).

Viscosity Measurements via a Low Field MRI Viscometer

Artem G. Goloshevsky[1]; Jeffrey H. Walton[2]; Young Jin Choi[1]; Jeffrey S. de Ropp[2]; Scott D. Collins[3]; Michael J. McCarthy[1]

[1]Department of Food Science and Technology, UC Davis, Davis, CA, USA
[2]NMR Facility, UC Davis, Davis, CA, USA
[3]MicroInstruments and Systems Laboratory (MISL), University of Maine, Orono, ME, USA

Introduction

The ability to monitor viscosity is essential for control of unit operations and for assuring product quality. This is particularly true in milk products as viscosity is an important parameter determining "mouth feel" which is perceived by the consumer as an indicator of quality. Recent work [1,2] has demonstrated the use of miniaturized Nuclear Magnetic Resonance (NMR) based measurements for the characterization of wide range of shear rates in a single measurement. Here several varieties of milk and milk substitute products are characterized via a miniaturized MRI viscometer.

Methods

Viscosity can be determined from NMR imaging of sample flow in a tube by analysis of the velocity profile [3]. The flow profile yields the shear rate $\dot{\gamma}$ via $\dot{\gamma}(r) = -(du(r)/dr)$. Knowledge of the pressure drop yields shear stress $\sigma(r)$ i.e. $\sigma(r) = -(\Delta P/2L)r$. Since the shear rate and shear stress are radially dependent, each radial position (r) can provide a viscosity data point $\eta(\dot{\gamma}) = \dot{\gamma}(r)/\sigma(r)$ at a different shear rate. Thus, the viscosity can be measured at a variety of shear rates in a single measurement. Here the fluids are modeled as power law fluids and the first derivative of the velocity profile is given by $\dot{\gamma}(r) = ((\Delta P/2KL)r)^z$, where $z=1/n$.

A package of two biaxial gradient coils and a Helmholtz RF coil was fabricated by photolithography and electroplating [3, 4]. Here, this package is used to acquire velocity flow profiles of several varieties of commercially available milk products: fat free milk, coffee creamer, reduced fat strawberry milk, reduced fat chocolate milk, "Rice Dream" rice drink, "Plain Silk" organic soymilk. The viscosities of all the fluids were measured with a cup and bob geometry using a commercial CVO viscometer (Bohlin Instruments, Gloucestershire, UK) and the MRI viscometer.

Results and Discussion

Typical flow images from the MRI viscometer are shown in Figure 1. The results of the measurements are summarized in Table 1. The condition of no wall slip was assumed for the MRI data. Results between the two methods are in quite good agreement.

Table 1	CVO measurement data		MRI measurement data			
	K (Pa s)	n	ΔP/L (Pa/m)	K, Pa s	z	n
fat free milk	0.0020±0.0001	1	76.98	0.0021	1.1±0.1	0.94±0.06
coffee creamer	0.024±0.001	0.92±0.01	831.16	0.023	1.062±0.078	0.94±0.07
strawberry milk	0.027±0.002	0.697±0.031	551.37	0.027	1.41±0.11	0.71±0.06
chocolate milk	0.14±0.01	0.52±0.02	1821	0.145	1.91±0.15	0.52±0.04
rice drink	0.00179±0.00003	1	70.86	0.0019	1.08 ±0.09	0.93±0.08
Soy milk	0.011±0.002	0.824±0.04	311	0.01064	1.17±0.08	0.86±0.06

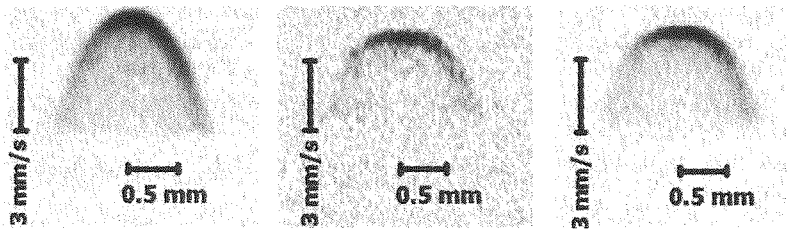

Figure 1. (a) strawberry milk and (b) chocolate milk are 4 signal averages and (c) chocolate milk is 20 averages. The intensity scaling is in arbitrary units and different for each image (for improved representation).

References

[1] Goloshevsky, A.G., et.al., Meas. Sci. Technol., **16**, 505-512 (2005)
[2] Goloshevsky, A.G., et.al., Meas. Sci. Technol., **16**, 513-518(2005)
[3] Arola, D. F., et.al. Rev. Sci. Instrum., **69**, 9 (1998).
[4] Walton, J.H., et.al., Anal. Chem., **75**, 5030 (2003).

NMR Profilometry and Normal Stress Differences in Concentrated Suspensions

Steve Altobelli[1], Lisa Mondy[2], Rekha R. Rao[2]
[1]New Mexico Resonance, [2]Sandia National Laboratories* Albuquerque, NM USA

Introduction

When a vertical cylinder rotates in a Newtonian fluid the free surface shape is determined by a balance between gravity and centrifugal force. For slow rotation the free surface is basically flat. A polymer solution, on the other hand, has a tendency to 'climb' the rod, and this reflects the microscopic structure of the polymeric liquid. In macroscopic terms the liquid is said to exhibit normal stress differences when sheared. The microstructure of concentrated suspensions of solid particles in a Newtonian liquid also produces easily noticed normal stress differences, which happen to be of the opposite sign from polymers.

Methods

We used standard 2- and 3-dimensional spin warp spin echo MRI to observe the free surface and fluid fraction of Newtonian liquids and concentrated suspensions flowing between vertical cylinders. Both concentric and eccentric geometries were studied.

Results

Examples of rod dipping observed in concentrated suspensions flowing in a concentric cylinder vertical Couette device will be presented. By using NMRI profilometry one may also observe de-mixing phenomena such as shear induced particle migration. We have seen particle concentration non-uniformities evolve in two ways. First, in suspensions of relatively large particles the particle concentration evolves radially, while in suspensions of fine particles a small vertical stratification has been observed. It is also possible to observe free surfaces of arbitrary connectedness and complexity that might be difficult to observe by other techniques. Examples of complex free surfaces visualized in eccentric vertical-axis Couette flows of viscous liquids and concentrated suspensions will be presented.

Discussion

We use NMR imaging to study the free surfaces of flowing neutrally buoyant concentrated suspensions and in Newtonian liquids. As Zarraga et al. pointed out, the free surface profile is related to normal-stress differences in concentrated suspensions. Thus, we can use NMR imaging to measure normal stress differences while we observe suspension de-mixing phenomena. NMR profilometry is applicable to complex free surfaces that cannot be studied with laser-sheet profilometry.

References

Zarraga, Hill and Leighton (J Rheol 44(2) 185 (2000))

*Sandia is a multiprogram laboratory operated by Sandia Corporation, a Lockheed Martin Company, for the United States Department of Energy's National Nuclear Security Administration under contract DE-AC04-94AL85000.

Visualization of seminiferous tubules of rat testes by high resolution MR imaging

Masayuki Yamaguchi[1, 2], Fumiyuki Mitsumori[1], Hidehiro Watanabe[1], Nobuhiro Takaya[1], and Manabu Minami[2]

1 National Institute for Environmental Studies, Tsukuba, Japan, 2 University of Tsukuba, Tsukuba, Japan

Introduction: There are lots of MRI reports in the scrotum describing its anatomical structures such as testes, epididymis, and vas deference [1, 2]. None of them succeeded in describing fine structures inside the testes probably due to their low spatial resolution and low tissue contrast. In the present study we succeeded in visualizing seminiferous tubules about 200 μm in diameter by improving the imaging resolution and increasing the T_2 and T_2* weightings. Changes in the image of the seminiferous tubules caused by ischemia and some chemical reagents will be presented.

Methods: All the measurements were performed using INOVA spectrometer (Varian, Inc. CA. USA) equipped with 4.7T magnet. A home-built quadrature surface coil was used for transmitting RF pulses and acquiring signals. Male adult Wistar rats were anesthesized, and their spermatic cords on the right were ligated in order to make ischemic testes. The left testes were saved as controls. Spin echo (SE) images (repetition time (TR) / echo time (TE) = 4000 / 100 ms) and gradient echo (GRE) images (TR / TE = 400 / 30ms, Flip angle = 20°) were obtained with a field of view of 34 x 34mm, matrix of 512 x 512, and slice thickness of 2mm.

Results and discussions: Both SE and GRE images demonstrate that many thin tubular structures with peripheral low signal and central high signal are tightly packed in the testes, and run toward variable directions (Figures). We assigned them as seminiferous tubules. In the ischemic testes at several hours after the ligation, ill-demarcated low signals appeared. This change was emphasized on GRE images compared with SE images. We believe that the low signals were caused by T2* effect of deoxy-hemoglobin due to hypoxia.

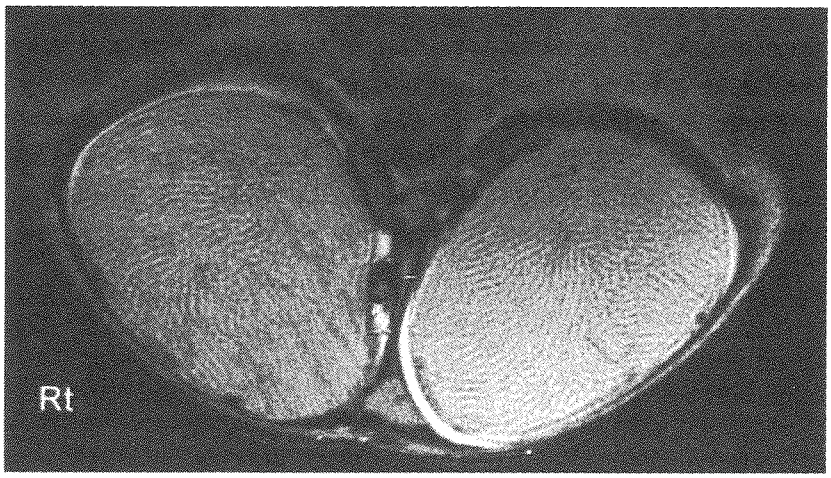

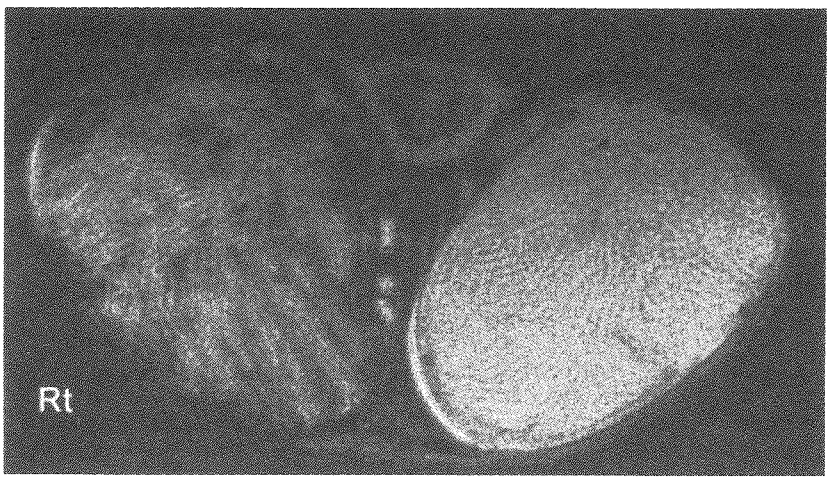

Conclusion: We succeeded for the first time in observing the seminiferous tubules by *in vivo* MR imaging. The characteristic low signals on T_2* weighted GRE images might be a good indicator of testicular ischemia. We think that *in vivo* high resolution MR imaging is a promising method for observing inner structures of both normal and diseased testes.

References [1] Baker LL, Hajek PC, Burkhard TK, et al, Radiology **163**:89-92(1987) [2] Rholl KS, Lee JK, Ling D, et al, Radiology **163**:99-103(1987)

Figures: Transaxial SE (top) and GRE (bottom) images of the rat testes

The right testis is under ischemic condition, and the left one is a normal control. In normal testis, seminiferous tubules are nicely demonstrated on both images. Note that characteristic low signals in the ischemic testis are enhanced on GRE image.

Using transport to map the brain: Stereotaxic Mn^{2+} injection and tract tracing by μMRI in animal models

E.L. Bearer, X. Zhang, J.M. Tyszka and R. E. Jacobs
Brown Medical School, Providence RI 02912 USA
California Institute of Technology, Pasadena CA 91125 USA

Higher order cognitive processing requires communication between neurons located at distant sites within the central nervous system. This communication depends on long axonal processes that arch from one cluster of neuronal cell bodies to another. Often these processes are grouped together into tracks readily detected even in whole brain specimens, others are smaller and only detected secondarily with histochemistry or tracing compounds that enhance their visibility. Traditionally, connections between neurons have been traced by the local delivery of a histologically detectible tracer that is transported within the neuron to distant sites and thereby outlines the communication pathway. These tracers must interact with the intracellular transport machinery to be delivered along the axon of a single neuron and must cross synapses to trace a multi-step pathway. The mechanisms of entry into the neuron, the type of transport that the agent used, and retention of the agent within the pathway are all important considerations in interpreting the consequent data. For example, whether a tracer only enters at active synapses or can also enter along neuronal processes influences its usefulness and the analysis of its distribution. Alternatively whether a tracer is transported in the retrograde and/or anterograde direction within processes affects its subsequent distribution and the interpretation of the structure of the pathway thus delineated.

To trace neuronal circuits in living brains by MRI, a contrast agent must display the same attributes as a histological tracer: be transported and cross synapses. We have focused on Mn^{2+}, which has recently become a widely used T_1 contrast agent for MRI. Despite its popularity, many aspects of Mn^{2+} tracing remain ambiguous. Evidence suggests that it enter neurons through voltage-sensitive Ca^{2+} channels and is actively transported in the anterograde direction, possibly on microtubule tracks. We have investigated biological mechanisms of Mn^{2+} transport in two systems: the optic tract and the hippocampal-basal forebrain connections. The optic tract is a well-defined system where many biological properties are known. The hippocampal-basal forebrain system is less well studied but of importance in neurological disorders such as Alzheimer's disease. Mn^{2+} tract-tracing in blind and sighted mice after injections into the or adjacent to the chiasm along with visual evoked potential measurements to assess visual system integrity will be presented. These highlight the need for additional study of the basic mechanisms of Mn^{2+} entry & transport. Mn^{2+} tract-tracing following injection of nanoliter volumes of Mn^{2+} into the hippocampus outline the hippocampal-fimbria-septal nucleus connection. Voxelwise analysis of 3D images warped into the same space allows quantitative statistical assessment of Mn^{2+} transport.

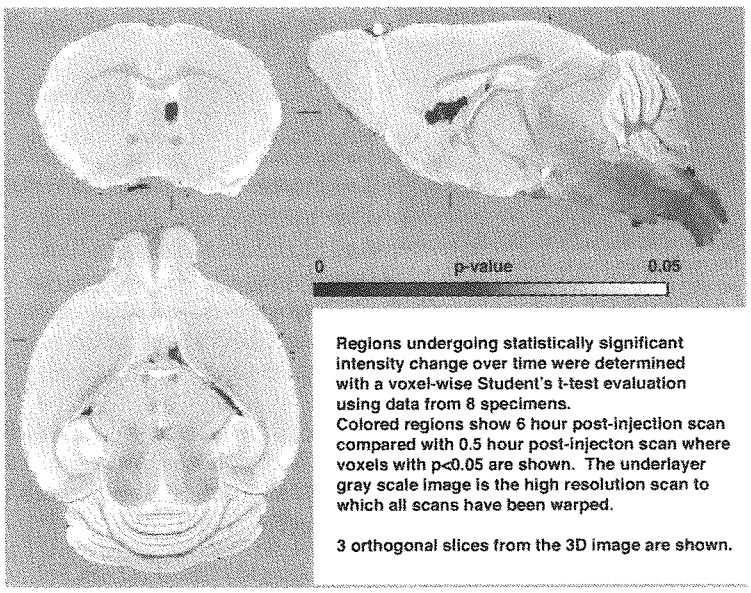

Regions undergoing statistically significant intensity change over time were determined with a voxel-wise Student's t-test evaluation using data from 8 specimens.
Colored regions show 6 hour post-injection scan compared with 0.5 hour post-injecton scan where voxels with p<0.05 are shown. The underlayer gray scale image is the high resolution scan to which all scans have been warped.

3 orthogonal slices from the 3D image are shown.

Right hippocampal injection of Mn^{2+} was performed on 8 animals, 3D MR images were acquired 0.5hr, 6hr, and 24hr after injection. All images were scaled and warped into the same STANDARD BRAIN image space to enable voxelwise comparisons. A map of statistically significant intensity differences between 0.5hr and 6hr time point scans is shown. Right fimbria and lateral septal nucleus are identified as different using the anatomy of the STANDARD BRAIN image shown in gray.

Supported by (NCRR-BIRN, NINDS (E.L.B.) and NIGMS (E.L.B) and The Moore Foundation)

NMR microscopy and relaxation time quantification of *Xenopus laevis* embryos using antibody-labeled iron oxide particles

Armin Purea[1], Robert Hock[2], Peter M Jakob[1], Andrew G Webb[3]
[1]Dept. of Experimental Physics 5, [2]Dept. of Cell and Developmental Biology,
University of Würzburg, Germany. [3]Dept. Bioengineering, Penn State University USA.

Introduction

High resolution magnetic resonance (MR) microscopy is an evolving technique for the reconstruction of 3D embryonic structure in developmental biology [1]. While specific contrast agents in light microscopy techniques are widespread and established, enabling unambiguous identification of various targets such as proteins, corresponding marker techniques are not yet as well established in MR microscopy. In this study, the applicability of ultrasmall superparamagnetic iron oxide (USPIO)-labeled antibodies in wild type *Xenopus laevis* embryos as a specific MR contrast agent [2] for indirect immunolabeling was evaluated, and the effect on relaxation times was studied quantitatively.

Methods

In vitro fertilization and culture of embryos were performed as described previously [3]. All embryos were fixed in MEMFA (0.1 M MOPS, pH 7.4, 2 mM EGTA, 1 mM $MgSO_4$, 3.7% formaldehyde) and placed in phosphate buffered saline prior to MR experiments, since formaldehyde-based fixation is known to strongly reduce tissue T_2 values [4]. Niewkoop and Faber (NF) stage 41 embryos were used for whole mount immunolocalizations using primary antibodies (ab1) directed to desmin, a characteristic protein found in mesoderm cells. To detect bound desmin antibodies, secondary antibodies (ab2) elicited in goat were iron oxide-labeled (50 nm diameter, dextran-coated; MACS, Miltenyi Biotech, Germany). MR imaging was performed on a 17.6 T (750 MHz) wide bore magnet using a Bruker Avance console, Micro2.5 microimaging gradients (G_{max}=1 T/m), and a homebuilt array of two individual 2 mm i.d. solenoid coils. Images were analyzed using Amira 3.0, and parameter fitting was carried out using IDL 6.0. 3D data sets of embryos were acquired with a FLASH sequence at five different echo times, and T_2* maps were calculated from regions of interest placed within the myotome structures containing mesoderm cells.

Results

MACS-labeled embryos show increased contrast between myotome structures and surrounding tissue. At an echo time of 5 ms, myotome structures become clearly visible in MACS-labeled specimens, while are visible only at later echo times in control specimens. Quantitative results show a corresponding T_2* shortening at the area of specific binding.

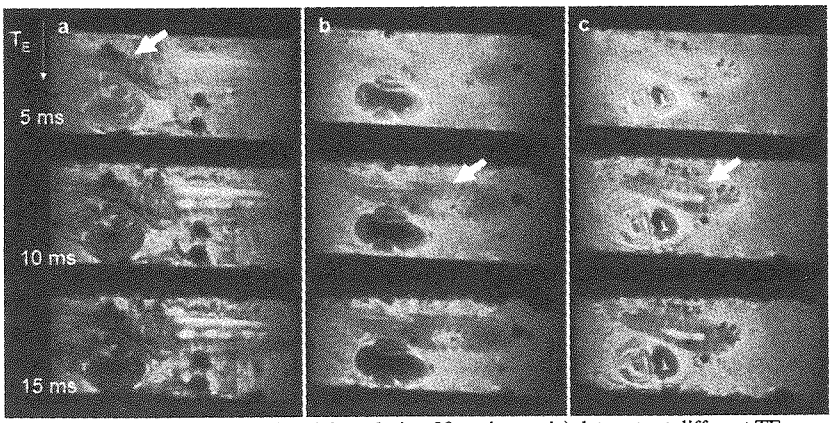

Fig.1: Slices from 3D FLASH (spatial resolution:30μm isotropic) data sets at different TE values, Embryo labeled with (a) ab1+ab2, (b) ab1 only, (c) ab2 only. Arrows indicate the position of myotome structures.

slice	ab1+ab2	ab1 only	ab2 only
1	16.08±0.38	18.87±0.30	21.43±0.68
2	16.22±0.72	15.70±0.30	23.72±1.52

Table 1: T_2^* values obtained from ROIs placed on myotome structures

Conclusions

By using commercially available iron oxide-labeled antibodies, image contrast can be altered to reflect the distribution of certain target molecules, such as mesoderm protein. While an effect on T_2* is observable and can be quantified, we are currently expanding our results to determine changes in T_1, T_2 and T_2* relaxation times in labeled and unlabeled embryos to clarify the effect of MACS particles when bound specifically in tissue.

References

[1] Jacobs RE et al., Nat Rev Mol Cell **4**, Suppl: SS10-SS16 (2003). [2] Pirko I et al., Proc. 11th ISMRM, Toronto, 832 (2003).
[3] Hock R et al., Dev Biol **158**, 510-522 (1993).[4] Bossart EL et al., Proc. 7th ISMRM, Philadelphia, 1928 (1999).

A Single-Shot Method for Capillary Pressure Measurement of Porous Media Using Centrifuge and SPRITE MRI

Quan Chen and Bruce J. Balcom
MRI Centre, Department of Physics, University of New Brunswick, Fredericton, Canada

Introduction

Capillary pressure is the most fundamental rock-fluid characteristic in multi-phase flows, just as porosity and permeability are the most fundamental properties in single-phase flow in porous media. The centrifuge method for capillary pressure curve measurement was introduced by Hassler and Brunner [1] in 1945. This method involves increasing the centrifuge speed in steps and measuring expelled liquid from the core at equilibrium for each step. However, the traditional method for calculating the capillary pressure and fluid saturation at the inflow end of the core is based on three assumptions [2]. (1) The capillary pressure is varying linearly over the length of a core; (2) The effect of gravity can be ignored; (3) The capillary pressure is zero at outflow end of the core. These assumptions may result in significant errors in the measurement of capillary pressure curves. Furthermore, changes in the rock pore structure due to ultra centrifugal forces, will introduce additional errors [3], and some friable and unconsolidated rock samples may be broken during ultracentrifugation

Traditional centrifuge methods for capillary pressure measurement are time consuming. A full capillary pressure curve requires approximately 15 different centrifuge speeds. The experiment requires a very expensive ultracentrifuge with precise speed control over a wide range of speeds. A special coreholder and stroboscope for collecting and measuring the expelled fluid are also required for the measurement.

Methods and Results

We have observed for most sedimentary rocks and concretes that free induction decay (FID) is single exponential and the effective transverse relaxation time (T_2^*) is largely insensitive to water saturation. The single exponential FID behaviour arises from a Lorenzian distribution of the internal magnetic field, induced by a large susceptibility difference between pore filling fluid and solid matrix, and an intrinsic disordered pore structure in these porous media [4]. These features ensure that Centric Scan SPRITE (single-point ramped imaging with T_1 enhancement) is a natural spin density image method, since its local image intensity has simple T_2^* contrast [5-7].

We propose a single-shot method [8] to measure the capillary pressure curve of a long rock core using a single-moderate-speed centrifuge experiment and 1D Centric Scan SPRITE MRI to determine the fluid saturation distribution, S(r), along the length of the sample, without any assumptions. A full capillary pressure curve can be determined by the relation of S(r) and capillary pressure distribution, $P_c(r)$, along the length of the core.

A comparison of the capillary pressure curves obtained with the single-shot method and with the mercury intrusion porosimetry, yields remarkably consistent results.

Conclusions

In the current work, a new single-shot method to determine the capillary pressure curve is introduced. This method combines a single-moderate-speed centrifuge experiment for long rock cores and a SPRITE MRI technique to directly determine the fluid saturation distribution along the length of the core, without any assumptions. The proposed method for determining the capillary pressure curve is rapid, cheap, and precise. The capillary pressure curve can be obtained straightforwardly with about 40 spatial image data points. The duration of the experiment is approximately 15 times less than the traditional method. Since only a single moderate rotational speed is employed, the outflow boundary condition can be maintained, and the effect of gravity can be neglected. In addition, the long rock cores employed for the single-shot method result in a relatively small radial effect compared with the traditional method.

References

[1] Hassler G. and Brunner E., Trans. AIME, **160**, 114 (1945).
[2] Ruth D. and Chen Z., Log Analyst **36**, 21 (1995).
[3] Chen Q., Kinzelbach W., Ye C. and Yue Y., J. of Environmental Quality. **31**, 500 (2002).
[4] Chen Q., A. Marble, B. Colpitts, and B. Balcom, J. Magn. Reson. (in press, 2005).
[5] Chen Q., Gingras M. and Balcom B., J. Chem. Phys. **119**, 9609 (2003).
[6] Balcom B., MacGregor R., Beyea S., Green D., Armstrong R. and Bremner T., J. Magn. Reson. A **123**, 131 (1996).
[7] Halse M., Goodyear D., MacMillan B., Szomolanyi P., Matheson D. and Balcom B., J. Magn. Reson. **165**, 219 (2003).
[8] Chen Q. and Balcom B., J. Chem. Phys. **122** (in press, 2005).

Hp-Xe NMR Study on Activated Carbon Electrode in EDLC

Koji Saito [1], Moriaki Hatakeyama [1], Satoshi Mitani [2] and Isao Mochida [2]
1) Nippon Steel Corporation Advanced Research Lab. Futtsu City, JAPAN, 2)Kyushu University

1. INTRODUCTION

The electric double-layer capacitor (EDLC) using activated carbon as electrodes has been recognized as an efficient storage device for the electric power because of its better rate capability and longer cycle life as compared to secondary batteries in spite of its low energy density [1,2]. Recently new applications utilizing such performances have been attempted as an energy storage device for electric vehicle or pulse-current supply. In order to meet the specification for new application, it is necessary for a particular activated carbon to have much higher energy densities per both weight and volume than those of the conventional ones. In this study, activated carbon was obtained from optically anisotropic spherical carbon by NaOH activation to follow the physical and chemical behaviors of an organic electrolyte Et_4NBF_4 in PC on the activated carbon since such an activated carbon was reported to show and excellent performances in EDLC [3] using Hp-Xe NMR Method [4].

2. EXPERIMENTAL

Hyper-polarized ^{129}Xe gas was prepared through laser-aided polarization apparatus (Toyoko Kagaku Co., Japan) which contacted Rb vapor with Xe gas under the irradiation of laser near the external magnet. The polarized ^{129}Xe gas (10mL) was introduced by plastic syringe into a 10mm-size glass NMR tube containing 1g of porous standard materials with the well-defined average pore size. The ^{129}Xe-NMR spectrum was obtained on the JEOL alpha-400 spectrometer of 400MHz. The Xe-NMR shift was referred to that of the ^{129}Xe gas without any adsorbent (0 ppm) as the external standard. M500 was degassed overnight at 150 centi-degree under vacuum before ^{129}Xe-NMR measurement.

3. RESULTS

^{129}Xe-NMR spectrum of M500 with specific surface area of $500m^2/g$ is shown in Figure 1. The spectrum showed a sharp peak at 0ppm and a broad one at the higher chemical shift. A sharp and a broad peaks can be assigned to the non-adsorbed ^{129}Xe and the adsorbed ^{129}Xe on the pore walls of M500, respectively. Chemical shift of the adsorbed ^{129}Xe on the pore wall of M500 was found to be 100ppm. Average pore size was obtained by comparing the chemical shift on the maser curve. Average pore size of M500 was noted as 0.97nm.

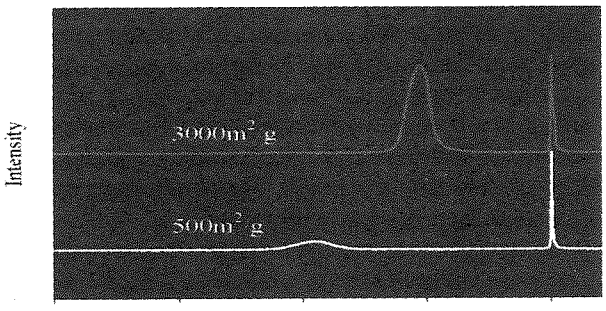

Fig.1 ^{129}Xe-NMR spectrum of M500 and M3000

4. DISCUSSION

The electric field under the charge enhances the adsorption of the electrolytes or its dissociated ions in the more polarized states to form the electric double layer on the surface of the pore wall, storing the electric energy as the capacitor. In this stage, electrolyte or its ions move into or out of the pore to enhance the polarized adsorption for the double layer in the electric field. There are electrolytes present at the outer surface, in pores and on the surface of the pore wall. There are also several kinds of pores. The discharge desorbs the adsorbed species to reduce the thickness of the double layer, releasing the electric energy. Hence several states of the electrolyte or its ions must be present in the charged as well as impregnated stages.

5.CONCLUSION

Hp-Xe NMR is a sole and powerful method to solve the chemical and dynamic behaviors of the electrolyte ions and polar solvent present in the pore or adsorbed on the pore wall of the electrode carbon.

REFERENCES

[1] Nishino, A. J. Power Sources 1996, 60, 137. [2] Christen, T.; Carlen M. W. J. Power Sources 2000, 91, 210. [3] Takeuchi, M.; Koike, K.; Maruyama, T.; Mogami, A.; Okamura, M. Denki Kagaku 1998, 66, 1311. [4] Saito K, Kimura A. and Fujiwara H. Magn.Reson Imaging , 2003, 21, 401

Measurement of Inter-Phase Exchange Rates and Bubble Velocity in Gas-Fluidization with Laser-polarized ^{129}Xe

Ross Mair[1,2]; Tina Pavlin[1], Ruopeng Wang[1,2]; Matthew Rosen[1]; Donald Candela[3]; Ronald Walsworth[1]

[1] Harvard-Smithsonian Center for Astrophysics, Cambridge, MA, USA.
[2] Massachusetts Institute of Technology, Dept. of Nuclear Engineering, Cambridge, MA, USA.
[3] University of Massachusetts, Amherst, MA, USA.

Gas fluidization is a process in which solid particles experience fluid-like suspension in vertical gas flows [1]. Efficient mixing is easily achieved among fluidized solid particles, in which concentration and temperature gradients can be quickly eliminated [2]. Fluidization has been widely applied in food processing, pharmacy and other chemical engineering fields. However, an understanding of the combined dynamics of the particles and gas is far from complete, as such a system is difficult to model mathematically, due to the large number of degrees of freedom and inelastic collisions among particles.

We are using NMR techniques and laser-polarized ^{129}Xe as the fluidizing gas to experimentally probe gas dynamics in a fluidized bed. Previous NMR measurements studied the solid particles, which give stronger NMR signals, but convey no direct information about the gas flow [3,4]. Our experimental scheme [5] is especially useful for cases where bubbles exist. Most commercial fluidized beds operate in the bubbling fluidization regime, in which bubbles emerge at the bottom of the column and expand while rising. Bubbles help agitate the bed, achieving better particle mixing, but also providing a shortcut for gas to escape the bed without making contact with particles. The gas exchange rate in and out of the bubbles is a measure of the efficiency of the system in terms of enhancing the contact between the solid and gas phases.

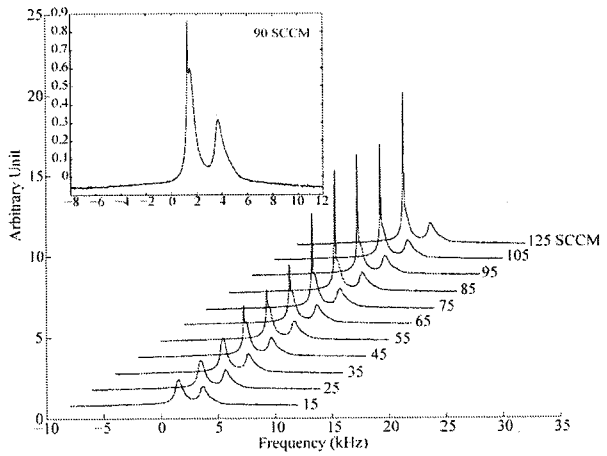

Figure 1 : ^{129}Xe spectra recorded from a bed of ~ 50 μm alumina particles being fluidized by laser-polarized xenon. The amplitude of the narrow peak, due to ^{129}Xe in the bubbles, increases with flow rate. The other peaks are from the interstitial xenon (emulsion) and xenon adsorbed on the particles.

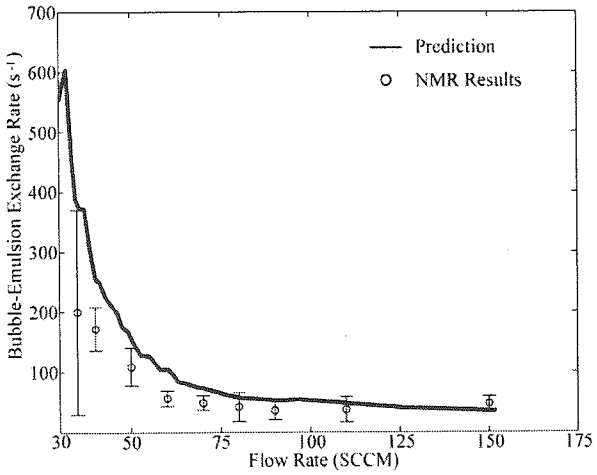

Figure 2 : Xenon exchange rate measurements as a function of gas flow rate for gas transfer between the bubble and emulsion phases in the alumina particle bed. The predicted curve is based on Davidson's model [2] and visual measurements of bed expansion.

Fig. 1 shows typical ^{129}Xe NMR spectra obtained from a bed of alumina particles. We measure the exchange rate of xenon moving between the bubble and emulsion phases by suppressing the ^{129}Xe NMR signal from the emulsion and adsorbed phases, and then monitoring the bubble peak as a function of an exchange or mixing time. The measured values of bubble-emulsion exchange are shown in Fig. 2. The error bars are due to variations in the number of bubbles during the measurement, a phenomenon prominent at lower flow rates. More recent measurements use the inherent T_2 sensitization of the PGSE sequence to select the bubble peak alone, and measure the actual bubble rise velocity.

[1]. D. Geldart, *Gas Fluidization Technology*, John Wiley & Sons Ltd, New York (1986).
[2]. D. Kunii and O. Levenspiel, *Fluidization Engineering*, Butterworth-Heinemann, Boston (1991).
[3]. R. Savelsberg, D. E. Demco, B. Blumich and S. Stapf, *Phys. Rev. E*, **65**, 020301 (2002).
[4]. C. Huan, X. Yang, D. Candela, R. W. Mair and R. L. Walsworth, *Phys. Rev. E*, **69**, 041302 (2004).
[5]. R. Wang, M. S. Rosen, D. Candela, R. W. Mair and R. L. Walsworth, *Magn. Reson. Imaging*, **23**, 203-207 (2005).

Handy Production of Hyperpolarized ^{3}He and MRI of Mouse Lung

Hirohiko Imai, Michiko Narazaki, Hiroyuki Inoshita, Atsuomi Kimura, and Hideaki Fujiwara

Division of Health Sciences, Graduate School of Medicine, Osaka University,

1-7 Yamadaoka, Suita, Osaka 565-0871, Japan

Introduction

Hyperpolarized noble gases (^{3}He and ^{129}Xe) are known to yield large NMR signals despite the low density in gas state. These hyperpolarized noble gases have been applied to MRS and MRI of the lung and brain in order to gain information on the structure and function of the tissue in vivo [1-3]. In this study, we produced the hyperpolarized ^{3}He gas handily to acquire the ^{3}He image of the mouse lung. Thus the basic data of the ^{3}He lung imaging have been obtained for the future application to diagnosis of the human lung.

Methods

Hyperpolarized ^{3}He gas was produced by K-Rb hybrid spin-exchange optical pumping [4] on our home-built hyperpolarizing system. A cylindrical glass cell containing K-Rb alloy and approximately 220cm^3 of the mixture of ^{3}He and N_2 gases at atmospheric pressure was heated to 473K and irradiated the laser light whose output power was 90W. After completion of the ^{3}He polarization period, the hyperpolarized ^{3}He gas was transferred to a mouth mask attached to a male ddY mouse. The mouse under anesthesia inhaled the gas mixture spontaneously through the mask to which the oxygen gas was applied additionally. The ^{3}He images of the mouse lung were acquired by gradient echo sequence on the Varian INOVA 400WB spectrometer at 9.4T.

Results

The polarization level of ^{3}He amounted to as much as 6% after polarization of 90min. The ^{3}He images of the mouse lung were acquired within 50sec (FIG.1). The spatial resolution of the image was 1.56mm/pixel.

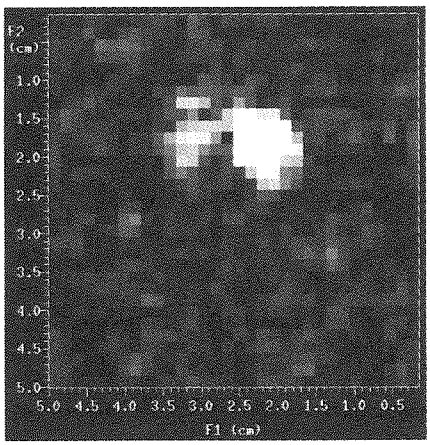

FIG.1. Hyperpolarized ^{3}He image of mouse lungs

Discussion

Since we operate our hyperpolarizing system at atmospheric pressure, we can transfer directly the hyperpolarized ^{3}He gas from the polarizing cell to the mouse with a constant flow rate. As a result, it has become easy and safe to handle, leading to the successful application to acquire the mouse lung image. However, the polarization level of ^{3}He was low compared to the recent literature data due to the low pumping pressure. It is necessary to attain higher polarization level of ^{3}He toward the high-quality ^{3}He image acquisition.

Conclusion

We tested the hybrid method of ^{3}He polarization at atmospheric pressure and the hyperpolarized ^{3}He image of the mouse lung was obtained successfully.

References

[1] Woodhouse N., Wild J. M., Paley M. N. J., et al., J. Magn. Reson. Imaging **21**, 365 (2005)

[2] Swanson S.D., Rosen M.S., Coulter.K.P., et al., Magn. Reson. Med. **42**, 1137 (1999)

[3] Swanson S.D., Rosen M.S., Agranoff B.W., et al., Magn. Reson. Med. **38**, 695 (1997)

[4] Babcock E., Nelson I., Kadlecek S., et al., Phys. Rev. Lett. **91**, 123003 (2003)

Imaging V/Q in Lungs by Mapping the ^{19}F T_1 of Inert Fluorinated Gases

Natalie Adolphi and Dean Kuethe, New Mexico Resonance, Albuquerque, NM 87106, USA

Introduction: The ventilation-to-perfusion (V/Q) ratio is the ratio of gas flow to blood flow in the lung. The V/Q ratio will be low where ventilation is obstructed due to diseases such as emphysema or asthma. We present a method for mapping ventilation-perfusion ratios (V/Q) in the lung by imaging the ^{19}F longitudinal relaxation time (T_1) of an inert fluorinated gas, in this case SF_6. Compared to hyperpolarized noble gases currently used for lung imaging, inert fluorinated gases are significantly less expensive, more abundant, and easier to handle, and they require no polarizing apparatus. We further take advantage of the fact that, in inert fluorinated gases, the T_1 is dominated by the spin-rotation interaction, mediated by molecular collisions. In the lung, the T_1 is roughly linear in the SF_6 concentration because collisions of SF_6 with less massive molecules (O_2, CO_2, H_2O) contribute differently to relaxation than SF_6-SF_6 collisions. Further, in a subject breathing 30%SF_6:70%O_2, the concentration of SF_6 is increased wherever V/Q is low, due to the removal of O_2 by perfusion. Using these known relationships, T_1 images are readily converted to V/Q images. Note that for this method, the subject breathes a 30%SF_6:70%O_2 mixture during the entire procedure, which should be well-tolerated by patients with obstructive lung disease. This is an advantage over our previous method of mapping V/Q using SF_6 spin density images [1], which required a reference image made while the subject breathes a normoxic gas mixture.

Methods: We have developed a modified Look-Locker [2] T_1 sequence, optimized for measuring the T_1s of SF_6 in lungs, which cover the range 0.8-1.3 ms. The pulse sequence consists of a π pulse, followed by a series of eight ~$\pi/4$ inspection pulses at 0.04, 1.00, 1.93, 2.89, 3.81, 5.00, 6.74, and 9.54 ms after inversion (TR=11.7 ms). The T_1 sequence is combined with 3D FID projection imaging [3] at 1.9 T to spatially resolve T_1. The T_1 sequence is repeated for 1750 different imaging gradient directions (G=6.9 mT/m), with an FID (880pts, 1MHz) acquired immediately after each inspection pulse. An image (2 mm isotropic resolution) corresponding to each inspection pulse in the T_1 sequence is constructed, and T_1 is determined from a 3-parameter fit of the time dependence of the signal in each image voxel.

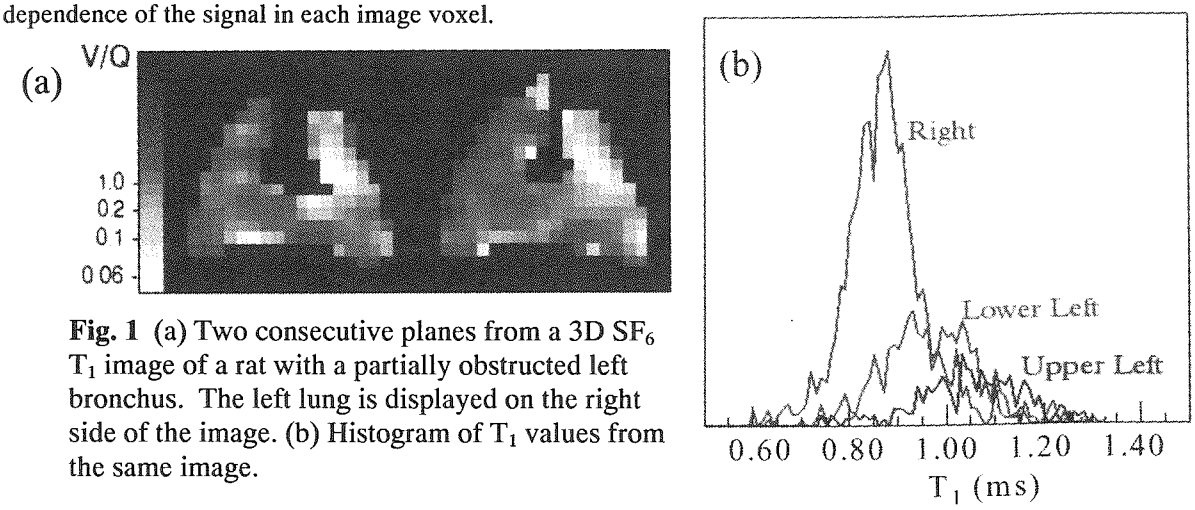

Fig. 1 (a) Two consecutive planes from a 3D SF_6 T_1 image of a rat with a partially obstructed left bronchus. The left lung is displayed on the right side of the image. (b) Histogram of T_1 values from the same image.

Results: Fig. 1(a) shows two planes from a 3D T_1 image (Nex=108, total image time=88 min.) of a mechanically ventilated rat. The left bronchus is partially obstructed by a bead with a narrow hole in the center. Here, the expected T_1 for healthy lung tissue is 0.89 ms (V/Q=0.85). The average T_1 of the 1023 voxels in the right (unobstructed) lung is 0.88 ms (standard deviation = 0.08 ms), in very good agreement with the expected value. In the left lung, the obstruction due to the bead is evident. In the lower left lung (434 voxels), T_1ave=0.97 ms (V/Q=0.19). The upper left lung (225 voxels) shows a greater degree of obstruction, with T_1ave=1.05 ms (V/Q = 0.10).

Conclusions: Combining a modified Look-Locker T_1 sequence with FID projection imaging, we obtained a T_1 map of SF_6 gas in the lungs of a live rat that quantifies V/Q at a meaningful resolution. Although the resolution is not as high as that of our prior V/Q mapping technique based on SF_6 spin density imaging, the advantage of breathing a high-O_2 gas mixture during the entire procedure motivates us to further refine this new technique.

References: [1] D.O. Kuethe et al, 'Imaging obstructed ventilation with NMR using inert fluorinated gases,' J. Appl. Physiol. 88:2279-86(2000), [2] D.C. Look and D. R. Locker, 'Time saving in measurement of NMR and EPR relaxation times,' Rev. Sci. Instrum. 41:250-1(1970). [3] D.O. Kuethe et al, 'Imaging lungs using inert fluorinated gases,' Magn. Reson. Med. 39:85-8 (1998).

Detecting cracks by imaging inert fluorinated gases

Dean O. Kuethe and Markus D. Scholz

New Mexico Resonance, Albuquerque, USA

Introduction Michelangelo's famous statue David has cracks in his ankles but people are having a hard time figuring how deep they are. It is hard to construct high resolution imaging devices like X-ray CT systems around large priceless objects. We want to explore the possibility of using MRI to image gases like SF_6 and C_2F_6 in cracks with an MRI system one could assemble on site. For example, a C-shaped magnet weighing perhaps only a ton could be positioned, with utmost care, around one of David's ankles. We would not want to use liquids because of possible harm to David.

Methods SF_6 and C_2F_6 are easy to image because the short T_1s allow for very rapid signal averaging. We have imaged SF_6 and C_2F_6 in samples that fit in a 55 mm diameter birdcage coil, using our 1.9 T, 30 cm bore MRI system. The idea is to obtain results from which we can calculate the feasibility of a transportable gas imaging system. We made an artificial crack between two sheets of polycarbonate that is 2 mm wide at one end and tapers to 0 mm at the other. We can tell the narrowest crack visible with a given imaging scheme from the position along the crack at which it is barely visible. By using hard pulses to excite the entire sample in the presence of frequency-encoding gradients, *à la* Lauterbur (1973) we lose very little signal to T_2 decay. With short data acquisition times, this scheme is also good for imaging samples with inhomogeneous broadening.

To introduce complications inherent to rocks, we also imaged SF_6 in thermally shocked Inada granite. This granite presents a serious challenge because it contains ferromagnetic minerals.

Results A result, which appears paradoxical at first, is that one can detect smaller cracks with lower resolution images. This dramatically makes the distinction that detecting a crack by gas MRI is different from resolving it. To detect a crack, the voxel which contains a crack has to have enough signal to stand out from the noise background. Cracks appear as spatially rare bright objects in a signal-free background. Assuming a crack extends in two dimensions, the signal grows with the square of linear voxel dimension while noise is reduced by the square root of voxel dimension because of the narrower acquisition bandwidth made possible by lowered imaging gradients. Thus, a factor that gas MRI has in its favor over X-ray CT is that it does not have to resolve cracks to detect where they are.

So far, we can detect 50 micrometer cracks in images with nominal 0.7 mm resolution using a 30 minute acquisition time. This extrapolates to being able to detect 50 micrometer cracks using a 20 cm diameter coil and a 0.5 T magnet with approximately a 30 day acquisition time.

A potential problem is ferromagnetic minerals. Although we managed to image SF_6 gas in a granite sample, it was difficult. The problem is that to overwhelm the intrinsic magnetic gradients, one needs strong imaging gradients. This forces one to make a high resolution image. In addition, the image distortion appears to be worse for SF_6 gas than for imaging water in the same cracks at the same resolution. Luckily, many statues, like David, are made from materials like Carrara white marble, which have very low iron content. We are in the process of trying to obtain cracked samples of white marble.

Conclusions Lab experiments provide encouraging results for the prospect of detecting cracks in precious objects with gas MRI, provided the material causes only modest inhomogeneous broadening.

We thank the NIH, grant R01EB002072, for financial support.

Lauterbur, P. C., *Nature*, **242**, 190-191 (1973).

Elementary Premises for Pure Phase Encoding – The Role of Time.

[a,b]Gregory Stoch, [a]Bruce Balcom

[a]*MRI Center, Department of Physics, University of New Brunswick, P.O. Box 4400, Fredericton, Canada E3B 5A3*

[b]*Department of Magnetic Resonance, Institute of Nuclear Physics PAN, Radzikowskiego 152 Kraków, Poland*

Pure phase encoding MRI data processing in its more extensive form engages three domains: spin evolution timescale, *k*-space and the object space. Understanding the mutual relationships between these domains is important both for correct data handling and for methodological improvements. It seems that there has been no consistent (yet simple) theoretical framework for this field so far. Data manipulation patterns are based on theorems valid for frequency encoding, using *k*-space concepts as the foundation for understanding. This phenomenological approach works sufficiently well in many situations, however it leads to misconceptions for pure phase encoding - quite frequently in our experience. The formal structure of phase encoded data is similar to that of frequency encoding although the usefulness of the *k*-space concept may be questioned. For example the *k*-space formalism conjugates signal and spin density [1] yet is inherently inconvenient to handle discussion of image distortions.

Phase encoded images are geometrically correct and not affected by chemical shift, magnetic susceptibility and dipolar and quadrupolar interactions [2]. The method is therefore essentially immune to spin evolution-time dynamics. Our approach has the potential to account for these features located at a fundamental level. We start from general premises, where distortions are naturally incorporated into equations. This is contrary to other elementary approaches [1,3] which begin with the idealized signal, yet experience difficulties how to put distortions back into it on the following stages of consideration. Our goal is to reveal relationships between spin evolution, gradient and object domains and to emphasize the fundamental distinction between the experimental and spin evolution time. This leads to a derivation of the method itself and reveals the link between pure frequency and pure phase encoding. We show explicitly the reason for distortion-free images given by pure phase encoding method. In particular we show why chemical shift and magnetic susceptibility do not affect the data. We further analyze measurements with steady- and transient- states, and have derived the relevant point spread function for the resulting images. The importance of the transient state for dynamical contrast is presented by means of a relevant, simple model.

References:

[1] Callaghan P.T, *Principles of Nuclear Magnetic Resonance Microscopy*, Oxford: Clarendon; 1991, 95 p.

[2] Bruce J. Balcom, Rod P. MacGregor et al., *Journal of Magnetic Resonance* **123**, 131-134 (1996).

[3] Blümich R. NMR *Imaging of Materials*. Oxford: Clarendon; 2000. 31 p.

Fast Gradient-Assisted Correlation Peak Imaging

Nikolas Salisbury Andersen & Walter Köckenberger
Sir Peter Mansfield Magnetic Resonance Centre, School of Physics and Astronomy,
University of Nottingham, University Park, Nottingham, NG7 2RD, United Kingdom,
n_s_and@yahoo.co.uk, +44 (0)115 9515161, fax +44 (0)115 9515166

Introduction

Correlation Peak Imaging (CPI) experiments record hybrid 2D spatial+2D spectral datasets and therefore enable metabolic mapping with increased spectral resolution compared to 2D+1D spectroscopic imaging methods such as Chemical Shift Imaging (1). CPI, however, being a 4D experiment comes with the drawback of long acquisition times or severe compromises with respect to resolution. Here we demonstrate a novel CPI sequence giving the possibility of shorter acquisition times and better temporal resolution or alternatively more signal accumulations allowing higher spatial resolution or lower detection limits.

Methods

Recently techniques for fast acquisition of 2D NMR spectra in a single scan using gradient echoes have been introduced for samples with sufficiently long T_2^* (2). Here we employ a phase-modulated single-scan COSY pulse sequence (3,4) with water suppression; using 3 smoothed chirp pulses (5) for slice selection and encoding of one spectral dimension and additional orthogonal gradient lobes for spatial phase encoding in 2 dimensions after mixing (Figure 1).

Results

A high quality 31x31 spatial X 64x64 COSY spectral data set of a glucose (4mm inner tube) / glutamine (8mm outer tube) sample was recorded as a proof of principle (Figure 2). The in-slice resolution is 320μm x 320μm and the spectral width covered is 1360Hz or 3.4ppm at a ^{1}H frequency of 400MHz. Excellent separation is achieved in the spectral dimensions as demonstrated by the extraction of a clean image of the inner compartment from the glucose cross peak next to the glutamine diagonal peak. The method enables recording of a 15x15x64x64 data set with a recycle delay of 2s in 10-15min depending on the k-space weighting scheme. We intend to apply the technique to in-vivo systems. While developed on an NMR microscope, it is also worth noting the method becomes more attractive with lower fields and large voxel sizes as found in larger imaging systems.

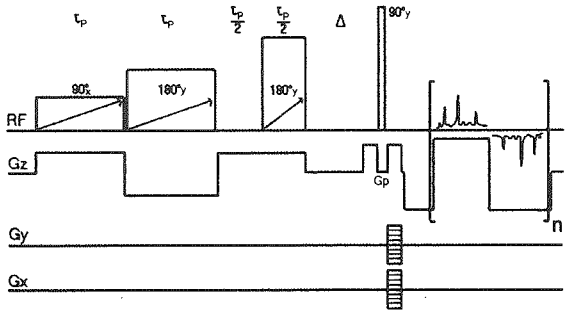

Figure 1 – Sequence for fast CPI (water suppression omitted). Gp denotes gradient pulses for coherence pathway selection.

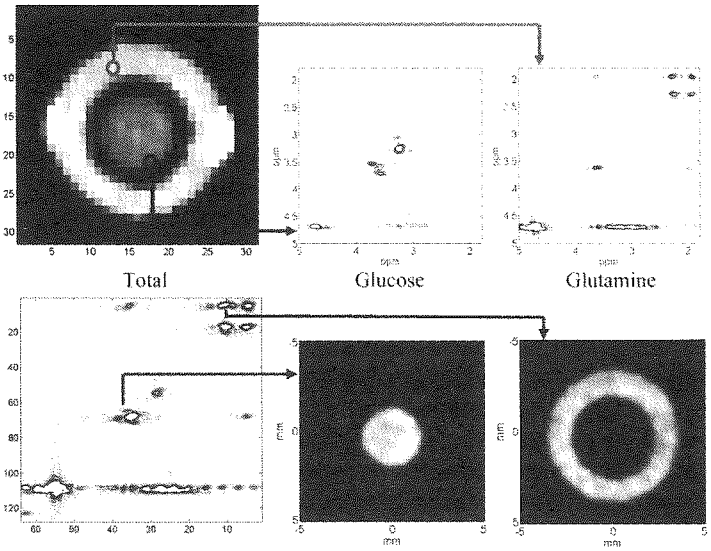

Figure 2 – Ways of examining a 4D CPI data set. Top: Extraction of COSY spectra of the compounds found in particular sample voxels in the total image. Bottom: Extraction of the spatial distribution of compounds giving rise to cross peaks in the total COSY spectrum. Concentrations: 0.3M, solvents: H_2O, slice thickness: 8mm. A Hanning filter with 5-step discretization was applied for acquisition in the k-dimensions giving a total acquisition time of 1h20min for a 31x31x64x64 raw data set with a recycle delay of 3s.

References: **1)** Ziegler A et al. *JMR* **B112**p141-150 (1996); **2)** Frydman L et al. *JACS* **125**p9204-9217 (2003); **3)** Tal A et al. *JMR* in press (2005); **4)** Andersen NS et al. *MRC* in press (2005); **5)** Cano K et al. *JMR* **155**p131-139 (2002)

Hurricanes in a Tube: Visualizing and Applying Spin Turbulence in MR Microscopy

Yung-Ya Lin, Susie Y. Huang, Sandip Datta
Department of Chemistry and Biochemistry, University of California, Los Angeles, California, USA

Introduction

Magnetic resonance (MR) microscopy combines high-field spectroscopic instrumentation with powerful gradient units to provide detailed spatial information about chemical and dynamical events. At high fields, two readily observed nonlinear feedback fields, radiation damping and the distant dipolar field (DDF), combine to generate turbulent spin dynamics in routine experiments *(1,2)*. Here we use MR microscopy to image the spatial and temporal development of the recently discovered spin turbulence and apply the dynamics to enhance contrast arising from spatial variations in chemical exchange.

Theory and Methods

Following the simple pulse-gradient sequence $[\theta_x\text{-}(GT)_z]$, the magnetization evolves under the joint reaction fields to sample various dynamical regimes *(3)*. Unstable transient dynamics at short times lead to spin turbulence and chaos in the long-time steady state. Figure 1 shows microscopic, axial MR images of a 5-mm tube of water at 14.1T that exhibit patterns characteristic of different stages of the dynamics. Such patterns originate from the intrinsic spatial variations in water ^{1}H precession frequency caused by inhomogeneous static and/or radiofrequency fields and nonuniform DDF at the sample boundary *(4)*. These small variations are enhanced by an avalanching amplification process mediated by the positive feedback interaction between radiation damping and the DDF *(1,5)*, analogous to the propagation of hurricanes from tiny climatic disturbances in temperature and moisture.

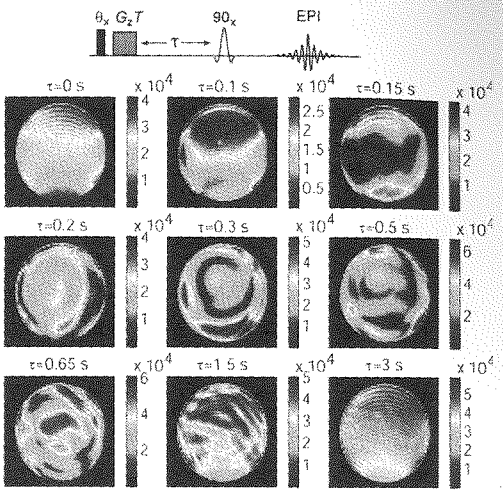

Figure 1. Experiments showing the development of spin turbulence in water at 14.1T as a function of evolution time τ. θ=120°, *GT*=5G·ms/cm.

Applications and Results

Instead of amplifying intrinsic spatial variations, the initial stage of the turbulent spin dynamics can be used as a novel contrast enhancement mechanism to amplify spatial variations in MR parameters that reflect underlying structural information. For example, Figure 2 shows simulations of a brain phantom with an embedded "tumor region" having the same ^{1}H density and relaxation times as surrounding tissue, but slightly different resonance frequency (+5 Hz) reflecting a small difference in oxygenation level. At short times (0.2 s), the contrast between the normal and tumor tissue is amplified to reach a steady optimum value. At longer times (2 s), the magnetization becomes random and uncorrelated with respect to neighboring voxels, resembling the onset of spatiotemporal chaos.

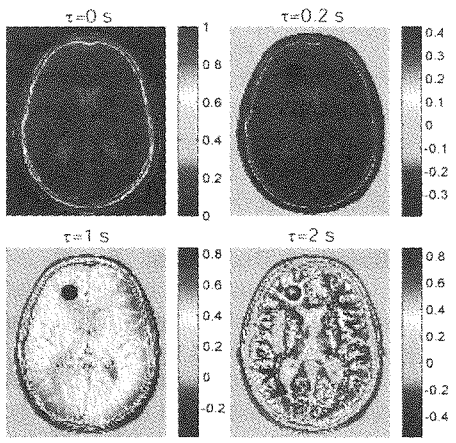

Figure 2. Simulations of a brain phantom with an embedded tumor (+5 Hz offset). Pulse sequence same as in Fig. 1 except θ=115°.

The contrast enhancement mechanism simulated above is confirmed experimentally in Fig. 3, where significant sensitivity and contrast enhancement is achieved by integrating the avalanching amplification with an RF control pulse scheme *(6)* to detect differences in chemical exchange rate through saturation transfer.

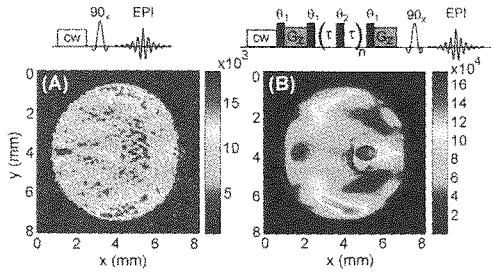

Figure 3. Difference images of a phantom containing 5% ethanol solution (outside) and an inner capillary of pure water, acquired in the absence (a) and presence (b) of an RF pulse sequence designed to control turbulent spin dynamics during free evolution. θ_1 = 90°, θ_2 = 180°, GT = 1 G·ms/cm, n = 7, and τ = 35.7 ms.

Discussion and Conclusion

The capability of visualizing spin turbulence, coupled with the ease of manipulating spin states by RF pulses, renders MR microscopy an ideal tool for studying the spatiotemporal dynamics that emerge at high fields. Furthermore, the positive feedback from the interplay of the reaction fields amplifies contrast in the early stages of spin turbulence and can be easily incorporated into existing detection methods, as demonstrated here through simulations and experiments on simple phantoms and elsewhere by tissue samples *(5)*.

References: 1. Lin, Y.-Y.; Lisitza, N.; Ahn, S.; Warren, W. S. *Science* **290**, 118-121 (2000). 2. Jeener, J. *J. Chem. Phys.* **116**, 8439-8446 (2002). 3. Datta, S.; Huang, S. Y.; Lin, Y.-Y. *J. Chem. Phys.* (submitted). 4. Bowtell, R.; Gutteridge, S.; Ramanathan, C. *J. Magn. Reson.* **150**, 147-155 (2001). 5. Huang, S. Y.; Datta, S.; Akhtari, M. et al. *Science* (submitted). 6. Huang, S. Y.; Walls, J. D.; Vu, L. et al, *Phys. Rev. Lett.* (submitted).

Magnetic Resonance Measurements of Starch Food Samples to Determine Spatially Resolved Oil and Water Content

Heather Hickey[1], Bryce MacMillan[1], Ben Newling[1], Manoharan Ramesh[2], Paul Van Eijck[2], Bruce Balcom[1]
[1]UNB MRI Centre, Department of Physics, University of New Brunswick, Fredericton, NB, E3B 5A3, Canada,
[2]Potato Processing Technology Centre, McCain Foods Limited, Florenceville, NB, E7L 3K5, Canada

Introduction:

In the food industry, time-domain nuclear magnetic resonance (TD-NMR) has proven to be a quick, accurate, non-invasive and effective way of investigating product quality [1, 2]. In the case of fried starch foods, the oil and moisture content within the fried coating is of particular importance [3, 4]. During immersion frying it is believed that steam released through an extracellular pore system, formed by the weakening of cell wall adhesion, opens up a pathway for oil penetration into the potato tissue. The degree of oil migration into the cellular matrix of the food during the deep frying process determines its taste, textural quality and the extent to which moisture migration from the core will sodden the crust subsequent to cooking.

Our goal was to determine crust thickness and quantify relative amounts of oil and water in fried food crusts. Based on the framework of bulk MR relaxation measurements of a model starch food sample, a 3D MRI technique employing a relaxation time based magnetization preparation was explored as a viable option in mapping relative oil and water content in both partially fried and fully fried French fry samples.

Methods:

Model starch food crust samples were allowed to equilibrate to different levels of relative humidity, producing static samples with oil to water ratios ranging from 20:1 to 1:1. T_2 decay curves of each sample were acquired and both an exponential decay fitting and distributed exponential analysis were performed.

T_2 relaxation time measurements were also performed on cooked starch food samples. Spatial resolution, which was not possible in bulk TD-NMR measurements, is required for measuring the relative amounts of oil and moisture specifically in the crust of the cooked starch food product. These samples were subsequently imaged with both Conical-SPRITE and T_2 weighted Conical-SPRITE imaging techniques in order to determine crust thickness and the oil to water ratio in a region of interest at the crust.

Results & Discussion:

There was a direct correlation between the weightings of the T_2 components and the known oil and water content of the model starch food samples. These results provided a basis upon which MRI techniques were applied to investigate the oil:H_2O ratio of cooked starch food coatings.

Results from high resolution Conical-SPRITE imaging revealed a crust thickness of between 290 μm and 570 μm in the case of a frozen partially fried starch food sample (Fig 2-a), and between 380 μm and 850 μm in the case of a fully fried starch food sample at ambient conditions (Fig 2-b).

Signal intensity from a set of T_2 weighted images, in the region of the crust, was fit to a biexponential decay. The relative weightings of the oil and moisture T_2 signal components correspond to an oil:H_2O ratio of ~2.8 in the fry crust.

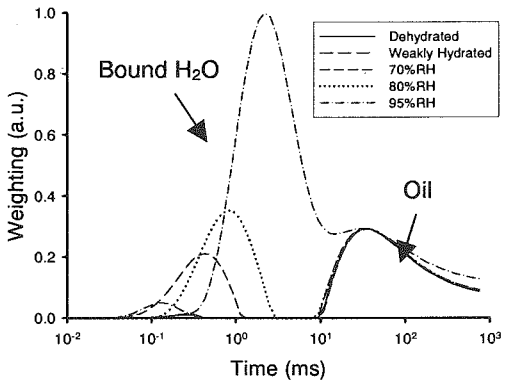

Figure 1. Bimodal distribution of T_2 values of model starch food sample with increasing humidity.

Conclusions:

Cooked starch food sample crust thickness was determined accurately by Conical-SPRITE MRI. The oil to water ratio in the crust of a fully fried starch food sample was determined to be ~2.8.

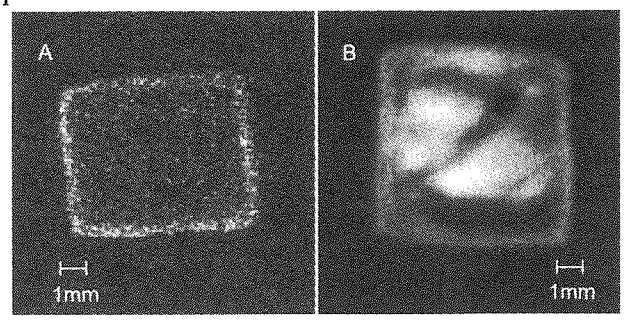

Figure 2. 2D slices of 3D multiple point Conical-SPRITE images. A) Frozen partially fried starch food sample at -25°C (left). B) Fully fried starch food sample at 8°C (right).

References:

[1] Ruan et al., *Lebensm.-Wiss. U. Techno.*, **31**, 516 (1998).
[2] Bank, *Concept. Magnetic. Res.*, **9**, 83 (1997).
[3] Saguy et al., *J. Agri. Food Chem.* **45**, 4286 (1997).
[4] Bouchon & Aguilera, *Int. J. Food Sci. Tech.*, **36**, 669 (2001).

Observation of Moisture Distribution in Various Types of Cooked Spaghetti

Kentaro Irie[1], Akemi K. Horigane[2], Shigehiro Naito[2], Akio Fujita[3], Hirofumi Motoi[4], and Mitsuru Yoshida[2]

[1]Initio Foods Inc., Chiyoda-ku, Tokyo, Japan. [2]National Food Research Institute, Tsukuba, Ibaraki Japan. [3]Nisshin Foods Inc., Chuo-ku, Tokyo, Japan. [4]Nisshin Seifun Group Inc., Iruma-gun, Saitama, Japan.

Purpose: Typical forms of cooked spaghetti consumed in Japan, (i.e. fresh, dried, frozen, luncheon, and long life spaghetti), were examined for their moisture distribution by micro-MRI to evaluate the quality as cooked food.

Methods: Each type of spaghetti was heated by its recommended cooking method. Two strings of the cooked spaghetti were cut into 1 cm lengths, placed on an acrylic plate, and wrapped with polyethylene film to prevent moisture loss. They were placed in an NMR tube (10 mm o.d.), which was inserted into a birdcage type RF coil with an inner diameter of 10 mm for MRI measurement on a NMR spectrometer (DRX300WB, Bruker) at a magnetic field of 7.1 T with a spin echo pulse sequence. The matrix size was 128 × 64, the size of voxel was 78 × 78 × 1000 μm^3, and the total scan time was 2 min 17 sec. Moisture content was calculated from spin-spin relaxation time (T_2) of water proton, based on the correlation between T_2 and moisture content[1)] of pulverized durum semolina standard gel samples. For mechanical property test, a spaghetti string was clamped by a wedge-shaped jig at a speed of 0.5 mm/sec, and the position of the jig and the load level were measured in real time using a material tester (EZ-test, Shimadzu) at 25°C.

Results and Discussion: Boiled samples of dried and frozen spaghetti had a distinct low moisture region at the center, which was not clearly observed in the other types of boiled spaghetti samples[2)]. In particular, the moisture content of boiled long life spaghetti was found to be almost homogeneous. Texture of cooked spaghetti samples was evaluated using force-distance curve of mechanical property test. For dried and frozen spaghetti, higher force was observed at the region corresponding to their low moisture rigid core compared to the other types. The luncheon spaghetti and long life spaghetti showed a lower breaking force and a larger dip after the peak force representing their soft and brittle texture caused by their moisture homogeneity. Quick-cooking spaghetti "Pronto" with a wedge-shape flute was also observed. The MR images clearly showed process of closing of the flute with moisture distribution change during boiling. Effect of the asymmetric moisture distribution on texture will be discussed.

Conclusion: These results indicated that micro-MRI could be used for the quality evaluation of cooked spaghetti through imaging of the moisture distribution, which reflects the mechanical property.

References:

1) Kojima, T. I. et al., *J. Food Sci.* **66,** 1361–1365 (2001).

2) Irie, K. et al., *Cereal Chem.* **81,** 350-355 (2004).

A Study of Moisture Distribution in Rice Grains during Soaking Using Gradient Echo Method

Akemi K. Horigane[1], Hitoshi Takahashi[2], Sachio Maruyama[3], Kenichi Otsubo[1] and Mitsuru Yoshida[1]

[1]National Food Research Institute, Tsukuba, Ibaraki, Japan.

[2]Akita Research Institute of Food & Brewing, Akita, Akita, Japan.

[3]Graduate School of Life and Environmental Sciences, University of Tsukuba, Tsukuba, Ibaraki, Japan.

Introduction: The moisture distribution, as well as total moisture content, is an important factor for determination of the gelatinization and mechanical properties of rice grains. It reflects morphological structure of rice grains and conditions of processing, soaking and cooking. We have already examined the changes of moisture distributions in developing rice caryopses and in cooked rice grains using the spin echo method [1-3], The route of water penetration and moisture distribution in rice grains during soaking are also important factors affecting the mechanical property of cooked rice. In this study the gradient echo method was employed to demonstrate the quick change of moisture distribution during soaking in rice grains of low moisture content (<30%). The moisture penetration patterns were correlated with the morphological feature of the grains.

Materials and Methods: Brown and milled rice grains of Japonica type rice cultivars, Koshihikari and Yamadanishiki were used. These cultivars had the different cell density of the starch storage tissues in the core of endosperm. The former has normal endosperm, and that of the latter has a white core due to low cell density. NMR spectrometer with a 7.1 Tesla magnet (DRX300WB, Bruker) and the ParaVision (Bruker) software package for NMR imaging were employed to produce three-dimensional (3D) images by a 3D-gradient echo pulse program. A rice grain fixed in a thin plastic sample holder was inserted in an NMR tube (5 mm). MRI measurement was immediately started after injecting water into the tube with a grain. Measurement parameters were set not to exceed 3 or 5 min of total scan time, resulting in the repetition time of 85 or 140 ms and flip angle of 40° or 60°, respectively. The echo time was 1.1 ms, and spatial resolution was 65 ×65 × 130 μm^3.

Results and Discussion: The penetration of water in rice grains during soaking was observed with high sensitivity and spatial resolution by the 3D gradient echo method. In milled rice grains of Koshihikari, water began to penetrate from the surface of the ventral side and the bottom part of endosperm, from which embryo had been removed. Then cracks were formed, and water diffused into all parts of the grain through the cracks. The water penetration in Yamadanishiki started from the same sides as Koshihikari, while the water spread more quickly into the white core without making cracks. As a result water content became high around the central line in Koshihikari and in the white core in Yamadanishiki, in which the cell density was lower than in other parts of endosperm. As for brown rice grain of both cultivars the water penetration was slow, and no water was observed in cracks or in the white core until 8 hr of soaking. The penetration from surface is main route in the brown rice grains although water penetration was controlled by the seed coat. The gradient echo MR images clearly showed the effects of cell density in the endosperm and the morphological structure of the rice grain on the route and rate of the water penetration.

References:

1) Horigane A.K. *et al, J. Food Sci.* **64**, 1-5, (1999). 2) Horigane A.K. *et al, J. Food Sci.* **65**, 408-412, (2000).
3) Horigane A.K. *et al, J. Cereal Sci.* **33**, 105-114, (2001).

MR flow imaging in plants: Using new techniques to solve old questions

Carel Windt, Frank Vergeldt and Henk Van As
Laboratory of Biophysics, Wageningen University, Wageningen, the Netherlands

In order to model plant performance, crop yield and drought resistance, knowledge of the internal distribution of water, energy (sucrose) and nutrients within plants is of key importance. New techniques, such as the pressure probe and genetic engineering, have identified the driving forces and molecular mechanisms that govern water transport in plants up to great detail. However, despite more than a century of research, conventional methods still do not allow water transport to be measured *in planta*. To finally test the validity of the two long-standing (and in certain cases controversial) theories that describe water movement in the plant, noninvasive methods such as MRI microscopy are needed. It has previously been shown that it is possible to measure and quantify water transport in the relatively fast flowing xylem pathway, which flows from the roots to the leaves [1]. Here, we demonstrate a full q-space pulsed field gradient (PFG) imaging approach to quantitatively measure the very slow phloem flow of sucrose containing water from the leaves to the roots. Secondly we present a coupled T_2-displacement imaging routine that allows us to separate pools of water within a single pixel on the basis of displacement, thus making it possible to separately analyze the T_2 relaxation behavior of the pools of stationary and flowing water within the same pixel. The latter makes it possible to study parameters such as vessel diameter and permeability, and correct for T_2 decay during flow labeling for the purpose of flow quantification.

MRI microscopy was performed in an open 0.7 T MRI system with a plan parallel gradient set for easy access. This setup allowed plants up to a size of 2 meters to be placed, upright, inside the electromagnet. A number of full-grown plants and a small tree were used as model systems. Linear displacement of water was measured using a full q-space flow imaging approach, using either spin echo or stimulated spin echo where long observation times Δ were needed [1]. Measurement time was reduced using fast k-space sampling by turbo spin echo. An SE or STE-PFG-TSE experiment like this yields a propagator for every pixel of an image, allowing the amount of stationary and flowing water per pixel to be calculated, as well as the average linear displacement (in both positive and negative direction) and the average volume flow. In order to measure displacement and T_2 relaxation simultaneously, we combined PFG with CPMG to yield SE-PFG-MSE. In a typical coupled T_2-displacement imaging experiment 64 echoes were acquired and q-space was sampled completely using 32 equidistant steps, with an image matrix of 64 x 64. After Fourier transformation a multidimensional dataset results, in which, for every voxel and for every echo, a complete propagator is available for analysis.

Flow measurements using SE-PFG-TSE and STE-PFG-TSE yielded calculated flow maps of water transport in the plant. In addition to xylem flow, we have been able to measure the slowly downward moving phloem sap flow which is particularly difficult to measure because of the small flowing volumes and low flow velocities (up to 0.5 mm/s). By measuring both flows we have been able to draw up a balance of water circulation in the plant, turning up surprising results. At night, up to 50% of the water moving up to the leaves (up to 50%) was not lost to the environment, but re-circulated inside the plant. The ability to re-circulate water may well be associated with the ability to function under conditions of drought stress.

Some authors regard xylem vessels as vulnerable pipelines that are isolated from surrounding tissue. Using STE-PFG-TSE it was possible to visualize exchange processes between vessels and surrounding tissue by measuring displacements with increasing flow labeling times, following the approach presented by Tallarek *et al* [2]. The presence of exchange indicated that xylem vessels are not isolated from the rest of the stem, but have access to stationary water that is present in tissue around the vessels.

T_2 in plant tissue is largely dependent on cell size, and changes in tissue T_2 have been shown to reflect changes in membrane permeability [3]. Application of coupled T_2-displacement imaging on a plant showed that it is possible to distinguish the T_2 of stationary water, associated with cells surrounding flow-conducting vessels, from the T_2 of flowing water within the vessels. The method thus gives access to sub-pixel information with regard to amplitude as well as T_2. This makes it possible to correct for T_2 decay during the flow labeling time Δ, which is of particular importance for the quantification of flow. Because T_2 is sensitive to vessel size and membrane permeability, coupled T_2-displacement imaging provides a means to study vessel sizes as well as changes in the permeability of vessels and associated cells.

[1] T.W.J. Scheenen, F.J. Vergeldt *et al*, *Journal of Magnetic Resonance* **151**, 94-100 (2001).
[2] U. Tallarek, F.J. Vergeldt *et al*, *Journal of Physical Chemistry B* **103**, 7654-7664 (1999).
[3] L. van der Weerd, M. Claessens *et al*, *Journal of Experimental Botany* **52**, 2333-2343 (2001).

MR Study of Morphology and Water Content in Living Tree Tissues

Maks Merela[1], Primo Oven[1] and Igor Serša[2]

[1]*University of Ljubljana, BF, Department of Wood Science and Technology, Ljubljana, Slovenia*
[2]*Jo ef Stefan Institute, Ljubljana, Slovenia*

The aim of our study was to test feasibility of three dimensional magnetic resonance microscopy in researches of morphology and water content in living tree tissue and to present its advantages in comparison to conventional histology and gravimetric measurements of the moisture content. Living wood is comprised of functionally specialized cells arranged in axial and radial directions [1]. Vessels are water conducting axial elements in range of diameter from 8 to 85 μm and embedded in supporting tissue represented by fiber tracheids. In the study we investigated intact and traumatic structures of a beech branch as well as water distribution in these tissues by series of planar images extracted from a 3D image set and by volume rendered images calculated at different view angles.

A beech (*Fagus sylvatica* L.) branch with two small dead branches (knots) was cut from a tree and coated with air and water impermeable coating to prevent it form drying. The sample was inserted in a RF micro probe of a 2.35 T magnet and imaged by the 3D spin-echo technique at parameters: field of view 30^3 mm^3, matrix size 256^3, echo time 2.4 ms, repetition time 500 ms and at 8 averages. The image was later processed by ImageJ (NIH Image) image processing software.

Cross-sectional planar images of intact tissue revealed high moisture in pith, in radially oriented xylem rays, in water conducting early wood and in wood producing a cambial zone. In xylem growth rings we could distinguish late (autumn) wood from early (spring) wood. The cross-section image of a dead branch (left image) clearly revealed a position of the protection zone delimiting sound wood from the branch cavity. This zone is protecting living wood against dehydration and against ingression of atmospheric oxygen and pathogenic microorganisms. Volume rendered images (right images) clearly displayed anatomical structures of the branch. On the surface can be seen cavities at the position of two shed branches and increased increment of wood trying to close these two wounds. The images also enabled insight into spatial distribution of the moisture content. Surprisingly, the images showed that a part of the pith of dead branches still contained high moisture content. Our research demonstrated that structural response is associated with passive water distribution in mechanically injured tree tissues.

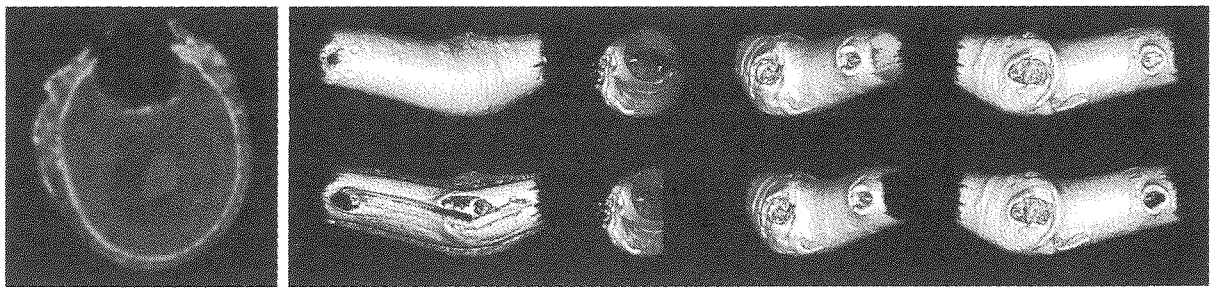

MR microscopy is a powerful tool for non-destructive characterization of water distribution in highly variable tissue and anisotropic material like wood is [2]. It can enable a long term monitoring of dynamics of moisture migration in wounded tissues of trees *in situ* and *in vivo*.

1. Dinwoodie JM (2000) Timber: its nature and behaviour; E & FN Spon: London and New York.
2. Bucur V (2003a) Nondestructive Characterization and Imaging of Wood, Springer-Verlag, Berlin.

Magnetic Resonance Imaging of Soluble Drug Release from non-Swelling Polymer Matrices

E. Karakosta and P. J. McDonald

Department of Physics, University of Surrey, Guildford, Surrey, GU2 7XH, UK

Abstract

Research in the area of controlled drug release is increasingly important in the pharmaceutical industry both from quality of life and commercial perspectives. One form of controlled release is that of active components incorporated in solid polymer matrices. The matrices can be either swelling (eg. HPMC) or non-swelling (e.g Eudragit) polymers and the active drug can be either soluble or non-soluble with the exception that non-swelling polymers cannot be usefully combined with insoluble actives. Although there has been much work[1], designing polymer matrix controlled release systems remains something of a black art. The pharmaceutical industry in particular is keen to see this turned into predictive capability. MRI is firmly established as valuable tool for analysing liquid transport in polymers and polymer dissolution. It can be used to follow the water ingress[2,3], the polymer swelling and dissolution[4] and the drug release in controlled release systems based on polymer matrices[5,6]. Water distribution maps can be obtained and used to test theoretical models.

The aim of this study is to determine the principal manufacturing parameters affecting the release of a soluble drug from a non-swelling polymer matrix and so to understand the dissolution mechanism. The matrix chosen for study is Eudragit. It is a copolymer of acrylic and methacrylic acid ester with low content of quaternary ammonium groups. The chosen drug is *Diltiazem Hydrochloride*. MRI experiments on Eudragit tables with different levels of compression, drug loading and particle size exposed to water were made in order to observe the ingress of the water into the tablets. NMR spectroscopy was used to assess the amount of drug released. PFG diffusion measurements of drug and water mobility in *Diltiazem Hydrochloride* solutions were made so as to estimate the self-diffusion coefficient of drug and water. Additional X-ray micro-CT and optical microscopy experiments were used to characterise the tablet microstructure.

Key experimental findings include:

(1) observation of rapid capillary uptake ($\leq$ 10mins) of water into the initial pore space of a tablet ahead of the primary dissolution. This porosity is very small, less then 4% for pure compact Eudragit and even less for drug loaded tablet;
(2) slow subsequent dissolution characterised by a sharp diffusion front which separates the invaded and un-invaded regions. The front advances according to Fickian diffusion. The dissolution process takes up to 24 hours in a 3 mm tablet;
(3) swelling of the whole tablet at intermediate drug loadings but no comparable swelling for either pure polymer or pure drug tablets;
(4) evidence that as water ingresses into the tablet, air voids start to accumulate and ripen within the sample.
(5) evidence that water ingresses faster into tablets with small drug particle size.

Attempts have been made to model the experimental results in terms of diffusion and solubility parameters and the measured microstructure. In particular, a dimensionless time, τ, is defined as

$$t = \frac{L^2 k}{D r_0}$$

where L is the tablet thickness (cm), r_0 is the drug particle size (cm), k is the dissolution constant (cm/s) and D is the water diffusion coefficient (cm^2/s). This compares the time taken for water to diffuse across the tablet with that for a drug particle to dissolve. It is found that for $\tau \gg 1$, diffusion is the dominant mechanism leading to a sharp diffusion front which progresses as $t^{1/2}$. For $\tau \ll 1$ dissolution dominates and smooth water profiles are predicted.

---

[1] Brazel, C. S. and Peppas, N. A., *European Journal of Pharmaceutics and Biopharmaceutics* **49**, 47 (2000).
[2] Thomas, N. L. and Windle, A. H., *Polymer* **23**, 529 (1982).
[3] Weisenberger, L. A. and Koenig, J. L., *Macromolecules* **23**, 1479 (1990).
[4] Siepmann, J., et al., *Pharm. Res.* **16**, 1748, (1999).
[5] Fyfe, C.A. and Blazek-Welsh, A.I., *J. Control. Rel.* **68**, 313 (2000).
[6] Melia, C. D., Rajabi-Saihboomi, A. R. and Bowtell, R. W., *Pharm. Sci. & Techn. Today* **1**, 32 (1998).

Determination of Water Transfer Coefficient into a Polymer Electrolyte Membrane in a Fuel Cell by Time-lapse Magnetic Resonance Imaging

Shohji TSUSHIMA, Kazuhiro TERANISHI, Shuichiro HIRAI

Research Center for Carbon Recycling and Energy, Tokyo Institute of Technology, Tokyo, 152-8552, JAPAN

Introduction

The polymer electrolyte fuel cell (PEFC) is considered to be a useful power source for automotive and on-site power generation. For higher energy efficiency and stable fuel cell operation, water management in the fuel cell is essential because a thin polymer membrane used as an electrolyte in the cell shows high ionic conductivity only in hydration. Thus, in practical fuel cell systems, supplied gases, *i.e.* hydrogen and air (oxygen), are humidified to keep membrane hydration under fuel cell operating condition. To establish a reliable method for water management, basic understandings of swelling process of the membrane in the fuel cell, especially quantification of water flux into the membrane from humidified gases is of great importance. In this study, we conducted time-lapse MRI experiment to monitor swelling process of the membrane assembled in a fuel cell and firstly determined water transfer coefficient by analysis on time variation of water content in the membrane measured by MRI.

Methods

A fuel cell specially-designed for MRI experiment [1,2] was used. To determine the water transfer coefficient, we examined the hydration process of the membrane in the fuel cell by time-lapse MRI. We measured the water distribution of the membrane every five minutes. The membrane was initially kept dry. Then we began to supply humidified nitrogen gas to the membrane in the fuel cell. The gas flow rate was 200 ml/min with supplied pressure at 0.1MPa. The gas temperature was kept at 60 °C all through the experiments. The dew point of the gas was varied from 40 to 60 °C by using a gas humidifying unit and temperature control system in MRI in order to investigate an effect of relative humidity on water swelling of membrane.

Results and discussion

Figure 1 shows time-lapse MRI results on swelling process of the membrane in the case of the dew point at 60 °C. Initially we can see no MRI signal in the membrane because the membrane was perfectly dehydrated by supplying dried nitrogen gas. Once we start to humidify the supplied gas, the membrane gradually swelled and reached to a steady state as seen in the MRI results. From the measured MRI results, we obtain time variation of averaged water content in the membrane after the flow of humid gas starts as shown in figure 2. Figure 2 also shows steady state of membrane hydration varied with dew point of the gas. To determine water transfer coefficient, we also conducted numerical simulation of membrane swelling process to fit experimental plots. The curves in the figure were fitted calculation results when the water transfer coefficient into the membrane was assumed to be 10^{-4}cm/s and shows excellent agreements with MRI results.

Conclusions

By conducting time-lapse MRI measurement to monitor swelling process of the membrane in the fuel cell and comparing numerical simulation results, we succeeded in determination of water transfer coefficient, which had been previously treated unknown parameter. This gives us profound insight for constructing reliable water transport model in overall fuel cell system.

References

[1] Tsushima, S. et al., *Electrochem. Solid-State Lett.*, Vol.7(9), A269 (2004).
[2] Teranishi, K. et al., *Electrochem. Solid-State Lett.*, Vol.8(6), A281 (2005).

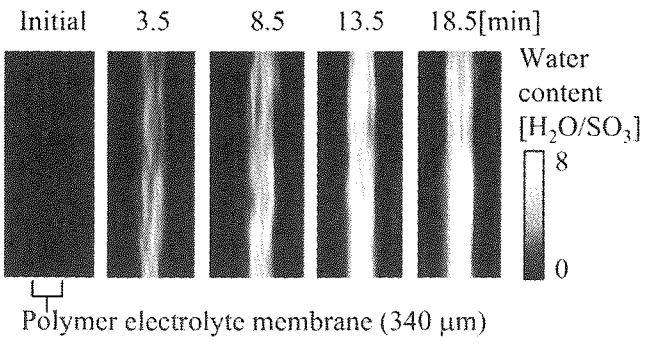

Figure 1: Swelling process of the membrane measured by Time-lapse MRI

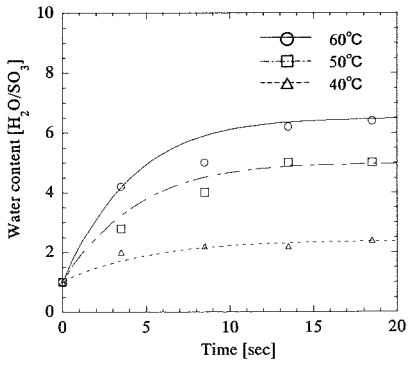

Figure 2: Time variation of water content of the membrane. Points: MRI results; Curves: Calculation results fitted with k=10^{-4}cm/s.

MRM Measurement of Material Heterogeneity in Polymer Electrolyte Membranes

Daniel T. Howe[*], Joseph D. Seymour[*], Sarah L. Codd[*], Scott C. Busse[+], Eric S. Peterson[#], E. Hubble Werre[*] and Benjamin F. Taylor[*].

Department of Chemical and Biological Engineering[*], Department of Chemistry and Biochemistry[+], Montana State University, Bozeman, MT USA. Idaho National Laboratory[#], Idaho Falls, ID USA.

As the use of fossil fuels for the generation of energy and transportation becomes more expensive, of limited supply and environmentally unsound, the development of viable fuel cell alternatives becomes more important. A comprehensive understanding of the proton exchange membranes used as electrolytes in certain types of fuel cells will play a major role in bringing the cost and reliability of fuel cell systems down to a competitive level with fossil fuels. Magnetic resonance microscopy (MRM) is well suited to the study of these membranes because it is non-invasive, and can spatially resolve material structure and give data on transport phenomena such as diffusion that cannot be determined by other methods. The goal of this research was to use NMR microscopy to study solvent mobility levels within the polymer membranes via spin-spin, T_2, magnetic relaxation and diffusion mapping. The molecular mobility can quantify membrane swelling and spatial heterogeneity of the membrane material. A key aim of the research is to correlate these findings with previous bulk NMR studies of solvent within polymer membranes. Prior bulk NMR studies of solvent molecular mobility at different hydration levels were unable to study the membranes fully submersed in solvents, as the free solvent signal would dominate the NMR signal from the solvent within the membrane. Spatial resolution of the NMR data provides the means to study fully saturated membranes, a condition of interest as hydration is related to membrane operation efficiency. The material homogeneity of the polymer in the thickness and surface directions of the membrane, an important factor in the reliable performance of fuel cells, was studied via T_2 mapping. Nafion®-117 was the proton exchange membrane studied because it is currently the most popular electrolyte used in the fuel cell industry and several bulk NMR studies have been conducted[1,2]. Results indicated that both solvent mobility and membrane swelling are highly dependant on the concentration of methanol used to prepare the samples, as seen in the bulk studies[1], and that solvent mobility can vary on the 20 micron level within the polymer in both the thickness and surface directions.

[1] S. Hietala, S. L. Maunu, and F. Sundholm, *Journal of Polymer Science* **38** 3277-3284 (2000).

[2] B. MacMillan, A.R. Sharp, and R.L. Armstrong, *Polymer* **40** 2471-2480 (1999); B. MacMillan, A.R. Sharp, and R.L. Armstrong, *Polymer* **40** 2481-2485 (1999).

A concentric barrel-type magnet assembly for unilateral NMR

Eiichi Fukushima, New Mexico Resonance, Albuquerque, USA

Introduction -- There is increasing interest in a unilateral apparatus capable of obtaining NMR/MRI signals from one side of the sample object [1]. The circumstances under which such measurements are valuable include monitoring contents of large tanks, detecting water inside walls, and changes in stiffness of car tires with use.

The most commonly used unilateral NMR device is the MOUSE developed at RWTH-Aachen in the group of B. Blümich [2]. It uses the fringe field of a U-shaped NdFeB-based magnet at close range and, therefore, has outstanding magnetic field strength compared to other designs albeit at rather close distances. Another strength of this technique is its relatively insensitivity to the presence of magnetic materials because it does not rely on having a uniform field.

Method -- The barrel magnet [3] was developed to try to extend the aspect ratio of the distance to the sample in units of the overall diameter of the device. Our target aspect ratio of 0.1 to 0.3, compared to ~0.05 typically for MOUSE, severely handicaps NMR reception by significantly decreasing the magnetic field strength and reducing the effective filling factor of the sample with respect to the transmit/receive coil.

The barrel magnet creates a uniform field region at a prescribed spot at some distance from the coil to increase the volume of the sample that obeys the resonance condition. It consists of a hollow, i.e., annular, cylinder that is magnetized in the axial direction. At some distance from the end of the barrel, there is a position on axis that is a saddle point in field strength; the field is a local maximum in the axial direction and local minima in directions orthogonal to the axial direction.

The uniformity of the field at the saddle point can be improved (or alternatively, the size of the region over which the field is uniform within some limit can be enlarged) by the use of a separate bar magnet located on axis of the barrel and oriented with the magnetization in the same direction as the magnetization from the barrel. Now the second derivative of the field in the axial direction can be set to zero. As a bonus, the second derivative in the radial variation can be reduced at the same time but the attempt to simultaneously minimize the second derivatives is stymied by the availability of only a limited number of sizes and strengths of magnetic materials.

Results -- We have modified a NdFeB barrel magnet (originally made by Sumitomo Special Metals, now Neomax) of dimensions 102mm diameter, 64mm inside diameter, and height of 81mm by adding a NdFeB bar magnet with both diameter and length of 25.4mm, obtained from ForceField in Ft. Collins, CO, USA. Adjusting the axial displacement of the bar magnet for best axial uniformity results in a reduction of the distance to the uniform field spot from 30 to 16mm, increase of the field strength at the uniform spot from 814 to 1040G, and approximately a ten fold increase in the size of the uniform field region which would lead to a factor of 1000 increase in effective sample size. Specifically, the axial homogeneity is better than 0.3% over 1cm and the radial homogeneity is better than 0.1% over 0.7cm or 0.3% over 1cm.

Discussion/Conclusions – There is an obvious trade-off between the distance to the working spot and S/N. However, a distance aspect ratio of 0.15 seem very reasonable, considering unilateral NMR performed with a barrel magnet without the modification discussed here [4]. The major problems encountered arises from the nonuniformity of NdFeB material but this is expected to improve with time.

Thus, we conclude that unilateral NMR at relative distances greater than what the MOUSE can do is quite feasible provided there are no magnetic materials nearby that will degrade the magnetic field uniformity.

Acknowledgments -- The anthor acknowledges the assistance, collaboration, and discussion with Armin Purea, Ron Kemmer, Shin Utsuzawa, Tomoyuki Haishi, Jasper Jackson, and Neomax.

1. Cooper, R. K., et al., *J. Magn. Reson.* **41**, 400-405 (1980); Marble, A. E., *J. Magn. Reson.* **174**, 78-87 (2005); Perlo, J., et al., accepted by *Science* (2005).
2. Eidmann, G., et al., *J. Magn. Reson.* A **122**, 104-109 (1996).
3. Fukushima, E., et al., US Patent 6,828,892.
4. Utsuzawa, S., et al., this meeting.

A Fourier-series based technique for simulating permanent magnets with applications in unilateral MR

Andrew E. Marble[1,2], Igor V. Mastikhin[1], Bruce G. Colpitts[2], and Bruce J. Balcom[1]

[1]MRI Centre, Department of Physics, and [2]Department of Electrical and Computer Engineering, University of New Brunswick, Fredericton, NB, Canada.

Introduction: Unilateral magnetic resonance (UMR) uses the fringe field from a planar permanent magnet (PM) assembly to polarize a sample displaced from the magnets[1]. Because the sample is external to the magnet array, UMR permits a range of large samples, inaccessible to conventional NMR, to be investigated. Central to UMR experiment design is the topology of the B_0 field generated by the PMs. The inherent spatial variation of B_0 defines the size and shape of the MR sensitive volume of the array, making simulation studies valuable both in the design and application of UMR instruments.

Many state-of-the-art commercial software package exist for simulating PM assemblies, however a simple, numerical strategy for describing magnetic fields in UMR is often desired. In this case, the surface charge approximation (SCA) is often employed[2]. The SCA is able to simulate the general shape of a PM array's magnetic field, however the solution becomes less accurate close to the magnets and is undefined on the magnet's surface. Because it is precisely the region near the magnets that is of interest in UMR, an improved simulation technique is desired. We have developed a simulation technique which uses a Fourier series expansion of the magnetic field profile at the surface of a PM array to describe the field everywhere. Simulations of PM arrays using our strategy agree with commercial software in regions near the magnets, where the SCA fails.

Methods: Our solution represents the magnetic scalar potential, ϕ, as a Fourier series (FS) and calculates the coefficients of this series directly from the FS expansion of the B_0 field at the face of the magnets. The magnetic field everywhere is then determined as the gradient of the scalar potential. In two dimensions, the solution

$$\phi(z,y) = \sum_{n=1}^{N} e^{-a_n y}\left[b_n \cos(a_n z) + c_n \sin(a_n z)\right] \qquad (1)$$

satisfies Maxwell's equations[3]. The associated magnetic field is defined as $B_0 = \nabla\phi$, and the y-component of this field at y=0 is

$$B_{0y}(z,0) = \frac{\partial\phi(z,0)}{\partial y} = -\sum_{n=1}^{N} a_n\left[b_n \cos(a_n z) + c_n \sin(a_n z)\right]. \qquad (2)$$

By assuming that B_{0y} is constant at the surfaces of the magnets and negligible elsewhere, a field profile at y=0 can be determined and expanded as a Fourier series. The coefficients of this series can then be related to the coefficients a_n, b_n, and c_n which fully describe the scalar potential through Eq. (1), and thus allow the field to be calculated at every point. Because the field for simple cases is expressed as an infinite series rather than a numerical integral as in the SCA, enhanced insight into B_0 for various PM arrays is possible.

Results: In order to validate our technique, the magnetic field over two PMs with opposite orientations, separated by a small gap was simulated. This magnet configuration is typical of many UMR arrays such as the NMR-MOUSE[1]. Figure 1(a) shows the magnet arrangement, and (b), (c), and (d) show contour plots of the magnitude of B_0 for this array simulated using commercial software (FEMLAB), the SCA, and the FS method respectively.

Discussion and Conclusions: Although the general shapes of all three field profiles shown in Fig. (1) are similar, the field calculated using the SCA is qualitatively and quantitatively different from the other plots, especially in the region above the gap between the magnets. As the MR sensitive volume is within this region, it is clear that the FS simulation technique provides results that are more suitable for use in further analysis. Furthermore, the SCA results cannot be displayed at y=0, as the solution is singular at this point. Our new simulation technique is general and can be applied to examine a wide range of UMR magnet arrays.

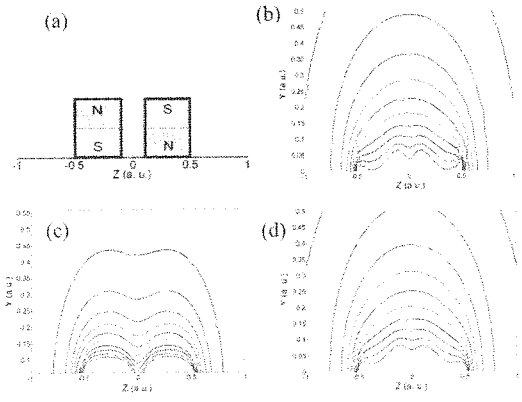

Figure 1: (a) permanent magnet arrangement; (b) commercial software simulation; (c) SCA simulation; (d) FS simulation. The upper surface of the magnets in (a) corresponds to y=0.

References:
1. Eidmann, Savelsburg, Blümler, et al., JMR A **122** 104-109 (1996)
2. Balibanu, Haily, Eymael, et al., JMR **145**, 246-258 (2002)
3. Marble, Mastikhin, Balcom, et al., JMR, **174**, 78-87 (2005)

SQUID-Detected Magnetic Resonance Elastography in Microtesla Magnetic Fields

Nathan Kelso[1], Kristie Koski[2], Michael Moessle[1], Whittier Myers[1], John Clarke[1], Jeffrey Reimer[3]
Departments of Chemistry[2], Chemical Engineering[3], and Physics[1]
University of California at Berkeley and the Lawrence Berkeley National Laboratory
Berkeley, CA USA 94720

We have used a SQUID-based microtesla magnetic resonance imaging (MRI) system to perform magnetic resonance elastography (MRE) experiments in a measurement field of 132 microtesla. Magnetic resonance elastography utilizes MRI coupled with mechanical deformation to measure three-dimensional displacement and strain fields in a sample. With appropriate data processing this allows for a quantitative map of the physical response of a material to an applied deformation. In the past, MRE experiments using conventional (1.5 tesla and above) MRI systems have demonstrated that MRE may be used as a non-invasive method for measuring stiffness of human tissues, which may aid in the detection and diagnosis of breast cancer and other cancers. Our MRE experiment consists of applying a small axial deformation to a cylindrical sample of 0.5% agarose gel. For samples approximately 30 mm in height, we were able to measure displacements on the order of 500 micrometers.

SQUID-Detected Magnetic Resonance Imaging in Microtesla Magnetic Fields, R. McDermott, N. Kelso, S-K. Lee, M. Mössle, M. Mück, W. Myers, B. ten Haken, H.C. Seton, A.H. Trabesinger, A. Pines and J. Clarke, *J. Low Temp. Phys.* **135**, 793-821 (2004).

Microtesla Magnetic Resonance Imaging with a Superconducting QUantum Interference Device, R. McDermott, S-K. Lee, B. ten Haken, A.H. Trabesinger, Alex Pines and John Clarke, *Proc. Natl. Acad. Sci.* 101(21), 7857-7861 (2004).

Low-field micro-coil probe development for portable NMR

Andrew F. McDowell, Eiichi Fukushima *New Mexico Resonance, Albuquerque, New Mexico, USA*
Todd Alam, *Sandia National Laboratory, Albuquerque, New Mexico, USA*
Laurel Sillerud, *Dept. Biochemistry & Molecular Biology, University of New Mexico, Albuquerque, New Mexico, USA*

Introduction: In collaboration with Sandia National Laboratories (SNL) and the University of New Mexico (UNM), we are developing a miniaturized NMR device, readily hand-portable yet capable of detecting minute amounts of biologically hazardous material. The basic concept is to look for the biohazard in a fluid flowing through a very small tube, with the tube walls functionalized to trap the target materials or cells within the NMR-sensitive region of the device. The biochemical aspects of the device are being developed at UNM, while the fluid control details are the responsibility of SNL, which is also manufacturing the sample coils using various techniques. Our job at New Mexico Resonance is to build these sample coils into NMR probes, test their performance, and provide guidance for coil design improvements. This presentation is a progress report.

Particular challenges: The overall design of the biohazard-detecting device is a small, hand-held Magnet-Probe-Fluid Control assembly attached to a portable Radio Frequency/Data Acquisition unit that is in turn interfaced to a laptop computer. Portability will require the use of a permanent magnet of small size. This fact, together with the goal of detecting minute amounts of material, leads us to consider a micro-coil as our detector.

While the size of the microcoil is well-suited to the permanent magnet, its electrical properties are not. Much of the previous work[1] in developing sub-millimeter micro-coils for the detection of very small samples has been done at high magnetic fields for maximal sensitivity. For portability, we are limited to low (~1T) magnetic fields. This not only limits our sensitivity, it also forces us to work at low resonance frequencies that are not particularly well suited to the low inductances of micro-coils. To produce a practical device, we need to provide for disposable sample tubes (or even entire probes) while keeping manufacturing costs down. Finally, we face the same challenge as all other attempts to build broadly applicable NMR devices: eliminating the need for expert technicians in the field. In our case, the challenge is particularly acute in the area of probe tuning, since the field of the permanent magnet will be highly temperature sensitive.

Methods: Our first micro-coil was produced at SNL using a laser milling process. A thin (5 μm) gold layer on the outside of a 500 μm OD capillary tube was patterned into a 37-turn, 2.2 mm long coil. This coil has an inductance of 19 nH (X_L = 5.3 Ω at 44 MHz) and resistance of 6 Ω. If built into a traditional NMR tank circuit, this coil would require a tuning capacitor of more than 600pF and the resulting probe would have a Q of about 1. We have taken a different approach: we tune and match the sample coil "remotely," placing the sample coil into its own shielded box and using a large, auxiliary coil and adjustable capacitor in a second box. This design has some advantages in meeting the goals of rugged, easy-to-use device.

We build prototype NMR probes for various designs and coils to test their performance. We use the small NMR console from MRTechnology, which is already optimized for work with permanent magnets, and a ~1T permanent magnet usually used for imaging small objects. The SNR performance, power requirements, and spectral resolution of the coil/probe designs are compared theoretically and experimentally.

Results: Our first measurements have been on a copper wire mockup of the SNL coil. We have used a quarter-wave cable to transform the low impendence of the mock sample coil and then positioned this impedance across the inductor in the remote tank circuit. This probe provides a SNR of about 8 for a 1 μL sample of doped water. The real laser-patterned coil will contain much less sample, but the coil's smaller size should improve its relative sensitivity. It is clear that signal detection is readily achieved, so that measurements comparing the performance of various coil designs will be possible. We plan measurements on laser-milled coils of various designs, flat coils produced by lithographic means, and traditional wire-wound coils.

[1]See, for example:
Peck, T.L. Magin, R.L., and Lauterbur, P.C., *J. Magn. Reson. B*, **108**, 114-124 (1995).
Grant, S.C., Murphy, L.A., and Magin, R.L., *IEEE Trans. Magn.*, **37**, 2989-2998 (2001).
B. Behnia and Webb, A.G., *Anal. Chem.*, **70**, 5326-5331 (1998).
Rogers, J.A., et al., *Appl. Phys. Lett.*, **70**, 2464-2466 (1997).
Seeber, D.A, et al., *Rev. Sci. Inst.*, **71**, 4263-4272 (2000).

Development of Local Shear Modulus Measurement System by MR Microscope

Mikio Suga[1], Kotaro Minato[2]

[1] Faculty of Engineering, Chiba University, Chiba, Japan

[2] Biomedical Imaging and Informatics, Nara Institute of Science and Technology, Ikoma, Japan

Introduction

There are several disease states which result in alteration of tissue stiffness. Magnetic resonance elastography (MRE) is a method that can visualize the propagating acoustic strain waves in materials being measured [1]. The local quantitative values of tissue stiffness are calculated from distribution of the acoustic strain waves in the MRE image. In order to observe tissues such as the early stage of tumors in detail, spatial resolution of the MRE image is not enough because of hardware limitation of the conventional MRI system. Therefore we developed an elasticity measurement system using an MR microscope.

Methods

Experiments were performed on the 1 T magnetic resonance microscope (MRmicro, MRTechnology, Inc.). Developed external vibration system is made of multi-layer piezoelectric element (AE1010D16, NEC-TOKIN) and bamboo rod as shown in Fig. 1. The resonant frequency of bamboo rod is about 220 Hz. The amplitude of external vibration is about 15 μm around 200 Hz and 5 μm around 500 Hz. The actuator was driven by a waveform generator. And the waveform generator was synchronized with an MR controller by trigger pulse. A modified phase-sensitive spin-echo sequence was used for data acquisition. Oscillating gradients (motion-sensitizing gradients, MSG) were synchronized with a mechanical excitation for encoding of the acoustic strain waves. The strain wave images with multiple initial phase offsets can be generated with increasing delays between MSG and mechanical excitation [2].

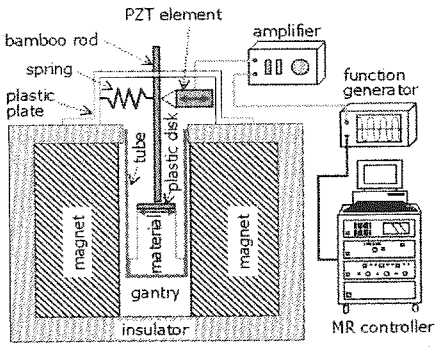

Fig.1. MR elastic microscope system

The object was a 0.9% cylindrical agar-gel phantom with two cylindrical 0.5% agar-gel inclusions (ranging 1.8 and 3 mm in diameter) perpendicular to the slice (Fig. 2 (left)). Typical parameters are the followings; field of view 25x25 mm^2, image matrix 128x128 $pixel^2$, slice thickness 2 mm, repetition times 750 ms, echo time 55 ms and mechanical vibration 500 Hz. To acquire shear modulus map, we applied a spatio-temporal directional filter [3] and instantaneous frequency method [4] to the strain wave images with four phase offsets.

Results and Discussion

The shear wave image and shear moduli map of an agar-gel phantom are shown in Fig. 2. The shear modulus at ROI 1, 2 and 3 were 7.7 (SD: 0.9) kPa, 3.8 (SD: 0.08) kPa and 5.2 (SD: 0.08) kPa, respectively. The shear modulus of 0.5% and 0.9% agarose gel measured by the viscoelastic analyzer (Rheogel-E4000, UBM Co. Ltd.) were 3.3kPa and 7.4kPa. The viscoelastic analyzer is able to measure average shear modulus from 8x4x2 mm^3 sample. For more accurate measurement of the shear moduli map, improvement of inversion algorithm and 3-D shear wave data acquisition will be needed.

Conclusions

In this research, we developed the MR elastic microscope system. When the embedded material's diameter is 3 mm or more, the shear modulus that was measured from the developed system almost corresponds to the shear modulus measured by the viscoelastic analyzer. These results suggest the developed MR elastic microscope system makes it possible to measure the shear modulus map no invasively.

Reference

[1] Muthupillai, R, et al., *Science*, 269, 1854–1857(1995). [2] Muthupillai, R, et al., *Magn. Reson. Med.*, 36, 266–274(1996). [3] Manduca, A, et al., *Medical Image Analysis*, 7, 465-473(2003). [4] Boashash, B, *Proc. IEEE*, 80, 520–538(1992).

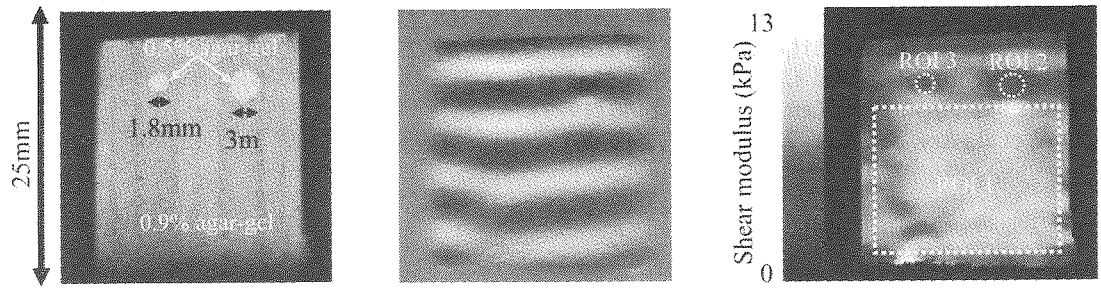

Fig.2. MRI image (left), shear wave image (center) and shear moduli map (right) of heterogeneous agar-gel phantom.

Construction and Initial Testing of an Optimized, Open-Access, Human-Scale, Very-Low-Field MRI Magnet for Orientational Lung Study

Leo L. Tsai; Matthew S. Rosen; Ross W. Mair; Ronald L. Walsworth

[1] Harvard-Smithsonian Center for Astrophysics, Cambridge, MA, USA.

Lung function is exquisitely sensitive to gravity. As such, there is significant interest within the pulmonary physiology community over how lung properties and function are affected by subject orientation. Although it is agreed that perfusion and ventilation are heterogeneous and orientation-dependent, there is much debate over exactly how the gas and blood are distributed [1], or even the degree of influence by gravity [2]. Gravity-dependent studies have been performed on animal models but until recently there have been no reliable methods to observe local ventilation in a completely non-invasive manner suitable for humans. Laser-polarized ^{3}He MRI [3] has proven to be an effective non-invasive tool for such studies, but imaging has so far been restricted to horizontal positions [4]. We recently demonstrated *in vivo* ^{3}He imaging of human lungs in the supine and upright positions in an open-access system operating at ~ 4 mT (40 G) [5]. While this showed the feasibility of performing such experiments, our results were hampered by low SNR, short T_2* due to B_0 inhomogeneity > 1000 ppm, and gradient coil heating which limited imaging speed.

We have constructed a second-generation open-access MRI system specifically designed for orientation-dependent pulmonary ^{3}He human imaging. The B_0 coils are a bi-planar, constant-current four-coil design [6], and can provide a field of up to 100 G (at 65 A) with a homogeneity better than 75 ppm in a 40 cm DSV, with the same footprint as the previous system. This design maximizes inter-coil distance (~ 90 cm) and is relatively insensitive to coil misalignment. The coils are mounted on circular aluminum flanges and an aluminum strut framing system allows inter-coil spacing to be finely adjusted. Planar gradient sets were designed and constructed to provide a magnetic field gradient up to 0.18 G/cm with linearity suitable for 256^2-pixel images on a 40 cm FOV, while maximizing coil separation (~ 78 cm). The entire system in enclosed in a commercial Faraday cage which provides >100 dB attenuation at ~ 250 kHz.

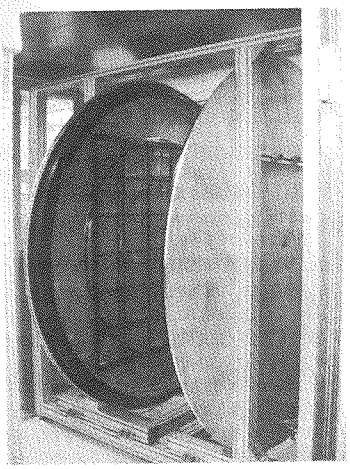

Figure 1: Open Access, Very-Low-Field MRI system. Main B_0 coils and support flanges, strut framing, and Faraday enclosure are seen.

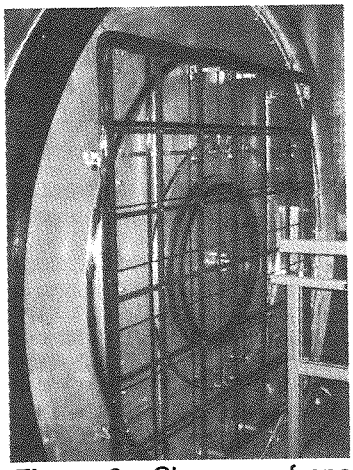

Figure 2 : Close up of one B_0 coil, showing secondary B_0coil, planar gradient coils, and a support at the magnet iso-center for phantoms

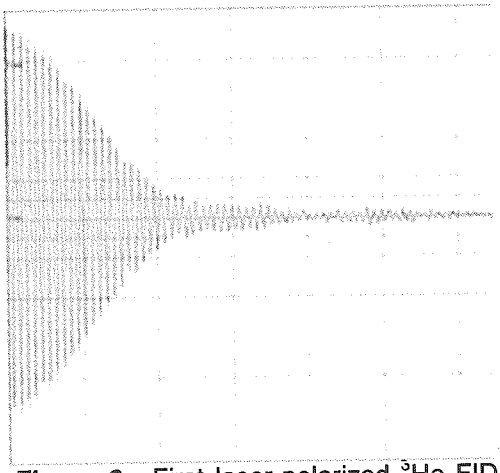

Figure 3 : First laser-polarized ^{3}He FID obtained from the Very-Low-Field MRI system, using the Tecmag MR console. B_0 = 45 G (B_0 current ~ 30 A), frequency = 146 kHz, T_2* ~ 16 ms, flip angle ~ 4º.

The system is now complete, and in its optimization stage. B_0 is being shimmed, and objects that distort B_0 are being removed. The Tecmag MR console is in operation, providing broadband RF control above 100 kHz. Gradient line filtering and optimum B_1 coil designs are being worked on. Laser-polarized ^{3}He signals have been obtained from phantoms, and work is progressing towards phantom imaging.

1. M. Mure and S. G. E. Lindahl, *Acta Anaesthesiol Scand.*, **45**, 150–159 (2001).
2. J. West and R. Glenny, *(letters to the editor) J. Appl Physiol.*, **93**, 1888–1891 (2002).
3. T. G. Walker and W. Happer, Rev. Mod. Phys., **69**, 629 (1997).
4. S. Fichele, N. Woodhouse, A. J. Swift, et al. *J. Magn. Reson. Imaging*, **20**, 331–335 (2004).
5. R. W. Mair, M. I. Hrovat, S. Patz, et. al., *Magn. Reson. Med.*, **53**, 745-749 (2005).
6. P. Morgan, S. Conolly, A. Macovski, Proc. 5th ISMRM, Vancouver, p. 1477 (1997).

Ultra Fast Acquisition Open Subsystem for EPRI Measurement.

[a,b]Gregory Stoch, [a]Bruce Balcom

[a]*MRI Center, Department of Physics, University of New Brunswick, P.O. Box 4400, Fredericton, Canada E3B 5A3*

[b]*Department of Magnetic Resonance, Institute of Nuclear Physics PAN, Radzikowskiego 152 Kraków, Poland*

The spiral *k*-space trajectory with the SPRITE technique [1] is a universal *MRI* protocol that is advantageous especially for EPR imaging, where the short signal lifetimes permit rapid data acquisition. This, however, induces the problem of a very large data stream and imposes significant requirements for synchronization in the experimental setup, as pointed out in our previous work [2]. The EPRI instrument presented was controlled using *LabView* to ensure synchronization between acquisition, gradient levels and digital delays. This architecture proved its overall capability, and the capabilities of the basic hardware components. The logical next step requires a fully distributed architecture for the system, gradually relinquishing time critical aspects from central control to lightweight and independent software modules. The main controlling code competes itself for resources with time critical parts of the setup and these requirements for the *LabView* environment are significant.

Our new approach to EPRI instrument control assumes the acquisition to be entirely autonomous from central control, and is truly modular in terms of software architecture based on MS-COM specification. The control code for adc board works on an independent PC and consists of a fast (2ns dwell time) acquisition card, gradient DAC and a small software module for Ethernet communication. This architecture guarantees minimum usage for system resources (CPU time and memory) which is critical to improve efficiency, modularity and quality control of the system. *LabView* control is precluded from potential conflict with time critical components by maintaining it on a separate PC. Necessary communication is ensured by Ethernet using TCP/IP which is the preferred protocol in network-distributed environments [3]. The maintenance of the architecture takes place using MS Visual C++ 7.0 with a set of custom-designed creators. That enables both easy modification of the software, and easy creation of new control components which are capable of communication with the *LabView* system. This strategy gradually removes *LabView* from the center of the controlling code, maintaining all its advantages as a convenient first-approach design interface. The presented architecture conforms to advanced standards in hardware control and is for the first time, to our knowledge, applied to a dedicated home built EPRI instrument.

References:

[1] Balcom B.J., MacGregor R.P. et al., *Journal of Magnetic Resonance* **123,** 131-134 (1996).

[2] Stoch G., Goora F., Colpitts B.C., Balcom B.J. *Electron Paramagnetic Resonance Imaging using a pure phase encoding technique*, Heidelberg Conference Abstracts (2003).

[3] Stoch G., *Control of NMR measurement based on TCP/IP protocol in multithreaded system environment*, abstracts of XXXII Polish Seminar on NMR, Bronowice 1-2 December 1999.

Development of a 2 Tesla permanent magnetic circuit for NMR/MRI

Tomoyuki HAISHI, *Masaaki AOKI, *Eiji Sugiyama
MRTechnology, Inc., *NEOMAX, CO., LTD., *JAPAN*
Email: haishi@mrtechnology.co.jp

Abstract

We have developed a 2.0T permanent magnetic circuit for NMR/MRI. In the previous study, the maximum field strength of permanent magnets for MRI was 1.0T [1, 3]. With using NdFeB magnetic materials and a special magnetic circuit design, it has been achieved that the magnetic field strength of 2.03 Tesla, ^{1}H center frequency of 86.3MHz, air gap of 60 mm, 10 ppm-homogeneous volume of 30 mm DSV (diameter spherical volume), outer size of 80 cm× 63 cm× 84 cm. NMR/MRI experiments were performed with using a compact NMR/MRI console [2] and RF solenoid coil. High resolution 3D MR microscopy images (100um res.) of a human finger *in vivo* were acquired in several minutes. Three chemical-sift lines in Ethanol spectrum (CH_3OH_2OH, 4 cc) were clearly measured with current shimming of higher orders. These result promises the stability and wide-use of the maintenance-free 2.0T permanent magnets.

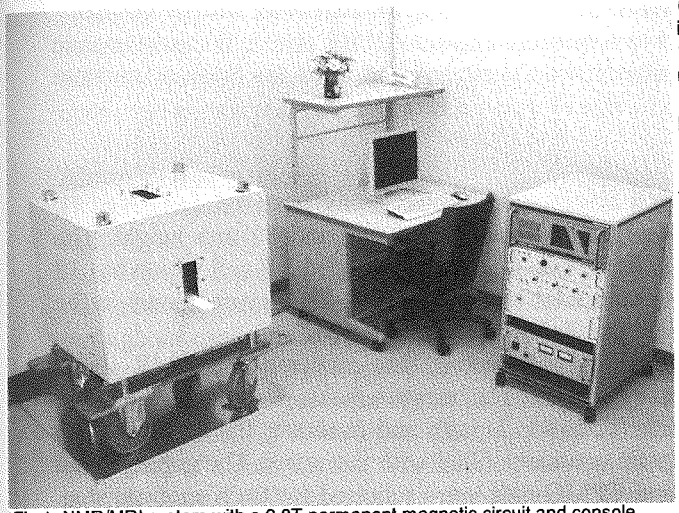

Fig.1. NMR/MRI system with a 2.0T permanent magnetic circuit and console.

Introduction

Figure 2 shows an example of permanent magnetic circuits which is used for usual medical MRI systems. Currently NdFeB materials have a maximum energy-product in magnetic materials. Almost of all 0.2T-0.4T whole body MRI system employ the typical magnetic circuit and NdFeB materials. This magnetic circuit is consisted of three major parts; yolks, magnetic-materials, and pole-pieces. The magnetic circuit has a advantage of its simple mechanical-structure, however the iron yolk cause a trouble of heavy weight more and more as increasing its air-gap or magnetic field-strength.

On the other hand we had developed a 4.4T permanent magnetic circuit [4] (figure 3, 50 kg, ID: 6 mm, Halbach type) for a polarizing lens for an instrument of linear accelerators. Unfortunately the 4.4T magnet did not have enough field homogeneity for NMR/MRI at its 6 mm diameter volume of the isocenter. Figure 4 shows a magnetic circuit design modified from Halbach type especially for NMR/MRI applications. In the previous study [1, 3] a 1.0T magnetic circuit (44 MHz, 10 ppm@ 20 mmDSV, 60 mm gap, 200 kg) was developed.

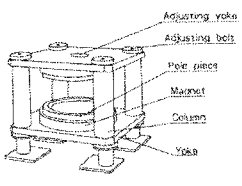

Fig.2. Column type circuit,

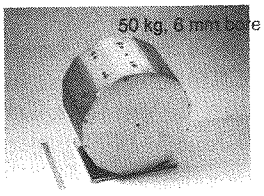

Fig.3. Halbach circuit (4.4T)

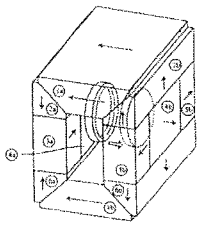

Fig.4. Yolkless circuit,

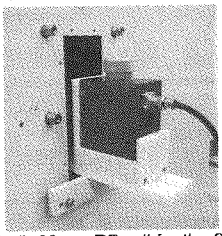

Fig.5. 30mm RF coil for the 2T

Materials and imaging experiment

The 2.0T magnet with NdFeB shown in figure 1 (left), has achieved that the field strength of 2.03 T, ^{1}H center frequency of 86.3MHz, air gap of 60 mm, 10 ppm-homogeneous volume of 30 mm DSV, outer size of 80 cm× 63 cm× 84 cm. The 2.0T magnet has double bores of vertical& horizontal crossing at the homogeneous volume and NMR/MRI samples are easily placed at the iso-center. The whole magnetic circuit is covered with thermal insulators, so that the resonance frequency changing caused by temperature drifts is reduced within 1kHz with using a PID control of heaters attached to the magnet.

NMR/MRI experiments for the 2.0T magnet were performed with using a compact NMR/MRI console [2] and RF solenoid coil (figure 5). A NMR spectrum of Ethanol (CH_3OH_2OH, 4cc) was measured with using higher order shim coils. A human fetus (*ex vivo, 16W, Courtesy of Prof. K. SHIOTA, University of Kyoto, Japan*) was imaged using a conventional 3D spin echo sequence; TR/TE = 100/12 ms, matrix = 512×256×128, T_{acq} = 4hour, voxcel size 120 um× 120 um× 240 um.

Result and discussions

The ^{1}H spectrum of Ethanol in a tube is shown in figure 6. As a result of the achievement for a few ppm of the field homogeneity with the shim coils, chemical sifts of three different intensities representing CH3, CH2, and OH ware acquired. The MR microscope images of the human fetus are shown in figure 7. The anatomical details *ex vivo* are clearly observed in this image.

One of the advantages for NMR/MRI systems with permanent magnets is that we can use RF solenoid coils for signal detections. In theory the SNR for solenoid RF coil is twice as much as the SNR for a quadrature birdcage coil in the same diameter of its coil dimension. According to the above estimation, a combination of the 2.0T and solenoid rivals a super-conducting 4.0T system at SNR.

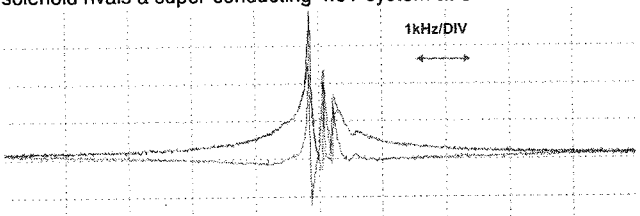

Fig.6. ^{1}H spectrum of Ethanol acquired with the 2.0Tmagnet

Conclusion

The first trial of development for a 2.0T permanent magnet for NMR/MRI was successfully done. The combination of the 2.0T and solenoid rivals 4.0T systems at SNR. The NMR/MRI experiments were performed with using a compact NMR/MRI console and RF solenoid coil. This result promises the stability and wide-use of the maintenance-free 2.0T magnet at morphology or small animal laboratories.

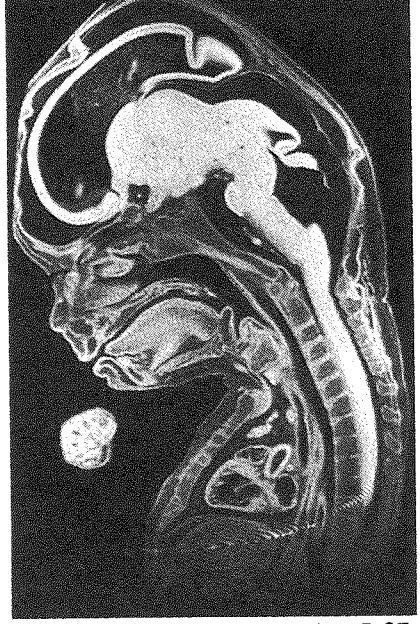

Fig.7. Human fetus (*ex vivo*), 3D-SE, 512x256x128, TR/TE=100/12.
Courtesy of Prof. K. SHIOTA, U of Kyoto.

References

[1]T.Haishi et al, Magnetic Resonance Imaging, 19, 875-880, 2001
[2]K. Kose et al, MRMics, 6th ISMRM, Sydney, 1998
[3]T.Haishi, ICMRM proc., Snowbird, USA, 2003
[4]M. Aoki, http://www.neomax.co.jp/

Unilateral NMR system by using a novel barrel shaped magnet

Shin Utsuzawa[1, 2], Ron Kemmer[3], Yoshito Nakashima[4]

[1]MRTechnology, Inc., Japan, [2]Institute of Applied Physics, University of Tsukuba, Japan
[3]University of Würzburg, Germany
[4]National Institute of Advanced Industrial Science and Technology, Tsukuba, Japan

Introduction

Estimating water-filled fractures is a serious problem to maintain building structures. Although NMR has great potential to measure water within concrete and natural rocks [1, 2], and there are several devices that enable NMR measurements on an external sample [3, 4, 5], use of such techniques *in situ* has suffered from the sensing distance in units of the device size. Recently, Fukushima and Jackson [6] proposed a barrel shaped magnet that possesses a region of zero first derivatives in all three spatial dimensions at a distance of 30 to 50% of magnet diameter. Such design would provide larger sensing distance with smaller magnet.

In this work, we attempted to use the barrel magnet as a portable unilateral NMR device for maintenance purposes in civil engineering. A miniature barrel magnet was fabricated and used for fracture aperture estimation.

Materials and methods

A miniature barrel magnet was designed to have a sweet spot 30 mm away from its end (Fig. 1). Dimensions of the magnet are 102 mm outer diameter, 64 mm inner diameter, and 82 mm height. The weight was about 3 kg. Field strength at the sweet spot is 814 G. A Double-D shaped RF coil which has 13 turns on each D-halves was constructed according to computer simulation (Fig. 2). Current flows in the opposite senses in the two D- halves to generate B_1 field parallel to the face of the coil.

For water-filled fracture aperture estimation, an analogue of fracture was prepared and NMR signal intensity was measured as a function of the aperture (Fig. 3). The measurements were done on three samples: Tako sandstone (Gumma, Japan), Aji granite (Kagawa, Japan), and concrete. Each sample was shaped into 70 x 55 x 30 mm^3 and immersed in a plastic container filled with tap water. The gap between the blocks (simulated fracture aperture) was varied and CPMG data were acquired for each aperture step. Summation of echoes, which is proportional to the product of porosity and average T_2 [7], was calculated to estimate fracture aperture with a small number of scans under low signal-to-noise ratio.

Results and discussion

As shown in Fig. 4, sum of echoes was proportional to the gap between blocks (again, simulated fracture aperture) up to 16 mm. Then it was saturated and remained practically constant. This result was consistent with the region of interest defined by B_0 field distribution and RF pulse width used in the experiment.

Acknowledgements

The authors thank Dr. Eiichi Fukushima at New Mexico Resonance for his invaluable advice.

Reference

[1] Young JJ, Szomolanyi P, Bremner TW, Balcom BJ, Cement and Concrete Research 34 (2004) 1459.
[2] Kleinberg RL, Kenyon WE, Mitra PP, J. Mang. Reson. A 108 (1994) 206.
[3] Kleinberg RL, Sezginer A, Griffin DD, Fukuhara M, J. Magn. Reson. 97 (1992) 466.
[4] Eidmann G, Savelsberg R, Blümler P, Blümich B, J. Magn. Reson. A 122 (1996) 104.
[5] Prado PJ, Magn. Reson. Imag. 21 (2003) 397.
[6] E. Fukushima and J. A. Jackson, U.S.Patent No. 6,828,892.
[7] A. Sezginer, C. M. Cao, N. Heaton, M. Herron, R. Freedman, G. Van Dort, Transactions of the SPWLA 40th Annual, Logging Symposium, Oslo, Norway, May 30-June 3, 1999, paper NNN.

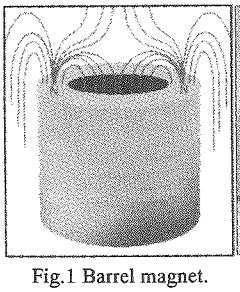

Fig.1 Barrel magnet.

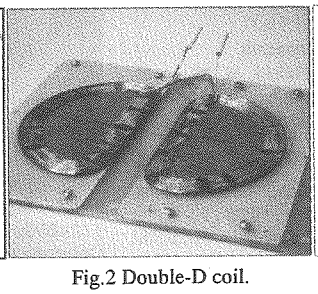

Fig.2 Double-D coil.

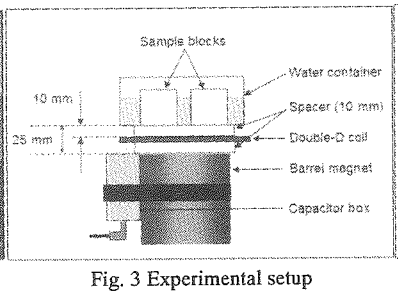

Fig. 3 Experimental setup

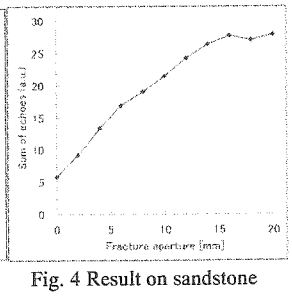

Fig. 4 Result on sandstone

Portable NMRI system for plant study by using a compact permanent magnet

Shin Utsuzawa[1, 2], Kenji Fukuda[3], Daisuke Sakaue[4]

[1]MRTechnology, Inc., Japan, [2]Institute of Applied Physics, University of Tsukuba, Japan
[3]Graduate School of Frontier Sciences, University of Tokyo, Japan
[4]University Forest at Tanashi, University of Tokyo, Japan

Introduction

There have been interests in observing physiological and pathological changes of plants *in situ*. Among many instruments, MRI has been used as a non-destructive and non-invasive way to study water status in plants [1, 2]. Although MR microscopes with super-conducting magnets have sufficiently fine resolution (<100 μm), they cannot accommodate a whole tree with spread branches. Moreover, because such systems require large amount of space and costs, most botanists are unable to use them over long period.

Recently, we showed that a compact MR microscope using a permanent magnet could visualize development of xylem cavitations caused by pine wilt disease [3]. In this poster, we report on a portable MR microscope used for the same purpose with smaller magnet (1/23 of weight). We also show that an open-type permanent magnet makes it easy to apply conventional measurement techniques simultaneously.

Materials and methods

The compact MR microscope used in this study consists of a C-shaped permanent magnet (Neomax Co. Ltd., Japan; 0.3 T field strength, 8 cm air gap, 60 kg weight) and a portable MRI console (MRTechnology, Inc., Japan). A pair of flat gradient coils was fixed onto the pole faces of the magnet, and a pine seedling was placed between them (Fig. 1). Non-destructive observations were conducted with keeping this setup throughout experimental period.

Experiments were performed on 3-year-old Japanese black pine (*Pinus thunbergii Parl*) seedlings in the same way with the previous report [3]. Acoustic emission from the xylem was monitored by an ultrasonic sensor (AE601, NF electronics, Co., Japan) at the same time as MRI measurements. The sensor was fixed on a head of a pushpin that was inserted into the xylem of the main stem. The AE signal was amplified by an AE-Tester (NF-electronics) and counted by a pulse count data logger (LOGBOOK B5-pulse, LOG-Denshi Co., Japan). In addition, leaf water potential was monitored using a pressure chamber (Model 600, PMS Instruments Co., USA) every morning.

Results and discussion

We observed that cavitation area rapidly enlarged and fused together within a few days until the whole xylem area was embolized as we did in the previous report [3]. During this explosive enlargement of embolized areas, AE events occurred frequently and leaf water potential decreased rapidly. Such correlation offers evidence that AE events monitored by ultrasonic transducer correspond to cavitation events in the xylem. This is the first report of a continuous visualization of "runaway embolism" [4] in tree xylem.

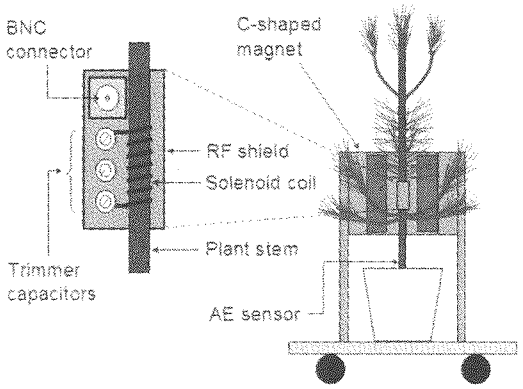

Fig. 1. Experimental setup for pine seedling measurement.

Acknowledgements

The authors thank Professor Katsumi Kose of University of Tsukuba and Dr. Tomoyuki Haishi of MRTechnology, Inc. for their supports in constructing and using the apparatus.

Reference

[1] Kuchenbrod E, Kahler E, Thuermer F, Deichmann R, Zimmermann U, Haase A, Magnetic Resonance Imaging 16 (1998) 331-338.
[2] Van der Weerd L, Claessens MMAE, Ruttink T, Vergeldt FJ, Schaafsma TJ, Van As H, J. Experimental Botany 52 (2001) 2333-2343.
[3] Utsuzawa S, Fukuda K, Sakaue D, Phytopathology 95 (2005) 737-743.
[4] Tyree MT, Sperry JS, Plant Physiology 88 (1988) 574-580.

Development of Compact MRI Systems for Bone Density Measurements

S. Tomiha[1], T. Furuya[1], N. Iita[1], F. Okada[1], K. Kose[1], T. Haishi[2]

1. Institute of Applied Physics, University of Tsukuba, Tsukuba, Ibaraki, Japan

2. MRTechnology, Tsukuba, Ibaraki, Japan

Introduction

A dedicated compact MRI for the calcaneus was developed and demonstrated its usefulness for routine bone measurements [1]. However, several objectives remained to be further developed. The first was to find the optimum of the region of interest (ROI) for bone density measurements in the calcaneus. The second was to reduce the measurement time. In the present study, we performed MRI and QUS measurements for several hundred female volunteers to obtain solutions to the problems described above.

Materials and Methods

Subjects were 416 female volunteers (age range: 16-79 years). After informed consent was received, trabecular bone volume fraction (TBVF) and speed of sound (SOS) was measured for the right calcaneus using the compact MRI and a QUS system. It took about five months to measure all the subjects.

Results

Figure 1 shows a sagittal cross-section of a heel and external reference phantoms acquired with a spin echo sequence (TR/TE = 1200/12 ms, slice thickness: 10 mm, FOV: 12.8 cm × 12.8 cm, image matrix: 128 × 128). Circles 1, 2, and 3 depicted on the calcaneus are circular ROIs with 20 mm diameters (ROI 1, 2, 3). Figure 2 shows a correlation between QUS and TBVF measured in ROI2. The correlation coefficient R^2 was 0.334. The correlation coefficients between QUS and TBVF calculated for these ROI are tabulated in Table 1. From these data, we have concluded that ROI2 is the optimum ROI for our compact MRI, because the correlation coefficients are maximized and the number of applicable subjects is relatively large. Figure 3 shows a histogram of T_2 of bone marrow protons calculated for 394 subjects in ROI2. The mean and standard deviation (SD) of the T_2 was 80.9 and 3.4 ms, respectively. As shown in Fig.3, the T_2 values were concentrated on the narrow range. Figure 4 shows a correlation between TBVF corrected by individual T_2 and that corrected by mean T_2 (80.9 ms). The correlation coefficient R^2 of 0.969 demonstrates that TBVF corrected by individual T_2 can be replaced by TBVF corrected by mean T_2. This result suggests that the spin echo image acquired for T_2 correction (TR/TE = 1200 / 96 ms) may not be needed.

Conclusion

MRI-TBVF and QUS-SOS measurements were performed for 416 female volunteers. As a result, an optimum ROI for TBVF calculation was determined and possibility of 50% measurement time reduction was suggested.

Reference

[1] Kose.K, Matsuda.Y, Kurimoto.T et al. Magn Reson Med 52, 440-444 (2004)

Table 1 Correlation between SOS and TBVF in three ROI locations.

ROI No.	Number of applicable subjects (%)	R^2
1	397 (95.4)	0.282
2	**394 (94.7)**	**0.334**
3	382 (91.8)	0.334

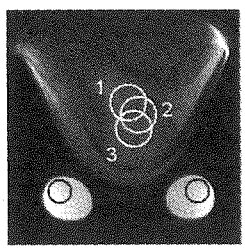

Fig. 1. A 2DSE cross-sectional image of a heel

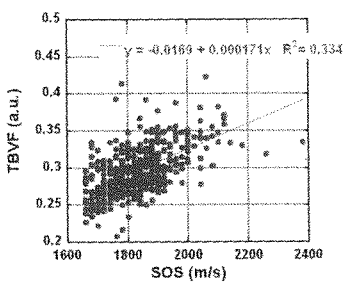

Fig. 2. Relationship between SOS and TBVF in ROI2

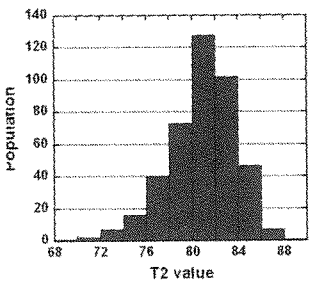

Fig. 3. Histogram of T_2 of bone marrow protons

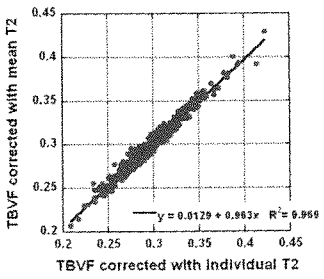

Fig. 4. Relationship between TBVF corrected by individual T_2 and that corrected by mean T_2

Optimized system design and construction of a compact whole hand scanner

S. Handa, S. Tomiha, K. Kose , T. Haishi*
Institute of Applied Physics, University of Tsukuba, Ibaraki 305-8573, Japan
*MR Technology Inc, Tsukuba, Ibaraki 305-8573, Japan

Introduction

It is widely accepted that MRI of hand is very useful for early diagnosis of Rheumatoid Arthritis (RA). However, hand is a difficult part for whole body MRI scanners, because patients must place their hands at the center of the magnets and gradients. To solve this problem, MRI systems with which patients can comfortably have hand MR examinations, are desired. We have already reported a compact hand scanner with installation space of about 6 m^2 and total weight of 1,500 kg [1,2]. In the present study, we have optimized a permanent magnet, gradient coil set, and pulse sequences for a hand and achieved about 4 m^2 installation space, about 700 kg total weight, and examination time of less than 15 minutes, which have enabled the MRI to be used in a small clinic for diagnosis of RA.

Materials and Methods

Figure 1 shows an overview of a compact whole hand scanner and planar gradient coil. The specification of the permanent magnet as follows; magnet field strength: 0.21 T, gap space: 16 cm, homogeneity region: 34.6 ppm over a 20 cm × 12 cm diameter ellipsoidal volume, and weight: 520 Kg. The planar gradient coil set was designed for the ellipsoidal linearity region using the target-field approach[3,4] and a genetic algorithm[5].

A healthy volunteer was imaged using the compact whole hand scanner. Coronal 3D spin-echo T_1-weighted images and a coronal STIR image were obtained with image matrix of 256 × 128 and 20.5 cm square FOV.

Results and Discussion

Figure 2 shows coronal 2D images of a hand selected from 3D image dataset (voxel size 0.8 mm × 1.6 mm × 4 mm) acquired with a 3DSE sequence (TR/TE= 160/13 ms) and a non-slice selective fat-suppressed T_2 weighted image acquired with a STIR sequence (TR/TI/TE= 1400/130/50 ms). As shown in these figures, detailed anatomical structures and inflammatory region are clearly observed. The SNR would be sufficient for early diagnosis of RA using a hand and wrist.

Conclusion

A compact whole hand MRI has been developed using a magnet and gradient coil set of which homogeneous regions were optimized for a hand. This system can be installed even in a small clinic for early diagnosis of RA.

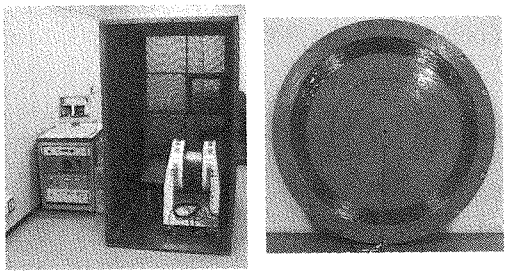

(a) (b)

Fig 1. (a) Overview of a compact whole hand scanner (b) A planar gradient coil set (Gz)

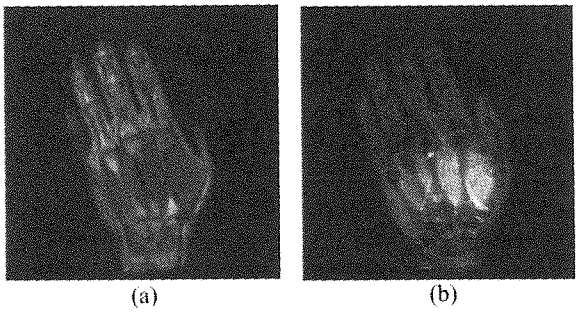

(a) (b)

Fig 2. (a) 2D coronal T_1-weighted image (b) STIR image

References

[1] T. Kurimoto, T. Furuya, S. Tomiha, T. Shirai, Y. Matsuda, T. Haishi, S. Utsuzawa, K. Kose, H. Yoshioka, Compact Hand MRI Systems using Permanent Magnets, 12th ISMRM Proc p1638, 2004.

[2] H. Yosioka, S. Ito, S. Handa, S. Tomiha, K. Kose, T. Haishi, A. Tsutsumi, T. Sumida, "Low field compact magnetic resonance imaging system for the hand and wrist in rheumatoid arthritis", submitted for publication.

[3] Turner R. A target field approach to optimal coil design. J Phys D: Appl Phys 1986;19:147-151.

[4] Jianming Jin: Electromagnetic analysis and design in magnetic resonance imaging, (CRC Press, 1998).

[5] S. Handa, F. Okada, K. Kose, "Effects of magnetic circuits on magnetic field gradients produced by planar gradient coils", 13th ISMRM Proc p851, 2005.

Development of Automatic Generator for Hyperpolarized ^{129}Xe Gas for NMR/MRI Applications

Ryo Tanaka[1], Norio Ohtake[1], Mineyuki Hattori[2], Koji Saito[3],
[1]Toyoko Kagaku Co. Ltd., R&D DEPT., Kawasaki, Kanagawa, 211-8502, JAPAN,
[2]Photonics, AIST, Tsukuba, Ibaraki, 305-8568, JAPAN
[3]Advanced Technology Research Lab., Nippon Steel Corp., Futtsu City, 293-8511, JAPAN

Introduction

The hyperpolarization (Hp) technique can increase the signal sensitivity of nuclear magnetic resonance (NMR) ten thousand times for ^{3}He and ^{129}Xe, and thus it enables instantaneous imaging of cavity gases [1] and various NMR experiments. This technology is expected as practical uses of analysis for industrial material and medical equipment *etc*. However, practical automated devices for the production of the Hp ^{3}He or ^{129}Xe gas have not been developed yet. In this report, we propose the development of the Hp ^{129}Xe gas generator which works under atmospheric pressure and applies a batch method to provide the Hp ^{129}Xe gas stably [2] by utilizing the technologies for a highly pure gas supply, a gas control system, cleanness at the semiconductor production equipment level, and highly accurate pressure control.

Apparatus

Figure 1 shows the developed automatic generator for Hp ^{129}Xe gas and the Pyrex glass pumping cell fabricated to include the rubidium metal. This apparatus is composed of two cylinder storage parts for the Xe - N_2 gas mixture and high-purity N_2 gas for purging the laying pipes, a pressure control part, Hp ^{129}Xe gas formation part and a system control part. This apparatus has mainly five advantages, (1) integration of pumping cell and the part of supply for Xe gas and laser (2) simple operation (3) large cell volume (about 300mL) (4) easily exchange of the pumping cell (5) temperature adjustment of the pumping cell with a jacket heater.

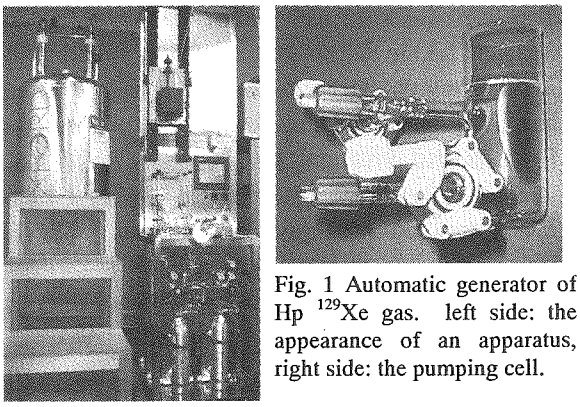

Fig. 1 Automatic generator of Hp ^{129}Xe gas. left side: the appearance of an apparatus, right side: the pumping cell.

Experiments

Hp ^{129}Xe gas was prepared through the developed automatic generator which contacted Rb vapor with Xe gas under the irradiation of laser (wavelength: 794.7±1nm), near the external magnet. The pumping cell was heated to ~413K. The polarized ^{129}Xe gas (10mL) was introduced by plastic syringe into a 10mm-size glass NMR tube. The ^{129}Xe-NMR spectrum was obtained on the JEOL alpha-400 spectrometer of 400MHz.

Results

Figure 2 shows the Hp ^{129}Xe-NMR spectrum and the thermal-^{129}Xe NMR spectrum. Each spectrum was measured 1 accumulation time and about 4,000 accumulation times. We confirmed the signal enhancement about 2,500 times and achieved a 2~3% polarization rate of ^{129}Xe for the Xe (98%)-N_2 (2%) gas mixture. It was confirmed to be able to measure a large amount of sample stably in a short time by using this device.

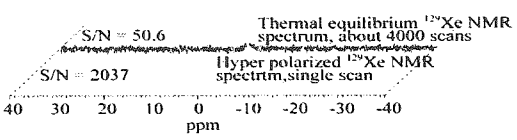

Fig. 2. Polarized ^{129}Xe gas spectrum obtained with (buttom) and without (top) laser polarization. The bottom spectrum reflects a ^{129}Xe NMR signal enhancement of 2500 given at 9.4 T.

Conclusion

We succeeded in the development of the device that uses a batch method to provide the Hp ^{129}Xe gas stably with a sufficient rate of polarization for practical NMR/MRI experiments. This research should facilitate further work on NMR/MRI to shorten the measurement times, to get more detailed information on samples.

References

[1] M. S. Albert, G. D. Cates, B. Driehuys, W. Happer, B. Saam, C. S. Springer Jr., A. Wishnia, Nature **370**, 199-201 (1994).
[2] H. Fujiwara, A. Kimura, Y. Yanagawa, T. Kamiya, M. Hattori, T. Hiraga, Journal of Magnetic Resonance, **150**, 156-160 (2001).

Sensitivity Advantages of Chemical Shift Imaging in Magnetic Resonance Microscopy

Nicole Seiberlich[1], Daniel Haddad[1], Mark Griswold[1], Andrew Webb[2], Peter M. Jakob[1]

[1]Dept. of Experimental Physics 5, University of Würzburg, Würzburg, Germany,
[2]Department of Electrical and Computer Engineering, University of Illinois at Urbana-Champaign, Urbana, USA

Introduction: As the spatial resolution in magnetic resonance microscopy increases, the effects of diffusion on the signal-to-noise (S/N) become more pronounced. When the resolution is on the same order as the mean free path traveled by the spins during encoding, the signal obtained in a typical frequency encoding experiment is highly attenuated due to diffusion. Alternative imaging sequences, such as chemical shift imaging, are not as strongly affected by diffusion [1-3]. This abstract presents a theoretical calculation of the sensitivity, or the S/N per unit time, of both experiment types, as well as an experimental confirmation of the theory.

Methods: For a gradient echo experiment, diffusion-related signal loss occurs during both phase and frequency encoding and is described by a diffusive attenuation factor, $f_{D,GE}$. However, for the CSI experiment, signal is attenuated only during the phase encoding step, resulting in a diffusive attenuation factor, $f_{D,CSI}$. After combining these factors with the standard sensitivity components (Ernst angle amplitude, preparation time effects, voxel volume, signal averaging, Johnson noise, total experiment time [4]), and setting experimental factors such as the T_{exp}, T_R, and excitation angle equal in both experiments, an expression for the relative sensitivity (CSI/GE) can be obtained:

$$\frac{\Psi_{CSI}}{\Psi_{GE}} = \frac{(1-e^{-T_R/T_1})\cdot(1-e^{-T_{AQ,CSI}/T_2^*})\cdot\sqrt{N_x\cdot BW_{CSI}}\cdot f_{D,CSI}}{e^{-T_E/T_2^*}\cdot(1-e^{-T_R/T_1}+2e^{-(T_R-1/2T_E)/T_1}-2e^{-(T_R-3/2T_E)/T_1})\cdot e^{T_{AQ,GE}\cdot as/2\cdot T_2^*}\cdot(1-e^{-T_{AQ,GE}/T_2^*})\cdot\sqrt{N_\delta\cdot BW_{GE}}\cdot f_{D,GE}} \quad (1)$$

Experiments were performed on an 11.7 Tesla system (AMX-500, Bruker, Karlsruhe, Germany), equipped with an imaging gradient system (maximum strength: 660 mT/m). A standard solenoidal microcoil with a diameter of 1 mm and a homogeneous sample of doped H_2O ($D = 2.2 \times 10^{-3}$ mm^2/s) with an inner diameter of 320 μm were employed. For the purpose of illustrating the theory, only symmetric echoes were collected.

Results: As predicted by the theoretical curve shown in Figure 1, CSI has a much higher sensitivity than frequency encoding at high spatial resolution. The experimentally measured values closely follow the theoretical ratio as calculated using Equation 1 (Figure 1). At the highest possible resolution given the gradient system used, 140 phase encoding steps and $\Delta x = 7.4$ μm, the theory predicts that the CSI experiment offers approximately 333 times greater sensitivity than the GE experiment.

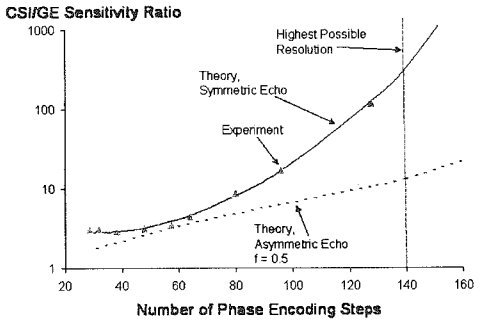

Figure 1: Theoretical and Experimental CSI/GE ratios.

As has been shown by many authors, the sensitivity of frequency-encoded microscopy experiments can be improved significantly by acquiring fractional rather than full-echoes. Figure 1 also shows the theoretical curve corresponding to a half-fractional echo, demonstrating that the CSI sequence still has a much higher sensitivity.

Conclusion: In imaging regimes where the distance traveled by spins during the encoding time is on the same scale as the spatial resolution, a CSI experiment offers significantly higher sensitivity than frequency encoded sequences due to the use of pure phase encoding gradients. Theoretical calculations describing the sensitivity ratio between the CSI and gradient echo experiments have been confirmed by experiments.

References:
[1] Cho, Z.H. et al, *Med. Phys.* **15**, 815-824 (1988)
[2] Ahn, C.B. et al, *Med.Phys.* **16**, 22-28 (1989)
[3] Gravina, S, Cory, D.G., *J. Magn. Reson. Ser. B* **104**, 53 (1994)
[4] Pohmann R, et al, A., *J. Mag. Reson.* **129**, 145-160 (1997)

CO Oxidation over CuO Catalyst Studied by ^{13}C MRI

Yuesheng Cheng[1], Bruce Balcom[1,2]
[1]Department of Chemistry, [2]UNB MRI Centre, Department of Physics, University of New Brunswick, PO Box 4400, Fredericton, NB, Canada E3B 5A3

Nuclear magnetic resonance imaging (MRI) has proven to be a unique experimental method, which has the potential to visualize chemical processes inside opaque reactors and catalyst grains in a non-invasive way under realistic reaction conditions [1]. Complete oxidation of carbon monoxide to carbon dioxide over catalyst is of particular interest in air-purification devices for respiratory protection and pollution control devices for reducing industrial and environmental emission. In CO combustion systems, it is obvious that ^{1}H MRI is not applicable. However, the sensitivity of ^{13}C, ~ 5700 times less than ^{1}H, precludes the application of conventional pure phase encode [2] and frequency encode methods. To overcome the sensitivity challenge, a ^{13}C enriched sample and a centric scan pure phase encode Chemical shift MRI (CSI) technique is utilized.

Centric scan CSI takes advantage of longitudinal saturation effects at the periphery of k-space to permit shorter experimental times and higher signal to noise ratio. A variable TR ensures no longitudinal saturation at the k-space origin, while maintaining a simple T_2 image contrast. Due to the relatively large chemical shift between CO (180 ppm) and CO_2 (125 ppm), ^{13}C chemical shift permits discrimination of CO and CO_2.

Using ^{13}C CSI we performed *in situ* studies of CO and CO_2 density distribution during the combustion inside a reactor. The reaction was assumed to be in spatial and temporal steady states when the MRI signal was accumulated. In our experiments, the ratio of the flow rate between CO and O_2 is controlled at 2:1 and 1:1 by the flow meters for two type of catalytic reactors (the three chamber reactor and single chamber reactor), respectively. We studied how CO combustion was influenced by temperature and gas inlet flow rates. The higher the temperature and slower the flow rate, the more CO was converted to CO_2. The CO_2 intensity distribution in a single chamber reactor was clearly predicted by the first order reaction rate.

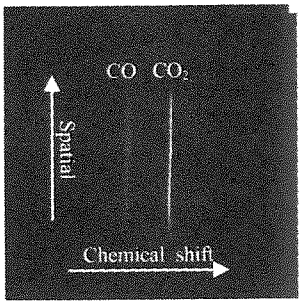

Figure 1. 0.0020 mole CO2 and 0.0022 mole CO were mixed and sealed in a 52mL glass vial.

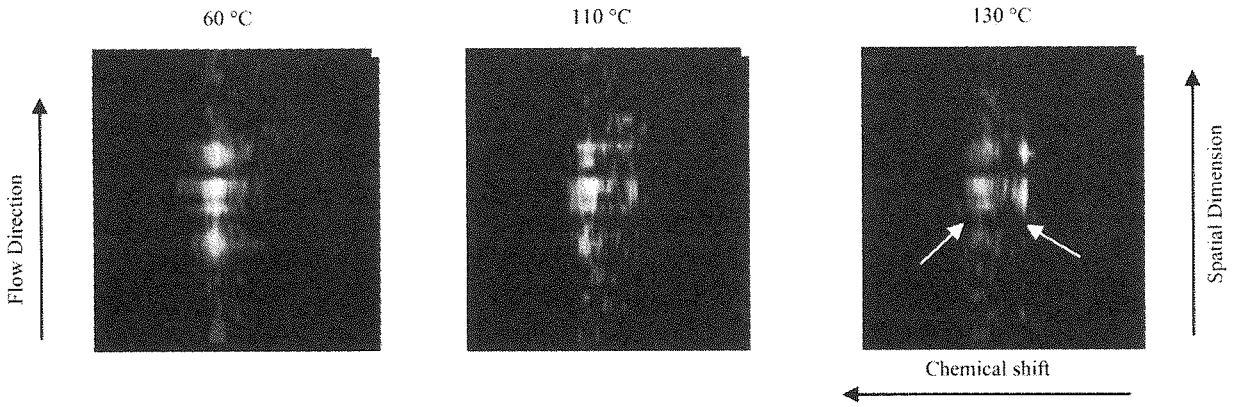

Figure 2. CO combustion in a three chamber reactor. CuO/Al_2O_3 was only in the middle chamber. The CO to O_2 flow rate was is 2:1. CO inlet flow rate was 2.45 ml/min.

References

[1] Koptyug, I.V., et al., Mag. Res. Imag. 21, 337-343 (2003)
[2] Balcom, B.J., et al., J. Mag. Res., 123, 131-134 (1996).

Shaped Pulses in Inhomogeneous Magnetic Fields

C. Coarna, T. J. Marshall, B. Newling
Department of Physics, University of New Brunswick, PO Box 4400, Fredericton, NB E3B 5A3, Canada.

Introduction

A number of materials MR developments require that measurements be made in a highly inhomogeneous magnetic field [1,2,3]. In such cases, *all* RF pulses are slice selective. Typically, little effort is made to tailor the shape of the selected slice, because shaped RF excitations are viewed as too lengthy in duration to be useful in materials MRI, where signal lifetimes are typically less than 1 millisecond. We explore some adaptations of inhomogeneous field imaging methods, which make use of shaped, selective RF pulses.

Methods

The utility of a number of conventional shaped pulses (*inc.* sinc and self-refocused pulse shapes) in the inhomogeneous field of a benchtop profiling magnet (Fig. 1 and [4]) were compared. The permanent gradient is on the order of 15 T/m. A sinc pulse of 25 microseconds therefore excited a slice of about 500 microns. In Fourier-transform style implementations of inhomogeneous field measurements [1], the homogeneity of the slice profile is an important advantage, despite the relatively lengthy pulse duration. In swept-frequency measurements, the reduced out-of-slice excitation (compared to a rectangular pulse) is a significant advantage, especially where slice-overlapping is used to improve spatial resolution [1].

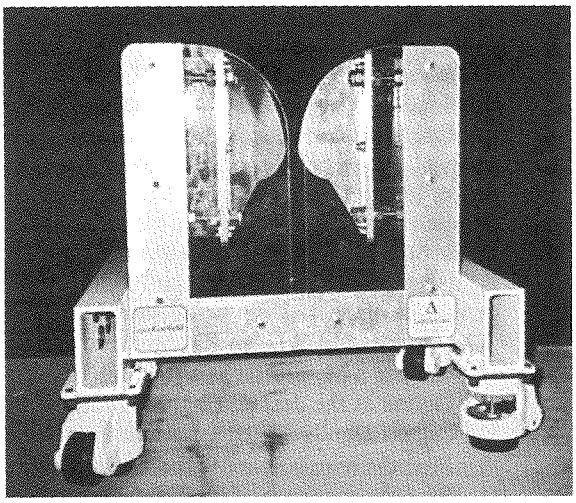

Fig. 1. Benchtop, permanent-gradient profiling magnet.

Results

We will compare measured magnetization responses to various standard shaped pulses and discuss the idiosyncratic difficulties of their implementation in a strongly inhomoheneous field, including the difficulty of choosing optimised pulse area [5].

Conclusions

There are uses for (lengthy) shaped pulses in inhomogeneous fields, in particular where the relaxation times are intermediate between crystalline solids and unconfined liquids (10^{-4}-10^{-2} s, for example). The relatively large pulse duration/bandwidth products of typical shaped pulses do not preclude their use in profiling measurements.

References

[1] McDonald, P. J. *et al. Rep. Prog. Phys.* **61**, 1441-1493 (1998).
[2] Hurlimann, *J. Magn. Reson.* **148**, 367-378 (2001).
[3] Perlo *et al. J. Magn. Reson.* **173**, 254-258 (2005).
[4] Glover *et al. J. Magn. Reson* **139**, 90-97 (1999).
[5] Kinchesh *et al. J. Magn. Reson.* **154**, 252-260 (2002).

Selective excitation pulse design for imaging short-T_2 materials

G.Fagiolo*, D. Rourke, W. Köckenberger
Sir Peter Mansfield Magnetic Resonance Centre, University of Nottingham, Nottingham, UK

Introduction: The problem of designing exact excitation pulses in nuclear magnetic resonance imaging can be successfully solved either by the use of a sequence of equally spaced hard-pulses computed with layer-stripping techniques such as the Shinnar Le Roux (SLR) Algorithm [1], or by the use of soft-pulses obtained with the inverse scattering technique [2]. These methods though neglect any relaxation.
Thus using such sequences in imaging materials with short transverse relaxation time (T_2) and long longitudinal relaxation time (T_1) (such as soft polymers) can produce poor results. In fact when applied to such materials, slice selective pulses computed with the previously mentioned methods result in broader-than-expected slices. We propose a modified SLR algorithm to take into account transverse relaxation for the design of pulse sequences producing the desired longitudinal magnetization (M_z) profile.

Methods: The effect of transverse relaxation cannot be neglected when T_2 is comparable to (or shorter than) the duration of the excitation pulse. The effect of T_2 relaxation on a slice-selective hard-pulse sequence computed with the SLR algorithm is to destroy the desired transverse magnetization (M_{xy}) profile and to broaden the M_z-profile. This loss of M_{xy} (due to fast spin-spin interaction) suggests a possible new way to produce a desired magnetization profile. Instead of designing an excitation pulse that would produce a given M_{xy}-response, it is better to compute a pulse sequence resulting in a desired M_z-profile. A non selective 90 degree hard-pulse is applied immediately after this pulse sequence and a spin-echo reads the so-obtained excited longitudinal profile. This differs from the method allowing for T_2 described in reference [3], where the desired response is specified as the stereographic projection ($M_{xy}/(1+M_z)$). The method we describe here is more suitable with fast T_2, as it results in magnetization being stored on the M_z-axis in a specified manner.
The modified SLR (MSLR) algorithm can be expressed in terms of the following points:

1. Choose a M_z-profile as a function of ω (i.e. frequency offset)
2. Define as the desired final M_z-profile a truncated Fourier Series to order N of the profile in point 1 (N must be sufficiently large to reproduce it with a good approximation)
3. Find the compatible M_{xy}-profile in absence of relaxation ($M_z^2(\omega)+|M_{xy}(\omega)|^2=1$)
4. Find the sequence of hard-pulses that generates it via the SLR algorithm (the result is a sequence of angles (θ_n,ϕ_n), θ_n is the amplitude of the n-th hard-pulse and ϕ_n is its phase)
5. Fix the ratio $R=\tau/T_2$ between the time interval τ between the SLR hard-pulses and T_2
6. Start from initial magnetization M=(0,0,1) and at each time step n, find the angles (θ^R_n,ϕ^R_n) that minimize the L_2-distance between the T_2-renormalized M_z-profile computed with the SLR angles and the M_z-profile evolved with T_2 relaxation and the (θ^R_n,ϕ^R_n) hard-pulse.

Results and conclusions: A 59-hard-pulses slice selective sequence of duration 6.8ms has been computed with the MSLR algorithm, to select a slice of 4kHz, assuming T_2=7ms and an available bandwidth of 50 kHz. Figure (a) shows the T_2-effect on the SLR sequence (thick dashed line) and the T_2-compensation obtained with the MSLR sequence (solid line). Figure (b) shows the measured M_z-profile of a soft polymer sample (*eraser*, T_2=7 ms) using the SLR sequence (dashed line) and the MSLR sequence (solid line). The compensation for the T_2-broadening is evident at the bottom of the slice. The experimental profiles show unexpected side lobes. Further work is in progress to account for this effect.

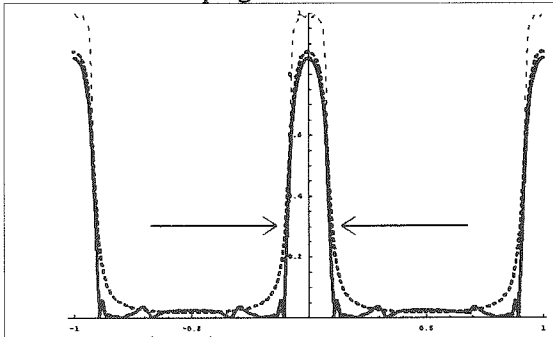

(a) Theoretical $|M_z(\omega)|$: fine dashed line desired profile, dashed line SLR algorithm, solid line MSLR algorithm.

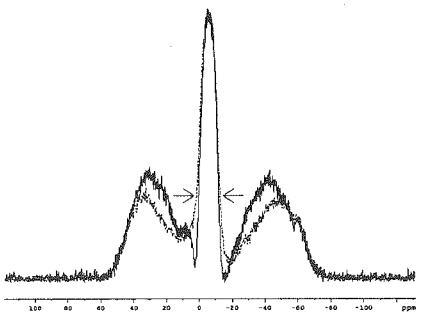

(b) Soft Polymer $|M_z|$-profile: dashed line SLR algorithm, solid line MSLR algorithm.

References: [1] J. Pauly, P.Le Roux, D. Nishimura, IEEE Trans. Med. Imag. 10, 1 (1991), [2] D.E. Rourke, P. Morris, Phys. Rev. A 46, 3631 (1992), [3] D.E. Rourke, L.Khodarinova, A.A. Karabanov, Phs. Rev. Lett.,92,163003 (2004)

*ppxgf@nottingham.ac.uk

Does a k-space span limitation effect MRI resolution?

[a,b]Gregory Stoch, [a]Bruce Balcom

[a]*MRI Center, Department of Physics, University of New Brunswick, P.O. Box 4400, Fredericton, Canada E3B 5A3*

[b]*Department of Magnetic Resonance, Institute of Nuclear Physics PAN, Radzikowskiego 152 Kraków, Poland*

In MRI, the *k*-space is sampled in a limited range during the measurement and the resulting data is Fourier transformed in order to yield a final real space image [1]. A natural question arises. Does the *k*-space span limitation fundamentally affect the image resolution? This question is valid for all reciprocal spaces related through discrete Fourier Transformation. *MRI* is just one example. It is commonly believed [2,3,4] that such a limitation produces an extra *Point Spread Function* (PSF), accounting for the impact of the *k*-space span limitation in image space. This *point spread function* has a width of 1.2 pixels. We have compared this function as obtained for continuous and discrete *k*-space data, separately. We show analytically, that a discrete Fourier Transform, as commonly employed in MRI image reconstruction, does not inherently lead to any image blurring described by a Point Spread Function.

Direct calculation reveals that the *k*-space span limitation, expressed in terms of simple *sinc* function, makes no impact on the discrete data samples in the reciprocal domain. Conclusions drawn from continuous Fourier transform integrals do not automatically apply for discrete data. The conventional sampling PSF width of 1.2 pixels is a prime example of this problem. For discrete spaces the effect of *k*-space span limitation does not exist as a separate phenomenon.

References:

[1] Blümich R. NMR Imaging of Materials. Oxford: Clarendon; 2000. 208 p.

[2] Gravina S.l and Cory D.G. *Sensitivity and Resolution of Constant-Time Imaging, J.Magn.Reson.* Series B 104, 53-61 (1994).

[3] Prado P.J., Balcom B.J., Mastikhin I.V., Cross A.R., Armstrong R.L., Logan A. *Magnetic Resonance Imaging of Gases: A Single Point Ramped Imaging with T_1 Enhancement (SPRITE) Study, J.Magn.Reson.* **137**, 324–332 (1999).

[4] Mastikhin I.V., Mullally H., MacMillan B., Balcom B.J.: *Water Content Profiles with a 1D Centric SPRITE Acquisition*, J..Magn. Reson. **156**, 122–130 (2002)

Development of a projection reconstruction method for a portable MR microscope using a permanent magnet

Nachiko Iita, Katsumi Kose

Institute of Applied Physics, University of Tsukuba, Tsukuba, Japan

INTRODUCTION

By using a yokeless permanent magnet, a compact MR microscope with about 1.0 T field strength can be constructed. Because such a magnet uses Fe-Nd-B material and the temperature coefficient of the residual magnetic flux density of this material is very large (-1100 ppm/deg), it is indispensable to stabilize the magnet temperature and to follow the resonance frequency by an NMR lock technique (1). The NMR lock technique, however, increases the measurement time and the frequency drift between the NMR lock operations cannot be corrected. To solve this problem, we developed a projection reconstruction technique which can correct frequency drift using every projection data.

MATERIALS AND METHODS

We used a portable MR microscope with a yokeless permanent magnet which has 0.983 T magnetic field strength at 30 °C, 40 mm air gap, and 13 mm dsv homogeneous region (Fig.1). The size and weight of the magnet was 28 cm (W) × 24 cm (H) × 18 cm(D) and 85 kg. Although the magnet temperature was regulated to be 30±0.1 °C to stabilize the resonant frequency, temperature drift of about 1 kHz was observed during about one hour of the measurement time. We thus acquired projection data and corrected the resonance frequency deviation by setting the center of the weight of the projection data to the center of back-projection.

RESULTS AND DISCUSSION

Figure 2 shows cross-sectional images (2mm slice thickness, 80 μm^2 pixel) of asparagus (a, b) and myouga (c, d) stems reconstructed from projection data measured using a 2D spin echo sequence (TR=500, 1000ms, TE=15ms) with and without the above correction. These are images obtained from averages of eight images consecutively measured at time intervals of 256 sec (for a and b) and 128 sec (for c and d). As shown in the figure, clear cross-sectional images which have no blurring effect from the drift of the magnetic field were obtained by using the proposed correction method. These images demonstrate usefulness of the proposed method.

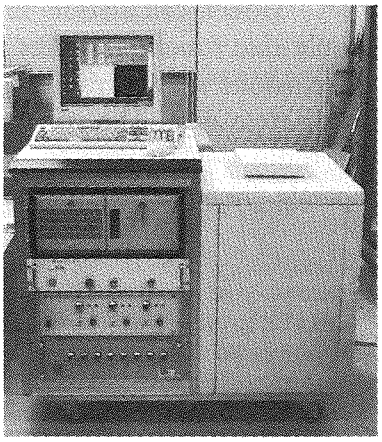

Fig.1 Portable MR microscope using a yokeless permanent magnet

REFERENCES

(1) Haishi T, Uematsu T, Matsuda Y, Kose K. Development of a 1.0 T MR Microscope using a Nd-Fe-B Permanent Magnet. Magn Reson Imag 2001;19:875-880.

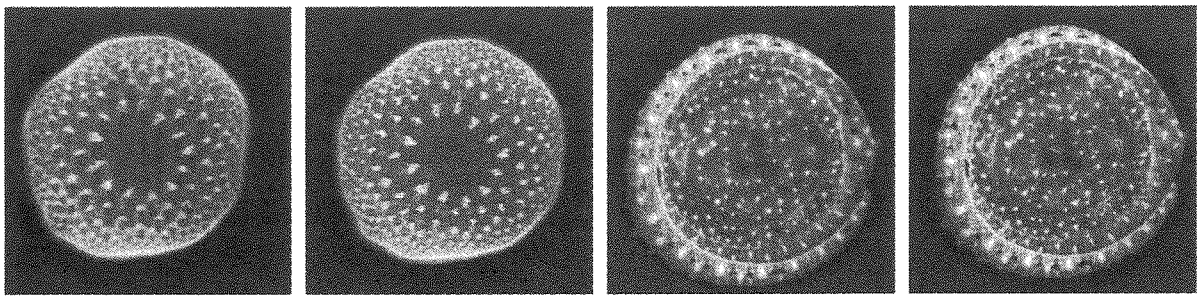

(a) Not corrected (b) Corrected (c) Not corrected (d) Corrected

Fig.2 Cross section of asparagus (a, b) and myoga (c, d). Eight reconstructed images were averaged.

Development of a 3D image distortion correction method

Fumi Okada, Shinya Handa, Katsumi Kose

Institute of Applied Physics, University of Tsukuba, Tsukuba, Japan

INTRODUCTION

Gradient coil design usually permits 5 % linearity error over the field of view (FOV). This design rule, however, produces several pixel-length positional error in the outer area of the FOV, which will produce serious error when geometric quantification is required. To solve this problem, we developed an image distortion correction method which utilized a 3D MR image of a phantom with 3D geometrical landmarks.

MATERIALS AND METHODS

We used a compact MRI system consisted of a permanent magnet (field strength: 0.21 T, gap: 16 cm, homogeneous volume: 20 cm diameter × 12 cm thickness ellipsoid) and a gradient coil set designed with the target field method and a genetic algorithm (1). A 3D phantom was made by putting a plastic object with 3D geometrical landmarks into a square acrylic container and filling it with $MnCl_2$ doped agar gel. The plastic object consisted of eight equally spaced phenol-resin plates with square lattice holes (1.5 mm in diameter) and nylon spacers (8 mm in length) between the plates. The 3D phantom was imaged using a 3D spin echo imaging pulse sequence (voxel size: 1 mm^3, image matrix: 128 × 128 × 256). The reconstructed image dataset was interpolated to a 256 × 256 × 512 voxel image by using a 3D Fourier transform. The interpolated dataset was used as a 3D geometrical reference image.

The image distortion correction was performed as follows: coefficients a, b, c, and d in the equations which described the image distortion, for example $u(x,y) = ax + bxy^2$, $v(x,y) = cy + dx^2y$, were determined using the reference image. In the above equations, (x,y) and (u,v) represent the object (real or undistorted) coordinate and the image (distorted) coordinate. An undistorted image $I(x,y)$ was obtained by equating $I(x,y) = I'(u(x,y),v(x,y))$, where $I'(u,v)$ represent distorted (measured) MR image. 3D image distortion correction was performed as "successive" 2D image distortion corrections in xy, yz, and zx planes.

RESULTS AND DISCUSSION

Figure 1 shows comparison between original (a and c) and corrected images (b and d). A curved plane shown in Fig.1(a) was corrected to a flat plane as shown in Fig.1(b). Large geometrical distortions observed in the outer region of the original images were well corrected. These results demonstrate usefulness of our method.

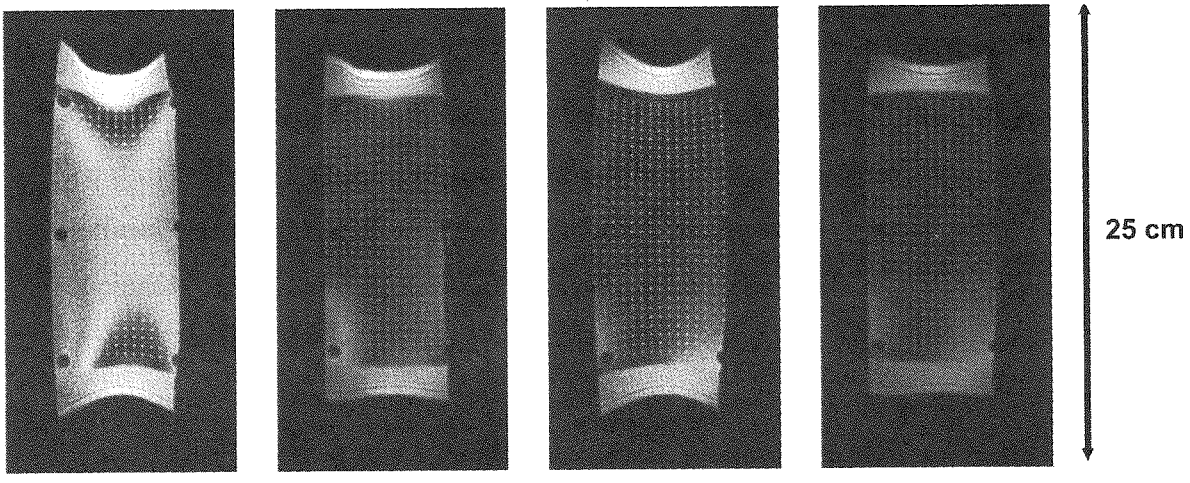

(a) original, y = 0mm (b) corrected, y = 0mm (c) original, y = 27mm (d) corrected, y = 27mm

Fig.1

REFERENCE

(1) S. Handa, F. Okada, K. Kose, Effects of magnetic circuits on magnetic field gradients produced by planar gradient coils, 13th ISMRM Proc. p851 (2005).

PFG-NMR Analysis of W/O/W Emulsions with Inter-Compartment Exchange

Jason P. Hindmarsh*, Jiahong Su, John Flanagan and Harjinder Singh

Riddet Centre, Massey University, Private Bag 11 222, Palmerston North, New Zealand.

* Corresponding Author. Tel.: +64 6 350 5856; Fax: +64 6 350 5655.
E-mail address: j.p.hindmarsh@massey.ac.nz

Abstract

Presented is an application of pulsed field gradient (PFG) NMR techniques to the analysis of W/O/W multiple emulsions with inter-compartment exchange. The methods involve monitoring the diffusional behaviour of different components of the emulsion. An established PFG-NMR model of exchange between two compartments to accommodate spherical inner compartments was adapted to predict the W/O/W emulsion oil membrane permeability, the inner compartment volume fraction and a representation of the inner compartment droplet size distribution. The models were fitted to PFG-NMR experimental data of W/O/W emulsions. Predicted levels of oil droplet swelling were consistent with laser scattering droplet sizing and the predicted oil membrane permeation coefficients were consistent with those reported in literature for similar W/O/W emulsion formulations. The addition of a sugar (sorbitol) to either the inner or outer water compartment of the W/O/W emulsion resulted in an increase in the oil membrane permeability. Inner compartment droplet size distribution measurements indicate that swelling, rupture and coalescence is likely to have occurred during the secondary emulsification and emulsion ripening. Future work will involve verifying the accuracy of predictions and improving the modelling methodology. The method is a novel application of existing PFG-NMR techniques and in its present form still constitutes a fast, non-invasive (no addition of a tracer) and *in situ* method to analyse the relative permeability, stability and yield of different formulations of multiple emulsions with a single PFG-NMR experiment.

Behaviors of ions in liquid electrolytes under the steady direct current measured by multi-nuclear DC-PGSE NMR

Kikuko Hayamizu and Mineyuki Hattori
National Institute of Advanced Industrial Science and Technology
AIST Tsukuba Center 5, Tsukuba, Ibaraki 305-8565, Japan

The translational motions of ions in electrolytes are one of the most important phenomena in the field of electrochemistry. We have reported the self-diffusion coefficients of Li^+, anions and solvents of the solution, gel and polymer electrolytes measured by ^7Li, ^{19}F, ^1H PGSE NMR. The electric current effects on the ion transfer are essential factors to understand the devices such as batteries, capacitors and so on. Here we apply the steady direct current to the solution electrolytes to measure the ion diffusion phenomena.

Experimental method: A special PFG multi nuclear probe with electrodes was supplied by JEOL. The direct current (DC) was varied up to ±3.5V. The maxim PFG was about 1T/m. The temperature was controlled at 30°C. A 10mm sample tube was used with electrodes of the distance 10mm. The solvents used were typical for the lithium batteries, such as propylene carbonate (PC) and diethyl carbonate (DEC) and the lithium salts were $LiBF_4$ or $LiN(SO_2CF_3)_2$. The pulse sequence used is shown in the following. The time intervals t for preparing period of the DC and Δ are the important parameters to study the effects of the DC. The pulse repetition time was set to 30s and initially Δ was set to 50ms.

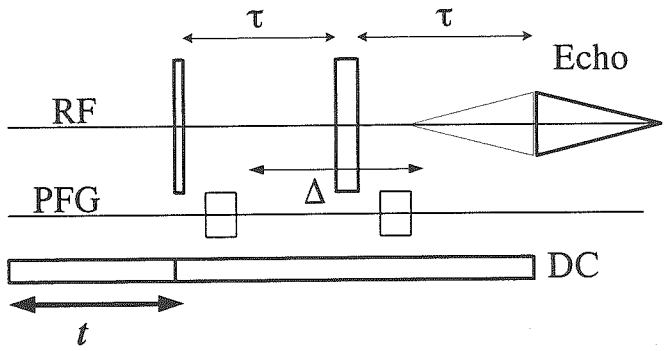

Results and Discussion: The self-diffusion coefficients of Li, anion and solvents without application of the DC always agreed with the values measured by PFG probes without electrodes. We noticed the time interval to approach to equilibrium state under the DC is very long and the measurements were repeated carefully. As the initial process, the diffusion plots of ions varied from straight to curved ones by increasing the preparing period t with hastening the translational motions. After some time interval, the same procedure was repeated and found that the diffusion plots were always straight lines and the apparent diffusion coefficients increased with t being 0 to 500ms and reached to equilibrium state. When the polarity of the DC was inverted, the trends agreed well within the experimental error. Without the DC application, the ions and solvent are known to diffuse freely with the self-diffusion coefficients of the order of $10^{-10}m^2s^{-1}$ and their values are contributed by the isolated and paired ions. Under the DC, the isolated ions are supposed to be accelerated. From the present measurements, the ion diffusion route could be created by the applied DC and electric microstructure remains after the DC was removed.

Membrane Gas Diffusion Measurements with MRI

Ziheng Zhang[1], Alexei V. Ouriadov[1], Chris Willson[2], Bruce J. Balcom[1]
[1]MRI Centre, Department of Physics, University of New Brunswick, Fredericton, New Brunswick, Canada E3B 5A3
[2]ElectraStor, 333 West Street, Pittsfield, MA 01201, USA

Gas transport across polymeric membranes is fundamental to many filtering and separation technologies [1]. To elucidate transport mechanisms, and understand the behaviours of membrane materials, accurate measurement of transport properties is required. This is particularly useful, if the measurement is connected to the material function.

We report a new Magnetic Resonance Imaging (MRI) methodology to measure membrane gas phase diffusion coefficients. The MRI challenges of low spin density and short gas phase relaxation times, especially for hydrogen gas, have been successfully overcome with a modified one-dimensional, Single-Point Ramped Imaging with T_1 Enhancement, (SPRITE) measurement [2-3].

This new diffusion measurement combines the diaphragm-cell diffusion measurement [4] with MRI methods. The experimental apparatus is a modified one-dimensional diaphragm cell which permits measurement of the diffusion coefficient in experimental times of less than one minute. Two kinds of sample gas, hydrogen and sulfur hexafluoride are selected. The polymeric membrane was, FAS-300, used as a gas separator in metal hydride batteries. The H_2 gas diffusion coefficient was 0.54 ± 0.01 mm^2/sec, while that of sulfur hexafluoride was 0.13 ± 0.01 mm^2/sec, at ambient conditions.

(A) (B) (C)

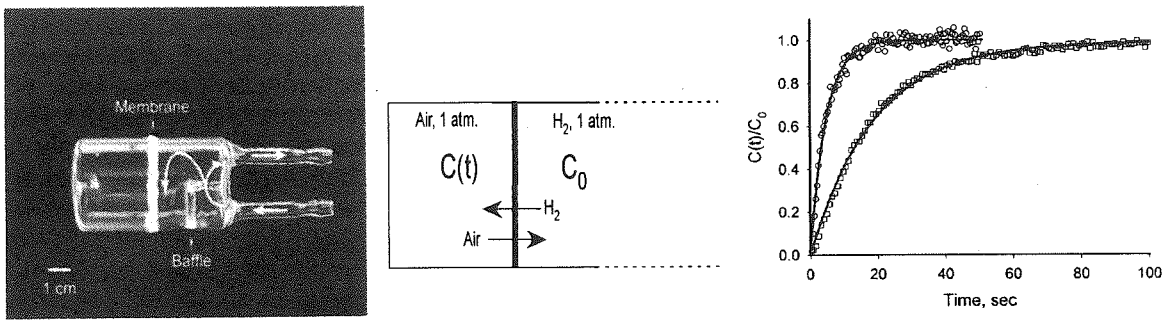

Figure A. Schematic of the diaphragm cell apparatus. One glass chamber was cut into two parts and epoxied back together with the sample membrane in between. "Left" and "right" chambers are separated by the membrane. A small glass baffle deflected the input gas stream. The entire chamber was 6.2 cm in length and 3.5 cm in diameter. The film was 0.09 mm thick.

Figure B. Schematic diagrams illustrating the boundary conditions corresponding to diffusion into the left chamber from a constant concentration reservoir. The thick vertical line is the FAS-300 membrane.

Figure C. The Diaphragm-Cell result for H_2 and SF_6 diffusion into the left chamber. Experimental data is fit to Eq.5. The symbols (○) represent the ratio, $C(t)/C_0$, for a hydrogen gas experiment. The average diffusion coefficient was 0.54±0.01 mm^2/s. Symbols (□) correspond to the same experiment and apparatus, but for sulfur hexafluoride gas diffusion. The average diffusion coefficient was 0.14±0.01 mm^2/s.

[1]. R. Rautenbach, R. Albrecht, Membrane Processes, John Wiley & Sons Ltd., 1989.
[2]. Balcom, B.J., et al., J. Mag. Res., 123, 131-134 (1996).
[3]. I. V. Mastikhin, H. M., et al., J. Mag. Res. 156, 122-130 (2002).
[4]. E. L. Cussler, Diffusion: Mass Transfer in Fluid System, Cambridge University Press, 1984.

Detecting microscopic anisotropy in gray matter and in a tissue phantom using d-PGSE

M.E. Komlosh[1], R. Z. Freidlin[2], F. Horkay[1], Y. Assaf[3,4], P. J. Basser[1]

1. Section of Tissue Biophysics and Biomimetics, NICHD, NIH, Bethesda, MD 20892 USA. 2. CBEL, CIT, NIH. 3. Department of Neurobiochemistry, Faculty of Life Sciences, Tel Aviv University, 69978, Israel. 4. Levie-Edersheim-Gitter Institute for Functional Brain Imaging, Tel Aviv Sourasky Medical Center.

Introduction: Diffusion weighted imaging is commonly used to characterize brain pathology[1]. MR Diffusion measurements in gray and white matter reveal significant differences in their structure. While white matter typically show some degree of anisotropy, gray matter appears isotropic. White matter consists of highly ordered bundles at the molecular, microscopic and macroscopic scales, which explains the diffusion anisotropy measured at the macroscopic voxel length scale. Gray matter consists of oriented axonal projections and dendritic fibers at the microscopic scale, which are randomly oriented at the macroscopic voxel length scale. Thus, the apparent diffusion coefficient measured using a PGSE[2] sequence appears isotropic in gray matter at the resolution of MRI. In this study, we used the double PGSE[3,4] (d-PGSE) sequence (Fig. 1) to attempt to detect microscopic anisotropy in gray matter, and in a gray matter phantom.

Materials and Methods: PGSE and d-PGSE acquisitions were calibrated using isotropic standard solution (5 Centistokes PDMS). No observable artifacts were noted. A gray matter phantom was constructed consisting of an ensemble of randomly oriented 0.5mm long borosilicate glass tubes, with an inner diameter (ID) of 20μm and an outer diameter (OD) of 90 μm. The tubes are filled with water and immersed in deuterated dichloro-benzene. Both sequences were also used to interrogate a biological sample cortical gray matter obtained from a formalin fixed rhesus monkey brain.

Results and Discussion: Figures 2a and b show the d-PGSE signal attenuation for phantom and the cortical tissue, respectively. There is a significant difference in the attenuation profiles between the data obtained for diffusion gradients applied only along one of three co-linear directions (i.e., x-x, y-y and z-z) and data obtained for gradients applied along the six combinations of orthogonal directions (i.e., x-y, x-z, y-x, y-z, z-x, z-y). In a microscopically isotropic medium like PDMS, all nine curves overlap. However, in a microscopically anisotropic but macroscopically isotropic medium, one expects these two sets of curves to diverge as q increases. Cheng *et al.* [4] observed this divergence occurred at attenuations less than 1 part in 10^3. In light of this, the observation of this affect at much larger attenuations is remarkable. Moreover, the ability to detect this effect using low strength gradient suggests the possibility of biological and clinical applications. Currently we are in the process of modeling the spin dynamics in the tissue phantom. A 3-d Gaussian displacement distribution adequately describes the observed d-PGSE attenuation only at low q and short Δ (Fig 3). To describe the d-PGSE decay, we are planning to incorporate the effects of restriction and other relaxation mechanisms in our model.

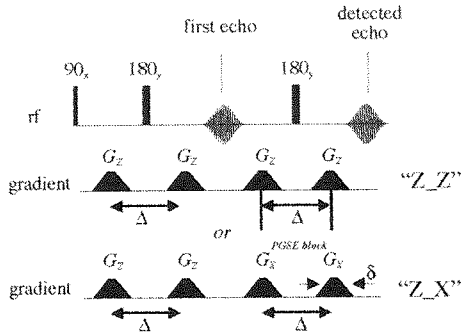

Figure 1: Double PGSE pulse sequence

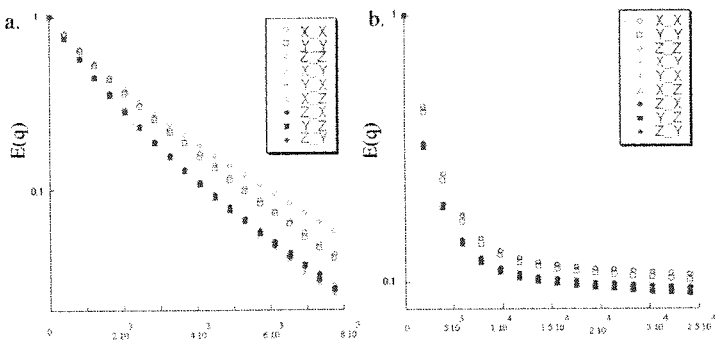

Figure 2: double-PGSE echo attenuation *vs.* $q=(1/2\pi)\gamma\delta G$ for: a) phantom. $G=300$ mTm^{-1}, $\Delta=110$ ms and $\delta=3$ ms. b) Rhesus monkey cortical tissue. $G=400$ mTm^{-1}, $\Delta=75$ ms and $\delta=6$ ms.

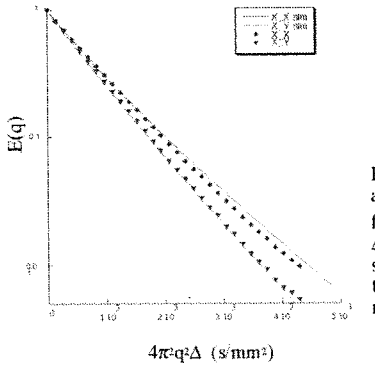

Figure 3: double-PGSE echo attenuation *vs.* $q=(1\ 2\pi)\gamma\delta G$ for: phantom. $G=300$ mTm^{-1}, $\Delta=15$ ms and $\delta=5$ ms. Blue squares and red triangles represent the experimental data. Solid lines represent the corresponding simulations.

References:

1. D. Le Bihan,. *et al. JMRI*, **13**, 534, (2001)
2. E. O. Stejskal, J. E. Tanner, *J. Chem. Phys.* **42**, 288, (1965)
3. P. T. Callaghan, *et al. Magn. Reson. Chem.* **40**, S15 (2002)
4. Y. Cheng, D. G. Cory *J. Am. Chem. Soc.* **121**, 7935 (1999)

In situ MRI Measurement of Conversion and Selectivity within a Three-Phase Trickle-Bed Reactor

Andrew J. Sederman, Michael D. Mantle, Christopher P. Dunckley,
Zhenyu Huang and Lynn F. Gladden
Department of Chemical Engineering, University of Cambridge, Pembroke Street,
Cambridge CB2 3RA, UK

Introduction

^{13}C DEPT-MRI is used to provide the first spatial mapping of alkene isomerisation and hydrogenation during an alkene hydrogenation reaction occurring within a trickle-bed reactor. The reaction of gas and liquid over solid catalyst particles in trickle beds such as this is of fundamental importance to a wide number of manufacturing processes including hydrocarbon processing, chemical and pharmaceutical manufacture, and the removal of pollutants generated by industry. However these reactors remain poorly understood and difficult to design due to the complicated coupling of hydrodynamics, mass-transport and reaction kinetics that they present. The poor understanding of multi-phase reactions means that many of the models used to predict trickle bed performance often fail to deliver sufficient accuracy.

Methods

The implementation of a pulse sequence combining the spatial resolution of a magnetic resonance imaging sequence with a ^{13}C DEPT magnetic resonance spectroscopy pulse sequence enables spatially resolved ^{13}C spectra to be recorded of natural abundance ^{13}C species – a necessity in these continuous flow reactors. The major problem associated with ^{1}H magnetic resonance techniques, when applied to heterogeneous catalysis, is that the large magnetic susceptibility differences between the different gas/solid/liquid phases make the ^{1}H spectra un-assignable due to spectral overlap. This problem may be overcome by utilising the greater chemical shift range of nuclei such as ^{13}C. Here, observation of the ^{13}C nucleus provides spectra from which direct identification of the products of isomerisation and hydrogenation are made. This technique is illustrated with respect to the hydrogenation of 1-octene over a precious metal/alumina catalyst. Images of local species concentration are acquired in 9 minutes while the reactor is operating in continuous flow mode.

Results and Discussion

Preliminary results show that MRI can detect local differences in octene conversion and degree of isomerisation through the bed. In addition, we have coupled these results with ^{1}H imaging of the liquid distribution during reaction to show how the liquid flow field is re-distributed during hydrogenation and as a function of reactant flow rates. We also demonstrate the ability of this technique to identify the effect of changing the hydrogen flow rate on the evolution of isomerisation and hydrogenation processes occurring along the length of the bed. Figure 1 shows a) a ^{1}H image of liquid distribution during reaction - the upper and lower bounds of the catalyst bed are indicated by the white lines; and b) a plot of the product distribution as a function of position along the length of the bed. Evaporation of the liquid at the top of the catalyst packing due to the exothermic reaction occurring is identified by the zero intensity pixels in a). This effect is seen as an apparent loss in the total amount of species present towards the top of the bed in b).

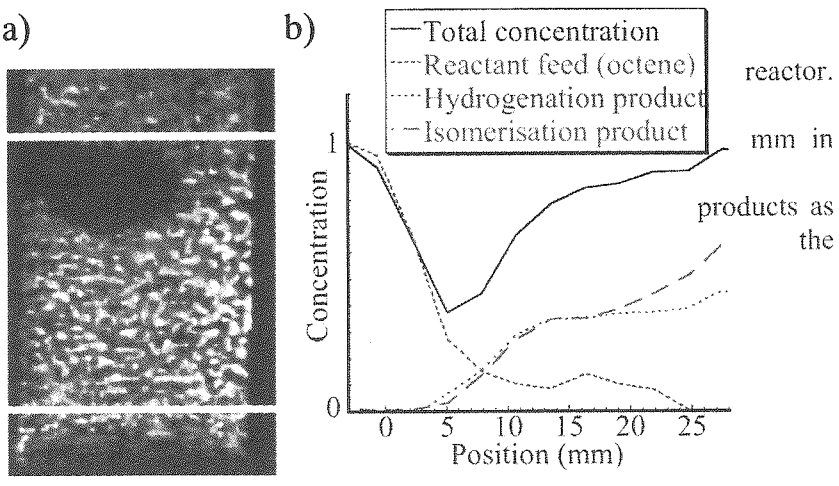

Figure 1
a) Liquid distribution in reactor. The upper white line corresponds to position 0 mm in b).
b) Concentration of feed and products as a function of position along length of the bed.

MR Measurement of the Impact of Column Walls on the Dispersion Time Dependence of Flow in a Cylindrical Bead Pack

Justin P. Gage[1], Joseph D. Seymour[1], Robert S. Maier[2], Sarah L. Codd[1] and H. Ted Davis[3]
[1]Department of Chemical and Biological Engineering, Montana State University, Bozeman, MT USA. [2]U.S.A.C.E Engineer Research and Development Center, Vicksburg, MS, USA. [3]Department of Chemical Engineering and Materials Science, University of Minnesota, Minneapolis, MN USA.

The time dependence of the approach to asymptotic dispersion for flow in cylindrical bead packs is of importance in designing tubular reactors and chromatographic columns and in understanding the applicability of laboratory column experiments to transport in natural granular media like soils and rock. Lattice Boltzmann (L-B) simulations of the longitudinal dispersion in cylindrical bead packs indicate strong dependence of both the time to reach asymptotic behavior and the amplitude of the dispersion coefficient on the ratio of column to particle diameter [1]. The time dependence of the dispersion coefficient is measured using PGSE in order to directly compare with the L-B simulations. The ability to apply volume excitation to spins in the interior of the flow in MR experiments provides the means to probe the bulk dispersion and compare to the dispersion including spins in the wall region. The preasymptotic behavior of the propagator is also studied to provide further insight into the dynamics leading to the observed dispersion behavior.

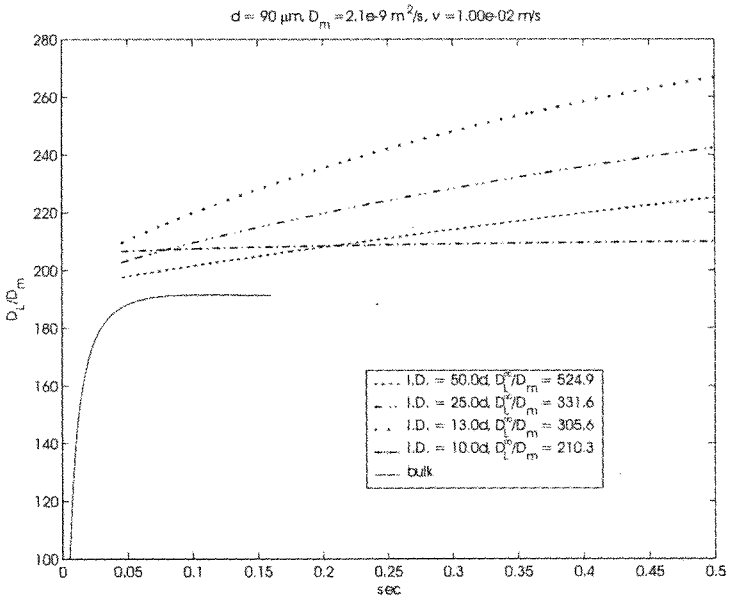

Figure 1. Lattice Boltzmann simulations of the time dependent longitudinal dispersion coefficient for water flow at 10 mm/s through a cylindrical bead pack of 90 μm beads in cylinders of varying internal diameter, 10, 13, 25 and 50 particle diameters. The bulk simulation is for a region of random packed spheres not impacted by wall induced packing heterogeneity.

[1] Maier, R.S., Kroll, D.M. *et al.* Enhanced Dispersion in Cylindrical Packed Beds. *Philosophical Transactions of the Royal Society of London A*, **360** 1-10 (2002).

A Fast-Switching, Large-Volume Gradient Set for Imaging Fast Flows

C. C. Poirier[2], B. Colpitts[2], B. Newling[1]
Departments of Physics[1] and Electrical & Computer Engineering[2], University of New Brunswick, PO Box 4400, Fredericton, NB E3B 5A3, Canada.

Introduction

We have recently introduced [1] a new, motion-sensitised, single-point imaging (SPRITE) technique to measure gas flow in a wind-tunnel type setting at Reynolds numbers in excess of 200 000 and speeds greater than 10 m/s. The principal advantage of the method lies in the short encoding time (t_P Fig .1), which permits the measurement of fast flows in fluids with short signal lifetimes. However, the short encoding time also requires that the magnetic field gradient be rapidly switchable. The current implementation of the technique relies upon a calibration measurement to correct for imperfect gradient switching. Realising that the method is far more reliant upon rapid gradient switching than it is upon gradient amplitude, we have designed a purpose-built, minimum-inductance gradient set. The design trades off gradient amplitude for rapid switching, despite a bore size of 12 cm.

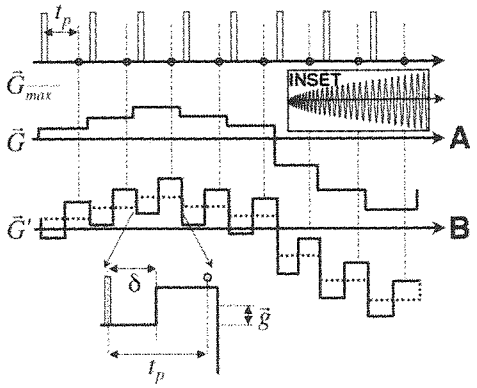

Fig. 1. Centric SPRITE pulse sequence (A) and the motion-sensitised adaptation (B).

Methods

The target-field gradient design approach of Turner [2] and Bowtell [3] was employed to design a three-axis set of distributed windings with minimized inductance. The maximum gradient amplitude of 5 G/cm is more than sufficient in motion sensitising metre-per-second flows.

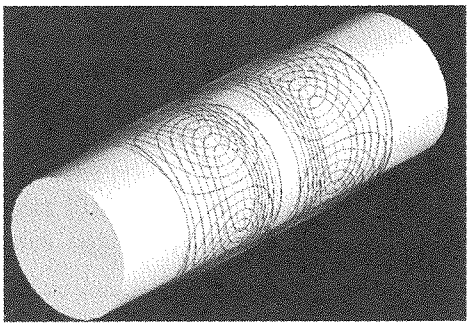

Fig. 2. *XYZ*, minimum inductance gradient design.

Results

We will compare calculated and measured gradient fields and improvements in rise-time over our more conventional gradient sets. The advantages of the rise-time improvements in the measurement of fast fluid flows will be demonstrated.

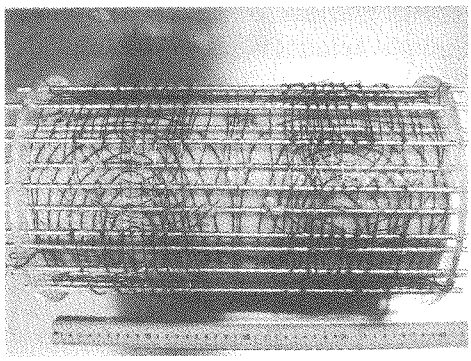

Conclusions

Specialised MR measurements do, on occasion, permit the use of specialised hardware, which may not be subject to quite the constraints of the equivalent apparatus designed for general performance. This has proven to be the case in the design of a low-inductance, low-gradient-efficiency (G/cm/A) three-axis gradient set for an application in which the most stringent requirement is in rapid switching.

References

[1] Newling, B. *et al. Phys. Rev. Lett.* **93**, 154503 (2004).
[2] Turner, *Magn. Reson. Imag.* **11**, 903-920 (1993).
[3] Bowtell, R. *et al., J. Magn. Reson.*. **131**, 286-294 (1998).

NMR Imaging study of flow behaviour of fluids viscosified by polymers

G. Maddinelli*, S. Carminati* and A. Guarneri±
*EniTecnologie S.p.A., via F. Maritano 26, 20097, S. Donato, Milan, Italy
±Eni S.p.A., Division E&P, S. Donato, Milan, Italy

NMR imaging techniques are becoming very useful for understanding complex flow dynamics involved in engineering problems. One the most promising applications are certainly velocity measurements methods based on the combination of pulsed field gradients spin-echo (PGSE) and imaging experiments[1]. This type of technique has been applied to investigate complex fluid dynamics tests[2], especially in the presence of geometrical constraints. The application of MRI to flow dynamic studies could be particularly useful in understanding some of the operations involved in oil production and drilling technology. In fact, MRI has a great potential in discriminating oil/water mixtures even in optically opaque media and also in measuring velocity profiles over a wide range of values avoiding interference with the flowing system. This feature makes MRI more attractive than other conventional techniques (e.g. ultrasound and laser Doppler methods). In this application, aimed to simulate drilling and production operations, we have assembled a 9 and 13 mm (I.D.) flow loop lines inside a 2 T, 31 cm horizontal-bore magnet. Flow was assured in a velocity range of 10-100 cm/sec. The studies were dedicated to investigation of the fluid rheology on the flow properties (Fig. 1). Viscous fluids with different concentration of Xanthan gum polymers (0.3-0.5 % in water, w/w), were adopted and consistent effects on flow regime were observed. In fact, restrictions or geometrical features introduced in the flow line to simulate drilling tools modified considerably the flow dynamics, giving rise to severe turbulence which could affect the process efficiency. FLASH imaging and double PGSE based techniques[3] were also applied to evaluate transient phenomena and fluctuations induced in the flow line at high flow rates. Early transitions from laminar to turbulent regime were observed even at very low Reynolds number (Re comprised between 300 and 500 compared to the theoretical transition value Re ~ 2300) indicating that when solutions viscosified with macromolecules are employed, flow dynamics can become very complex. This behaviour is reasonably related to the elastic properties of the large polymer molecules and their conformation under flow conditions. The results obtained are discussed and compared to the rheological and structural properties of the polymer. This type of NMR based simulations adopted was found very useful as an aid to evaluate conditions leading to the transition from laminar to turbulent regime.

Fig. 1 Experimental velocity profiles at different Reynolds Numbers

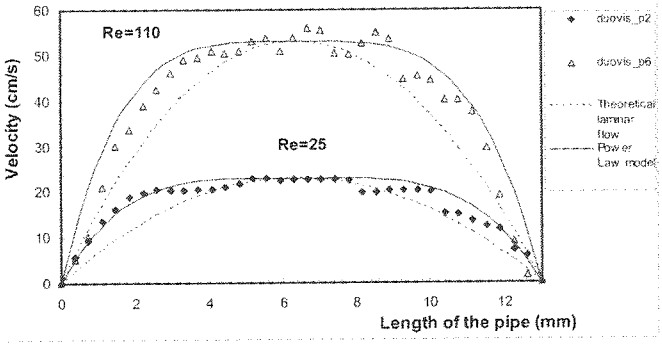

References

1. Callaghan P.T., Eccles C.D. and Xia Y. J. Phys. Sci. Instrum. 21, 820-822, 1988;
2. Xia Y., Callaghan P.T. J. of Magn. Res. 164, 365-368, 2003;
3. Callaghan P.T., Codd S.L., Seymour J.D. Concepts in Magn. Resonance,11, 181-202, 1999.

Magnetic resonance microscopy analysis of advective transport in a biofilm reactor

Sarah L. Codd, Erica J. Gjersing, Joseph D. Seymour, Philip S. Stewart and Kathryn O. Hoyt
Department of Chemical and Biological Engineering
and Center for Biofilm Engineering,
Montana State University, Bozeman, MT, USA

Magnetic resonance microscopy (MRM) has been used to characterize the advective transport in a biofilm capillary reactor [1, 2]. The biofilm generates non-axial flows that are up to 20% of the maximum axial velocity. The presence of secondary velocities of this magnitude alters the mass transport in the bioreactor relative to non biofilm fouled reactors and questions the applicability of empirical mass transfer coefficient approaches. The data will be discussed in the context of simulations and models of biofilm transport and conceptual aspects of transport modeling in complex flows will be discussed. The variation in the residence time distribution due to biofilm growth can be calculated from the measured propagator of the motion. Dynamical systems methods applied to model fluid mixing in complex flows are indicated as a template for extending mass transport theory to quantitatively incorporate microscale data on the advection field into macroscale mass transfer models.

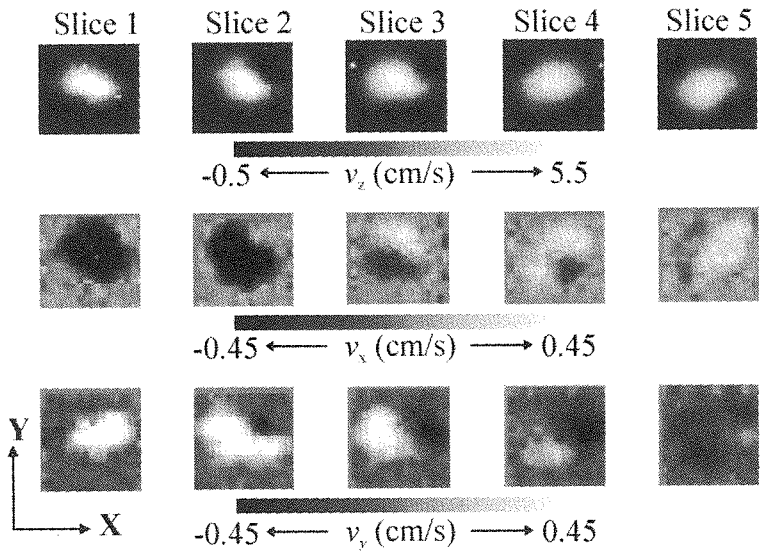

Figure 1. These images display the three components of velocity in five consecutive slices through the transverse cross section of the capillary. The direction of bulk flow is from slice 1 to 5 with each slice 300 μm thick and contiguous, positive axial velocity, white, out of the page. A negative (black) x-component represents flow to the left while a positive (white) x-component represents flow to the right. A negative (black) y-component represents flow down the page while a positive (white) y-component represents flow up the page. The oscillatory nature of the flow is clear with non-axial flow changing directions through the sequence of slices and going through a coherent clock-wise vortex flow in slice 3.

[1] Gjersing, E. L., Codd, S. L., Seymour, J. D.et al. *Biotechnology and Bioengineering* **89**. 822-834 (2005).
[2] Seymour, J. D., Codd, S. L., Gjersing, E. L.et al. *Journal of Magnetic Resonance* **167**. (2004).

NMR Determined Velocity and Hematocrit Profiles in a Couette Viscometer

Jennifer R. Brown, Sarah L. Codd, Giles R. Cokelet and Joseph D. Seymour
Department of Chemical and Biological Engineering,
Montana State University-Bozeman, MT USA.

Couette viscometer studies where torque is measured have suggested that when blood is exposed to a low shear rate, erythrocytes (red blood cells) aggregate and move away from the walls. Understanding erythrocyte migration away from vessel walls is useful for identifying physiological transport mechanisms, designing filtration devices[1] and designing microfluidic based sensors for blood[2]. A Rheo-NMR couette device with an inner rotating cylinder and fluid gap of 1.05 mm was used to steadily shear three chemically different red blood cell (RBC) suspensions. Velocity profiles as a function of radial position across the fluid gap were obtained and the derivative of polynomials fitted to these measured velocity profiles gave shear rates at each radial point. In an iterative calculation scheme using the Quemada equation[3], $\eta_r = \frac{\eta_a}{\eta_o} = (1 - 0.5kH)^{-2}$, and assuming a constant torque, $T = 2\pi r^2 \eta_{app} \dot{\gamma}$, across the gap; the radial hematocrit distribution, or volume fraction of RBCs in suspension, was calculated at all radial points. The following figure shows velocity profiles and corresponding hematocrit distribution profiles for the three RBC suspensions which are listed here in order of increasing RBC aggregation: RBCs suspended in isotonic, phosphate-buffered saline containing 0.5% albumin (filled squares); RBCs in plasma (open triangles); and RBCs suspended in plasma which had 1.48% by weight Dextran 110 added (filled diamonds). The RBC aggregation generates differing RBC concentration distributions resulting in spatially dependent rheological behavior.

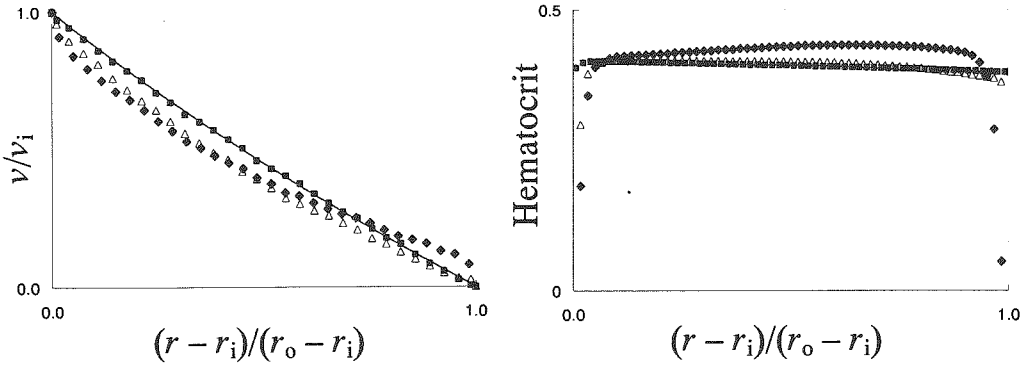

It was possible, with Magnetic Resonance Microscopy Methods, to use measured velocity data to map the hematocrit distribution as a function of location across the gap for the first time, as well as confirm the presence of a plasma layer at both the rotating and stationary wall of the couette which becomes larger as the tendency for RBCs to aggregate is increased.

[1] R. F. Probstein. *Physicochemical Hydrodynamics*, Butterworth -Heinemann, Stoneham, MA (1989).
[2] D. W. Inglis, R. Riehn, R. H. Austin and J. C. Sturm. Continuous Microfluidic Immunomagnetic Cell Separation. Applied Physics Letters, 85 (2004): 5093-5095
[3] D. Quemada. Rheology of Concentrated Dispersed Systems, Ii: A Model for Non-Newtonian Shear Viscosity in Steady Flows. Rheologica Acta, 17 (1978): 632-642

Dynamics in gas-fluidized granular systems by NMR velocity imaging

Silke Harms, Siegfried Stapf, Bernhard Blümich

Institute for Technical Chemistry and Macromolecular Chemistry, RWTH Aachen University, Worringerweg 1, 52074 Aachen, Germany

Granular materials are a class of systems of widespread interest, touching fields as diverse as food and pharmaceutical production processes, storage and packing of agricultural products, waste disposal and recycling, or powder technology; but also natural phenomena of equal economic importance such as avalanches, sand transport by wind or water, and sedimentation. Despite the impression of chaotic dynamics, granular particles experience the same physical forces like any other moving object, in particular gravity, friction and interparticle forces. They undergo the equivalent of phase transitions such as fluidization and evaporation. As such, they are of interest both from a theoretical point of view, as well as with the eventual motivation of understanding and improving reactor efficiency in applications such as coal combustion, heat exchange, drying, and catalytically controlled reactions.

The access to granular media, however, is limited to optically transparent systems, and a spatially resolved investigation of a three-dimensional granular bed requires a non-optical technique such as MRI which relies on a liquid-like component that gives rise to an NMR signal of sufficient lifetime. Liquid-filled pellets or natural seeds thus are suitable materials for investigating the motional parameters in arrays of granular matter. Granular matter in rotating drums[1], Couette cells[2], or shaken and vibrated beds[3,4] were among those geometries investigated by PFG NMR[5]. More recently, gas-fluidized beds were considered with respect to their solid[6] and gas phase[7] dynamics. A systematic study of the spatially resolved dynamics in fluidized beds has not been reported so far.

In this work, a combination of PFG-NMR imaging and velocity encoding methods were applied to investigate the dynamic behavior of a bed of poppy seeds subject to air flow, representing a model setup for fluidized bed reactors. The particle motion is described both from a statistical point of view, by determining propagators and dispersion coefficients representing an average over the whole bed volume, as well as combined with spatial resolution by generating velocity maps. The system under study is classified as a Geldart group D granular medium, which is often found to feature a behavior called spouted bed, being characterized by a pronounced upward motion following the air stream in the center of the bed. A qualitative agreement with predictions from the literature is found: velocity images of different horizontal slices in the bed confirm the notion of a toroidal particle flow pattern inside the shallow granular bed. Quantitative velocity images and statistical information about the random particle motion was obtained from monitoring the fluid component in the seeds by conventional spin-echo techniques.

[1] Nakagawa, M., Altobelli, S.A., Caprihan, A. et al., *Exp. Fluids* **16**, 54 (1993).
[2] Mueth, D.M., *Phys. Rev. E* **67**, 011304 (2003).
[3] Knight, J.B., Ehrichs, E.E. Kuperman, V.Yu. et al., *Phys. Rev. E* **54**, 5726 (1996).
[4] Yang, X.Y., Huan, C., Candela, D. et al., *Phys. Rev. Lett.* **88**, 044301 (2002).
[5] Fukushima, E., *Adv. Complex Systems* **4**, 503 (2001).
[6] Savelsberg, R., Demco, D.E., Blümich, B. et al., *Phys. Rev. E* **65**, 020301 (2002).
[7] Wang, R., Rosen, D.S., Candela, D. et al., *Magn. Reson. Imaging* **23**, 203 (2005).

Convection Flow Imaging by Dynamical MR Microscopy

Urša Mikac, Jasna Urbanija and Igor Serša

Jo ef Stefan Institute, Jamova 39, 1000 Ljubljana, Slovenia

Convection is a result of buoyancy forces caused by usually decreased liquid or gas density above a heath source. The liquid upraises above the heater and cools down in higher layers or when it reaches container walls. If the heater is heated with a constant and low power then the convection flow becomes stationary and laminar after a short transition time after turning the heater on. However, if the heater power is not constant the flow is laminar and unstationary and if the power is high the flow may change into fully developed turbulent flow. Convection flow of liquids and gases is often a challenging technological problem that can be successfully numerically solved for simple cases by solving Navier Stokes like flow equations, i.e., when flow is stationary and laminar. For other more complex convection flow conditions it is much harder to get reliable numerical simulation results and a direct measurement of the flow is highly desirable. We have developed an imaging method that can be used for measurement of slow (1 mm/s) laminar unstationary convection flow in water. The method is based on the spin tagging method [1] combined with a single shoot RARE imaging method [2].

A convection flow was made by electrically heating a small resistor at the bottom of a small cylindrical container that was filled with water. The container had 25 mm in diameter and was 32 mm long. The heating power of the 58 O resistor was adjustable by changing the voltage of the power supply from 0 V to a maximum of 15 V so that the power was in the range from 0 - 3.9 W. The convection flow was dynamically imaged by the RARE single shoot imaging sequence with 64 spin echoes of the echo time 2.14 ms that was preceded by a DANTE tagging sequence consisting two blocks of five equally spaced 32° hard RF pulses executed in the presence of the magnetic field gradient in the x direction for the first block and in the y direction for the second block (see the left image bellow). The DANTE sequence generated a mesh of inverted magnetization that after a time $TI = T_1 \ln(2)$ (this approximately 2 s for water) became equal to zero so that no signal was acquired from the mesh by the imaging sequence started at exactly that time. The imaging matrix was 64^2, field of view 30 mm and slice thickness 2 mm; the repetition time was 5s (2s for the mesh generation and 3s for the signal relaxation after the image scan). Sequence of images on the right show dynamics of establishing a stationary convection flow after turning the 0.15 W heater on. The images were acquired every 5s from the same axial cross-section through the cylinder.

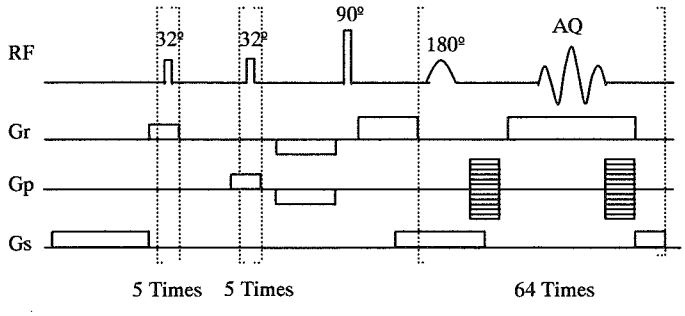

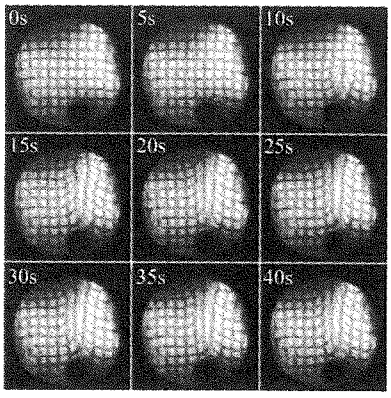

1. Mosher, TJ, and Smith, MB, *Magn. Reson. Med.* Vol. **15**, 334 (1990).
2. Hennig, J, Naureth, A, Friedburg, H, *Magn. Reson. Med.* Vol. **3**, 823 (1986).

MRI detection of acoustic streaming in gases

I.V. Mastikhin, B.Newling

MRI Centre, Physics Department, University of New Brunswick, Fredericton, NB Canada

Acoustic streaming is a bulk advective flow caused in the medium by attenuation of acoustic waves [1]. It is difficult to measure parameters of acoustic streaming in gases without affecting the gas dynamics.

Magnetic Resonance Imaging (MRI) is potentially capable of non-invasively obtaining 3-dimensional information on velocity and diffusion of gas, with no requirement of optical transparency of gas or the vessel. However, gases' densities are 1000 times lower and NMR signal relaxation times are 2-3 orders of magnitude shorter than those of liquids, making an application of clinical MRI methods to gases impossible.

We develop MRI methods for detection of acoustic streaming in thermally polarized gases. The first method [2], aimed at measuring lower velocities of gas, follows a preparation-readout scheme, with Pulsed-Field Gradient as a preparation and a single-point imaging method (SPRITE) as a readout. The second method [3] is a modification of a displacement-sensitized SPRITE sequence for higher gas velocities (m/s). Advantages and drawbacks of each method will be analyzed.

References.

[1]. W.L. Nyborg. Acoustic streaming. In: Physical Acoustics", (W.P.Mason, ed.), Vol.2, Part B, Academic Press, NY (1965).

[2]. Mastikhin IV, Balcom BJ, Prado PJ, Kennedy K. J MAGN RESON 136 (2): 159-168 FEB 1999

[3]. Newling B, Poirier CC, Zhi Y, Rioux JA, Coristine AJ, Roach D, Balcom BJ. PHYS REV LETT 93 (15): Art. No. 154503 OCT 8 2004

Measuring nanopore sizes with the T_1 of CF_4

Dean O. Kuethe and Andrew F. McDowell

New Mexico Resonance, Albuquerque, USA

Introduction The relaxation of roughly spherical perfluorinated gases, like CF_4, is dominated by spin-rotation interaction, which is mediated by molecular collisions (Armstrong, 1987). In normal laboratory conditions, the collisions are much more frequent than the Larmor frequency implying the extreme narrowing regime, $T_1=T_2$. The relaxation times are roughly proportional to collision frequency. If the gas is confined in a pore on the order of the bulk gas mean free path, collisions with the pore wall will be about as frequent as molecular collisions and the T_1 should get substantially longer (Lizak, Conradi, & Fry, 1991). If we can model this relationship quantitatively, we should be able to measure pore size with T_1. Because we can measure T_1 with high precision, this promises to be a precise measurement of pore size.

Methods We made samples of fumed silica with known surface to volume ratios S/V by squashing fumed silica with known surface area into polycarbonate cylinders. The material is mostly pore space with very little particle contact so the surface area remains constant with compression. The volume is simply the volume of the container minus the volume of silica and annular volume. We measured T_1 with an inversion recovery sequence.

Despite CF_4's critical temperature, 228 K, gas uptake measurements indicated that the density of gas in pores was higher than bulk gas density. To fit the T_1 data we had to include the effect of absorption. We tried two different models. In a condensation model, molecules become briefly stuck on the walls, during which time the relaxation rate is zero. In a wall potential model, molecules accelerate toward the wall when in the attractive potential of wall molecules, which gives them a higher average velocity and density. Although the models are different in concept, having stationary *vs.* fast molecules near the wall, both predict longer T_1s and higher density in pores with high S/V, in agreement with our data.

Results There is a strong, calibratable relationship between S/V and T_1. The two models fit the data equally well.

Conclusions T_1 is a great way to measure S/V. To find out more about what the molecules are doing in the pores, we would need additional data, perhaps at different temperatures.

We thank the NIH, grant R01EB002072, and Sandia National Labs, PR 522388 for financial support.

Armstrong, R. L., *Magn. Reson. Rev.* **12**, 91-135 (1987).

Lizak, M. J., Conradi, M. S., and Fry, C. G., *J. Magn. Reson.* **95**, 548-557 (1991).

Imaging SF_6 and C_2F_6 gases in lab rat lungs: To avoid cooking larger animals, use C_2F_6

Dean O. Kuethe and Natalie L. Adolphi

New Mexico Resonance, Albuquerque, USA

Introduction SF_6 is a great gas to image in lab rat lungs because its $T_1=T_2=T_2^*$ is about 1 ms and one can signal average very rapidly, applying hard rf pulses in the presence of imaging magnetic field gradients. However, because the deposition of heat from rf pulses (SAR, specific absorption rate) increases with increasing body size, this scheme would not be applicable to people because of the danger of cooking them. The $T_1=T_2=T_2^*$ of C_2F_6 is 4.5 times longer than SF_6, which can allow substantial reduction in cooking danger. One can apply a much longer, lower power rf pulse in the absence of a gradient without the pulse length being a substantial fraction of T_2. For a given flip angle SAR decreases with pulse length. By narrowing the sample bandwidth by eliminating the gradient and using the longer T_2 gas, we can reduce SAR by a factor of 40. Fortunately, the longer T_2 will allow enough time to start collecting data and then ramp the gradient. SAR is further reduced by 1/4.5 by signal averaging 4.5 times less. The fortunate thing is that so long as $T_1=T_2^*$, the 1/[illegible] factor loss in signal-to-noise ratio (SNR) from less signal averaging can be recovered by the [illegible] factor gain from narrower acquisition bandwidth. The gas spaces in lungs are much more magnetically homogeneous than the tissue. The inherent T_2^* is long enough for the relation $T_1=T_2^*$ to hold for C_2F_6. Because this seems a little like getting something for nothing, we wanted to test whether the SNR is really the same when using SF_6 or C_2F_6.

Methods We make the simplest comparison to see if the SNR is preserved by lengthening the timing parameters of the pulse sequence by 4.5 when imaging C_2F_6 as opposed to SF_6. We imaged the two gases in the same rat, using the same pulse sequence, in both cases using hard rf pulses in the presence of imaging gradients. For C_2F_6 we lengthened the FID acquisition time by 4.5 times and signal averaged 4.5 times less often.

Results The two images are comparable in SNR. For lab rats, SF_6 has the advantage that it forces one to use an acquisition time so short that the images are insensitive to additional sources of magnetic inhomogeneity, like ferromagnetic objects and poor B_0 homogeneity. For rats SAR is not a problem; in fact it can be beneficial because it is about the correct level to help maintain an anesthetized rat's body temperature.

Conclusion For larger animals, including people, we suggest using C_2F_6, with its 4.5 times longer $T_1=T_2=T_2^*$. The SNR is the same but the cooking danger can be reduced substantially.

We thank the NIH, grant R01EB002072, for financial support.

Estimation of the True Relaxation Time T_1 of Hyperpolarized ^{129}Xe Gas in Mouse Lung: Calculation on a Ventilation Model with the Aid of Normal Gas at Thermal Equilibrium

Michiko Narazaki, Hirohiko Imai, Tetsuya Wakayama, Atsuomi Kimura, and Hideaki Fujiwara
Division of Health Sciences, Graduate School of Medicine, Osaka University
1-7 Yamadaoka, Suita, Osaka 565-0871 Japan

INTRODUCTION

Hyperpolarized (HP) ^{129}Xe inhalation experiments can give different kinds of information on the function of lung and brain. For example, the washin and washout curve analysis with lung or brain can give physiological parameter of capillary blood flow as well as the magnetic resonance parameter of relaxation time T_1. This situation is somewhat different with PET(positron emission tomography) from which capillary blood flow is known to be obtained more readily. However, MRI/MRS is considered to be more beneficial because relaxation time can be obtained which will reflect the physiological condition very sensitively. In the present study the ^{129}Xe signal was observed to oscillate in the steady state of inhalation experiment, and this oscillation is analyzed on a simple model of ventilation. The calculation shows that the relaxation time T_1 will be determined when this oscillation observed from the HP gas is compared with that observed from the fluorinated gas at thermal equilibrium. Here the fluorinated gas is used as a gas without uptake into the body, and the slope in the semi-logarithmic plot of the washout curve is usable instead of the oscillation in the steady state.

Inert Gas Ventilation Model

The inert gas is assumed to be inhaled and mixed in lungs in an instant and then exhaled from lungs within a respiration cycle of Δt(Fig.1). In such a case, fluorinated gas at thermal equilibrium with very short relaxation time T_1 will give NMR signals which oscillate with the cycle of Δt, and the oscillating intensity will give ratio of the tidal volume divided by the alveolar volume, R_F/V_A. This ratio of R_F/V_A is also measurable as the slope in the semi-logarithmic plot in the washout experiment. When HP Xe gas is inhaled instead of the thermal equilibrium gas, oscillation will be realized similarly in signals but the intensity will be affected by the relaxation time T_1 since the HP gas magnetization decreases spontaneously with this time constant. Therefore, detailed calculation of the signal intensities observed with the HP gas as well as with the gas at thermal equilibrium is expected to give the true relaxation time T_1 in the lung.

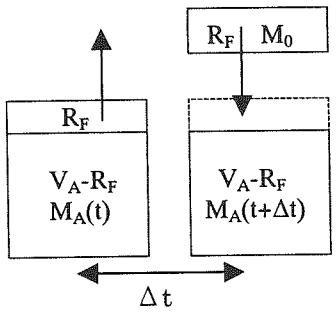

Fig. 1 Ventilation Model of Lung used in the Calculation
V_A: alveolar volume
R_F: tidal volume
M_0:magnetization of HPinflow gas
M_A: magnetization of residual gas
Δt : respiration cycle

Results and Discussion

Our detailed calculation has given following Eqs. for the estimation of T_1:

$$T_1 = \Delta t/\{\ln(\cos\theta) + \ln(1 - \text{ratioF}) - \ln(1-\text{ratioXe})\} \quad \text{- - - - [1]}$$

$$T_1 = \Delta t/\{\ln(\cos\theta) + \ln(1 + \Delta t\ \text{slopeF}) - \ln(1-\text{ratioXe})\} \quad \text{- - - [2]}$$

where θ is the pulse angle used to measure the ^{129}Xe NMR, ratioX means the intensity ratio in the steady state of inhalation, *i.e.*, oscillated amplitude divided by the maximum intensity, in the observation of nucles X (X=^{19}F or ^{129}Xe), and slopeF means the slope in the semi-logarithmic plot in the ^{19}F washout experiment.

The experimental results of θ=14.8°, slopeF= -0.261, ratioXe= 0.174, Δt=0.5 sec have given the value of T_1= 28.7 sec which further gives the perfusion term of $\lambda Q/V_A$= 0.033 when combined with the value of T_1^*= 14.7 sec.[1] This perfusion term is well within the literature data, supporting our successful calculation. Since the true relaxation time is long, *i.e.*, relaxation rate is fast, compared to the ratios or slopes of the observed values, precise determination of the experimental values is very important for the reliable estimation of the true relaxation time in mouse lungs.

Reference

1. Narazaki, M *et al*, Proc. Intl. Soc. Mag. Reson. Med. **13**, 1841 (2005).

Spin relaxation of polarized Xe atoms at the liquid-solid interface

Takako Yamamoto, Kiyoshi Ishikawa, and Yoshihiro Takagi

Graduate School of Material Science, University of Hyogo, Hyogo 678-1297, Japan

We study the spin relaxation of hyperpolarized ^{129}Xe atoms at the interface between liquid and solid. The polarization of Xe atoms decays in bulk solvents mainly due to the magnetic dipole interaction with the nuclei in solution. Since the moving magnetic dipoles interact transiently with each other, the lower viscosity leads to the smaller decay rate at the fast motion limit. On the other hand, the wall relaxation can be dominant in the low-viscosity solution because Xe atoms collide with the cell walls within the relaxation time of bulk solution. Therefore, the minimal value typically appears in the temperature dependence of decay rate. If we succeed in suppressing the wall relaxation, the resonance signals will be detected many times without the replacement for depolarized atoms. In addition, we can find the weak perturbations hidden under the veil of both relaxations in the finite size of cell. The spin relaxation at the gas-solid surface has been reported as to the cross-relaxation of ^{129}Xe nuclei with the protons of coating material [1] and the relaxation of ^{3}He nuclei due to the magnetic sites [2]. The wall relaxations in solutions are, however, not fully understood.

We measured the decay rate of spin polarization of Xe atoms dissolved in the deuterated ethanol (ethanol-d_6). The walls of glass cell were coated with the deuterated paraffin (eicosane-d_{42}). The use of deuterated materials is essential to investigating the surface interaction. The Xe atoms were polarized by the spin-exchange optical pumping with a flow-type Xe polarizer [3]. The polarization was approximately 4 %, and total pressure of mixed gas (^{4}He, N_2, and natural abundant Xe) was 290 kPa. The decay rate of Xe gas is less than that of the dissolved atoms. The polarizations of Xe atoms in liquid and gas phases are subject to the wall relaxations with the different time constants. This situation induces the complex decay phenomena if Xe atoms pass freely over the gas-liquid boundary. We used the glass cell designed to minimize the exchange rate of Xe atoms between both phases [4]. The translational motion of Xe atoms and ethanol molecules was of the convection rather than the diffusion at the time scale longer than 0.1 s. It was confirmed by the steady-gradient spin-echo diffusiometry. Therefore, Xe atoms collides many times with the walls within the relaxation time. Figure 1 shows the temperature dependence of decay rate and its change by the coating. The decay rate around 240 K is significantly smaller in the coated cell than in the uncoated cell. Taking account of the dependence of decay rate on the field strength and the surface area of coating as well as the temperature, the suppression of spin relaxation was found to be because the characteristic time of relative motion between deuterons and Xe nuclei at the interface is different from in the solution.

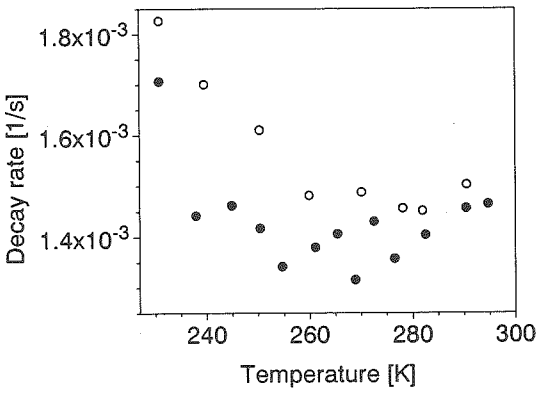

Fig. 1 The decay rate of Xe polarization dissolved in ethanol-d_6 for the coated (solid circle) and uncoated (open circle) cell at 0.33 T.

[1] Driehuys B., Cates G., and Happer W., Phys. Rev. Lett. **74**, 4943 (1995).
[2] Jacob R., Morgan S., and Saam B., Phys. Rev. Lett. **87** 143004 (2001).
[3] Ishikawa K., Imai H., and Takagi Y., J. Chem. Phys. **120**, 7602 (2004).
[4] Ishikawa K., Imai H., and Takagi Y., Phys. Rev. A **70**, 042712 (2004).

Long-distant delivery of hyperpolarized ^{129}Xe using a capillary tube

Tatsuya Asanuma*, Takashi Hiraga, and Mineyuki Hattori
National Institute of Advanced Industrial Science and Technology (AIST),
Ikeda, Osaka 563-8577, Japan

Introduction

The utility of hyperpolarized noble gases such as ^{129}Xe and ^{3}He is rapidly becoming apparent in a wide variety of disciplines. The particular interest in entirely new medical imaging is induced by the attempt to establish a real time high-resolution diagnosis system [1]. In this technique, however, the long-distant delivery of the hyperpolarized ^{129}Xe must be realized with little or no loss of polarization under continuous flow conditions. From a fluid dynamics point of view, we report that the hyperpolarized ^{129}Xe spin can be successfully delivered using capillary tubes with the inside diameters of 0.25 and 0.53 mm.

Experiments

The gas flow system consists mainly of a homebuilt apparatus, similar to that shown in a previous publication [1], that provides a continuous flowing gas stream carrying the hyperpolarized ^{129}Xe gas. The homebuilt probe was connected to the apparatus using a fused silica capillary tube, and then was inserted into a permanent magnet with a field B_0 of 0.3±0.01 T. Two silica tubes with the inside diameters of 0.25 and 0.53 mm, respectively, N025 and N053, were used as delivery paths without any pre-treatments. The interior surfaces of the tubes are not coated with any chemical reagents. The tube length L was changed from 1 to 22 m. The natural abundance Xe gas (100%) and Rb vapor (99.99%) were mixed at 145 °C±3 and optically pumped at the wavelength of 794.7± 1 nm, with circularly polarized light, by using a 60 W semiconductor laser.

The signal intensity M_0 of hyperpolarized ^{129}Xe was detected by a NMR spectrometer (Thamway Co., Ltd.) at 3.574 MHz ^{129}Xe frequency. The data were acquired in the direction of increasing flow rate Q that was determined by the difference in pressure in both ends of the tube. The maximum signal intensities M_{max} in M_0 vs Q curves were normalized by that of N053 with L of 1 m.

Results and discussion

Figure 1 shows the dependence of the maximum intensity M_{max} on the tube lengths L of N025 and N053. M_{max} for both tubes appeared at higher flow rates with increasing L, which is considered to reflect the conductance of Xe gas. According to our analysis, the observed M_{max} for N053 correlated to the variation of the flow rate Q. This fact suggests that the amplitude of M_{max} is approximately proportional to the density of hyperpolarized ^{129}Xe in the NMR cell. One of some models for explanation is that surface relaxation could be significantly reduced by delivering the hyperpolarized ^{129}Xe spin in a laminar flow using a capillary tube. This result is in agreement with the expectation that the nonequilibrium ^{129}Xe nuclear spin polarization can be time-independent under "laminar" flow conditions in steady state [2].

The difference of M_{max} observed between N025 and N053 might be related to the presence of a stenosis or expansion in both ends of the tube, because in such a case the depolarization of ^{129}Xe spin due to flow fluctuation can be induced by the onset of turbulent flow.

Conclusions

The xenon's high sensitivity to its local magnetic environment was successfully applied to prove the usefulness of capillary tubes with an inside diameter ≤ 0.53 mm. Extensions of this technique should enable farther distant deliveries of ^{129}Xe gas with a higher concentration of hyperpolarized ^{129}Xe, which will be useful for *in situ* studies of biomedical materials with short spin-lattice relaxation times for ^{129}Xe.

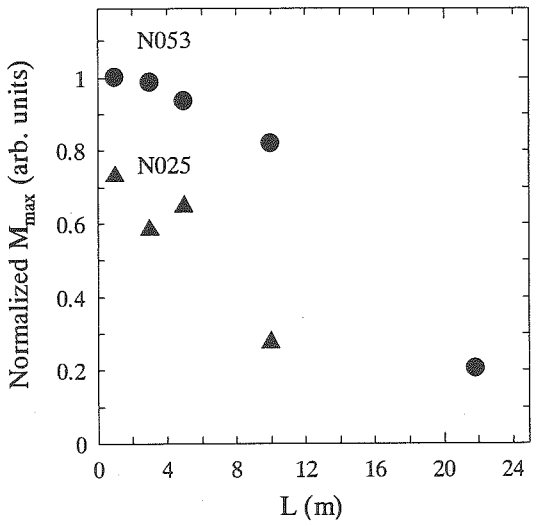

Fig. 1. Dependence of the maximum signal intensity M_{max} for hyperpolarized ^{129}Xe on the tube lengths L.

References

[1] M. Hattori *et al.*, *International Congress Series*, **1265**, 144 (2004).

[2] E. Brunner *et al.*, *J. Magn. Reson.*, **138**, 155 (1999).

Direct Molecular Solution of Hyperpolarized Gases through Hollow Fiber Membranes

P. P. Zänker[1], P. Blümler[1,2], H. D. Lemke[3], H. W. Spiess[1]

[1] *Max Planck Institute for Polymer Research, 55128 Mainz, Germany*
[2] *ICG-III: Phytosphere, Research Centre Jülich, 52425 Jülich, Germany*
[3] *Membrana GmbH, R&D3785 Obernburg, Germany*

Purpose: It is often claimed that one application of hyperpolarized (HP) gases is that of a contrast agent in bio/medical MRI. Although xenon is a suitable candidate for this, there are certain problems that have to be overcome. Simply inhaling is problematic due to the necessary presence of oxygen and the slow passage into the cardiovascular system. Nevertheless first images in small animals are possible this way [1]. Alternatively the Xenon is dissolved in a suitable liquid and then injected [2]. Here the HP-Xe is typically frozen out, vaporized in the presence of the liquids and dissolved by shaking. This process is hard to control and definitely not suitable for hospitals. Most technical solutions of dissolving gases are based on bubbling, which is problematic because most fluids of interest make perfect foams. Hence the following problems needed to be solved:

- short distance between liquid and gas for a quick solution
- avoidance of physical phase transitions
- achievement of a molecular solution without foam or bubbles
- temperature and pressure control of the process

Methods: Our solution is the use of oxygenator membranes (like in heart-lung machines) in specially designed modules. In the first prototype the solvent is circulated through the membrane module and a reservoir inside the NMR probe driven by a nonmagnetic membrane pump. At the same time hyperpolarized Xenon counter-flows through the hollow fiber membranes and dissolves into the liquid. This process is monitored by NMR spectroscopy.

Results and Discussion: It is clearly demonstrated that xenon is quickly dissolved in this way with all the above mentioned conditions. The dissolution process occurs fast, as the maximum signal amplitude is reached already about 10 seconds after the switch-on of the pump. No bubbles occur and no gas-peak was detected in the solution. Several liquids were tested (water, blood plasma, clinically approved blood substitutes and nutrition solutions) and the signal of ^{129}Xe mainly depends on its solubility in the fluid and its polarization. The pumping velocity is of lesser importance however has to be optimized with respect to the T_1 of Xe in the solutions. However, no variation (within reasonable limits) of any of these parameters caused any observable foaming.
It is shown that by this process Xenon can be dissolved molecularly in blood (or plasma) and in other liquids that could be used as contrast agents. Additionally such hyperpolarized solvents can also permit new experiments in structure elucidation of complex biological systems [3], which are momentarily hampered by low concentrations and/or strong foaming.

Conclusion: Hollow fiber membranes which are already optimized for the efficient solution of gases in liquids (blood/oxygen) fulfil all requirements for dissolving HP-gases quickly, without noticeable loss of polarization or foaming and in an already clinically approved way. Therefore, their application is extremely promising for the generation of contrast agents and other applications which require gases with ephemeral physical properties (e.g. PET tracers, para-H_2) to be dissolved efficiently.

1. S.D. Swanson, M.S. Rosen, B.W. Agranoff, K.P. Coulter, R.C. Welsh, T.E. Chupp, "Brain MRI with Laser-Polarized ^{129}Xe", *Magnetic Resonance in Medicine* 38, 695-698 (1997).
2. B. M. Goodson, "Using injectable carriers of laser-polarized noble gases for enhancing NMR and MRI", *Concepts in Magnetic Resonance*, 11(4), 203-223 (1999).
3. E. Brunner, "Enhancement of Surface and Biological Magnetic Resonance Using Laser-Polarized Noble Gases", *Concepts in Magnetic Resonance*, 11(5), 313-225 (1999)

On line monitoring of polymerisations by hyperpolarized ^{129}Xe NMR

Kerstin Münnemann[a], Bernard Blümich[a], Wolfgang Häsing[b], Stephan Appelt[b]

[a]Lehrstuhl für Makromolekulare Chemie, ITMC, RWTH Aachen, Worringerweg 1, D-52074 Aachen, Germany
[b]Zentrallabor für Elektronik, Forschungszentrum Jülich, D-52425 Jülich, Germany

One of the main goals in polymer engineering is the production of polymers with well defined physical and chemical properties. In order to achieve this, a narrow distribution of molecular weights for a certain polymer is required. Therefore, it would be desirable to follow a polymerisation on line instead of analysing the degree of polymerisation afterwards, e.g. by end group analysis with ^{1}H or ^{13}C NMR.

In recent years, ^{129}Xe NMR spectroscopy was proposed as a technique to investigate the amorphous phase of solid polymers, and it could be demonstrated that the chemical shift of Xe in the void space of a polymer depends strongly on the chain length of the polymer [1]. We report the application of hyperpolarized ^{129}Xe NMR spectroscopy to follow polymerisation reactions on line for the first time. We studied the ring opening polymerisation of tetrahydrofurane (THF) which follows a cationic living mechanism and the free radical polymerisation of styrene. For both polymerisations the monomer was mixed with a certain amount of initiator (without solvent) and put quickly into a 4.7 T NMR magnet. A continuous flow of hyperpolarized Xe was applied to the polymerisation systems which was produced by means of spin-exchange optical pumping with a home-built Rb-Xe hyperpolarizer [2]. The hyperpolarized Xe dissolves continuously into the reaction bulk and can be detected by NMR spectroscopy. We observed that the NMR line of Xe dissolved in the reaction bulk shifts strongly during the polymerisation process and also the line shape is changing significantly during the reaction as can be seen in Fig. 1a).

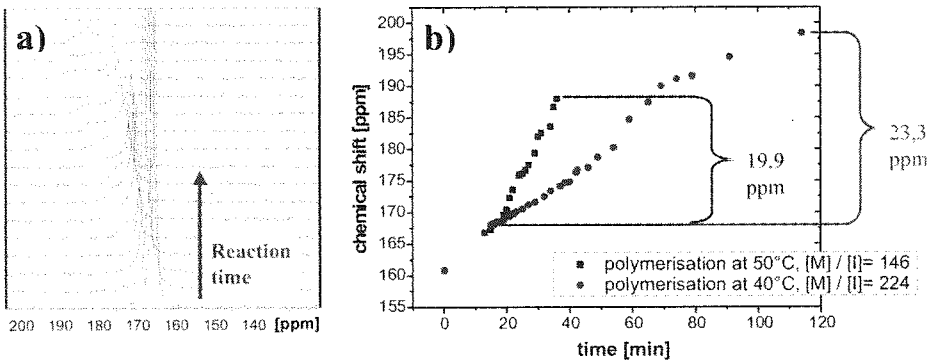

Fig.1: a) Stack plot of Xe spectra demonstrating the shift of the Xe resonance of dissolved Xe and the changing line shape during the progress of the cationic polymerisation of THF b) Plot of chemical shift versus reaction time for this polymerisation at 40°C (circles) and 50°C (squares) with different monomer/initiator ratios.

The chemical shift of the dissolved Xe is influenced by a sum of two contributions which are changing while the reaction is proceeding: the one is due to the decreasing amount of monomer and the other due to growing polymer chains. The broadening of the Xe line can arise from a distribution of polymer chain lengths within the reaction bulk which leads to different Xe resonances which cannot be resolved. Fig.1b) depicts the dependence of the chemical shift of the Xe inside the reaction bulk on the reaction time for different polymerisation temperatures and different initial monomer/ initiator ratios . It can be seen that the reaction proceeds faster at higher temperature and that the resulting chemical shift change scales with the monomer/initiator ratio and therefore with different degrees of polymerisation. For this reason it should be possible to calculate the reaction constant of a certain polymerisation from the chemical shift data versus time after establishing a calibration by a different analysis technique like GPC or end group analysis.

[1] Stengle, T. R., Williamson, K. L., *Macromolecules*, **20**, 1428-1430 (1987).
[2] Appelt, S., Häsing, F.W., Baer-Lang, S., Shah, N. J., Blümich, B., *Chem. Phys. Lett.* **348**, 263 (2001).

Spatially Resolved Measurement of Core Porosity

F. Marica,[a] Q. Chen,[a] A. Hamilton,[b] C. Hall,[b] T. Al,[c] and B.J. Balcom[a]

[a] MRI Centre, Department of Physics, University of New Brunswick, Fredericton, NB, Canada

[b] Centre for Materials Science and Engineering, The University of Edinburgh, Edinburgh, Scotland, UK

[c] Department of Geology, University of New Brunswick, Fredericton, NB, Canada

Standard spin-echo MRI methods generally fail when applied to realistic porous media due to multi-exponential spin-spin relaxation time T_2 decay and restrictions on the minimal echo time. The density weighted, centric scan, Conical SPRITE technique, employed in the current work for local porosity measurements in fluid saturated porous media, is appropriate for overcoming the problems caused by the short effective spin-spin relaxation times T_2^* that are associated with these systems.

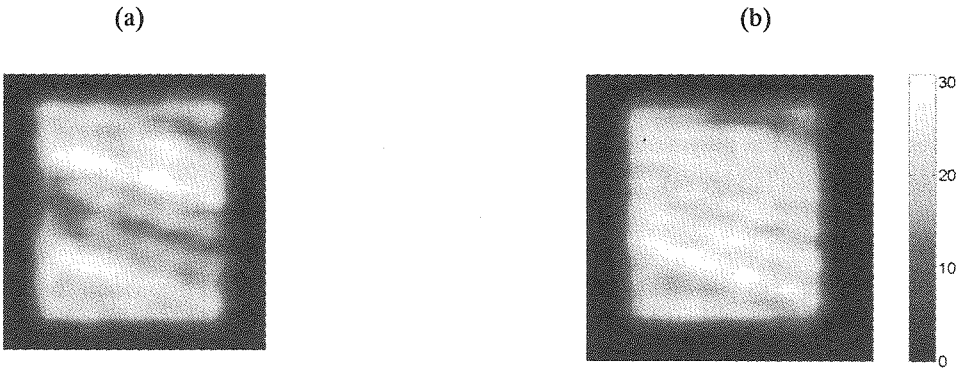

Figure 1. (a) The 2D slice from a 3D image dataset (magnitude map) for a Locharbriggs sandstone. (b) The porosity map of the chosen 2D slice. The images have been cropped to remove the reference and have been smoothed by zero-filling.

Most porous sedimentary rocks have a single exponential T_2^* decay due to susceptibility-difference-induced field distortion and this relaxation feature for rocks is essential to the quantitative nature of the proposed experiment.

The methodology is tested on a series of sandstone core samples. These samples vary in both porosity and degree of local heterogeneity due to bedding plane structure. The MRI porosity measurement is in good agreement with traditional gravimetric measurements of porosity for uniform samples. Spatially resolved porosity measurements reveal significant porosity variation in some samples. According to these maps and profiles, porosity is a spin density driven parameter and the local image intensity is both a spin density and a T_2^* driven parameter. This novel MRI technique should have applications to the characterization of local porosity in a wide variety of porous media.

Magnetic Resonance Imaging of Water Distribution in Thermally and Mechanically Fractured Granite

Makoto Yamaguchi[1], Kazunori Suzuki[1], Stephen Altobelli[2], and Dean Kuethe[2]

[1]Institute of Research and Innovation, Kashiwa, Chiba 277-0861, Japan
[2]New Mexico Resonance, Albuquerque, NM 87106, U.S.A.

Fluid flow through rock fractures has been extensively studied in relation to migration of radioactive elements from geological disposal sites. Nondestructive imaging methods are expected to help to understand how fluid flows are governed by local and network structures of fractures. We have shown that magnetic resonance imaging (MRI) of liquids in thermally fractured granite samples with SPRITE method as the method is less susceptible to image distortion due to magnetic field inhomogeneity by para/ferromagnetic mineral grains. While coarse-grained Inada granite showed images of networked fractures, fine-grained Okazaki granite showed bright spots presumably due to pores in feldspar grains [1]. However its sensitivity is low which is inherent to single point imaging and digital resolution is limited by available maximum gradient strength. To visualize movement of water in the rock cores by 3D MRI measurement, we investigated three possibilities which are effective in obtaining water distribution with higher resolution and shorter acquisition time.

Two MRI systems were used in this study: One is a system with a vertical 7T SCM, a RF probe with gradient coils, a Tecmag Apollo console, and gradient amplifiers (Resonance Research). Another is a system with a horizontal 1.9T SCM, a Tecmag Libra console, a water-cooled gradient coil, and Techron gradient amplifiers.

Cylindrical samples (15mmØ for 7T and 50mmØ for 1.9T) of Inada and Okazaki granites were heated to 923K for 1h to thermally induce fractures. After cooling to room temperature, the samples were immersed into water and evacuated. Following three methods were examined:

1) Improvement of signal acquisition efficiency of SPRITE: Multiple point sampling has been proposed to improve signal acquisition but that results in nonuniform data points in k-space which prohibit application of Fourier-transform to obtain images. Recently Balcom *et al.* reported that chirp Z-transform can be applied in this case to obtain images from datasets with multiple point sampling [2]. The method was effective not only for improvement of signal to noise ratio but also to obtain images with higher digital resolution.

2) Spin echo imaging: Large fractures in rocks or concretes can be visualized by spin echo method as water in those fractures gives long T_2 [3]. The sequence with phase encoding for two directions resulted in images showing networked fractures even in the case of fine-grained Okazaki granite, which did not show such fractures but bright spots by SPRITE as the sequence gives T_1-weighted image.

3) FID sampling: Kuethe *et al.* developed a sequence for imaging lungs which samples FID signals of fluorinated compounds with very short T_2 by changing direction of gradients radially [4]. Since the sequence is highly efficient and less sensitive to susceptibility artifact, it was expected to be suitable for imaging of fractures in rock cores. Obtained images showed fractures and dark spots with bright fringes also appeared which were presumably induced by susceptibility

We also did spin echo imaging of mechanically fractured Inada granite. Samples after triaxial compression under controlled circumferential distortion rate showed a flat slantwise fracture induced by shear stress. Naturally occurred fractures in granite were also imaged and SPRITE was effective in the case of rock cores hydrothermal alteration results in faster relaxation by deposited minerals. A preliminary study on D_2O intrusion into H_2O saturated core showed the intrusion process by 3D spin echo imaging. These results show fractures and pores in crystalline rocks can be visualized magnetic resonance imaging and it is expected to be more fruitful if microfocus X-ray CT images showing distribution of mineral grains are combined with MR images.

References

[1] Yamaguchi, M. *et al., Magn. Reson. Imaging,* **23**, *325* (2005). [2] Balcom, B. private communication. [3] Young, J.J. *et al., Cement and Concrete Res.* **34**, *1594* (2004). [4] Kuethe, D. *et al., Magn. Reson. Med.*, **39**, *85* (1998).

Influences of Magnetic Impurities on Proton Spin Relaxation of Water in Clay

Kaz Nagashima

Tokyo Magnetic Resonance Inc., Tokyo, Japan
Port and Airport Research Institute, Kanagawa, Japan

^{1}H spin relaxation of water in magnetite-doped aqueous kaolin clay slurry was investigated at 8.51 MHz (0.2 Tesla). The spectra at high magnetite contents clearly showed two distinct resonances, presumably one from surface-associated water and the other from free interstitial water. The difference in the frequency of the two resonances increased as much as 1700 Hz (200 ppm) with addition of magnetite 100 mg into 15 wt% aqueous slurry. The longitudinal relaxation data were analyzed with UPEN program [1]. The observed T_2* values at low magnetite dosages were in accordance with the predicted values from the resonance intensities and from the estimated magnetic susceptibilities. The T_2 relaxation displayed a multi-exponential character when the water content of slurry was high, but apparently it became closer to mono-exponential as the water content decreased. The transverse relaxation rates (R_2) linearly increased as a function of magnetite added. Based on the comparison of data obtained with spin echo and CPMG sequences, an empirical equation was derived to quantitatively describe the signal loss due to diffusion.

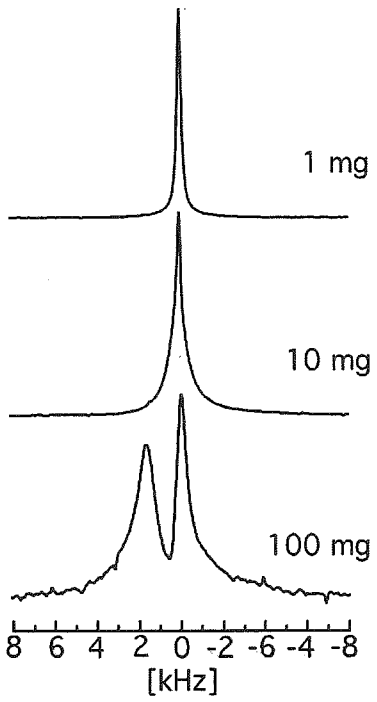

Fig. 1. Changes in the ^{1}H NMR spectra of water in clay slurry (40 g of slurry with 15 wt% solid concentration, room temperature). Indicated are the amounts of magnetite added. The separated spectra at high impurity contents were referenced to the free water resonance.

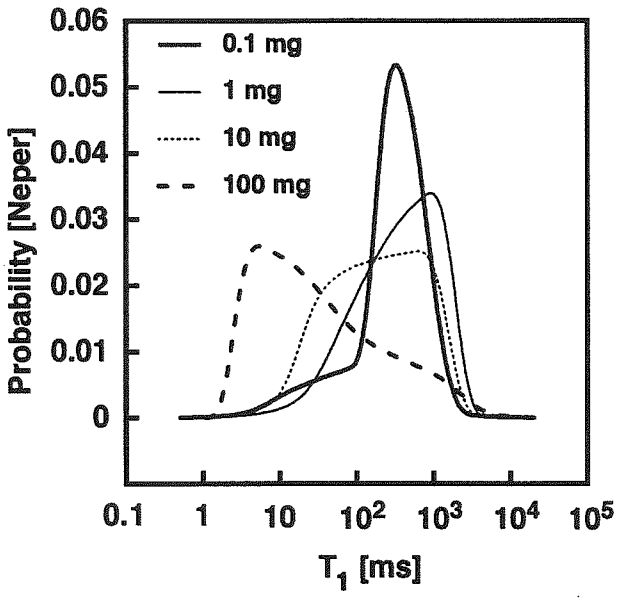

Fig. 2. Shifts in the apparent T_1 distribution as a function of magnetite amount. Although the non-magnetic physical characteristics of the slurries are the same, the NMR data yield totally different results. Pore-size analysis with NMR becomes difficult when magnetic impurity content is high.

[1] Borgia, G. C., Brown, R. S., and Fantazzini, P., *J. Magn. Reson.* **132**, 65-77 (1998).

^{1}H and ^{19}F MRI of Physically Blown Foam

Steve Altobelli[1], Lisa Mondy[2], Rekha R. Rao[2], Ed Russick[2]
[1]New Mexico Resonance, [2]Sandia National Laboratories* Albuquerque, NM USA

Introduction

Polymeric foams are low-density systems that are good thermal- and vibration-insulators. Although they have many industrial applications processing of these foams is still not well understood. We combine experimental observations with finite element model development to help understand the manufacture of physically blown, thermosetting foam. In this context physically means the blowing agent boils to form the gas phase, as opposed to chemically blown foam where a reaction occurs producing the gas, (as in polyurethanes). A simplified computational model is developed based on the growth of volume source points scattered in a polymer matrix. The spatial distribution of blowing agent is determined with Nuclear Magnetic Resonance imaging, which can detect both the protons in the uncured epoxy matrix and the ^{19}F in the volatile blowing agent.

Methods

This contribution describes our progress in obtaining time resolved images of the blowing process, which lasts less than 45 minutes and requires that the sample be heated above 60C. We built a water-jacket that fits inside a vertical solenoid rf coil and accommodates a 100ml plastic sample bottle. The rf probe can be tuned to either ^{19}F (75.6 MHz) or protons (80.3 MHz) in our 30 cm horizontal bore, 1.9T system. Our first goal is to choose imaging strategies. We measured proton T_1 and T_2 for both epoxy components at room and elevated temperature. We also examined the ^{19}F spectrum, which consists mainly of two clusters of lines 3.6 kHz apart and devised a simple method to saturate one group of resonances.

Results

RARE type proton imaging is possible for the hot epoxy, which has much longer T_2 than at room temperature. After curing, T_2^* is very short, and so far even SPRITE type imaging has not been possible in our system. ^{19}F imaging is possible at both room and elevated temperature. It appears that T_1 is spatially inhomogeneous in the cured samples.

Discussion

Physically blown foam is a useful, but complex, system. We are developing a combined experimental and numerical modeling approach to understanding and use these foams. NMR imaging provides a unique and powerful tool in this system, but there are many practical issues still to be resolved and many NMR techniques (for instance diffusion weighting) that remain to be attempted.

*Sandia is a multiprogram laboratory operated by Sandia Corporation, a Lockheed Martin Company, for the United States Department of Energy's National Nuclear Security Administration under contract DE-AC04-94AL85000.

NMR Microscopy of Calcium Polyphosphate Drug-Delivery Bioceramics

Joshua M. Bray [1,2], Steven D. Beyea [1,2], Mark Filiaggi [3] & Carlo Petrone [3]

[1] Institute for Biodiagnostics (Atlantic), National Research Council of Canada
[2] Dept. of Physics, [3] School of Biomedical Engineering, Dalhousie University
Halifax, Nova Scotia, Canada

In recent years, biomaterials implanted into the body for repair or reconstruction of tissues have demonstrated increasing potential in regenerative medicine and adjunctive therapies. One such application is the use of porous bioceramics[1] (which may be inert, bioactive or resorbable) as enhanced localized drug delivery devices, offering alternative delivery routes and release mechanisms.[2] Conventional drug delivery systems such as capsules and pills release the drug immediately into the system, and the remaining drug in the carrier is released at a decreasing rate in an approximately first order manner (with the exception of continuous intravenous delivery).

Bioceramics with tailored microstructure have potential as long-term and/or variable rate drug delivery vehicles, with properties finely tuned for the particular problem.[3] The success of these materials depends upon the ability to optimize the microstructure in terms of pore size, porosity and surface area so as to release compounds at the appropriate stages of healing.

We have previously demonstrated the application of Magnetic Resonance Imaging (MRI) to studies of the microstructural properties of ceramics.[4-6] In the current experiments, we apply MR microscopy to the study of the temporal and spatial evolution of resorbable calcium polyphosphate (CPP) bioceramics. *In vitro* measurements of structural evolution during material degradation, and corresponding studies of the temporal evolution of the drug elution behaviour are used to evaluate these materials as implantable drug delivery devices. One-dimensional transport of saline into an initially dry CPP ceramic is shown in Fig. 1.

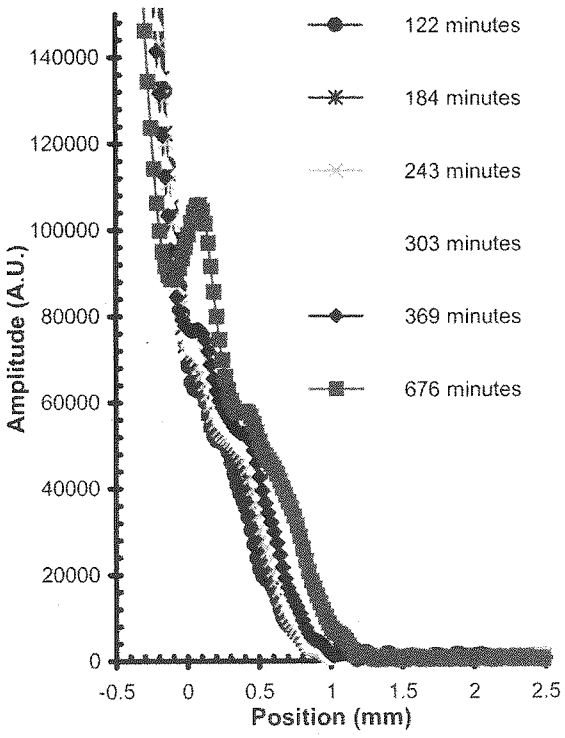

Figure 1.
MR Profiles of 1D saline ingress into an initially dry CPP bioceramic (4 mm o.d., 2 mm thickness). Images were measured at 11.7 Tesla (Bruker Avance/DRX-500) with a spatial resolution of 42 microns.

1. L.L. Hench "Bioceramics" *J. Am. Ceram. Soc.* **81**. 1705-28 (1998).
2. A. Lasserre *et al* "Ceramic Drug-Delivery Devices" *Crit. Rev. Thera. Drug. Carrier Sys.* **15**, 1-56 (1998).
3. A. Dion *et al* "Vancomycin release behaviour from amorphous calcium phosphate matrices intended for osteomyelitis treatment" *Biomat.*, in press.
4. S.D. Beyea *et al* "Non-Destructive Characterization of Nanopore Microstructure: Space Resolved BET Isotherms using NMRI" *J. Appl. Phys.***94**, 935-941 (2003).
5. S.D. Beyea *et al* "Studies of Porous Media by Thermally Polarized Gas NMR: Current Status" *Mag. Reson. Imaging* **21**, 201-205 (2003).
6. S.D. Beyea *et al* "Spatially Resolved Adsorption Isotherms of Thermally Polarized Perfluorinated Gases in Y-TZP Ceramic Materials using NMR Imaging" *Appl. Magn. Res.* **22**, 175-186 (2002).

Funding provided by the Natural Sciences and Engineering Research Council of Canada, and the Canadian Foundation for Innovation.

Lithium Imaging in Concrete Materials

Joshua J. Young[a,b], Bruce J. Balcom[a], Theodore W. Bremner[b], M.D.A. Thomas[b]
[a]MRI Centre, Department of Physics and [b]Civil Engineering, University of New Brunswick, P.O. Box 4400, Fredericton, NB, Canada, E3B 5A3

Alkali-silica reaction (ASR) is a major problem in concrete structures. ASR is an expansive reaction involving certain siliceous minerals found in some aggregates and alkalis present in cement paste pore water solution. The expansions produced by ASR cause cracking and serviceability problems in concrete structures. Lithium can be used to prevent ASR expansion [1]. Lithium is commercially used two ways: as a means to reduce further distress in ASR-affected structures by topical application of lithium solutions or as a means to use ASR aggregates in new structures when other methods of ASR mitigation are not feasible. However, the mechanism by which lithium is able to control ASR expansion is not fully understood other than that a critical quantity of lithium is needed in the pore solution of cement paste to arrest the expansion [2]. There are several destructive methods to determine lithium concentrations in concrete specimens; however, they are very time consuming and provide poor spatial resolution. MRI has been investigated as an alternate method to non-destructively determine the spatial distribution of lithium in concrete specimens [3].

The T_1 and T_2* bulk relaxation times of lithium (^{7}Li) in concrete materials are on the order of one millisecond and tens of microseconds. The short relaxation times and the need for quantitative images dictate the use of centric SPRITE methods for these measurements. The very short specimen T_2* require using very short encoding times to produce quantitative density images. Short encoding times require high strength magnetic field gradients. High magnetic field gradients lead to bandwidth limits on the radio frequency pulse. Normally the radio frequency pulse length is limited by the ratio of the T_1 of the specimen and the experimental repetition time. The pulse length is then set to a fixed value to maximize signal through the flip angle, however, in this experiment it is limited by the signal bandwidth. Since there is a k-space variation of the magnetic field gradient strength, the bandwidth limit varies with k-space point acquisition. By varying the pulse length from a longer pulse at the center of k-space to the bandwidth limiting case at the edge of k-space there are pronounced improvements in the acquired signal due to the increased flip angle at the center of k-space. In this presentation we outline the benefits of a variable flip angle excitation scheme for the lithium imaging problem.

Figure 1 is 1D Centric SPRITE image of lithium penetration into concrete. The image has a nominal resolution of 1.56 mm and was acquired in 30 minutes. The specimen was a concrete core 35 mm diameter and 40 mm long extracted from a slab that had been treated with a lithium nitrate solution. The sample had a bulk T_2* of 50 us and a bulk T_1 of less than 1 ms. The results indicate that lithium has penetrated 25-30 mm into the slab.

References
[1] McCoy, W.J., and Caldwell, A.G. Journal of the American Concrete Institute, **22:9** 693-706 (1951).

[2] Diamond, S. Cement and Concrete Research, **29:** 1271-1275 (1999).

[3] Young, J.J., et al. Seventh CANMET/ACI International Conference on Recent Advances in Concrete Technology, Las Vegas, Nevada, pp. 231-238 (2004).

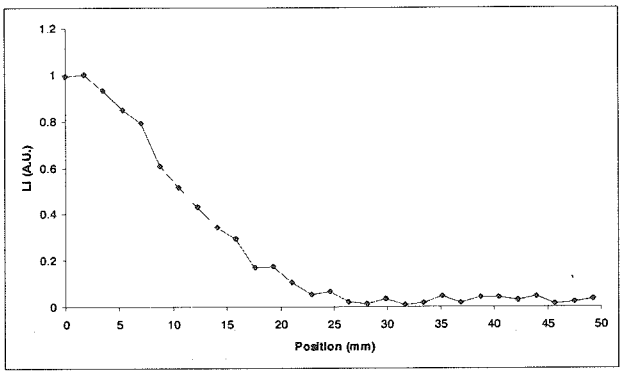

Figure 1 Centric SPRITE Image of Lithium Penetration into Concrete

Parameter imaging for analysing the spatial distribution of coke residues in porous catalyst pellets

Xiaohong Ren[1,3], Dahai Tang[1], Siegfried Stapf[1], Andreas Jess[2], Bernhard Blümich[1]

[1] Institute for Technical Chemistry and Macromolecular Chemistry, RWTH Aachen University, Worringerweg 1, D-52074 Aachen, Germany
[2] Department of Chemical Engineering, University Bayreuth, D-95440 Bayreuth, Germany
[3] College of Material Science and Chemical Engineering, Zhejiang University, Zheda Road 38, 310027 Hangzhou, PR China

In catalytic hydrocarbon conversion processes, coke deposition on the internal catalyst surface, which blocks the active sites and inhibits the molecular transport, is a major cause of catalyst deactivation. These residues lead to the deactivation of the catalyst in a twofold way. First, the coke fills a substantial amount of the void space, thus reducing the accessibility of the pore space – the increase of the pore space tortuosity has been demonstrated by PFG NMR techniques [1]. Second, coke deposition on the internal catalyst surface also blocks the active metal sites directly and affects the surface chemistry. This second effect is best observed by a change of the spectral signature, e.g. of the ^{129}Xe line of adsorbed gaseous Xenon [2], or by its influence on the relaxation properties of adsorbed liquid species [2,3,4]. This kind of deactivation is reversible, and the catalyst can be regenerated by burning off the coke with oxygen diluted in nitrogen. Regeneration of a coked catalyst particle is a gas–solid reaction and involves both chemical reaction and transport processes, and the pore diffusion strongly influences the effective reaction rate of burn-off, at least for particle diameters and temperatures relevant for industrial (fixed bed) processes (>1 mm, >400°C). Radial gradients of the carbon content are thus established during the unsteady process of coke burn-off.

This study focuses on the micro- and macroscopic distribution of coke in the catalyst particles during deactivation and regeneration, where metal-laden and metal-free Al_2O_3 substrates are compared with each other. Transverse relaxation times were shown to correlate with the coke content, providing a further probe to local sample properties beyond the already mentioned dependence of the diffusion coefficient [1]. For large (5 mm diameter) catalyst pellets, where the spatial distribution of coke becomes important, these contrasts are exploited in combination with 2D NMR imaging for the generation of parameter images. Regeneration processes were performed for identical samples but at different temperatures, leading to different degrees of heterogeneity of residual coke as a function of regeneration time. From series of differently encoded cross-sectional images, T_1, T_2 and diffusion coefficient parameter maps are obtained which clearly reveal radial heterogeneities in the samples found also from destructive classical techniques, and uneven coke distributions for supposedly fully spent catalyst pellets are identified which are inaccessible by other techniques. After calibration following known relations, maps of the coke distribution, in recycled catalyst grains are obtained which demonstrate the efficiency of the regeneration reaction at different recycling temperatures.

[1] Ren, X., Bertmer, M., Stapf, S. et al., *Appl. Cat. A* **228**, 39 (2002).
[2] Ren, X. Stapf, S., Kühn, H. et al., *Magn. Reson. Imaging* **21**, 261 (2003).
[3] Stapf, S., Kimmich, R., Seitter, R.-O., *Phys. Rev. Lett.* **75**, 2855 (1995).
[4] Levitz, P., Korb, J.-P., Petit, D., *Eur. Phys. J. E* **12**, 29 (2003).

NMR studies on rubber reinforcement properties of pyrolysis carbon black

Xiaohong Ren[1,2], Siegfried Stapf[1], Bernhard Blümich[1],
Jie Zhou[2], Geng Li[2], Yongrong Yang[2]

[1] Institute for Technical and Macromolecular Chemistry, RWTH Aachen University, Worringerweg 1, 52074 Aachen, Germany
[2] College of Material Science and Chemical Engineering, Zhejiang University, Zheda Road 38, 310027 Hangzhou, PR China

Pyrolysis has been found to be an environment friendly process for recycling of used tires. Pyrolysis carbon black (CB_p) is one of the recycling resources, which can be used as rubber reinforcement filler[1-3]. However, because of reduced structural and interior surface properties, CB_p has only the potential to replace commercial carbon black grades in certain rubber applications, such as conveyer belts and rubber boots. Modifications in the structure of CB_p to make it more attractive to the rubber industry have shown little success. In this work, methods to improve the surface roughness and micro-dispersion property of CB_p were developed. The rubber reinforcement properties of pyrolysis und modified carbon black were investigated und compared with those of commercial carbon black using Nuclear Magnetic Resonance (NMR) techniques[4-5].

The quantitative analysis of the chemical crosslink structure in sulfur-vulcanized rubber with different CB_p were conducted firstly. Peaks specific to the chemical crosslinks structures produced under different conditions were assigned using ^{13}C NMR. The ^{13}C NMR crosslink density results were correlated with the vulcanization curves.

From the short part of ^{1}H transverse relaxation time (T_2) , the influence of the carbon black on the mobility of the chain fraction near the filler particles were analyzed[4]. Parameter selective T_2 image of different carbon black filled natural rubber samples were investigated. the variation in T_2 were clearly visible. The T_2 distribution of the sample with coupling agent modified pyrolysis carbon black was more homogenous than that of the samples with other CB_p, and it was similar to that of commercial carbon black.

Considering that the Xe atom is very mobile and it absorbs only in non-crystalline region of the polymer, the crystalline domains (carbon black) can be treated to form a diffusion barrier of Xe[6]. The diffusion coefficient (D_{Xe}) of ^{129}Xe in rubber samples investigated by PFG NMR using the 13-interval PGSTE sequence to analyze the average size of the domains, and the dispersion of carbon black in rubber were estimated. Moreover, for the same samples, the self-diffusion properties of small penetrating molecules (heptane, cyclohexane) were also studied.

[1] Williams, P. T., Besler, S., and Taylor, D. T., *Proc. Inst. Mech. Eng.*, **207**, 55 (1993).
[2] Roy, C, Labrecque, B., and De Caumia, B., *Resour, Conserv. Recycl.* **4** , 203 (1990).
[3] Roy, C., Darmstadt, H., et al., *Fuel Pro. Techn.*, **50**, 87 (1997).
[4] Litvinov, V. M., and Prajna, P. D., *Spectroscopy of rubber and rubbery materials*, Rapra Technology Limited, Shawbury, Shrewsbury, Shropshire, UK, (2002).
[5] Blümich, B., *NMR imaging of materials*, Oxford University Press, Oxford, (2000).
[6] Saito, K., Kimura, A., and Fujiwara, H., *Magn. Reson. Imag.*, **21**,401 (2003).

Structure and Molecular Dynamics of Constrained Soft Materials as Studied by NMR and MRI Techniques[1]

Farida Grinberg
University of Leipzig, Linnéstrasse 5, 04103 Leipzig, Germany

Methods of NMR and MRI have continuously intervened in all areas of fundamental and applied research with up-to-date applications reaching from drug screening methods to geophysical exploration. Recent successes in molecular engineering and nano-sciences have resulted in ever expanding production of new materials with complex structures and non-trivial structure–property relationships. In many cases, a complex functionality of these materials is achieved due to specific molecular ordering on meso- and macroscopic length scales. This in turn is accompanied by multiple molecular (individual or collective) dynamical processes that tend to range over many time decades. Complex fluids like liquid crystals, polymers, colloids give rise to extremely slow spin relaxation mechanisms in the range of milliseconds and longer. The challenging problems of modern NMR/MRI are concerned with addressing hierarchic structures, multi-scale molecular dynamics and ever increasing role of interfacial phenomena.

Problem of decomposing numerous overlapping stochastic processes in constrained fluids demands an application of many complimentary NMR techniques and extending the relaxation studies to the longest time scale probed by NMR. In our work we investigate the effects produced by nano- to micrometer scale constraints on dynamical and structural properties of organised fluids using a combination of several NMR techniques: the dipolar-correlation effect and the stimulated echo studies [1, 2], 2D-exchange spectroscopy [3], the field-cycling and temperature dependent relaxometry [2, 4], diffusion studies with help of the Pulsed Field Gradient NMR [5], NMR imaging [6, 7] including maps of molecular diffusivities and of the mean squared dipolar fluctuations (MSDF). Experimental data are supported by the Monte-Carlo simulations. In liquid crystals and polymers, constraints are found to strongly affect molecular collective and non-collective orientational fluctuations. Quantitative parameters like correlation times below and above phase transitions and the correlation length of the surface-induced order were determined. The MSDF associated with residual dipolar couplings was proven to be an extremely useful contrast parameter for NMR mapping [6]. The advantages of employing various map parameters for characterization of materials are discussed.

References

[1] F. Grinberg and R. Kimmich. *J. Chem. Phys.* **105**, 3301-3306, 1996.
[2] F. Grinberg, M. Vilfan, E. Anoardo. In *NMR of ordered liquids*, edited by E. E. Burnell and C. A. de Lange, Kluver Academic Publishers (Boston, Dordrecht, London), 2003.
[3] F. Grinberg. In NATO SCIENCE SERIES "Magnetic Resonance in Colloid and Interface Science", edited by J. Fraissard and O. Lapina, Kluver Academic Publishers, Dordrecht, 2002.
[4] R. Kimmich. *NMR: Tomography, Diffusometry, Relaxometry* (Springer-Verlag, Heidelberg, 1997).
[5] F. Grinberg, G. Majer, A. Skripov, Phys. Rev. E, submitted, 2005.
[6] F. Grinberg, M. Heidenreich and W. Kuhn, *J. Magn. Reson.*, **159**, 87-91, (2002)
[7] F. Grinberg. In Handbook of Modern Magnetic Resonance, G. Webb, Ed., Kluwer Academic Publishers, (London), 2005.

Acknowledgements
I cordially thank Prof. Dr. R. Kimmich for the most fruitful co-operation during a multi-year stay in his laboratory at the University of Ulm. My warmest thanks go to the NMR group leader at the MPI for Metals Research Dr. habil. G. Majer for the most enjoyable and fruitful mutual work. I thank Prof. Dr. J. Kaerger at the University of Leipzig for helpful discussions and excellent research conditions. I further thank all co-authors of the common papers.

[1]Experiments demonstrated in this work were performed in three German research institutions: the University of Ulm, the Max-Planck Institute for Metals Research (Stuttgart) and at the University of Leipzig.

Spatial Mapping of Solid and Liquid Lipid in Confectionery Products using a 1D Pure Phase Encode MRI Technique

[1]Bruce J. Balcom, [1]Kumud Deka, [1]Bryce MacMillan, [2]Alejandro G. Marangoni, [3]Gregory R. Ziegler and [1]Ben Newling
[1]University of New Brunswick, [2]University of Guelph and [3]Penn State University

The migration of fat is a common problem with chocolate coated confectionery products. Fat migration can lead to many undesirable changes such as softening of the coating, hardening of the filling, drying of the filling and re-crystallization of fat that leads to the phenomenon known as fat bloom. Sensory changes also occur due to fat migration since flavors are oil soluble and migrate with the fat, thereby disturbing the flavor balance of the product. Fat recrystallization can also lead to texture changes.

Researchers have used different approaches to detect and quantify fat migration. The quality of results obtained is dependent on the method used. The major difference between methods is in the means of quantifying the concentration of the diffusing species.

The extent of migration is most commonly analyzed using gas liquid chromatography or by analysis of the iodine index to give the iso-oleic acid content. The combination of these two tests is used to measure the migration of fat from biscuits to the enrobing chocolate. These methods give the fatty acid distribution, but no information regarding the state or mechanism of movement of the fats. Other methods are required in combination with these techniques to yield a complete picture of the migration process.

The extent of migration has also been determined by measuring the solid fat content of the different components. The solid fat content in bulk is normally determined by pulsed NMR methods. However, the existing body of MRI work does not provide information on the total fatty acid distribution (solid and liquid) [1]. Conventional MRI imaging can only detect signal from the liquid protons, since the signal from solid protons decays very rapidly (tens of micro-seconds) after the NMR excitation. Therefore, spatially-resolved measurement of solid/liquid fat rely upon calibrated inference from the liquid fat signal. This is clearly not satisfactory.

Until now, imaging the solid lipid in chocolate has been a challenge. In this work, a 1D centric scan SPRITE (Single Point Ramped Imaging with T_1 enhancement) technique [2] coupled with a dedicated high strength magnetic field gradient set [3] is employed to acquire solid and liquid lipid images. We present one-dimensional images (profiles) of a dynamic hazelnut oil absorption experiment. A Gaussian-Sinc function is used to fit the solid lipid component [4]. We also present one dimensional spatially resolved solid/liquid distribution maps from a 5 mm thick chocolate sample.

References

[1] Guiheneuf, T. M., et al., Visualization of liquid triacylglycerol migration in chocolate by magnetic resonance imaging, *J. Sci. Food Agric.* **73(3)**, 265-273 (1997).

[2] Derbyshire, W., et al., Fitting of the beat pattern observed in NMR free-induction decay signals of concentrated carbohydrate-water solutions, *J. Magn. Reson.* **168(2)**, 278-283, (2004).

[3] Mastikhin, I. V., et al., Water Content Profiles with a 1D Centric SPRITE Acquisition, *J. Magn. Reson.* **156(1)**, 122-130 (2002).

[4] Deka, K, et al., Quantitative Density Profiling with a Pure Phase Encoding and a Dedicated 1D Gradient, *J. Magn. Reson.* (2005), submitted.

Estimation of Ungelatinized Region in Cooked Spaghetti from Moisture Distribution and Mechanical Property

Akemi K. Horigane[1], Kentaro Irie[2], Shigehiro Naito[1], Tatsurou Maeda[3], Hirofumi MotoiI[3] and Mitsuru Yoshida[1]

[1]National Food Research Institute, Tsukuba, Ibaraki, Japan, [2]Initio Foods Inc., Kanda-nishiki-cho, Chiyoda-ku, Tokyo, Japan, [3]Nisshin Seifun Group Inc., Oi-machi, Iruma, Saitama, Japan.

Introduction: The texture of cooked spaghetti with a thready core of ungelatinized starch, which is called "al dente", is preferred by consumers. The deterioration of texture of pasta or noodles after cooking was caused by the homogenization of moisture content due to diffusion[1)]. We have investigated the moisture distributions in several kinds of cooked spaghetti by micro-MRI to clarify the relationship between the moisture distribution and mechanical properties[2)]. As the moisture diffusion should be different in ungelatinized and gelatinized starch, determination of ungelatinized region is necessary for water diffusion study of pasta. In this study ungelatinized region in cooked spaghetti was estimated from the moisture profile obtained by MRI. The mechanical property of cooked spaghetti with ungelatinized region was discussed in connection with their moisture profile.

Materials and Methods: Dried spaghetti of a 1.7 mm diameter was made from durum semolina, and was boiled for varied boiling time. T2 maps of cooked spaghetti were obtained using a NMR spectrometer with a 7.1 Tesla magnet (DRX300WB, Bruker) and the ParaVision software package (Bruker) for NMR imaging. The sample treatment and measurement of T_2 maps of cooked spaghetti followed the method reported by Irie et al[2)]. The moisture distributions of cooked spaghetti were calculated from the T_2 maps using the relationship between T_2 values of gelatinized flour and moisture contents[1)]. The micro-structures of cooked spaghetti stained by fluorescence dye were observed under a fluorescence microscope (BX-51, Olympus). The force-displacement curves were obtained by a material tester (EZ test, Shimadzu), and their first and second derivative curves were calculated.

Results and discussion: The spaghetti strand cooked as "al dente" could be divided into two regions, i.e. hard core and periphery with softer texture. Collapse of starch granules was observed in the periphery, not in the core, with the microscopic observation. The moisture gradients in these regions calculated based on the T_2 maps were different, and their intersection located at the boundary between the regions. The moisture content at the intersection just after cooking was about 45% for all samples despite of difference in boiling time. This value is considered to be lower moisture content limit for the starch gelatinization in this type of samples. The intersection stayed at the same location until 2 hours after boiling although the moisture content at the point increased with the holding time. The second derivative curve of force-displacement curve was demonstrated to have a specific peak corresponding to the intersection of moisture gradients of gelatinized and ungelatinized regions in the boiled spaghetti.

Conclusions: The analysis of moisture profile enabled estimation of the ungelatinized region in the cooked spaghetti strands. The border between the gelatinized and ungelatinized regions may also be estimated from a specific peak on the second derivative curve of force-displacement curve.

References:

1) Kojima, T. I. et al., J. Food Sci. **66**, 1361–1365 (2001).
2) Irie, K. et al., Cereal Chem. **81**, 350-355 (2004).

The relationship between NMR parameters and respiratory metabolism inside cucumber fruit after harvest

Shinichiro Kuroki[1)], Jeffrey H. Walton[2)], Yoshinori Kawagoe[3)], Yoshio Makino[3)], Seiichi Oshita[3)]

[1)] Hiroshima University Collaborative Research Center, Higashi-Hiroshima, JAPAN
[2)] University of California Davis NMR Facility, Davis, USA
[3)] Graduate School of Agricultural and Life Sciences, The University of Tokyo, Tokyo, JAPAN

Introduction

Water in fruits and vegetables is the medium in which biochemical reactions occur. Therefore there is a close relationship between and physico-chemical property (dynamic state) of water and physiological state in the tissue (Ishida et al., 2000). 1H-MRI is a unique tool which can obtain information on the dynamic state of water in vivo. MRI measurements enable acquisition of a spatial distribution of water density and mobility. On the other hand, respiratory metabolism of postharvest horticultural products is known as an effective index for comprehending their physiological state. Respiration rate mainly depends on atmospheric temperature and oxygen concentration. Most of the previous studies made little attention to internal gas condition of the products; however, a considerable distribution of oxygen concentration exists inside the products, i.e., it is expected that respiration rate inside fruits and vegetables vary by internal oxygen concentration at each place. The objective of this study was, therefore, to examine the dynamic state of water via NMR relaxation time, as it relates to respiratory metabolism in cucumber fruit. Temporal variation in water mobility during storage was also investigated.

Materials and Methods

Parthenocarpic English cucumber fruits (*Cucumis sativus* L., cv. unknown) grown in a greenhouse were used. The fruit (about 37mm in diameter and 230mm in length) was harvested early in the morning and transported at ambient temperature from a local farm to a laboratory in UC Davis. Fruit in control was stored in a film bag and ventilated once a day to maintain atmospheric gaseous composition of fruit surroundings. The other fruit was stored and not ventilated to keep low O_2 and high CO_2 condition in the bag (MA condition).

^1H density and T_2 images of the transverse plane at the middle of the longitudinal axis of the fruit were obtained by MRI (Biospec 7T, 300MHz, coil diameter 72mm, Bruker BioSpin, located at UC Davis). A small glass and a micro capillary containing tap water were taped along the side of each fruit to ensure the experimental accuracy of NMR parameters and to obtain the images at the same transverse plane of the fruit, respectively. Using the spin-echo method, 16 images were sequentially acquired through each transverse slice plane with the constant repetition time (T_R=1500ms) and the echo time ranging from 13 to 208ms in 13ms increments for calculation of ^1H density and T_2 values. ^1H density and T_2 images were reconstructed and displayed on a 256x256 pixels array corresponding to 48x48mm. Each image was 1mm thick with an in-plane resolution of 187.5μm. Temperature during storage and MRI measurement was maintained at 19.8±0.5℃.

Results and Discussion

Large differences in quantity of water in each part of cucumber fruit were observed from ^1H density image. The amount of water was largest the seeds and was successively less in order in skin and its vicinity, flesh and placenta. Water in the flesh decreased with storage period, specifically. This result suggested that the decline in fresh weight during storage due to transpiration was a loss of water mainly from the flesh.

In T_2 image, means of each ring area between concentric circles in which origin was the fruit center were calculated to examine T_2 dependence on radial direction. T_2 at seeds in control was significantly greater than that under MA condition. Therefore, MRI enabled to detect an depression effect of low O_2 and high CO_2 condition on the respiratory metabolism inside the fruit. T_2 in seeds and that in flesh increased and decreased during storage period, respectively. In addition the closer to skin, the higher the T_2 was. These results show there is an O_2 concentration gradient that decreases as it approaches the center of fruit (Kuroki et al., 2003) and its temporal variation during storage.

Conclusions

It was shown that NMR parameters such as ^1H density and T_2 were useful probes to detect the spatial distribution of the amount of water and the activity of respiratory metabolism. We clarified that (1) the water that existed in the flesh was lost by transpiration, and (2) T_2 depended on O_2 concentration and metabolic activity in each tissue.

References

Ishida et al., Annals of Botany 86: 259-278, 2000.
Kuroki et al.,62nd JSAM Annual Meeting, 189-190, 2003

Water Behavior and Water Channel Gene Expression in Vegetative and Flower Dormant Buds of Peaches Having Different Chilling-requirement during Winter Period

Suravoot YOOYONGWECH[1], Akemi K. HORIGANE[2], Mitsuru YOSHIDA[2], Masami YAMAGUCHI[3], Sumiko SUGAYA[1] and Hiroshi GEMMA[1]

[1]University of Tsukuba, Tsukuba, Ibaraki, Japan, [2]National Food Research Institute, Tsukuba, Ibaraki, Japan, [3]National Institute of Fruit Tree Science, Tsukuba, Ibaraki, Japan.

Introduction: Temperate fruit trees have a phase of development called dormancy allowing the tree to survive under unfavorable conditions in winter (Faust et al., 1997). Dormancy is a process affected by various integrated factors. One of these factors is water content of buds, which can be associated with dormancy-related transitions in genes and physiological level (Dennis, 1994). However, conventional methods for measurement of water content could not give enough data for understanding of the developmental process of the dormant buds. We thus used MRI to investigate the water status in low-chill and high-chill peach buds from dormancy until flowering together with water channel gene expression.

Methods: The vegetative and flower buds of 5-year old of a low-chill cultivar, Coral and 10-year old of a high-chill cultivar, Kansuke Hakuto were collected during winter from November, 2004 until February, 2005. The spin-spin relaxation time (T_2) was measured on an NMR spectrometer (DRX300WB, Bruker) with a 7.1 Tesla magnet using following parameters: repetition time 2 sec; echo time, 4.5 msec; field of view, 10 × 10 mm^2; matrix size, 128 × 128; slice thickness, 1 mm, and two transient acquisitions were accumulated. T_2 maps were calculated by ParaVision program (Bruker). In order to check the expression of water channel (*Pr-PIP1*) gene, RNA was isolated from the Coral and Kansuke Hakuto buds during 2002-2003 season by modified CTAB-based extraction method, and analyzed by Northern blotting hybridized with *Pr-PIP1* DNA probe.

Results and Discussion: Coral showed 50% bud break in middle of December, and Kansuke Hakuto in late January. Changes in the average T_2 values in primordia, basal-part, and vascular bundle of the flower buds were compared between the cultivars. Increase of T_2 was observed earlier in Coral than in Kansuke Hakuto for every part of the buds. Kansuke Hakuto clearly showed high T_2 value in last stage. The vegetative buds showed similar changes. The analysis of mRNA of vegetative buds showed that the *Pr-PIP1* expression of the Coral buds increased at a high level throughout December, 2002 to February, 2003. In Kansuke Hakuto, the expression slightly increased in December, and maintained at high level until the February. T_2 map change showed water dynamics in buds.

Water transport during dormancy and bud-break was estimated from the T_2 of each part. Water movement was detected in the buds even at resting stage. The results imply that an aquaporins (water channels) might be involved in water transportation in buds during winter period.

References:

Faust, M., Erez A., Rowland L.J., Wang S.Y. and Norman H.A. Hort. Sci. **32**(4), 623-629 (1997).

Dennis, F.G., Jr. Hort. Sci. **29**(11), 1249-1263 (1994).

Visualisation of the water distribution in plant roots and model soils for the study of root/soil interactions

A. Pohlmeier[1], J. Lindenmair[2], A. M. Oros-Peusquens[3] and P. Blümler[2]

[1] *Institute Agrosphere ICG IV, Research Centre Jülich, D-52425 Jülich, Germany*
[2] *Institute Phytosphere ICG III, Research Centre Jülich, D-52425 Jülich, Germany*
[3] *Institute of Medicine IME, Research Centre Jülich, D-52425 Jülich, Germany*

Purpose: The aim of this project is a feasibility study of root-soil interaction by means of MRI. Therefore it is important to non-invasively monitor the water distribution in the soil and/or the growth (3D-structure) of the plant root.

Methods: 3D MRI data sets of ricinus roots in unsaturated model soils: natural sand (0.15 mm) and a mixture of sand with 6.5% clay minerals were acquired in a standard medical scanner at 1.5T, where the planting vessel is placed inside the head coil. The relaxation behaviour of the different soils are compared for two pulse-sequences: CISS and GRE with a medium flip angle and short T_R, but varying the echo time in a range between 2.5 and 10 ms. With this setup the root growth is monitored over a period of 11 days.

Results: As expected the visibility of the water inside the soil compartment strongly depends on the pore sizes and content of paramagnetic centres. Figure 1 clearly shows that even for short echo times of 3 and 4 ms, respectively, the water in the coarse pore system "sand" has not been relaxed, and is hard to distinguish from the root system. Whereas in the finer pore system of the sand/clay mix essentially only the root system is visible, although both soils contain comparable amounts of water.

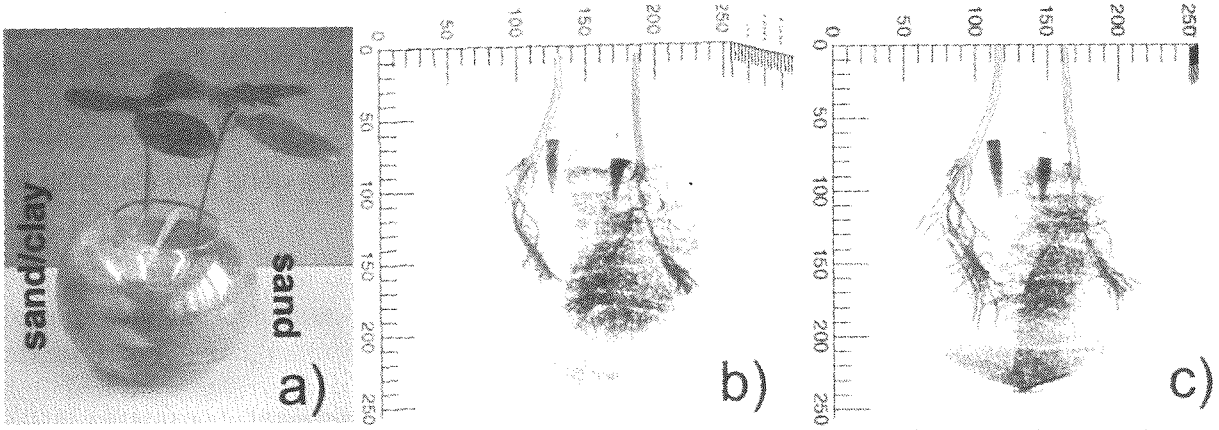

Figure 1: a) Setup: Two ricinius plants in sand/clay mix (left) and pure sand (right). b) Central slice through a 3D-MRI data set in the same orientation. c) comparable position 5 days later to demonstrate root growth.

Discussion: It is clearly demonstrated that MRI is an ideal method to non-invasively study root growth. However the quantification of water in the soil is problematic, due to the varying pore sizes and content of para- or even ferromagnetic impurities in "normal soil". Although, the shown example clearly demonstrates that the chosen soil greatly influences the MRI-contrast, it would be ideal to switch the contrast between "root only" and "root and water in soil" by the pulse-sequence only. Therefore, various soil samples have to be tested for their T_1 and T_2 relaxation behaviour.

Development of a novel reporter system using NMR and MRI to measure gene expression in living cells

Fuminori Sugihara, Sewon Ki, Koji Kasahara, Kaoru Serizawa, Akiko Kobayashi, Kiyoshi Watanabe, Masahiro Shirakawa, Tetsuro Kokubo

Graduate school of integrated science, Yokohama City Univ. 230-0045 Tsurumi, Yokohama, Japan

We are developing a reporter assay system using NMR and MRI to measure gene expression in living cell. In this assay system, gene expression (the process of conversion of information encoded in a gene to mRNA and then protein) is "reported " by polyphosphate ^{31}P NMR signal and quantified in a relative manner.

At first, a number of genes predicted to involve in accumulation of polyphosphate in yeast *Saccharomyces cerevisiae* are screened and we took several genes as reporter gene. Next, we made test constructs which have several kinds of promoter sets in the promoter of reporter gene and measured the amount of polyphosphate in yeast cell by ^{31}P-NMR and mRNA of reporter gene by Northern blotting after appropriate liquid culture. As a result, the correlation of the amount of polyphosphate to mRNA of reporter gene yielded good correlation coefficient.

Applying this assay system for MRI, chemical shift selective (CHESS) imaging method was introduced. After some modification, polyphosphate selective image of yeast colony and capillaries were acquired successfully. At the same imaging experiment, we found correlation between the amount of polyphosphate and ^{1}H T_1 time of yeast. Although the mechanism of the correlation between them is still unclear, higher sensitive imaging of gene expression is available by using ^{1}H signal instead of ^{31}P.

In future, we plan to utilize this method for promoter analysis of yeast gene and also plan to apply this reporter system for model animals and plant.

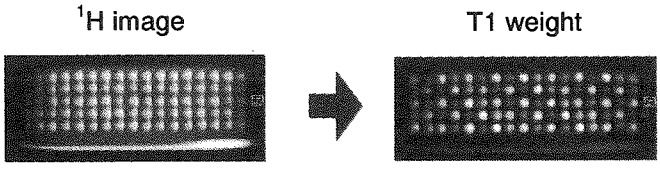

Fig. 1 Colony image and ^{1}H T_1 weighted image of colony plate
6 types of yeast strains were arrayed and cultured on culture plate. After several days of culture, images were acquired using Burker DRX-500 and Micro imaging probe Micro5.

Magnet resonance imaging of NCL- and NCL related mouse models

A Haapanen[1], U AboRamadan[2], C von Schantz[3], J Fuhrmann[4], TJ Jentsch[4], T Braulke[5], P Saftig[6], A Jalanko[3], T Autti[6] and J Tyynelä[1]

[1]Institute of Biomedicine/Biochemistry, University of Helsinki, [2]Department of Neurology and [6]Department of Radiology, Helsinki University Central Hospital, and [3]Molecular Medicine, NBHI, Helsinki, Finland; [4]Center for Molecular Neurobiology and [5]Department of Biochemistry, Children's Hospital, University of Hamburg, Germany; [6] Biochemical Institute, University of Kiel, Germany.

At present, there are multiple mouse models available for NCL-diseases. In addition, the chloride channel ClC-3 and ClC-7 knock-out mice show neuropathological features closely resembling those seen in NCL mice. Here we report the *in vivo* magnet resonance imaging (MRI) findings on CLN1 (imaging age 4 months), CLN5 (4 months), CLN6 (9 weeks), ClC-3 (9 weeks), ClC-7 (24 days) and CTSD (25 days) deficient mouse models, all of which were imaged in a 4.7 T scanner (PharmaScan, Bruker, Germany).

Of the studied mice, the brains of CTSD and ClC-7 mice were most severely affected, showing a profound generalized atrophy. CTSD mice exhibited global increase of the signal intensity (SI) on midsagittal T_2-weighted images. Interestingly, more lateral nuclei of the thalamus (VPM and VPL) showed increased SI on T_1 –weighted images of both CTSD and ClC-7 mice.

ClC-3, CLN1 and CLN6 mice were moderately affected: ClC-3 and CLN1 mice showed decreased areas of the cerebral cortex and thalamus. On T_2-weighted images, ClC-3 and CLN6 deficient mice showed decreased SI values in the posterior (Po) and lateral posterior mediorostral (LPMR) thalamic nuclei. In addition, the SI of the corpus callosum was increased in all three models. CLN5 deficient mice were mildly affected, showing only increased area of the hippocampus and a mild increase of the SI in the corpus callosum.

From these data we can conclude: Firstly, increased SI of the corpus callosum is a common feature that these mouse models share. Secondly, both structural and SI changes of the cerebral cortex and, particularly, thalamus, were observed in all mouse models, except CLN5 deficient mice, which show a relatively slow progression of the disease. These findings are in good agreement with MRI findings in human NCL patients, showing altered SI of the periventricular white matter and specific thalamic nuclei.

Development of Targeted Contrast Agents for MRI of Prostate Cancer

Laurel Sillerud,[1] Natalie Adolphi,[2] Rita Serda,[1] Marco Bisoffi[1] and Dean Kuethe[2]
University of New Mexico[1] and New Mexico Resonance[2]
Albuquerque, NM 87106, USA

Introduction: New detection methods are needed for prostate cancer, particularly for metastatic disease, in order to provide patients the best possible staging and treatment. Our aim is to locate primary tumors or distant metastases using MRI with contrast agents targeted specifically to cancer cells. We take advantage of the fact that many types of prostate cancer cells express high levels of prostate specific membrane antigen (PSMA) on their cell surface. The imaging strategy is to use superparamagnetic iron oxide nanoparticles (SPIONs), attached to an antibody that binds to PSMA, to specifically enhance the contrast of PSMA-expressing prostate cancer cells. The use of antibody-conjugated MRI contrast agents to specifically target cancer cells has been demonstrated previously for some other cancers.[1] The use of monoclonal antibody (Mab) J591, conjugated to a radioisotope, has been used for gamma camera imaging of PSMA-expressing cancers.[2] Here, we demonstrate the first MRI contrast agent targeted specifically to the external cell surface of PSMA-expressing prostate cancer cells.

Methods: A number of cell lines were investigated by flow cytometry and reverse transcriptase polymerase chain reaction to determine their level of expression of PSMA. Two cell types were chosen for MRI experiments: LNCaP cells, which express a high level of PSMA, and DU-145 cells, which do not express PSMA. Conjugation of Mab 3C6 to commercial streptavidin SPIONs (Dynabeads® or MACS® beads) was achieved using the standard avidin-biotin reaction. LNCaP and DU-145 cells were cultured *in vitro*, allowed to bind with biotinylated 3C6 antibodies, and then incubated with streptavidin SPIONs. The cells and bound contrast agent were separated from unbound SPIONs by repeated centrifugation. The cells were then resuspended in agarose gel and layered into a plastic test tube. MR imaging was performed in a 1.9 T Oxford horizontal bore magnet using a Tecmag Libra spectrometer, Resonance Research shielded gradient set, and a Morris Instruments birdcage probe. The T_1 and T_2 contrast were investigated using 2D spin echo (T_1-weighted ,T_2-weighted), inversion-recovery-prepared 1D spin echo, 2D gradient echo, and 3D-FID projection imaging.

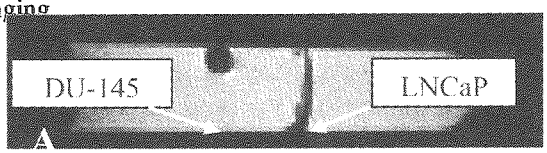

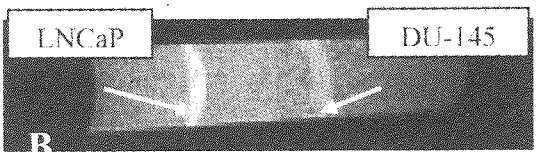

Results and Discussion: Fig. A shows a T_2-w 2D spin echo image of a sample prepared with Dynabeads® (1 μm diameter, 37% iron oxide by weight), showing good T_2 contrast of the LNCaP cells relative to both the DU-145 cells (located below the air bubble) and the background agarose gel. Measurements of T_2 for each sample component indicate that the SPION concentration is 13 times higher in the LNCaP cells compared to the DU-145 cells. Fig. B shows a T_1-w 2D spin echo image of a sample prepared with MACS® beads (50 nm diameter, 57% iron oxide by weight). The MACS® beads have a smaller magnetic moment resulting in reduced T_2/T_2^* effects; however, the smaller diameter results in more rapid spatial variations of the magnetic field in the regions immediately surrounding the beads. The diffusion of water through these more rapidly varying fields leads to a shorter correlation time for magnetic field fluctuations, causing enhanced T_1 relaxation. The LNCaP cells show good T_1 contrast, while the DU-145 cells show weak contrast relative to the background agarose. For the MACS® sample, T_1 measurements indicate that the SPION concentration is 3 times higher in the LNCaP cells than in the DU-145 cells. The difference we observe in the *in vitro* binding specificity of the Dynabeads® compared to the MACS® beads warrants further investigation.

Conclusions: In these *in vitro* experiments, we have shown that one can synthesize and image an MRI contrast agent specifically targeted to PSMA-expressing prostate cancer cells, using Mab 3C6 conjugated to commercial SPIONs. Depending on the size of the SPION, either T_1 or T_2/T_2^* contrast can be achieved, allowing for great flexibility in the choice of MRI sequence. Experiments on mice with subcutaneous LNCaP and DU-145 tumors are currently underway to test the effectiveness of the contrast agents *in vivo*.

References: [1] e.g., Remsen LG, et al. Am J. Neuroradiol. 1996;17:411-8; Artemov D, et al. Magn. Reson. Med. 2003;49:403-8. [2] Bander NH, et al. J. Urol. 2003;170:1717-21.

Diffusion and T_2 changes after seizures induced by glutamatergic drugs lasting 60 minutes

J. Munasinghe, M.Acosta, M. Banerjee, A. Silva, A. Koretsky, M Rogawski, A. Yamaguchi, W. Theodore
National Institute for Neurological Disorders and Stroke. NIH. Bethesda. MD. 20850. USA.

Epilepsy is a serious neurological disorder affecting 1% of people. Glutamate receptors have been implicated in altered excitation and inhibition leading to functional and structural derangements associated with epileptogenesis. MRI and animal models can be used to study the evolution of lesions associated with epilepsy, underlying mechanisms, regional anatomic vulnerability, and response to therapy. Previous studies have shown altered t2 and diffusion after prolonged status epilepticus. We used three different glutamate receptor agonists, Kainic acid (KA), AMPA and ATPA (a specific gluR5 receptor agonist) to induce seizures; saline was used as control. After amygdala injection in rat brains, T_2 and diffusion image maps were generated to quantitate changes in different brain regions after seizures lasting 60 minutes.

Rats anesthetized with ketamine / xylazine had MR-compatible cannulae placed stereotaxically in right basolateral amygdala. After several days rest, they were intubated and anesthetized with isoflurane. Lines were placed in femoral artery to monitor blood pressure, and femoral vein for drug and fluid administration. Body core temperature was maintained at 37 degrees with a heated circulating water pad. Blood gases were analyzed at frequent intervals. MR imaging was performed on a 7T Bruker Avance scanner. Animal heads were stereotaxically fixed. Intra-amydgala studies were done with a 72 mm radio frequency coil operating in transmit receive mode. Ten nanomoles of KA (n = 3 rats), AMPA (n=4 rats), ATPA (n=4 rats) in 5 microliters of saline was injected over five minutes; two rats had saline alone. Pilot images were obtained to locate the cannula/amydgala site and five 1 mm thick axial amydgala centered slices were selected. Eighty minutes post infusion of an agent, multi echo T_2 weighted (TE=10 ms, 16 echos, TR= 3 s, Matrix 128x128) and stimulated echo diffusion weighted sequences (b = 4, from 0 to 3000 g/cm, TE= 20 ms, Δ=32 ms, TR= 2.5 s, matrix 64x64) with same geometry (FOV=3.2 cm) were performed in three orthogonal directions. T_2 and ADC maps were generated and regions of interest (ROI) were placed in left and right amygdale. Because cerebral blood flow studies, suggested focal specific amygdala glutamate receptor stimulation leads to widespread brain activation, additional ROIs were placed on the hippocampi, sensory and motor cortices of both hemispheres. Animals' vital signs were stable during pre and post agent administration and interference due to agent accumulation before dispersion, and local edema proximal to the cannula site, was negligible.

There was a significant drug effect on average ADC value in right amygdala ($F = 7.9$; $p<0.01$). KA and ATPA led to larger reductions than AMPA. Average ADC was not significantly affected in other regions. KA also reduced ADC along read direction in right amygdala (ATPA data not available). All three agents increased T_2 in left and right hippocampus and left amygdala. KA had the greatest effect.

This study shows that seizures induced by amygdalar infusion of glutamatergic agonists lead to decreased diffusion in the epileptogenic region, and increased T_2 signal in more widespread limbic cortex. Our study shows that MRI evidence of potential cytotoxic injury (reduced diffusion and increased T_2 may be related to cytotoxic edema) can occur acutely after one hour of seizure activity. T_2 and ADC changes may have been limited to limbic, rather than affecting more widespread cortical regions due to the relatively short seizure duration.

Articular Cartilage Microstructure Analysis Using Diffusion Tensor Imaging

Roger Meder, Sally K. de Visser and James M. Pope
School of Physical and Chemical Sciences, Queensland University of Technology, Brisbane, Australia.

Introduction: Although osteoarthritis is the leading cause of disability in the United States, affecting an estimated 20% of the population, and with socio-economic costs totalling $82 billion per annum (1), the fundamentals of the progression of osteoarthritis remain poorly understood. This results in an inability to optimise treatment regimes.

The aim of this study was to use diffusion tensor MR micro-imaging to observe differences in magnitude and anisotropy of water diffusion between 'healthy' cartilage and cartilage which was enzymatically degraded to simulate arthritic damage. The success of this method provides researchers with a new technique with which to investigate changes in cartilage due to osteoarthritis.

Methods: Diffusion tensor images (156 x 156 μm in plane resolution, 2 mm slice thickness) of cartilage from eight bovine patella grooves were obtained at 4.7 T using pulsed field gradient spin echo sequences. Diffusion tensors were obtained using δ 2 ms and Δ 8 ms. The samples were oriented at the 'magic angle' (2, 3) to obtain maximum signal through the depth of the cartilage sample. The parameters determined were: maximum and mean diffusivity, direction of the maximum diffusion eigenvector with respect to the normal to the articular surface and fractional anisotropy of diffusion. Samples were maintained prior to analysis in Minimum Essential Medium with Earle's salts. Samples were imaged before and after enzymatic treatment. All enzymatic treatments were performed overnight (14 hours) at 37 ºC on an orbital incubator, with four samples being treated with trypsin (0.1 g/mL) and four with collagenase Type VII (300 U/mL).

Results: Both mean and maximum diffusion eigenvalues decrease from the articular surface to the deep zone and the eigenvector which corresponds to maximum diffusivity, exhibits systematic changes in its orientation, which in turn reflects the expected change in orientation of the collagen macrofibrillar bundles. Degradation with trypsin results in an increase in diffusivity of between 10-20% in the deep zone of the cartilage (see figure), with no apparent change in fractional anisotropy or eigenvector, whereas degradation with collagenase results in no discernible change in ADC, FA or maximum diffusion eigenvector.

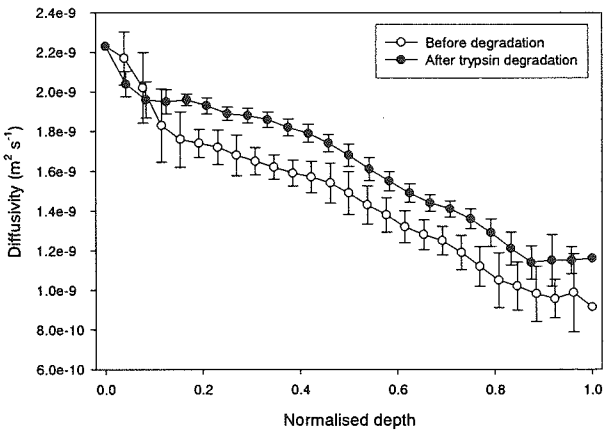

Discussion: We have demonstrated that analysis of the eigenvalues and eigenvectors resulting from diffusion tensor imaging can be used to probe the microstructure of articular cartilage. Specifically we have demonstrated that the orientation of the maximum diffusion eigenvectors reflects the gross arrangement of the collagen fibre bundles in arcades. Furthermore the magnitude of diffusion, as determined from the eigenvalues, is shown to decrease from the articular surface towards the deep zone and reflect changes due to degradation using trypsin. These results suggest that the data obtained from the water self-diffusion tensor can be used to investigate changes in the micro-structure and hydrodynamics of cartilage resulting from enzymatic degradation or naturally occurring arthritic decay. In the event that the cartilage micro-fibrils become less highly oriented, then the angular alignment of the maximum diffusion eigenvector would be expected to become more random. Additionally if voids appeared in the tissue the mean diffusivity would be expected to increase and the fractional anisotropy to fall. In the case of trypsin degradation we have shown that observable changes in the diffusivity result from increased mobility of the fluid due to proteoglycan depletion.

1. Praemer A, Furner S, Rice DP, *American Academy of Orthopedic Surgeons,* Rosemont, IL, (1999).
2. Xia Y. *Magn Reson Med* **39**, 941-949 (1998).
3. Xia Y. *Invest Radiol.* **35**, 602-621 (2000).
4. Meder R, de Visser SK, Pope JM. *Osteoarthritis and Cartilage* (submitted)

Effects of stress-shielding on the dynamic viscoelasticity and ordering of the collagen fibers in the Achilles tendon

Kazuya Ikoma*, Yoshiteru Seo, Yasuo Mikami*,**
Yoshiaki Kusaka*, Toshikazu Kubo***
Department of Orthopaedics*, Graduate School of Medical Science,
Kyoto Prefectural University of Medicine, Kyoto, 602-8566, JAPAN
Department of Regulatory Physiology**,
Dokkyo University School of Medicine, Tochigi, 321-0293, JAPAN
Department of Orthopaedic Surgery***, Murakami Memorial Hospital,
Asahi University, Gifu, 500-8523, JAPAN

Introduction: Structural and compositional homeostasis of the tendons and ligaments are maintained owing to tensile stress, which is exerted during daily activities. Stress-shielding to the tendons and ligaments due to cast fixation or nerve palsy may cause structural and compositional alterations of these tissues, and leading to contracture of the involved joints. The effects of stress-shielding on both the viscoelastic properties and micro-structure of collagen fibers in the Achilles tendon were studied by a viscoelastic spectroscopy and ^{1}H double-quantum filtered NMR spectroscopy and MRI.

Materials and Methods: The right hind-limb of twenty Japanese white rabbits were immobilized for four weeks in a cast with the ankle in plantarflexion. Bilateral Achilles tendons were dissected and the right Achilles tendons were used as a stress-shielding model (SS group). The left Achilles tendons served as controls (control group). Dynamic viscoelasticity of the Achilles tendons of the both groups was measured using a viscoelastic spectrometer (VES-F-3; Iwamoto). In addition to a static tensile load of 100 g, a cyclic tensile load of 20 g at frequencies ranging from 0.1 to 80 Hz was applied to determine dynamic storage modulus (E') and dynamic loss modulus (E"). Proton double-quantum filtered (^{1}H-DQF) NMR signals were analyzed to determine the residual dipolar coupling of bound water molecules in the Achilles tendons. The Achilles tendon in an NMR sample tube was directed parallel to the static magnetic field of the NMR spectrometer operating at 7.05 Tesla (AMX-300 wb; Bruker). ^{1}H-DQF NMR signals and MRI were obtained employing the following pulse sequence:

$90°$-$\tau/2$-$180°$-$\tau/2$-$90°$-t_{DQ}-$90°$-(acquisition),

where τ is the creation time and t_{DQ} is the evolution time of the DQ coherences. A large part of the water molecules in the tendon tissue are aligned along the longitudinal axis of the tendon because of their strong binding to the collagen fibers. Therefore, the residual dipolar coupling of bound water molecules in the Achilles tendon, which quantifies the degree of ordering of water molecules, can also quantify the degree of longitudinally ordered structures of the collagen fibers.

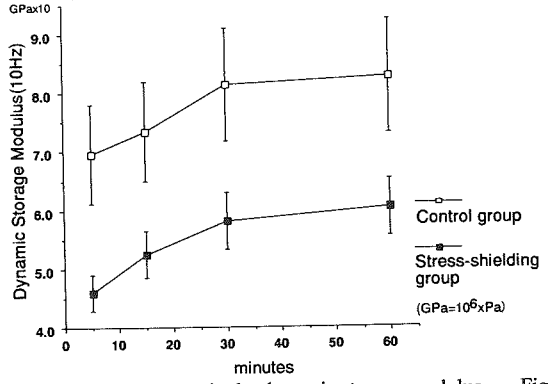

Fig.1 Time-dependent changes in the dynamic storage modulus.

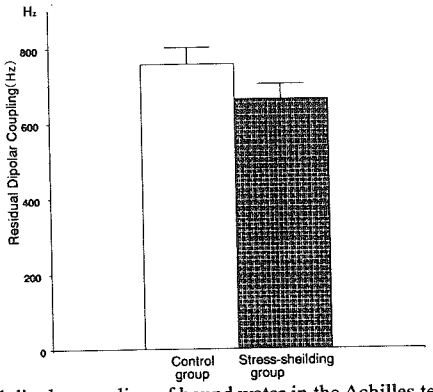

Fig.2 The residual dipolar coupling of bound water in the Achilles tendon

Results and Discussions: Both the E' and E" decreased significantly in the Achilles tendons of the SS group (Fig. 1). E' and E" are indicators of elasticity and viscosity of the tendon, respectively. Our results showed that the Achilles tendon became less viscous and less elastic through stress-shielding. We assume that these changes in the mechanical properties may be attributed to the disordered structure of the longitudinally aligned collagen fibers in the Achilles tendons of the SS group. The results of the ^{1}H-DQF NMR examination demonstrated significantly reduced residual dipolar coupling in the Achilles tendons of the SS group (Fig. 2). These findings support the hypothesis that stress-shielding may result in disordering of the collagen fibers, which may in turn account for the changes in viscoelastic properties.

REFERENCES:

1. Tsoref L, et al., *MRM* **39**, 11, 1998.
2. Seo Y, et al. *MRM*, **42**, 884, 1999.

Lung tissue: for good resolution, keep acquisition time even shorter than $2T_2$*

Dean O. Kuethe and Natalie L. Adolphi

New Mexico Resonance, Albuquerque, USA

Introduction It is common knowledge that to avoid point spread in an image, the acquisition time for frequency-encoded data T_{acq} should be approximately twice the time constant for signal decay from inhomogeneous broadening T_2* or shorter, *i.e.*, $T_{acq}=2T_2$*. Nonetheless, in numerous attempts to image lung tissue, this rule has not been followed (*e.g.*, Gewalt, 1993). Although the long T_{acq}s that have been utilized afforded high signal-to-noise ratios (SNR) because of narrow acquisition bandwidth, they resulted in poor images of lung tissue. The point spread lowered the effective resolution so that lung parenchyma was smeared out over multiple pixels. It seemed to us that if one wished to sacrifice resolution to improve SNR, the better thing to do would be to lower the resolution by increasing voxel size. To test this hypothesis, we made three images of rat lungs: a high resolution image with T_{acq}/T_2*=2, an image at the same nominal high resolution with T_{acq}/T_2*>2, and a lower resolution image with the same T_{acq}/T_2*=2.

Methods We used hard rf pulses in the presence of frequency-encoding gradients *à la* Lauterbur (1973). Such zero echo-time projection imaging (ZEPI) is often used for imaging solids. It is inherently 3D and very insensitive to motion. We used the same 50,000 projection directions in all three images. Two FIDs with opposite gradient direction comprise one line of frequency-encoded data so T_{acq} is twice the FID acquisition time. The nominal resolution and T_{acq}/T_2* for the three images were (0.25 mm, 1.4), (0.36 mm, 1.4), and (0.25 mm, 6.3).

Results To our knowledge, the 0.25 mm resolution image using T_{acq}/T_2*=1.4 is the world's best MRI of a living vertebrate's lung. Even though it has superior SNR, the 0.36 mm resolution T_{acq}/T_2*=1.4 image is second best. The divisions between lung lobes are not as distinct. Although it is also superior in SNR to the best image, the 0.25 mm resolution, T_{acq}/T_2*=6.3 image is similar to previous ZEPI images of rat lungs in which the lung parenchyma is smeared over multiple pixels and extends into the large airways, which should appear black. The lobe divisions are not discernible.

Discussion Even though lung lobe divisions are thinner than 0.35 mm, they are discernible in the lower resolution image because they are bright objects in a darker background, like point sources adding intensity to voxels that include them. The discernibility depends on the intensity being assigned to the proper pixels, and not spread to adjacent ones. These observations support our hypothesis that increasing voxel size is more effective than lengthening T_{acq}, if the goal is to increase SNR at the expense of resolution.

To examine the effect of point spread on resolution, Callaghan and Eccles (1987) use the example of two voxels containing point sources separated by one signal-free voxel. In analogy to optical resolution, the two points are barely resolved when the intensity of the center pixel I_c is detectably lower than the intensity of the point pixels I_p. To take the analysis a step further, we calculated that for a moderate noise level, *e.g.*, N=10, $(I_p+N)/(I_c+N)$ reaches a maximum for T_{acq}/T_2* substantially less than 2, *e.g.*, 0.8. We concluded that when one has the SNR available, it can be put to use for better resolution by using T_{acq} even shorter than T_2*.

We thank the NIH, grant R01EB002072, for financial support.

Callaghan, P. T., and Eccles, C.D., *J. Magn. Reson.*, **71**, 426-445 (1987).

Gewalt, S. L. *et al.*, *Magn. Reson. Med.*, **29**, 99-106 (1993).

Lauterbur, P. C., *Nature*, **242**, 190-191 (1973).

Physiological Noise in SENSE-EPI

R.A. Waggoner, M. Costagli, K. Ueno, K. Tanaka, and K. Cheng
RIKEN - Brain Science Institute, Wako-shi, Saitama, Japan

Introduction: Accelerated Parallel Imaging techniques such as SENSE (1) show great promise in many areas of MRI, including BOLD-fMRI. A potential draw back for MRI techniques, especially fMRI is the loss of SNR with increasing acceleration factor (R). Krüger et al. (2) postulated that the variance in an EPI time series is the sum of the intrinsic variance and the physiological induced variance. For SENSE-EPI data de Zwart et al.(3) extended this description of the noise to Eq. 1

$$\sigma_t^2 = \sigma_{ph}^2 + Rg^2\sigma_i^2 \qquad [1]$$

Where σ_t^2, σ_{ph}^2, and σ_i^2 are the temporal, physiological and intrinsic variances, respectively, and g is the SENSE geometry factor (1). Hu et al. proposed a retrospective method for reducing two principle components of the physiological noise. The respiratory and cardiac cycles are simultaneously monitored during the EPI acquisition, then a fitting procedure is used to remove modulations in the data caused by these sources (4). Eq. 1 indicates that as R, or g increases, σ_t^2, becomes more a function of σ_i^2 than σ_{ph}^2. This leads to the question of whether the retrospective correction of cardiac and respiratory noises is beneficial in SENSE data.

Methods: EPI time series of four subjects were collected on a Varian Inova 4T (Varian Inc., Palo Alto CA.). A 4-channel dome-shaped "Duyn" array (Nova Medical Inc. Wakefield, MA) was used to collect the data. The accelerated images were reconstructed as described by Pruessman et al. (1). Time series of 1000 volumes were collected with R= 1, 2, and 4. The full image matrix was 64x64 (20x20cm), with three 5mm slices. The R=1 data was 4-shot, the R=2 data was 2-shot, and the R=4 data was one shot. The shot to shot Tr was 53ms and Te/FA = 25ms/15° . In the R=1 and 2 cases, the slice segments were interleaved, in order to keep the T1 effects constant for all time series. For each time series, the variance of each pixel in the brain was calculated, both with and without retrospective physiological correction (RPC). Relative Variance maps were calculated using Eq. 2.

$$\mathrm{Re}lativeVariance(RV) = \frac{\sigma^2_{t,withRPC}}{\sigma^2_{t,withoutRPC}} \qquad [2]$$

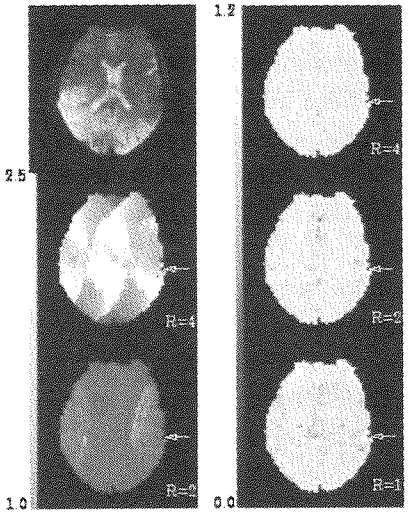

Fig.1. Example image and g-factor maps

Fig.2. Example Relative Variance maps.

Results and Discussion: Fig. 1 shows an image of one slice from Subject 1 as well as the g-factor maps for that slice, for both R=2 and 4. Since in the R=4 case, R equals the number of receive coils, g is quite large. Fig. 2 shows the RV maps for the slice in Fig. 1. The dark grey spots in the R=1 RV map, indicate areas where RPC has significantly reduced the variance locally. This would be a reduction in the variance caused by the cardiac cycle in tissue close to a vessel. Since respiration modulation is a global effect, RPC corrections for respiration should yield an average RV of less than one. Table 1 shows that for the R=1 is well below 1. With increasing R, the amount of dark grey areas drop in Fig. 2, but are still visible in the R=2 case. Fig. 3 shows a plot of one readout line in the RV map (indicated by the arrows in Fig. 2. Three peaks well below 0.8 can be seen for the R=1. In the R=2 case, the peaks are still there, but reduced. In the R=4 case, for this line in the image, no improvement from the cardiac RPC can be seen. In Fig. 2 areas where RPC has helped in the R=4 case can be seen, but they are rare. Table 1 shows that across all subjects, there is no global improvement (respiratory correction) with RPC in the R=4 case, and only a small improvement in the R=2 case. All subjects showed significant local regions (cardiac) that were improved by RPC even with R=2.

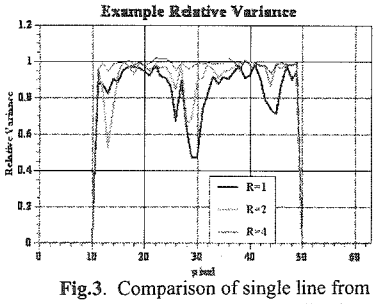

Fig.3. Comparison of single line from Relative Variance maps. The line is indicated by the arrow in Fig. 2.

Table 1
Average Relative Variance and g-factor

	Subject 1	Avg.(n=4)
R=1 Avg. RV	0.93	0.94
R=2 Avg. RV	0.97	0.96
R=4 Avg. RV	0.99	0.99
R=2 Avg. g	1.03	1.02
R=4 Avg. g	2.16	2.18

Conclusions: It has been shown in numerous reports that g-factor increases more slowly with R as the number of receive channels increases (for example ref. 5) Therefore, the results presented here show that RPC can still be helpful when R is less that the number of receive channels. But as R approaches the number of receive channels, RPC becomes ineffective.

References:

1. Pruessmann,KP et al. *MRM.*, **42**, 952-962(1999).
2. Krüger, G et al. *MRM.*, **45**, 595-604(2001).
3. de Zwart, JA et al. *MRM.*, **51**, 22-26(2004).
4. Hu, X et al. *MRM.*, **34**, 201-212(1995).
5. Moeller, S et al. *ISMRM* **12**, 2388(2004).

Imaging of living mice using a 1-T compact MR imaging system

Yusuke Inoue[1], Tomoyuki Haishi[2], Yukihiro Nomura[1], Kohki Yoshikawa[3], Takahiro Seki[1], Kyoko Kohara[1], Chieko Kai[1], Toshiyuki Okubo[1], Kuni Ohtomo[4]

Institute of Medical Science, University of Tokyo, Tokyo, Japan; MRTechnology Inc, Tsukuba, Japan; Komazawa University, Tokyo, Japan; Graduate School of Medicine, University of Tokyo, TokyoJapan.

Introduction

MR imaging of living mice draws a growing attention; however, high cost and low research accessibility may prevent the use of MR imaging in routine mouse experiments. Recently, a compact MR imaging system using a 1-T permanent magnet was developed [1]. In this study, we imaged living mice on the system using a T1-weighted 3D FLASH sequence and investigated appropriate techniques and parameters to obtain images of acceptable quality in a reasonable imaging time.

Methods

Data were acquired using MRmini (MRTechnology), consisting of a 1-T permanent magnet made of Nd-Fe-B material and a compact console, and a solenoid coil of a 30-mm inner diameter. The entire system was installed in a space of 1.5 x 3 m, without magnetic shielding, within a laboratory of a specific pathogen-free (SPF) animal facility. Mice were anesthetized with isoflurane inhalation and fixed on a polymethylmethacrylate holder. After appropriate positioning was confirmed on localizer images, coronal images of the entire trunk was obtained using a T1-weighted 3D FLASH sequence. Typical imaging parameters were TR/TE/FA = 40/3.6 or 6.7/57º, matrix = 256 x 128 x 64, voxel size = 0.26 x 0.26 x 0.52 mm, NEX = 1, and acquisition time = 5 min 28 sec.

Results

Four mice were imaged with and without restraint of respiratory motion, which was achieved by tightly wrapping the mouse and holder together with paper tape, and importance of respiratory motion in distorting the quality of 3D FLASH images was indicated. Data acquisition using 32 or more partitions provided images of acceptable quality. To assess appropriate TR and FA, 32-partition images were collected for a mouse using various TRs (30, 40, 50) and FAs (71º, 64º, 51º, 36º, 28º). Reduction in FA depressed the effect of noise visually, however, decreased image contrast and made the contours of organs less clear. Based on the balance between noise reduction and preservation of contrast, FAs of 51º-64º were judged to be appropriate. Longer TR also reduced the effect of noise at the expense of prolongation of acquisition time. In six mice, 64-partition images were acquired using various TRs (40, 50, 60) and FAs (64º, 57º, 51º). Although the combination of TR of 40 and FA of 64º resulted noisy images, the remaining combinations offered images of acceptable quality in all mice. The liver, spleen, kidneys, lungs, heart, gallbladder, adrenal glands, ovaries, and lymph nodes were visualized. The visualization of the kidneys was sometimes affected by artifacts related to peristalsis, which was reduced with decreasing FA. In mice bearing subcutaneous tumor xenograft, the tumors were clearly delineated. The administration of Gd-DTPA improved the delineation of the kidneys, and the injection of Gd-BOPTA improved the delineation of the liver and kidneys.

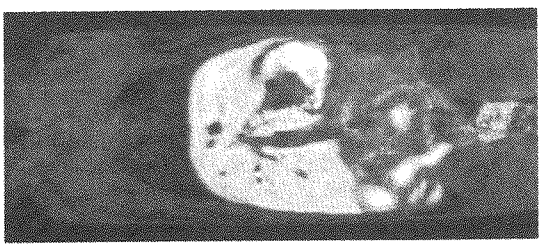

Discussion

Acceptable qualities of T1-weighted 3D FLASH images were obtained on the compact MR imaging system, and the morphologies of various organs and subcutaneous tumors could be assessed. The imaging time to cover the entire trunk with a spatial resolution of 0.26 x 0.26 x 0.52 mm was typically 5 min 28 sec, and total experiment time, from the start of induction of anesthesia to the end of data acquisition, was less than 20 min. Considering the convenience of installation and maintenance and easiness of operation, the system appears to be suitable for routine application to mouse experiments in common animal facilities and biomedical laboratories.

Conclusions

The 1-T compact MR system enables to image living mice with acceptable quality and reasonable time and is expected to be useful for routine experiments of mouse models.

Reference

Haishi T, Uematsu T, Matsuda Y, et al., Magn Reson Imaging 19, 875-80 (2001).

3D High-Resolution MR Imaging of a Human Tooth Pulp Chamber

Dušan Šuštercic[1], Igor Serša[2]

[1]*University dental clinic, Zaloška 2, 1000 Ljubljana, Slovenia*
[2]*Jo ef Stefan Institute, Jamova 39, 1000 Ljubljana, Slovenia*

Precise assessment of anatomical features of a human tooth pulp chamber is essential for a successful endodontical treatment. The shape of dental pulp anatomy is often difficult to predict correctly. In many cases dental pulps of first, second, third molars, premolars or even incisors or canines have different number of root channels, which may be irregularly shaped and may have pulpo-periodontal communications. A standard X-ray radiograph of human tooth is obtained by absorption of X rays in hard dental tissues, such as dentine or enamel. Therefore, it yields an image of pulp's projection in 2D in one orientation only. The X-ray image is also an inverse image of the pulp and the pulp's shape can be judged just from its outline. X-ray radiographs therefore do not provide sufficient information on pulp's anatomy, which makes the outcome of the endodontical treatment unpredictable. An efficient 3D imaging technique could minimize these problems as it would enable precise assessment of pulp anatomy in 3D and enable visualization of all root channels and fine anatomical details. Therefore MR microscopy [1] and micro CT scanning [2] have great potentials to become future standards for dental pulp imaging.

The aim of our study was to visualize a human tooth pulp chamber anatomy by 3D MR microscopy and to evaluate its possible clinical use. Experiments were done on a 100 MHz (proton frequency) superconductive magnet equipped with MR microscopy accessories. 25 human premolars and molars extracted due to orthodontic or surgical indications were included in the study and were imaged by the same 3D MR microscopy technique. The technique was the 3D spin-echo imaging method at parameters: TE/TR = 2.4 ms / 600 ms, 100 μm resolution in all three spatial directions; 256x128x128 imaging matrix and at 8 averages; the imaging time was 22 hours. The teeth were stored in PBS solution for maximum 7 days before MR imaging. All images were post processed by ImageJ program (NIH) to render the pulp chamber's surface and to visualize it in 3D.

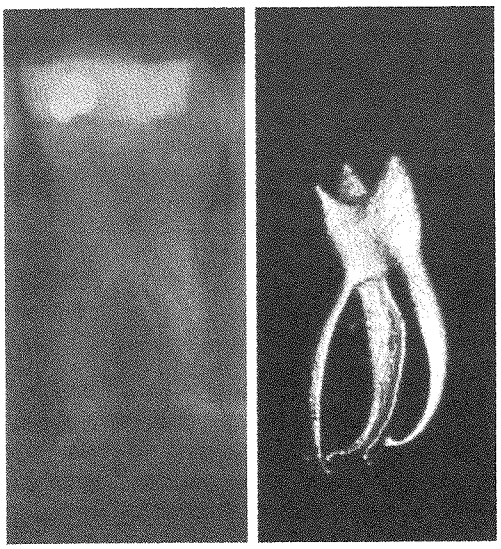

Images show a first molar imaged by the conventional X-ray radiography (left) and by the volume rendered 3D MR microscopy (right). In MR microscopy signal comes from the pulp directly and the pulp can be therefore much better visualized than by X-ray radiography. Unfortunately, due to limitations of the present hardware, high-resolution MR imaging of human teeth can be done *in vitro* only as the scanning time is too long and there is no dedicated hardware for *in-vivo* tooth MR microscopy. In spite of that, MR microscopy is very promising tool for studying the pulp anatomy. It enables precise determination of a number and a shape of root channels; it can visualize communications between the channels and can even reveal fine anatomical details such as pulpo-periodontal communications.

1. Lockhart PB, Kim S, Lund NL. *J. Endod*, **18**, 237-244, (1992).
2. Abrahams JJ, *Radiology*, **219** (2), 334-345, (2001).

Quantifying Inter-Subject Differences Between Two In-Situ Bee Brains Using Magnetic Resonance Microscopy and Nonrigid Registration

Daniel Haddad[1*], Torsten Rohlfing[2*], Frank Schaupp[3], Randolf Menzel[3], Axel Haase[1]
*both authors have contributed equally to this work
[1] Lehrstuhl für Experimentelle Physik 5, Universität Würzburg, Würzburg, Germany
[2] Neuroscience Program, SRI International, Menlo Park, CA, USA
[3] Institut für Neurobiologie, Freie Universität Berlin, Berlin, Germany

INTRODUCTION: Confocal laser scanning microscopy (CLSM) is currently used as the standard method for 3D imaging of insect brains. We are interested in particular in the honey bee (*Apis melifera*). Unfortunately, CLSM imaging requires removal of the brain from the head capsule and chemical treatment of the specimen (immunohistological staining), both of which can substantially deform the brain compared to its *in-vivo* shape. The usability of the CLSM images for applications such as morphometry and inter-subject shape analysis is, therefore, extremely limited. In earlier work [1] we have shown that Magnetic Resonance Microscopy (MRM) can perfectly be used for *in-situ* visualization of the honey bee brain. The acquired 3D images show good contrast and thus provide a rich representation of anatomical details without the aforementioned deformations. The purpose of the study presented here is the quantification of shape differences between bee brains visualized *in-situ* using MRM. To this end, a nonrigid registration (i.e., anatomically correct alignment) was performed between 3D MRM datasets from two bee brains, and the resulting 3D deformation field was analyzed.

METHODS: The MR datasets were acquired using a 3D Spin-Echo Sequence (TE=14.3ms, TR=1.5s) with nominal spatial resolutions of 15.6 x 15.6 x 60 µm and 15.6 x 15.6 x 30 µm [1]. Subsequently, the MRM images were registered using a nine degree of freedom (DOF) affine transformation (three translations, three rotations, three anisotropic scale factors). As final step, a nonrigid registration was performed using a free-form deformation algorithm [2]. We started with a 400 µm control point spacing (720 DOFs) that was refined three times to a final spacing of 50 µm (66, 177 DOFs).

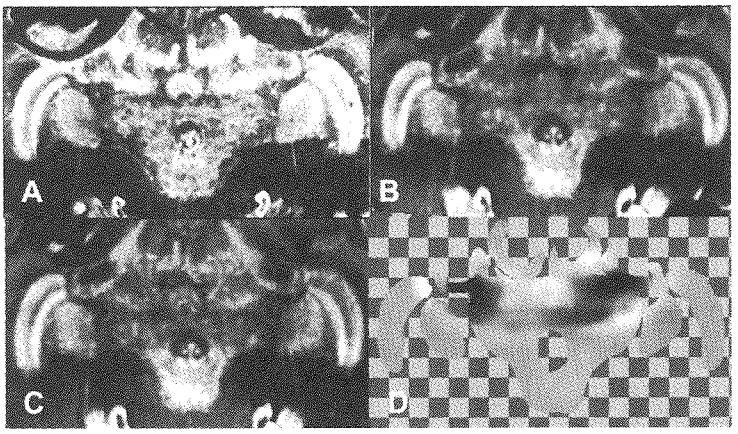

Fig. 1. (A) Reference MRM image (after image enhancement operators as described in [2]). (B) Floating (i.e., deformed) MRM image after affine alignment. (C) Floating MRM image after nonrigid registration. (D) Jacobian determinant map of the nonrigid coordinate transformation between (B) and (C). The Jacobian determinant of the transformation at each pixel, which describes the local volume change, is shown for the brain only (manual segmentation; checkerboard shows non-brain areas) using a logarithmic gray scale. White represents local volume gain of 10%, black represents local volume reduction of 10%. Gray represents no (or little) volume change.

RESULTS: In the affine registration step, we found anisotropic scaling factors of 0.95, 0.97, and 0.96 in *x*, *y*, and *z* direction, respectively. This is on the same order of magnitude as the average scale difference we found between an MRM and 20 typical CLSM bee brain images, and one third of the respective maxima [3]. We note, however, that the scaling factors between MRM and CLSM were on average 0.92 in the *x* direction and 1.05 in the *z* direction. That is, a lateral volume loss appeared to be compensated for by an increase in brain thickness. In contrast, the two brains in the present study appear to be related by a global, almost isotropic scaling factor. Thus, between the two MRM brains only an almost linear scaling adjustment was necessary to correct differences in the size of the brains. On the other hand, comparing CLSM and MRM datasets, a real deformation of the brain's 3D shape was observed. This was confirmed by analyzing the Jacobian determinant map of the nonrigid coordinate transformation (Fig. 1) which shows that for the MRM data only minimal deformation was required to align large parts of the brains.

DISCUSSION AND CONCLUSION: While analysis of a larger number of MRM images is needed for definitive conclusions, the present study lends further credibility to results we found in earlier work [3], comparing CLSM images of 20 bee brains to a single MRM image of a different bee brain. If, as our results here indicate, the brains of two different bees are in fact very similar, then shape differences we found between CLSM and MRM were very likely the result of the specimen preparation process, rather than evidence of inter-individual variability. Consequently, in order to study the *in-situ* shape of the bee brain, we cannot rely on CLSM images alone. MRM images are needed to correct the spatial distortion caused during the specimen preparation for the CLSM measurements and may even prove to represent an ideal replacement of CLSM for this purpose.

REFERENCES:
1. Haddad, D., Schaupp, F., Brandt, R., et al., *Journal of Insect Science*, **4** (2004).
2. Rohlfing, T., Maurer, C.R., *IEEE Transactions on Information Technology in Biomedicine*, **7**, 16-25 (2003).
3. Rohlfing, T., Schaupp, F., Haddad, D., et al., *Journal of Biomedical Optics*, **10**, 024018 (2005).

High resolution 3D MR microscopy of chemically-fixed human embryos for 3D anatomical database

Y. Otake[1], S. Hara[1], S. Handa[1], K. Kose[1], S. Yamada[2], K. Shiota[2]

1 Institute of Applied Physics, University of Tsukuba, Tsukuba, Ibaraki, Japan

2 Center for Congenital Anatomy Research, Kyoto University, Kyoto, Japan

INTRODUCTION

Our group acquired 3D MR microscope images of 1,204 chemically-fixed human embryos selected from the "Kyoto Collection of Human Embryos" for about two years using a super-parallel microscope operated at 2.34 T (1, 2). The size of the image matrix was fixed to 128 × 128 × 256 throughout the embryos and the voxel size was varied from 40 to150 μm^3. These voxel dimensions were mainly limited by the SNR of the NMR signal obtained at 2.34 T. In the present study, to achieve much higher spatial resolution we developed an MR microscope using a 9.4 T superconducting magnet and measured chemically fixed human embryos.

MATERIALS AND METHODS

The MR microscope consists of a 9.4 T vertical wide bore (89 mm RT bore) superconducting magnet (JASTEC, Kobe, Japan), a gradient coil set, RF coils, and an MRI console. We used a home-built gradient coil set. For the RF coils, we developed several solenoid and saddle-shaped coils with locally tuned chip capacitors (Fig.1). The MRI console consisted of a PC, transceiver (DTRX-4, DS Technology, Saitama, Japan), gradient driver (3CH, ±35V, ±15A, Jyonan-Denshi, Tsukuba, Japan), and class AB wideband power amplifier (300-500MHz, 200W, Thumway, Shizuoka, Japan). A Carnegie Stage (CS) 16 chemically-fixed human embryo was image with a 3D gradient echo sequence with 256 × 256 × 512 image matrix.

RESULTS AND DISCUSSION

Figures 2 and 3 show mid-sagittal cross sections selected from 3D image datasets of the same CS21 embryo acquired using the super-parallel MR microscope operated at 100 MHz and the 400 MHz MR microscope. Figure 2 was acquired with a spin echo sequence (TR=100 ms, TE=10 ms, NEX=16, 128 × 128 × 256 image matrix, 120μm^3 voxel). Figure 3 was acquired with a gradient echo sequence (TR=100 ms, TE=6 ms, NEX=8, 256 × 256 × 512 image matrix, 60μm^3 voxel). Because Fig.2 uses the Fourier interpolation. Very fine anatomical structures were definitely observed only in Fig.3. In conclusion, several times SNR increase was confirmed from 100 MHz (solenoid) to 400 MHz (saddle coil) but optimization of the system is required for high-resolution and large-matrix image acquisition.

Fig.1 Saddle-shaped (ϕ9mm)

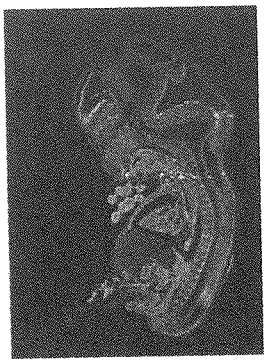

Fig.2 CS21 at 100MHz (120μm^3)

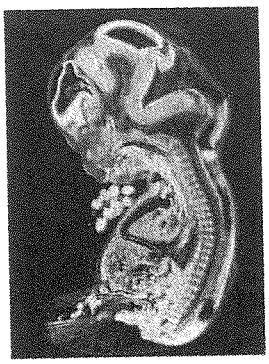

Fig.3 CS21 at 400MHz (60μm^3)

REFERENCES

(1) Y. Matsuda, S. Ono, S. Handa, Y. Otake, T. Haishi, K. Kose, C. Uwabe, K. Shiota. 3D MR Microscopy of the Human Embryo Collection (Kyoto Collection): Final Report for 1,200 Human Embryos. 13th ISMRM Proc. p68, 2005.

(2) The mid-sagittal sections of the 1,204 embryos can be seen at http://mrlab.bk.tsukuba.ac.jp/human_embryo/

3D MR microscopy of a large number of chemically-fixed human embryos using a super-parallel MR microscope

Y. Matsuda[1], S. Ono[1], S. Handa[1], Y. Otake[1], K. Kose[1], T. Haishi[2], S. Yamada[3], C. Uwabe[3], K. Shiota[3]
1. Institute of Applied Physics, University of Tsukuba, Tsukuba, Japan. 2. MRTechnology, Tsukuba, Japan.
3. Center for Congenital Anatomy Research, Kyoto University, Kyoto, Japan.

INTRODUCTION

Kyoto University has a large collection of human embryos (40,000~50,000) that were collected from 1961 to 1974 (1). This is believed to be the largest human embryo collection in the world. Because such a collection would never be obtained again, their non-destructive 3D measurements are highly desired. We therefore started a project to acquired 3D MR microscopic images of thousands of the human embryos in 1999.

MATERIALS AND METHODS

Human embryo specimens were chemically fixed in Bouin's fluid and stored in 10% formalin solution (1). About 1,200 undamaged and normal appearance specimens, ranging from Carnegie stage (CS) 13 to 23, were carefully selected from the collection. The specimens were imaged in NMR sample tubes filled with formalin solution using a 4 or 8 channel super-parallel MR microscope with a horizontal bore 2.34 T superconducting magnet (2). The imaging pulse sequence was a T_1 weighted 3D spin echo sequence (TR=100ms, TE=8-12ms). The image matrix was 128 × 128 × 256. The voxel size was varied from 40 μm^3 to 150 μm^3.To improve the SNR, 16 or 24 times signal accumulations were performed.

RESULTS AND DISCUSSION

Acquired 3D image datasets were interpolated from 128 × 128 × 256 to 256 × 256 × 512 voxels using a zero-filled Fourier transform technique. Mid-sagittal cross-sectional images of the embryos were selected after 3D rotation of the interpolated 3D image datasets. Figure 1 shows typical mid-sagittal images selected from 3D image datasets of CS13 to CS23 embryos. It took about two years to acquire the 3D images of 1204 embryos.

Figures 2 and 3 show a T1W sagittal image (TR/TE =100 ms/8 ms) and an Nissl-stained anatomical section as presented in a textbook (4), but converted to a gray scale and contrast-inverted. As shown in the figures, the image contrast of the T1W image is quite similar to that of the stained anatomical section. This result demonstrated the T1W 3D images could be used for the 3D anatomical database of human embryos.

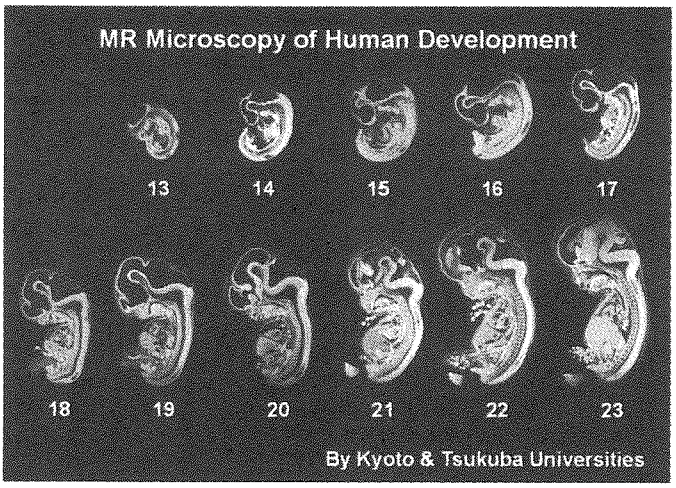

Fig.1 Mid-sagittal sections of CS13-23 embryos

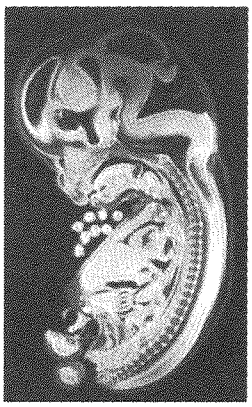

Fig.2 T1W image

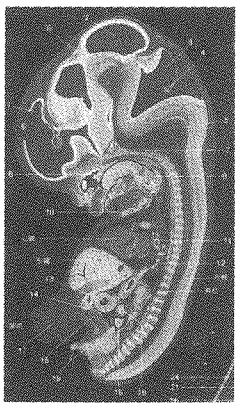

Fig.3 Stained section

REFERENCES

1. Nishimura H, Takano K, Tanimura T, Yasuda M. Normal and abnormal development of human embryos: first report of the analysis of 1,213 intact embryos. Teratology 1968;1:281-290.
2. Kose K, Haishi T, Matsuda Y, Anno I. Super-parallel MR microscope. In: Proceedings of the 9th Annual Meeting of ISMRM, Glasgow, 2001, p 609.
3. Matsuda Y, Utsuzawa S, Kurimoto T, Haishi T, Yamazaki Y, Kose K, Anno I, Marutani M. Super-parallel MR microscope. Magn Reson Med 2003;50:183-189.
4. Drews, U. Taschenatlas der Embryologie. 1st edition, Stuttgart: Georg Thieme Verlag; 1993.

Ab initio study of hyperfine parameters using the all-electron mixed-basis method

Mohammad Saeed Bahramy,* Marcel H.F. Sluiter, and Yoshiyuki Kawazoe

Institute for Materials Research, Tohoku University, Sendai, 980-8577 Japan

Abstract

Within density functional theory, an efficient and accurate method for calculating hyperfine parameters has been developed. The so-called mixed basis method expands the one-electron wave-functions in terms of both highly localized nucleus-centered functions and plane waves and thereby affords an accurate representation for the spin density both in the immediate vicinity of the nucleus and in the bonding regions. The current method is compared with experiment and the best computational methods reported in the literature. The mixed-basis approach is shown to yield highly accurate isotropic and anisotropic hyperfine parameters with modest computational effort. In addition, the role of core and valence shell spin polarization and its corresponding effect on the hyperfine parameters have been investigated.

In vivo observation of 5FU dynamics by chemical shift imaging - Comparison of fast imaging sequences -

Yoko Kanazawa[1], Yoshiyuki Hirano[123], Sachiko Koike[1], Eiji Yoshitome[1], Koichi Ando[1], Masafumi Fujita[2], Minoru Onozuka[3], Hiroo Ikehira[1]

1.National Institute of Radiological Sciences, Chiba 263-8555, JAPAN, 2.Gifu University, Graduate School of Medicine, Gifu 501-1194, JAPAN, 3.Kanagawa Dental College, Yokosuka 238-8580, JAPAN

Introduction: Chemical shift imaging under minimal relaxation weight should be a robust method for *in vivo* dynamical study of drugs and labeled compounds. Fast imaging sequences are compared at 7T with 5FU administrated mice.

Methods: 7T/400mm/SS system (NIRS, KOBELCO, Bruker) was used with small RF coils of 72mm ^{1}H-^{19}F, $^{1}H/^{19}F$ (Bruker), and 40mm ^{1}H-$^{19}F/X$ (Doty). Fast Spin Echo, FISP and Flash are compared as the sequences for ^{19}F chemical shift selective imaging. 5FU was administrated orally to C3H/He mice bearing tumor cells such as NFSa etc. as subcutaneous tumor. Whole body ^{19}F spectra were taken to determine the resonance frequencies to be used in the chemical shift selective imaging with FISP, FSE and Flash. Coronal projection images were obtained in the case of interleaved chemical shift selection of FSE[1]. Minimum TE's were 3.2ms for FISP and 10 ms for FSE under chemical shift selection of band width 1800 Hz.

Results: Signal intensity and S/N evaluated by the phantom of single line were FISP = FSE > Flash. Both FISP and FSE gave ^{19}F chemical shift images of comparable quality. However, FISP and FSE showed their respective advantages in *in vivo* experiments. In more detail, the signal of 5FU with short T_2 was detected better by FISP. Simultaneous acquisition of several chemical shifts was attained by FSE without any signal attenuation.

Discussion: FISP was suitable in imaging short T_2 signals as expected. The ability of FSE in simultaneous imaging of several compounds and the robustness against susceptibility problem has advantage in dynamical study especially when many metabolites are involved. The employment of both methods will cover the wide range of *in vivo* objects.

[1] Doi Y and Kanazawa Y, 4th ICMRM, 1997, Narazaki M, Kanazawa Y al., 5th ICMRM, O22 1999. Kanazawa Y and Doi Y, 12th ISMRM, 2497, 2004.

Accurate Determination of the Human Olfactory Bulb and Tract using High Resolution MR Imaging at 4 Tesla

E. Gunde[1], S.D. Beyea[2,3,5], K. Good[1], R. Leslie[4], H. Milliken[1] and N. Carrey[1]

Departments of [1]Psychiatry, [2]Physics, [3]Radiology, [4]Anatomy & Neurobiology, Dalhousie University
[5]Institute for Biodiagnostics (Atlantic), National Research Council of Canada
Halifax, Nova Scotia, Canada

Considerable evidence links psychotic disorders (including schizophrenia) with abnormalities in brain regions associated with the sense of smell. This, together with the well-documented fact that many schizophrenia patients have difficulties processing odours, provides the rationale for olfactory (sense of smell) testing of patients diagnosed with psychotic disorders.

We are therefore using MRI to examine and measure the size (volume) of specific brain regions in patients with first episode psychosis, as well as healthy (normosmic) subjects. Specifically, we are using high field (4-Tesla) MR imaging to acquire high-resolution anatomical images of the olfactory bulbs (OB). In order to facilitate accurate volumetric analysis of the OB, we acquire MP-RAGE images with isotropic voxel sizes at high resolution (< 0.2 microlitres).

In the current work we will present initial data, demonstrating the ability of high field MRI to determine OB volume, as well as validation studies performed using an olfactory bulb phantom. Studies are currently underway to determine potential abnormalities in OB volume in patients with psychotic disorders. This information will provide a basis for further clinical and preclinical investigations of neurodegenerative processes and/or abnormalities in neurogenesis in individuals with psychotic disorders.

Excitation Methods for Single-Scan 2D NMR

Nikolas Salisbury Andersen & Walter Köckenberger
Sir Peter Mansfield Magnetic Resonance Centre, School of Physics and Astronomy,
University of Nottingham, University Park, Nottingham, NG7 2RD, United Kingdom,
nikolas@magres.Nottingham.ac.uk, +44 (0)115 9515161, fax +44 (0)115 9515166

Introduction

Recently techniques for the fast acquisition of 2D NMR spectra in a single scan using gradient echoes have been introduced (1). Originally multiple frequency selective pulses were used. Later continuous excitation schemes involving frequency-modulated chirp pulses resulting in amplitude modulation in the indirect dimension through a storage step were proposed (2,3). Very recently phase-modulated schemes have also been described. (4,5). Here we demonstrate two general phase-modulated schemes and outline applications for spectroscopy and spectroscopic imaging.

Methods

The goal of an excitation sequence for single-scan 2D NMR is to provide a range of evolution times (t_1) depending linearly on the position in the sample. A single chirp pulse applied in the presence of a magnetic field gradient fulfils this requirement but gives rise to a quadratic phase roll across the spectral window. This phase roll can be partly suppressed by the addition of a chirp 180° pulse and a evolution delay (6). This scheme can be adapted for single-scan 2D NMR by swapping the order of the 180° pulse and the delay while adding a positive and a negative gradient pulse, both of duration t (3):

chirp RF: 90°x(t) -½t- 180°y(t)
Gz: +(t) -(t)

A more elaborate scheme using three chirp pulses compensates for remaining B_1 depended phase deviations (7). In this case adaptation for single-scan 2D NMR can be done by addition of three gradient pulses of duration t and with alternating positive or negative amplitude:

chirp RF: 90°x(t) 180°y(t) -½t- 180°y(½t)
Gz: +(t) -(t) +(t)

An additional advantage of this scheme is a larger spread of t_1 values resulting in a faster spatial encoding of the indirect detected spectroscopic dimension.

A single-scan COSY sequence can be constructed by adding a hard 90°y mixing pulse surrounded by equal gradient pulses to facilitate coherence pathway selection and an oscillating gradient train for acquisition of the direct detected spectroscopic dimension.

Addition of orthogonal phase encoding gradient pulses immediately after mixing gives a fast version of the hybrid 2D spectral/2D spatial experiment previously described as Correlation Peak Imaging (CPI). This technique makes it possible to form metabolic maps from the spatial distribution of the cross peaks intensity of individual chemical compounds. Alternatively, 2D spectra can be obtained from the same data set for each individual sample voxel (8). In contrast to the conventional CPI technique which suffers from long experimental duration, our new scheme shows a substantial improvement in the required experimental time. We present a theoretical comparison of the two excitation strategies including computer simulations and a set of experimental data.

Results

* 64x64 single-scan 2D NMR experiments without a mixing element resulting in spectra, where only the diagonal is populated, were simulated and recorded on a 1:9 H_2O/D_2O sample to analyse the line shapes. The 3-pulse excitation scheme was found capable of producing spectra with narrower lines, especially at the base.

* 64x64 COSY spectra were recorded in 96ms to verify the computer simulations.

* A 4D 31x31x64x64 CPI data set was recorded on a phantom sample containing a 4mm tube with a glucose solution inside a 8mm tube with a glutamine solution in 1h20min with a recycle time of 3s and weighting of the k-space sampling by a Hanning window function. Excellent separation of peaks in the spectral dimensions was achieved. Assuming a recycle delay of 2s, this enables the acquisition of 15x15x64x64 CPI experiments in 10-15min, depending on the k-space weighting scheme, providing sufficient temporal resolution for *in-vivo* studies.

References: **1)** L Frydman et al. JACS 125p9204 (2003); **2)** P Pelupessy JACS 125p12345 (2003) ; **3)** Y Shrot et al. JMR 171p163 (2004); **4)** A Tal et al. JMR in press (2005); **5)** NS Andersen et al. MRC in press (2005); **6)** J-M Böhlen et al. JMR 84p191 (1989); **7)** K Cano et al. JMR 155p131 (2002); **8)** A Ziegler et al. JMR B112p141 (1996)

2D NMR Imaging in the Earth's Magnetic Field using Bar Magnets

Meghan E. Halse[1], Craig D. Eccles[1], Andrew Coy[1] and Paul T. Callaghan[2]

[1]*magritek Limited, Wellington, New Zealand*

[2]*MacDiarmid Institute of Advanced Materials and Nanotechnology, School of Chemical and Physical Sciences, Victoria University of Wellington, Wellington, New Zealand*

The local homogeneity of the Earth's magnetic field makes it possible to perform NMR on relatively large samples using a small, portable instrument, because no external static magnetic field is required. Such instruments have been employed for NMR measurements outside of the laboratory and also for teaching the principles of NMR. Herein we present a novel and yet simple method for imaging in the Earth's field in which two bar magnets, acting as magnetic dipoles, are used to generate the necessary magnetic field gradients.

The Earth's field is, relatively speaking, quite weak (on the order of 50μT) and so only a very small magnetic field gradient is required for imaging. Therefore two ordinary bar magnets placed on opposing sides of the probe, oriented such that their magnetic fields are of opposite polarity (Figure 1) can generate an approximately linear magnetic field gradient of the necessary strength over a region in the centre of the probe. A simple spin-echo experiment performed in the presence of this gradient can be used to achieve imaging in the Earth's field.

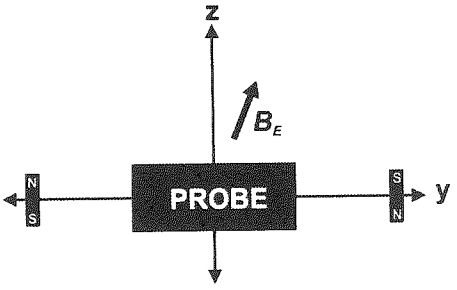

Figure 1: Imaging with two bar magnets

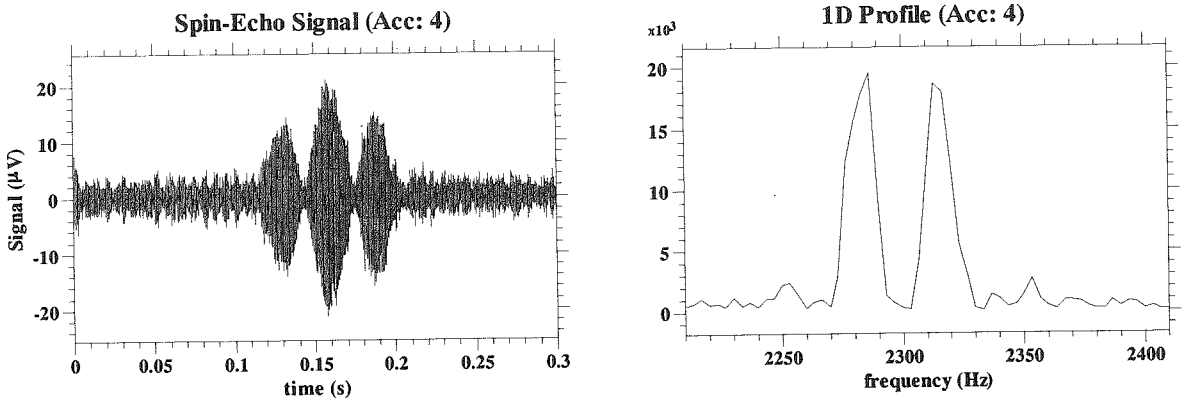

Figure 2: A sample spin-echo signal acquired in the presence of the bar magnet gradient. The Fourier transform is a profile through the sample (two cylindrical vessels filled with water)

Manually rotating the pair of bar magnets in the *xy*-plane allows for projections to be acquired over a range of angles. These projections can be combined to achieve a filtered back-projection image of the sample. In this manner, 2D MRI can be performed in the Earth's field with two bar magnets! This surprisingly obvious methodology provides a visual and intuitive way to introduce students to magnetic field gradients and their role NMR imaging.

1. Callaghan P.T., et al., Journal of Magnetic Resonance, 133, 148-154 (1998).
2. Terranova – an Earth's field NMR system - www.magritek.com/terranova.html

Tracking Diurnal Variations in the Earth's Magnetic Field using ^{1}H EFNMR

Meghan E. Halse[1], Andrew Coy[1], Craig D. Eccles[1] and Paul T. Callaghan[2]
[1]*magritek Limited, Wellington, New Zealand*
[2]*MacDiarmid Institute of Advanced Materials and Nanotechnology, School of Chemical and Physical Sciences, Victoria University of Wellington, Wellington, New Zealand*

The Earth's magnetic field provides a unique opportunity to perform NMR on large samples without the need for a homogeneous external static magnetic field. This opens up a wide range of possible applications; however, there exist a number of subtle nuances that affect the design and implementation of NMR experiments in the Earth's field. It is widely known that the Earth's magnetic field undergoes secular variations on a historical time scale. However, what is less well known is that there exist diurnal, or daily, fluctuations in the Earth's field that can occur on a time scale of minutes or even seconds. These daily, or diurnal, variations were first discovered in England in 1722 and are believed to be caused by electric currents induced in the Earth by currents in the ionosphere. The ionosphere currents are driven by solar activity and so this mechanism is consistent with the observed non-secular fluctuations in the Earth's magnetic field that have a period of approximately 24 hours and have been seen to be greater in the summer than in the winter. The frequency of an EFNMR signal is highly sensitive to any variations in the magnitude of the Earth's field. The goal of this experiment was to discover how precisely the diurnal variations in the Earth's field could be tracked using ^{1}H EFNMR.

The frequency resolution of the EFNMR spectrum is limited by the acquisition time, which for our experiments was 3s. This corresponds to a frequency resolution of 0.33Hz (8nT). This limited resolution can be greatly improved by considering the phase of the signal. A delay introduced between the signal excitation and detection allows the spins to evolve and acquire a phase offset directly proportional to the magnitude of the Earth's field. Any fluctuations in the Earth's field can then be calculated from the phase differences between spectra. Using this method a resolution as high as 0.006Hz (0.15nT) can be achieved. This is a 50-fold improvement over the frequency-based calculation.

Figures 1 and 2 present the variations in the magnitude of the Earth's magnetic field, ΔB_E, over a time period of 42 hours in Wellington, New Zealand. Figure 1 presents ΔB_E as calculated from the frequency of the EFNMR signal and Figure 2 presents ΔB_E as calculated from the phase.

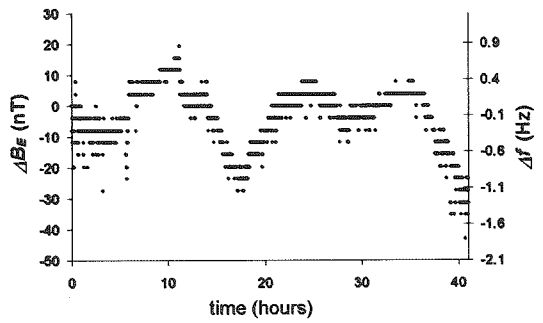

Figure 1: ΔB_E measured from frequency

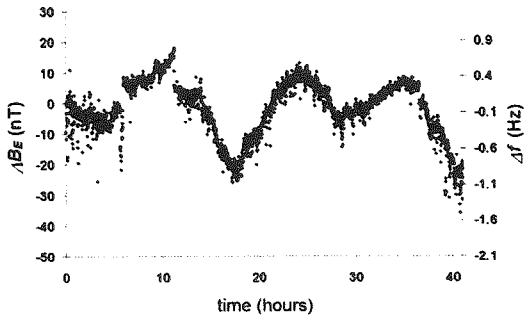

Figure 2: ΔB_E measured from phase

1. Callaghan, P.T., et al., Journal of Magnetic Resonance, 133, 148-154 (1998).
2. Mohoric, A., et al., Journal of Magnetic Resonance, 136, 22-26 (1999).
3. Terranova - an Earth's field NMR system by magritek Limited (www.magritek.com/terranova.html)

Nondestructive testing of PE pipes for gas and water transport

Kai Kremer[1,2], Bernhard Blümich[2], Federico Casanova[2], Juan Perlo[2]

[1]aachen, centre for technology, Roetgen, Germany
[2]Chair for macromoluclar chemistry, RWTH Aachen University, Germany

PE pipes are used more and more for water and gas transport. For work on PE pipes it is customary to squeeze pipes so as to stop the water or gas flow. The life time of those PE pipes is determined in life time tests at 80 °C and extrapolated to ambient temperature by means of Arrhenius-law. Residual stress from production is not taken into account and squeezing tests were performed only for 5 minutes.

We measured PE 100 water tubes at room temperature with a mobile NMR-Sensor (NMR-MOUSE) under different conditions:

a) New,
b) squeezed for more than 12 hours and subsequent relaxing,
c) squeezed, relaxed, and tempered at 80 °C,
d) tempered at 80 °C without squeezing,
e) tempered at 80°C, and squeezed/relaxed.

Transversel relaxation decays were measured by the CPMG method and analyzed by a biexponential fit. The fast relaxing component is attributed to the signal of the crystalline regions, and the slowly relaxing component to that of the amorphous regions. The amplitude ratio provides information about the degree of crystallisation and the relaxation rates about the site of the crystalline domains and the degree of order in the amorphous domains. It is shown, that PE tubes are clearly inhomogeneous. This goes hand in hand with residual stress. By tempering these residual stresses can be partially healed. Squeezing reduces the crystallinity and the average size of the crystals. Additional tempering reduces the order in the amorphous parts. With squeezing times shorter than 30 minutes these effects are extremely weak. Furthermore a tube, tempered at 80 °C, is more inflexible than an untempered one; it stays deformed. A longer exposition at 80 °C is sufficient to create new morphological structures.
The NMR measurements showed, that a life time prediction based on long time tests at 80 °C refer to tempered pipes, which at room temperature have different characteristics than untempered pipes. Also, results from pipes, squeezed only for some minutes at room temperature, are not transferable to pipes, which are squeezed for many hours.

Mouse MRI Probe for *Micro2.5*

H. Wakamatsu, M. Yokoi, Y. Imaizumi, F. Sugihara*, Y. Seo

Department of Regulatory Physiology, Dokkyo University of Medicine,
*Graduate School of Integrated Science, Yokohama City University

Introduction/Our new project is to detect minimal brain injury in the shaken-baby syndrome. We will take a rat model that was established by Ueda et al (Neuroscience Letters, **385**,82-86 2005). A high-spatial resolution image and a diffusion analysis can be useful to detect and follow pathological changes in the brain. In order to analyze rat brain stereotaxically, we have developed the stereotaxic coordinates in the magnetic devices. We have already established it for rat brain with much bigger magnet using Biospec 4.7/40. It is reasonable to take a higher field to get a better image from a small mouse brain. In order to establish general strategies and basically data with this device, we tried to make the stereotaxic coordinates for mice inside Micro2.5 gradient system (Bruker Biospin) that allows us only 39 mm in diameter for animal and RF coils.

Methods/A set of the conventional fixation devices (a bite bar and a pair of ear bars) was installed in an acrylic tube (5 mm thickness). The position of the bite bar can be adjusted either the level position (the stereotaxic coordinates) or -2 mm down position (best position for the RF-coil) (Fig. 1).

Results/Using this probe, we can get reasonable quality of images as shown in Fig. 2 (An GE image (TR/TE = 400/4.4 ms) with a slice thickness of 0.5 mm was obtained by AMX-300wb (7.05 T) with a 16-mm (o.d.) surface coil (Doty)).

Our plan/ We are now trying to install gas anesthesia system to keep a stable vital condition of mouse, and heat insulation system to keep body temperature of mouse.

Figure 1: Assembly of probe

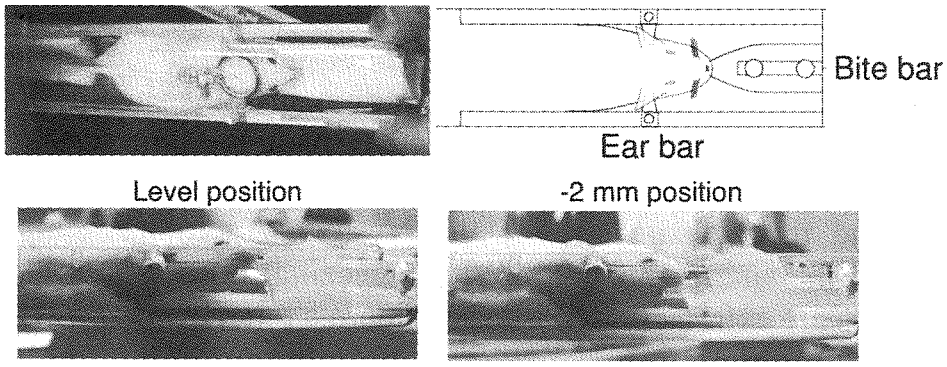

Figure 2: Transverse gradient-echo image of mouse brain

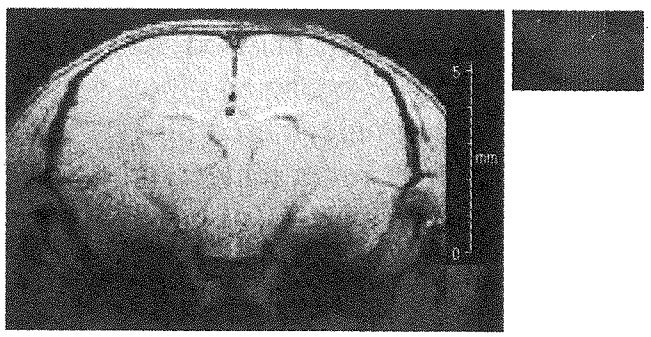

3D Isotropic High Spatial Resolution Gd-DTPA-Enhanced MRI of the Rat Choroid Plexus

Hideto Kuribayashi, David R Checkley Yi-Xiang Wang, Daniel P Bradley and John C Waterton
AstraZeneca Global Sciences & Information, Macclesfield, UK

INTRODUCTION

Choroid plexus presents in ventricles of the brain and is principally responsible for the production of cerebrospinal fluid. Although the human choroid plexus is easily identified in magnetic resonance imaging (MRI), it is challenging to assess that of rodents because of its small structure. Natt et al. (1) introduced 3D high spatial resolution MRI to minimize partial volume effects in order to reveal small cerebral structures of the mouse brain. Moreover, the choroid plexus is highly enhanced by Gd-DTPA because of the absence of a blood-brain barrier and the different permeability of choroidal epithelium compared to the other brain tissues (2). In the current study, a fast 3D contrast-enhanced (CE) MRI with 0.2-mm isotropic resolution was used to assess the choroid plexus in normal rats and to monitor the time evolution of the enhancement within the choroid plexus.

METHODS

MR images were acquired using a 9.4 T horizontal MRI system (UNITYINOVA and VnmrJ, Varian Inc.) with a 22-mm single turn surface coil (Varian). Animal studies were performed in full compliance with the UK Animals (Scientific Procedures) Act, 1986. Six female AP rats (167-189 g) were scanned under isoflurane/air anesthesia. A heparin-prepared catheter containing Gd-DTPA (0.4 mmol/kg body weight Gd-DTPA; Magnevist, Schering AG) was inserted into the rat tail vein before the MRI scans. After scout scans, six 3D spoiled gradient-recalled echo T_1-weighted images were acquired sequentially. An adiabatic half-passage RF pulse was used for excitation to improve B_1 homogeneity. The other parameters were: TR/TE = 12/2.5 ms, 2 averages, field-of-view = 25.6 mm × 25.6 mm × 25.6 mm, matrix = 128 × 128 × 128, spatial resolution = 0.2 mm × 0.2 mm × 0.2 mm. Scan time was 7 minutes per 3D image. Gd-DTPA was injected into the tail vein after 2 baseline 3D MRI scans. Total experiment time was approximately 80 minutes per rat.

Data processing was carried out using ImageBrowser (Varian). 3D contrast enhancement maps were constructed voxel-by-voxel. Using a threshold of 50% or more enhancement after Gd-DTPA administration than baseline, enhancing voxels of choroid plexus regions in the lateral ventricles were selected from horizontal sections of the first 3D contrast enhancement map.

RESULTS

Figure 1 shows three adjacent horizontal sections from the first 3D contrast enhancement map of a rat brain after Gd-DTPA injection. Enhancing regions in both lateral ventricles is clearly identified without blurring (arrows). The structure of those could be compared favourably to the region occupied by the choroid plexus shown in a rat brain atlas (3). The total volume of the enhancing choroid plexus in the lateral ventricle was 2.052 ± 0.480 $(mm)^3$ (mean ± SD, n = 6). The signal enhancement in the choroid plexus regions showed the maximum after Gd-DTPA injection and then decreased. The time evolutions of the signal enhancement percent change were in close agreement among all subjects.

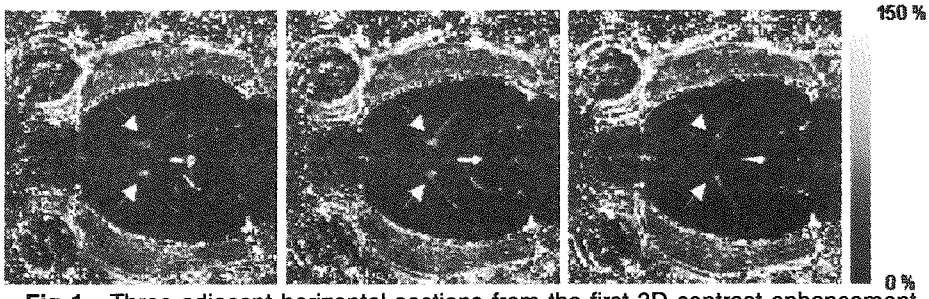

Fig 1. Three adjacent horizontal sections from the first 3D contrast enhancement map of a rat brain after Gd-DTPA intravenous injection. Choroid plexus in lateral ventricle regions (arrows) are enhanced clearly. Spatial resolution is $(0.2\ mm)^3$.

DISCUSSION

The region of the rat choroid plexus could be visualised using the 3D CE-MRI with both the $(0.2\ mm)^3$-isotropic spatial resolution and the 7-minutes imaging time. High sensitivity could be achieved by (i) high field of 9.4 T, (ii) a surface coil detection, and (iii) 3D acquisition. Additionally, the isotropic 3D T_1-weighted imaging permitted the observation of the thin-structured ventricles as hypointense regions from the other planes. CE-MRI is a powerful tool for assessment of perfusion, endothelial permeability, and interstitial volume. Although the temporal resolution of 7 minutes is too slow to permit compartmental modelling, the Gd-DTPA uptake obtained by the high spatial resolution 3D imaging may permit assessment of choroid plexus function in rodents.

REFERENCES

1. Natt O et al. J Neurosci Methods 2002;120:203-209. 2. Guermazi A et al. Clin Radiol 2000;55:503-516. 3. Paxinos G and Watson C. The rat brain in stereotaxic coordinates. London: Academic Press; 1986.

Micro-Imaging Cryogenic Probes

Daniel Marek[1], Oskar Schett[1], Dieter Gross[2], Marco Sacher[1], Thomas Oerther[2],

[1]Bruker BioSpin AG, Fällanden, Switzerland; [2]Bruker BioSpin GmbH, Karlsruhe, Germany

In NMR imaging significant S/N advantages can be obtained by reducing the noise of the detection system, especially for small samples. We present results obtained with a new cryogenically cooled microimaging probe. This probe technology utilizes RF coils cooled to about 20 K together with preamplifiers integrated into the probe and operated at 77 K, while the sample remains at ambient temperature. The temperature of the sample can be controlled in a range of 0...80 °C. A S/N enhancement factor of about 4 compared to conventional room temperature probes is obtained. This allows to reduce the measuring time by a factor of up to 16.

The objective of this development is to retain the ease of use of a conventional probe, while dramatically increasing the achievable S/N. The μI cryogenic probe is cooled by a closed-cycle cooling system, using a Gifford-McMahon cryocooler. The system is fully computer controlled and allows completely unattended cooldown, operation, and warmup. The setup is compatible with existing room-temperature microimaging hardware and is transparent to the user. The probe shown is designed for 5 mm diameter samples. The outer diameter of the probe is 40 mm. It is operated with a standard Bruker Micro 2.5 gradient system, which fits into a vertical bore magnet with an inner diameter of 89 mm. The probe operates at 9.4 T and is equipped with a proton channel. The major hardware components of this system are shown in Fig. 1.

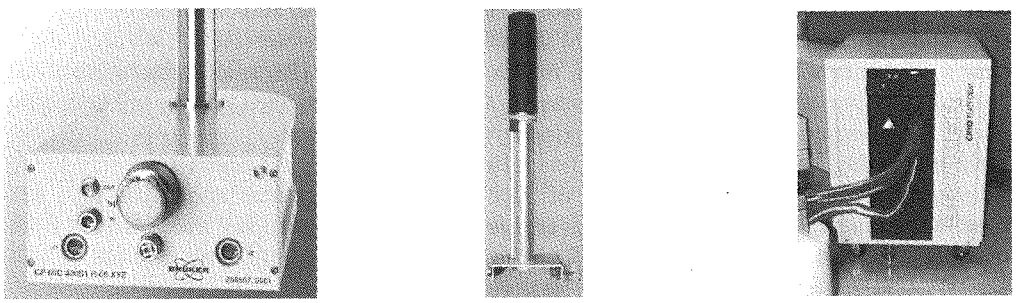

a) b) c)

Fig. 1: a) μI cryogenic probe, b) Gradient system, c) Cooling unit containing the Gifford-McMahon closed cycle cryocooler and associated auxiliary systems. For operation, the probe is inserted into the gradient system and connected to the cooling unit. The cooldown and all subsequent functions of the cooling system are automatic.

An example of data obtained with this probe is shown in Fig. 2.

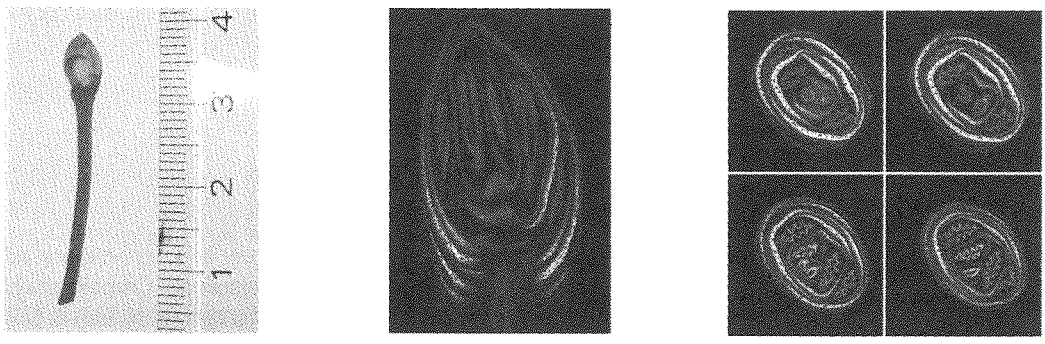

a) b) c)

Fig. 2: Images of a Lilac bud a) obtained at 400MHz using a spin echo method. b) 512 x 256 pixels, 15.6 μm x 15.6 μm resolution, 200 μm slice thickness, TR 750 ms, TE 8.7 ms, 8 averages. Experiment time: 25 min 36 sec. c) 256 x 256 pixels, 19.5 μm x 19.5 μm resolution, 300 μm slice thickness, TR 1000 ms, TE 5.8 ms, 1 average. Experiment time: 4 min 16 sec.

The system has potential for new applications in investigations of plants, insects or other small animals, embryos, histological samples, etc. Studies of the possible benefits with various samples and methods are underway.

INDEX

INDEX

INDEX

INDEX

INDEX

INDEX

INDEX

INDEX

INDEX

INDEX

INDEX

INDEX

INDEX

INDEX

INDEX

INDEX

INDEX

INDEX

INDEX

INDEX

INDEX

INDEX

INDEX

INDEX

INDEX

INDEX

INDEX

List of Attendees

LAST	FIRST	INSTITUTION	EMAIL
Adolphi	Natalie	New Mexico Resonance	nadolphi@nmr.org
Akutsu	Masaaki	LA Systems	akutsu@las.jp
Altobelli	Stephen	New Mexico Resonance	salto@nmr.org
Amar	Andrea	RWTH Aachen - ITMC	aamar@mc.rwth-aachen.de
Aoki	Ichio	Meiji University of Oriental Medicine	aoki@meiji-u.ac.jp
Arns	Christoph H.	Australian National University	christoph.arns@anu.edu.au
Asanuma	Tatsuya	AIST	t-asanuma@aist.go.jp
Balcom	Bruce J.	University of New Brunswick	bjb@unb.ca
Barbic	Mladen	California State University, Long Beach	mbarbic@csulb.edu
Bearer	Elaine	Caltech	ebearer@caltech.edu
Behr	Volker	University of Würzburg	behr@physik.uni-wuerzburg.de
Beyea	Steven	National Research Council Canada	steven.beyea@nrc-cnrc-gc-ca
Blümich	Bernhard	RWTH Aachen - ITMC	bluemich@mc.rwth-aachen.de
Blümler	Peter	MPI for Polymer Research	bluemler@mpip-mainz.mpg.de
Bray	Joshua	Dalhousie University	jmbray@dal.ca
Brown	Jennifer R	Montana State	jbrown@coe.montana.edu
Callaghan	Paul	Victoria University of Wellignton	paul.callaghan@vuw.ac.nz
Casanova	Federico	RWTH Aachen - ITMC	fcasanova@mc.rwth-aachen.de
Codd	Sarah L.	Montana State University	scodd@coe.montana.edu
Coy	Andrew	Magritek Limited	abdrew@magrite.com
Demas	Vasiliki	University of California, Berkeley	vdemas@berkeley.edu
Domoto	Takeo	Bruker Biospin	takeo.domoto@bruker-biospin.jp
Fagiolo	Gianlorenzo	University of Nottigham	gianlorenzo@mclink.it
Fujiwara	Hideaki	Osaka University	fujiwara@sahs.med.osaka-u.ac.jp
Fukushima	Eiichi	New Mexico Resonance	eiichi@nmr.org
Furuya	Takeshi	University of Tsukuba	furuya@mrlab.bk.tsukuba.ac.jp
Gage	Justin P	Montana State	justin_g@erc.montana.edu
Gardner	Sally	Queensland University of Technology	s.gardner@qut.edu.au
Grinberg	Farida	University of Leipzig	grinberg@physik.uni.leipzig.de
Gross	Dieter	Bruker Biospin	dieter.gross@bruker-biospin.de
Haase	Axel	University of Würzburg	haase@physik.uni-wuerzburg.de
Haishi	Tomoyuki	MR Technology, Inc.	haishi@mrtechnology.co.jp
Halse	Meghan	MdDiarmid Institute	meghan@magritek.com
Handa	Shinya	University of Tsukuba	handa@mrlab.bk.tsukuba.ac.jp
Hayamizu	Kikuko	National Institute of Advanced Industrial Science & Technology	hayamizu.k@aist.go.jp
Horigane	Akemi	National Food Research Institute	akhori@nfri.affrc.go.jp

List of Attendees

LAST	FIRST	INSTITUTION	EMAIL
Huang	Susie Y	University of California, Los Angeles	syhuang@chem.ucla.edu
Iita	Nachiko	University of Tsukuba	iita@mrlab.bk.tsukuba.ac.jp
Ikoma	Kazuya	Nishijin Hospital	k-ikoma@mva.biglobe.ne.jp
Imai	Hirohiko	Osaka University	h.imai@sahs.med.osaka-u.ac.jp
Ishida	Nobuaki	National Food Research Institute	nobu@nfri.affrc.go.jp
Ishikawa	Kiyoshi	University of Hyogo	ishikawa@sci.u-hyogo.ac.jp
Jackowski	Karol	University of Warsaw	kjack@chem.uw.edu.pl
Jacobs	Russell	Caltech	rjacobs@caltech.edu
Johns	Michael	University of Cambridge	mlj21@cam.ac.uk
Kanazawa	Yoko	National Institute of Radiological Sciences	y-kana@nirs.go.jp
Karakosta	Eleni	University of Surrey	e.karakosta@surrey.ac.uk
Khrapitchev	Alexandre	The University of New Brunswick	akh@unb.ca
Kim	Mi Jun	Kent State University	mkim2@kent.edu
Kimmich	Rainer	University of Ulm	rainer.kimmich@uni-ulm.de
Kobayashi	Masayuki	JEOL	
Köckenberger	Walter	University of Nottigham	walter.kockenerger@nottingham.ac.uk
Kojima	Tokiko	Saitama Prefectural Government	a0367076@pref.saitama.lg.jp
Komlosh	Michal E	NICHD INIH	michalk@mail.nih.gov
Koptyug	Igor	International Tomography Center, SB	koptyug@tomo.nsc.ru
Kosaka	Ken-ichi	Japan Superconductor Technology	kosaka-jastec@kobelco.jp
Kose	Katsumi	University of Tsukuba	kose@bk.tsukuba.ac.jp
Kremer	Kai	ACT, Aachen Center for Technology	kkremer@mc.rwth-aachen.de
Kuethe	Dean	New Mexico Resonance	dkuethe@nmr.org
Kuribayashi	Hideto	Varian, Inc.	
Kuroda	Yukio	Bruker Biospin	yukio.kuroda@bruker.jp
Kuroki	Shinichiro	Hiroshima University	skuroki@hiroshima-u.ac.jp
Lin	Yung-Ya	University of California	yylin@chem.ucla.edu
Lutti	Antonine	Victoria University of Wellignton	luttianto@scs.vuw.ac.nz
Maddinelli	Giuseppe	EniTecnologie SpA	gmaddinelli@enitecnologie.eni.it
Marble	Andrew	University of New Brunswick	andrew.marble@unb.ca
Marek	Daniel	Bruker Bio Spin AG	daniel.marek@bruker-biospin.ch
Mastikhin	Igor	University of New Brunswick	mast@unb.ca
Masumoto	Hidefumi	University of Tsukuba	masumoto@ctlab.bk.tsukuba.ac.jp
Matsui	Shigeru	University of Tsukuba	matsui@bk.tsukuba.ac.jp
McDowell	Andrew	New Mexico Resonance	amcdowel@nmr.org
Meder	Roger	Queensland University of Technology	r.meder@qut.edu.au
Mikac	Mojoca Urška	Jo ef Stefan Institute	urska.mikac@ijs.si

List of Attendees

LAST	FIRST	INSTITUTION	EMAIL
Mitsumori	Fumiyuki	National Institute for Enviromental Studies	mitumori@nies.go.jp
Muennemann	Kerstin	RWTH Aachen - ITMC	kmuennemann@mc.rwth-
Nagashima	Kazuomi	Tokyo Magnetic Resonance Inc	knaga@tmagres.com
Nakano	Hiroshi	National Institute of Advanced Industrial Science & Technology	nakano@ni.aist.go.jp
Narazaki	Michiko	Osaka University	mnarazaki@usa.net
Navon	Gil	Tel Aviv University	navon@post.tau.ac.il
Nomoto	Masao	JEOL	nomoto@jeol.co.jp
Oerther	Thomas	Bruker Biospin	oerther@bruker-biospin.de
Ogawa	Seiji	Hamano Life Science Research Foundation	ogawa@hlsrf.or.jp
Ogawa	Kuniyasu	Keio University	ogawa@mech.keio.ac.jp
Okada	Fumi	University of Tsukuba	okada@mrlab.bk.tsukuba.ac.jp
Otake	Yousuke	University of Tsukuba	otake@mrlab.bk.tsukuba.ac.jp
Perlo	Juan	RWTH Aachen - ITMC	jperlo@mc.rwth-aachen.de
Prado	Pablo	Quantum Magnetics,	pprado@qm.com
Purea	Armin	University of Würzburg	purea@physik.uni-wuerzburg.de
Reimer	Jeffrey	University of California, Berekley	reimer@berkeley.edu
Saito	Koji	Nippon Steel	saito@re.nsc.co.jp
Salisbury- Ande	Nikolas	University of Nottigham	ppxnsa@nottingham.ac.uk
Sasaki	Yutaka	Kyoto University	sasaki@scphys.kyoto-u.ac.jp
Sasano	Jun	Japan Superconductor Technology	
Seiberlich	Nicole	University of Würzburg	neseiber@physik.uni-
Seki	Mitsuo	Varian, Inc.	mitsuo.seki@varianinc.com
Seo	Yoshiteru	Dokkyo University School of Medicine	yseo@dokkyomed.ac.jp
Serša	Igor	Jo ef Stefan Institute	igor.sersa@ijs.si
Seymour	Joseph	Montana State	jseymour@coe.montana.edu
Song	Yi-Qiao	Schlumberger	ysong@SLB.COM
Stapf	Siegfried	RWTH Aachen - ITMC	sstapf@mc.rwth-aachen.de
Stoch	Gregory	University of New Brunswick	stoch@unb.ca
Suga	Mikio	Chiba University	mikio.suga@faculty.chiba-u.jp
Sugihara	Fuminori	Yokohama City	buntoku@tsurumi.yokohama-
Tanaka	Ryo	Toyoko Kagaku, Co.	tanaka-ryo@toyoko-jp.com
Tomiha	Sadanori	University of Tsukuba	tomiha@mrlab.bk.tsukuba.ac.jp
Ueki	Sadao	Bruker Biospin	
Utsuzawa	Shin	MR Technology, Inc. / University of Tsukuba	utsuzawa@mrtechnology.co.jp
Voelkel	Ruediger	BASF AG	ruediger.voelkel@basf-ag.de
Waggoner	R. Allen	RIKEN - Brain Science Institute	raw@postman.riken.go.jp
Wakamatsu	Hisanori	Dokkyo University School of Medicine	h-waka@dokkyomed.ac.jp
Walton	Jeffrey	Univeristy of California	jhwalton@ucdavis.edu

List of Attendees

LAST	FIRST	INSTITUTION	EMAIL
Watanabe	Tokuko	Aoyama Gakuin	tokuko@luce.aoyama.ac.jp
Windt	Carel	Wageningen University	carel.windt@wur.nl
Xia	Yang	Oakland University	xia@oakland.edu
Yamaguchi	Masayuki	National Institute for Enviromental Studies	d52m-ymgc@asahi-net.or.jp
Yooyongwech	Suravoot	University of Tsukuba	yooyongwech@yahoo.com
Yoshida	Mitsuru	National Food Research Institute	mitsuru@nfri.affrc.go.jp
Zanker	P.P.	MPI for Polymer Research	